Crust formation and thermal history of Mars

Valentin Bonnet Gibet

THESE

en vue de l'obtention du grade de Docteur, délivré par

l'ECOLE NORMALE SUPERIEURE DE LYON

École Doctorale N° 52
PHYSIQUE ET ASTROPHYSIQUE

Discipline : Sciences de la Terre
Spécialité : Géodynamique

Soutenue publiquement le 23/10/2023, par :

Valentin Bonnet Gibet

Crust formation and thermal history of Mars

-

Formation de la croûte et histoire thermique Martienne

Devant le jury composé de :

BARATOUX, David Directeur de recherche	Université Félix Houphouët-Boigny	Rapporteur
CHOBLET, Gaël Directeur de recherche	Nantes Université	Rapporteur
SAUTTER, Violaine Directrice de recherche	Sorbonne Université	Examinatrice
LABROSSE, Stéphane Professeur des universités	ENS de Lyon	Examinateur
WIECZOREK, Mark Directeur de recherche	Université Paris Cité	Examinateur
MICHAUT, Chloé Professeure des universités	ENS de Lyon	Directrice de thèse

Laboratoire de Géologie de Lyon
Adresse
46 Allée d'Italie
69007 Lyon, France

École doctorale PHAST
Université de Lyon

Optimism is a moral duty.

Karl Popper

Remerciements

Je voulais tout d'abord remercier mon jury pour m'avoir accordé le titre de docteur après une soutenance dont je garderais un très bon souvenir avec une très belle discussion qui m'aidera pour la suite de ma carrière.

Chloé, merci pour tout, tu m'as beaucoup apporté pendant ces trois années et demie. Travailler avec toi a toujours été un plaisir, tu es exigeante et juste et tu m'as poussé vers le haut. C'est un honneur d'avoir pu faire une recherche de qualité à tes côtés et j'espère que ce n'est qu'un début. Mark, merci, même si nous avons été moins en contact tu as toujours été présent quand j'en avais besoin.

Chères collègues doctorantes et doctorants qui m'ont accompagné, merci pour tout. D'abord merci aux anciens, Samuel, PJ, Chloé, Jean, Dédé, Quentin, Mélie, Auguste de m'avoir accueilli au laboratoire et merci aussi pour les soirées, j'espère qu'on se recroisera. Gros merci aux collègues de l'équipe, Line, Alexandra et Kathryn, pour tout le soutien et les moments passés en conférences. Cette équipe va perdurer et on aura plein d'occasion de se revoir ! Marwan, Valentine, Enguerrand, Asma et Cécile merci pour cette bonne ambiance de groupe que vous contribuez à instaurer. Clothilde et Camille, bon courage pour votre thèse qui débute, je suis convaincu que vous irez loin ! Danaé, merci pour tous. Et je n'oublie pas les collègues de la Doua, Anastasis, Auriane, Théo, Alex, Marine et les autres !

Merci au LGLTPE de m'avoir accueilli. Notamment Marie-Jeanne, merci pour ta patiente et ton empathie. Merci Manu, Aline, Salomé, Marianne, Marine, Laurence, Francis, Bruno, Bernard, Guillemette, Mathieu, Mathieu, Thierry, Julien, Hervé et j'en oublie. Fred, ça a été un plaisir de donner des cours à tes côtés et de discuter avec toi. Stéphane, merci encore une fois, toujours des échanges enrichissants. Merci Thomas pour ce que tu m'as apporté avec le Bayésien, toujours heureux de pouvoir échanger avec toi. Merci Fabien pour ton efficacité pour le code et pour les TP de méthodes numériques, j'ai beaucoup apprécié de les faire.

Merci aux membres de l'équipe Française de la mission InSight. Merci surtout à Daniele, pour m'avoir accompagné dans mon comité de suivi, tes conseils et discussions ont été précieux. Aymeric et Clément, super rencontres et beaucoup de rigolade ! Merci aussi à Henri, Mélanie, Zongbo, Marouchka et tous les autres ! Et surtout merci à Philippe d'avoir leader l'ANR avec tant de succès, ce fut un plaisir de participer à cette aventure. Merci aussi à l'équipe internationale d'InSight, c'était une aventure

incroyable que de suivre cette mission de l'intérieur.

Merci à tous les nantais qui m'ont toujours poussé vers la recherche. Merci Gabriel, Gaël et Christophe pour m'avoir pris en stage de master et d'avoir été là après. Merci à tous les enseignants qui m'ont donné des connaissances solides qui m'ont permis de réussir ma thèse.

Merci à tous mes potes, je ne pourrais pas vous remercier tous, mais vous vous reconnaitrez. Mais surtout merci Mégane, d'avoir été la meilleure pote et colocataire que j'aurais pu espérer, quitter Lyon c'est aussi la fin de notre vie ensemble et même si ça me rend triste, je garderai un très bon souvenir de ces deux ans de vis communes. Quentin, deuxième meilleur colocataire mais premier dans l'ordre chronologique ! Une rencontre improbable mais incroyable ! Anissa t'es la plus belle rencontre que j'ai faite à Lyon, force à toi pour la suite, t'es une girl boss. Vincent, Alexandre, Kasty et Charlet : merci d'être con, j'espère que vous le resterez qu'on continue de bien rigoler. Merci surtout à Charlet de m'avoir accueilli sur Lyon. Anthony (Aka Ricard) merci encore pour le punch, t'es un roi. Fabilo, Johann et les autres lyonnais que j'ai pu rencontrer, merci d'avoir été là. Merci Nicolas d'être un vrai frère même après tout ce temps (8 ans quand j'écris ces lignes). Merci Constant et Guillaume pour les bières. Marie W cœur sur toi ! Merci le 8.6 crew, malgré les épreuves notre groupe est toujours aussi unis. Pauline, merci de m'avoir accompagné durant ces trois années de thèse d'avoir été un soutien de tous les jours.

Pour finir je voulais remercier ma famille, mes sœurs, mes oncles, mes cousins merci d'avoir été là pour me soutenir et j'espère que j'ai pu vous rendre fières. Aude, Aurore, merci d'avoir toujours été des sœurs aimantes et protectrices. Merci Papa et Maman, ma réussite est en partie la vôtre. Nous sommes passés par tellement d'épreuves, notre vie à tous les trois n'a pas été toujours simple, mais vous n'avez jamais hésité à tout sacrifier pour que je réussisse.

Table des matières

Préambule **1**

1 Mars, sa croûte et sa dichotomie, état des connaissances scientifiques **5**
1.1 Croûte Martienne marquée par une dichotomie hémisphérique 5
1.1.1 La Dichotomie Hémisphérique 5
1.1.2 Limite spatiale de la dichotomie 6
1.1.3 Trois unités géologiques principales 8
1.2 Géochimie martienne 12
1.2.1 Météorites martiennes 12
1.2.2 Observations orbitales et in-situ 15
1.2.3 Une composante felsique dans les Hauts Plateaux 16
1.2.4 Modèles de composition martienne 17
1.3 Structure interne 18
1.3.1 Modèles d'épaisseur de croûte 18
1.3.2 Structure de la croûte 21
1.3.3 Noyau martien 25
1.3.4 Manteau 27
1.4 Formation, différentiation et évolution thermique de Mars 30
1.4.1 Formation et Différentiation 30
1.4.2 Évolution thermique et Convection solide 33
1.5 Formation de la dichotomie, évènement crucial de l'Histoire Martienne 39
1.5.1 Une origine endogénique 40
1.5.2 Une origine exogénique 44
1.5.3 Discussion 47
1.6 Problématique 48

2 An Asymmetric parameterised thermal evolution model of Mars **51**
2.1 Introduction 51
2.2 Thermal modelling 52
2.3 Mantle melting and crust extraction 54
2.3.1 Mantle melting 54
2.3.2 Crust extraction 57
2.4 Lid advection, Magma heating and crustal melting 58
2.4.1 Downward advection due to crust growth 58
2.4.2 Magma heating 60

2.4.3 Crustal melting . . . 61
2.5 Radioactive heat production and HPE distribution . . . 63
2.6 Thermal evolution . . . 65
2.6.1 Heat conservation in the core and mantle . . . 65
2.6.2 Growth of the lid . . . 66
2.6.3 Conservation of heat in the conductive lid . . . 66
2.6.4 Geometry . . . 67
2.7 Dimensionless numbers and critical parameters of the model . . . 67
2.8 Numerical Resolution . . . 68

3 A positive feedback mechanism between crustal thickness and melt extraction 69
3.1 Introduction . . . 69
3.2 Study of the instability for a simplified setup . . . 72
3.3 Model . . . 76
3.4 Initial Parameters, Reference case and Crustal Thickness Constraints . . . 76
3.4.1 Initial state . . . 76
3.4.2 Present-day crustal thickness of Mars from topography and gravity data . . . 77
3.5 Results . . . 78
3.5.1 Reference simulations . . . 78
3.5.2 Exploration of the effects of other model parameters . . . 85
3.6 Discussion . . . 90
3.6.1 Positive feedback mechanism . . . 90
3.6.2 Origin of the degree-one structure . . . 90
3.6.3 Crust enrichment in HPE . . . 91
3.6.4 Melt extraction and formation of a crust of limited thickness . . . 92
3.6.5 Crust construction and volcanism on Mars . . . 92
3.6.6 Insight results on Mantle structure . . . 94
3.6.7 Interpretation of Bouguer anomalies in terms of crustal thickness 94
3.7 Summary . . . 95

4 Asymmetric vs Symmetric thermal evolution 97
4.1 Introduction . . . 97
4.2 Observations . . . 98
4.2.1 Crustal thickness and dichotomy amplitude . . . 98
4.2.2 Present-day thermal state of the Martian mantle . . . 101
4.3 Systematic exploration . . . 102
4.3.1 Exploration method . . . 102
4.3.2 Exploration results . . . 105
4.4 Inversion using a Monte Carlo Markov chain algorithm . . . 113
4.4.1 Bayesian inverse problem . . . 113
4.4.2 Prior distribution . . . 113

4.4.3 Likelihood function . . . 114
4.4.4 Monte Carlo - Markov chain (MCMC) algorithm . . . 116
4.4.5 Initial thermal state . . . 117
4.5 Inversions Results . . . 117
4.5.1 Marginal distribution . . . 118
4.5.2 Posterior distribution of the Model outputs . . . 120
4.5.3 Best fitting model . . . 124
4.5.4 Joint distributions with the initial perturbation. . . . 126
4.6 Discussion . . . 128
4.6.1 Asymmetric vs symmetric geometry . . . 128
4.6.2 Comparison of asymmetric and symmetric parametric models with 3D ones . . . 130
4.6.3 Learning from the Bayesian inversion . . . 131
4.6.4 Difference of the model with the previous version . . . 134
4.6.5 Dichotomy formation . . . 135
4.7 Conclusion . . . 136

5 Martian Highlands differentiation **139**
5.1 Introduction . . . 139
5.2 Crustal solidus . . . 142
5.3 Systematic exploration . . . 145
5.3.1 Exploration description . . . 145
5.3.2 Exploration results . . . 145
5.4 Results of the inversion on crustal melting . . . 147
5.4.1 Inversion with crustal melting . . . 147
5.4.2 Marginal distributions . . . 148
5.4.3 Posterior distribution of different ouput . . . 150
5.4.4 Examples of thermal evolution with crustal melting . . . 152
5.4.5 Crustal meltings output . . . 155
5.4.6 2D joint distribution . . . 157
5.5 Discussion . . . 160
5.5.1 Partial melting of the crust and differentiation of the Southern Highlands . . . 160
5.5.2 Terra Cimmeria-Sirenum : A continental crust under formation . 162
5.5.3 Improving constraints on Highland differentiation. . . . 164
5.6 Conclusion . . . 165

6 Perspectives **167**
6.1 La lithosphère martienne est-elle assez résistante pour soutenir la dichotomie ? . . . 167
6.2 Un manteau lithosphérique fertile et primitif ? . . . 170
6.3 Un Volcanisme actuel sous Tharsis est-il possible ? . . . 172

Conclusion **177**

Appendix - A - Numerical resolution **181**

Appendix - B - Origin of lateral variation in crustal thickness on Mars and Mercury. **189**

Bibliographie **197**

Préambule

Le 26 novembre 2018, la mission InSight s'est posée sans encombre à la surface de Mars dans la région d'Elysium Planitia. Quelques mois plus tard, le premier sismomètre (SEIS) posé sur la surface martienne, contrairement aux missions *Viking* 1 et 2, était en fonctionnement. Le 7 avril 2019, le premier séisme martien est enregistré par le sismomètre et ouvre une nouvelle ère pour l'étude de Mars. Au total, 90 tremblements de Mars ("marsquakes"), 6 impacts et 1319 évènements sismiques seront enregistrés par la mission. Ces données ont permis de sonder l'intérieur de Mars et de contraindre, entre autres, l'épaisseur de la croûte, du manteau et du noyau. Mais InSight est loin d'être la première mission vers Mars. 22 missions martiennes ont réussi leurs objectifs avec différentes architectures, survols, orbiteurs, landers, ou rovers.

Mars est la quatrième planète du système solaire avec un rayon moitié moins grand que celui de la Terre, $R_p \approx 3390$ km. Mars est visible à l'œil nu depuis la Terre, ses paramètres orbitaux ont ainsi été déterminés tôt dans l'histoire des sciences. Son volume et sa masse sont respectivement 15% et 11% de ceux de la Terre et sa gravité, le tiers. Sa densité moyenne est de 3.93 g cm^{-3}, nettement inférieure à celle de la Terre. La planète tourne autour du soleil en un peu moins de deux années terrestres (686 jours) et un jour martien, un sol, équivaut à un peu plus d'un jour terrestre (24,62 h).

Les missions d'exploration ont, au fil des années, précisé la description de Mars. Les premiers survols ont montré une planète présentant d'importants volcans, comme Olympus Mons, le plus grand du système solaire. La surface est un désert minéral parsemé de dunes de sable rouge qui donne sa couleur caractéristique à Mars. L'atmosphère ténue et l'absence de champ magnétique en font une surface totalement inhabitable pour l'homme. Deux calottes polaires composées majoritairement de glace de CO_2 contrastent avec le reste de la planète. De larges bassins d'impact jonchent la surface, parmi les plus grands du système solaire. Une importante dichotomie hémisphérique coupe la planète en deux : Les Basses Plaines dans l'hémisphère nord et les Hauts Plateaux de l'Hémisphère sud. La température de surface est en moyenne de ~ -70°C et la pression de surface est de 6.0 mbar (moins de 1% de la pression atmosphérique terrestre) ; ces conditions ne permettent pas la présence de l'eau liquide en surface.

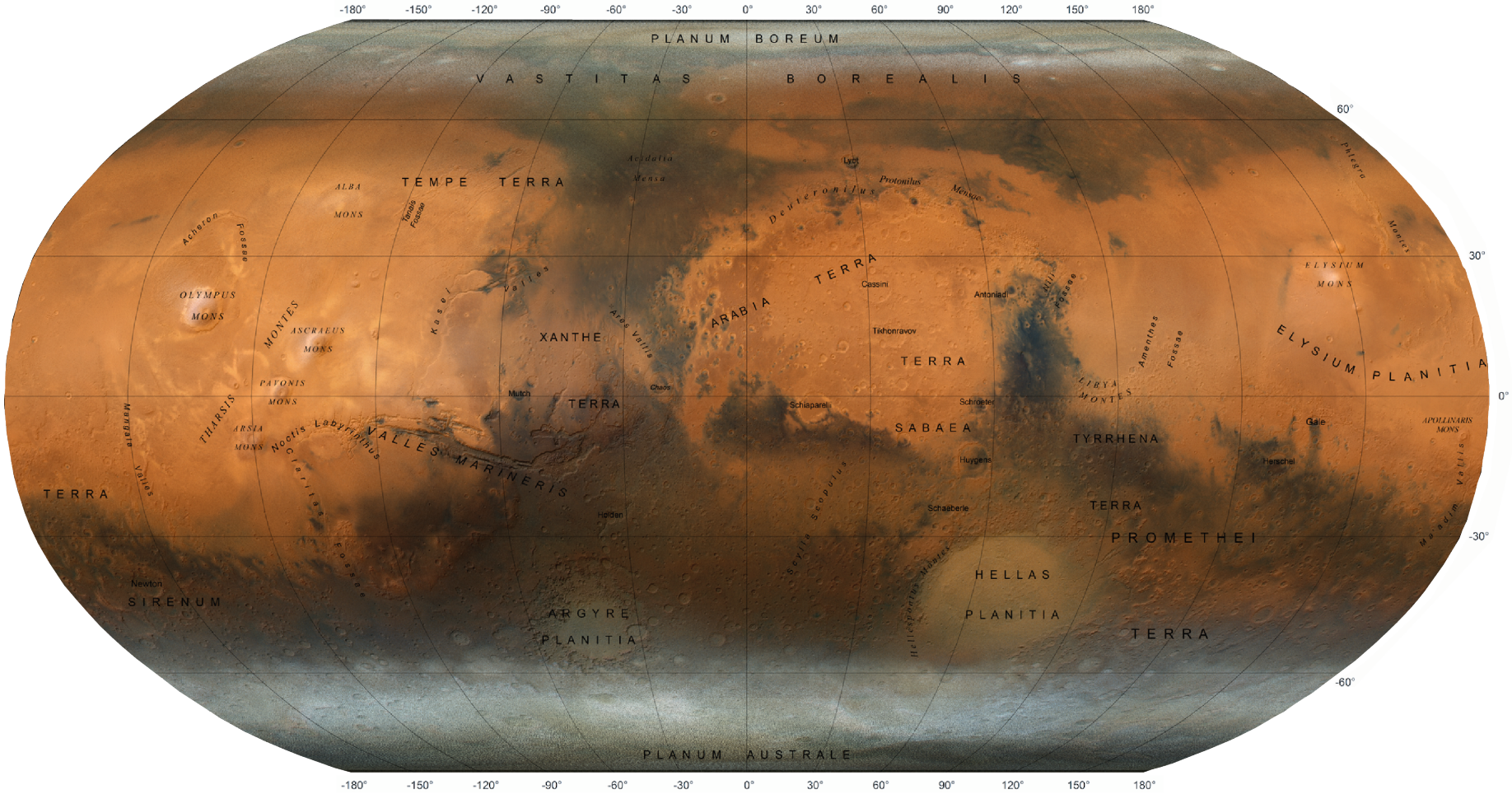

Plus de 3000 observations de l'instrument EXI à bord de la sonde Hope ont été assemblées pour créer cette image globale composite en couleur de Mars. Les données EXI ont été obtenues auprès du SDC (Emirates Space Data Center) et le relief ombragé est obtenu à partir des données d'élévation MOLA. Les structures indiquées viennent de la base de données de l'Union astronomique internationale avec les noms données par l'USGS. La carte utilise le système de coordonnés Mars 2000 et la projection Robinson. L'outil ArcMap a été utilisé pour combiner l'image globale avec les ensembles de données susmentionnés. Carte produite par Abdullah al Ateqi, Dimitria Atri et Dattraj B. Dhuri de l'Université de New York, Abu Dhabi. Carte disponible au lien suivant : https ://marsatlas.org/mars/maps

La surface a été ensuite imagée de manière précise par les sondes depuis l'orbite. D'autres structures géologiques furent décrites, comme des delta ou des chenaux inversés dans les Hauts Plateaux, caractéristiques d'un cours d'eau liquide. L'eau aurait coulé par le passé sur Mars. Des deltas, des lacs et même peut-être un océan sont observés à la surface de Mars ainsi que des roches sédimentaires détritiques et d'altération. Un cycle de l'eau a persisté sur Mars il y a 3.5 milliards d'années. Comment est-ce qu'une planète ayant présenté un cycle de l'eau par le passé peut être à présent un désert plus sec que le plus sec des déserts terrestres ? Le consensus actuel est la perte de l'atmosphère martienne à cause du vent solaire. La faible gravité de Mars a pour conséquence une faible vitesse libération, contrairement à la Terre et Vénus, des planètes telluriques avec une importante atmosphère. Le vent solaire peut alors facilement éroder l'atmosphère surtout depuis qu'un champ géomagnétique ne la protège plus. L'atmosphère martienne avait une pression plus importante avec un effet de serre et une température de surface plus chaude permettant la stabilité de l'eau liquide. Néanmoins, le climat de cette période ne fait pas encore consensus, il serait soit chaud et humide soit froid et sec.

L'habilité de Mars aurait été possible dans le passé, il y a $\sim$3.5-4 milliards d'années. Or, l'âge estimé de l'apparition de la Vie sur Terre est de 3.8 milliards d'années, donc Mars et la Terre aurait eu des conditions habitables en même temps. Quasiment toutes les roches terrestres de cette époque ont disparu à cause de la tectonique des plaques rendant difficile la découverte de traces de vie ancienne sur Terre. La surface de Mars est ancienne, la grande majorité des terrains ont plus de 3.4 milliards. On peut voir Mars comme un fossile de surface planétaire, préservé jusqu'à nos jours. Si la vie est apparu simultanément sur Terre et Mars, on a potentiellement plus de chance d'en trouver des traces sur Mars. Les missions Curiosity et Perseverance ont d'ailleurs détecté des traces de molécules organiques complexes à la surface. Une météorite martienne, ALH84001, a été au centre d'une controverse scientifique pour savoir si elle présentait des traces d'une vie martienne ancienne.

Mars est un objet d'étude assez unique dans le système solaire où toutes les principales disciplines des sciences de la Terre peuvent apporter une contribution dans la description présente ou passée de Mars. Grâce aux nombreuses missions d'explorations, Mars est, après le système Terre-Lune, la planète qu'on connait le mieux dans le système solaire. On peut alors commencer à comparer ces deux planètes. D'un côté la Terre est une planète avec une tectonique des plaques, un cycle de l'eau en activité, de la vie et de l'autre côté Mars est une planète volcanique avec un cycle de l'eau arrêté et pour le moment pas de trace de vie. Mieux comprendre le fonctionnement d'une planète tellurique nécessite de comprendre l'origine de ces différences. La planétologie comparée permet cela, mieux comprendre la Terre grâce aux autres planètes c'est mieux comprendre les autres planètes grâce à la Terre. L'étude de Mars permet de comprendre les processus géologiques à l'œuvre au début du système solaire sur les

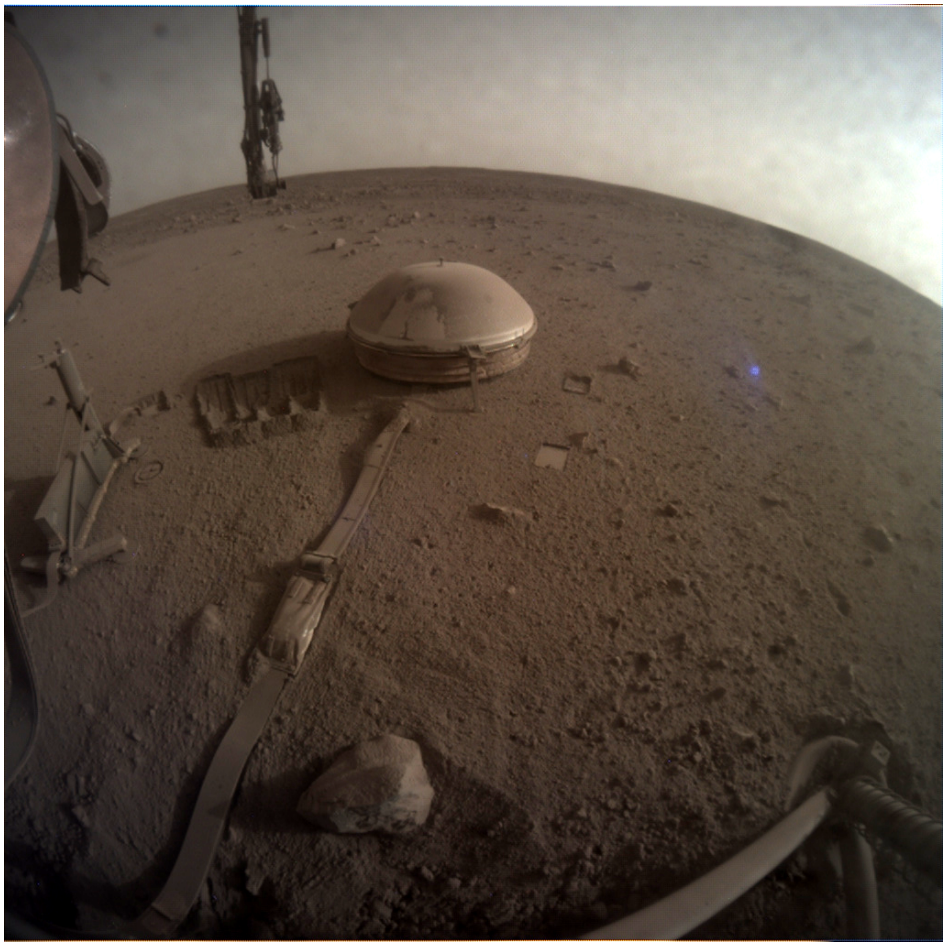

Légende : Cette image a été acquise le 11 décembre 2022, Sol 1436 de la mission InSight où l'heure solaire moyenne locale pour les expositions de l'image était 17 :21. Dernière Photo transmise par la sonde InSight avant son entrée en "Safe Mode" et la déclaration de la fin de la mission dans les jours suivants.

planètes telluriques dont les traces ont été effacées sur Terre.

Le 20 décembre 2022, la mission InSight ne répond plus aux communications avec la Terre et la mission s'achève en ayant apporté de toutes nouvelles contraintes sur l'intérieur de Mars. Ces nouvelles observations ont répondu à un certain nombre de questions, mais en soulèvent plus encore. Cet engouement pour l'étude de l'intérieur martien, poussé par la mission, est aussi le temps de revenir sur des questions qui n'ont pas été totalement répondus, comme la formation de la dichotomie. C'est dans ce contexte de fin de mission et à la lumière de ces nouvelles données que s'est déroulée ma thèse. J'ai, pendant ces trois ans, étudié la formation de la croûte et l'histoire thermique martienne en essayant d'apporter mon humble contribution à l'aventure collective qu'est la recherche scientifique.

Chapitre 1

Mars, sa croûte et sa dichotomie, état des connaissances scientifiques

1.1 Croûte Martienne marquée par une dichotomie hémisphérique

La dichotomie martienne entre les hémisphères nord et sud est la structure principale de la surface martienne. Elle a été mise en évidence très rapidement avec les premières mosaïques fournies par les missions *Mariner* 4, 6, 7 et surtout 9 (Hartmann, 1973; Mutch et al., 1976). Elle a été décrite dans un premier temps comme une dichotomie d'aspect, notamment par la quantité de cratères d'impacts, très différente entre les deux hémisphères. Le développement des missions orbitales dans les décennies suivantes a permis de définir que la dichotomie n'était pas seulement d'aspect, mais aussi une dichotomie de topographie, d'épaisseur de la croûte, de champ magnétique crustal, de géologie et de composition (Watters et al., 2007).

1.1.1 La Dichotomie Hémisphérique

Topographie Martienne

La mission Mars Global Surveyor et son instrument Mars Orbiter Laser Altimeter (MOLA) ont mesuré la topographie de la surface martienne avec une très haute résolution verticale et spatiale (Smith et al., 2001). La topographie est marquée par une forte différence entre l'hémisphère nord et sud (Figure 1.1a) avec une distribution bimodale des altitudes (Smith et al., 2001; Watters et al., 2007; Bouley et al., 2020). L'hémisphère sud est caractérisé par des hauts topographiques et l'hémisphère nord par les bas topographiques. La dichotomie d'aspect de surface est fortement corrélée spatialement avec la dichotomie de topographie. Les unités ont été nommées en lien avec leur topographie, avec les Basses Plaines ("Lowlands") dans l'hémisphère nord et les Hauts Plateaux dans l'hémisphère sud ("Highlands"). La transition d'une unité à l'autre est plus ou moins abrupte en fonction de la longitude avec des dénivelés relati-

vement faibles dans la région d'Arabia Terra et beaucoup plus importants vers Syrtis Major (Figure 1.1a). Un simple modèle isostatique d'Airy, où la topographie est expliquée totalement par un relief à l'interface croûte-manteau, permet d'expliquer la topographie par une forte différence d'épaisseur de croute ($\approx$ 40 km) entre les deux hémisphères (Figure 1.1b, Andrews-Hanna et al. 2008a).

Champ magnétique crustal

Lorsqu'une roche se forme à partir d'un magma, elle enregistre le champ magnétique ambiant et le fossilise en refroidissant sous la température de Curie. Un champ magnétique crustal rémanent a pu être détecté depuis l'orbite par différentes missions (MGS et MAVEN) et son intensité en surface a pu être déterminée par calcul (Purucker et al., 2000; Langlais et al., 2019). L'hémisphère sud présente des anomalies magnétiques de très grande amplitude ($>$ 100 nT) et l'hémisphère nord n'est magnétisé qu'en partie, montrant de faibles intensités. La forte intensité du champ magnétique crustal est la démonstration de l'existence d'une ancienne dynamo martienne à l'époque de la formation de la croûte des Hauts Plateaux (Acuña et al., 1999). Les bassins d'impact Hellas et Argyre (Figure 1.1a) ne présentent pas de magnétisation, la dynamo martienne devait alors être déjà arrêtée au moment de leurs formations, datés à $\sim$4.3 Ga (Giga-années). Les impacts responsables de leurs formations auraient supprimé le champ magnétique crustal pré-existant sans en former de nouveau en l'absence de champ magnétique global (Acuña et al., 1999).

1.1.2 Limite spatiale de la dichotomie

Deux provinces géologiques, caractérisant chaque hémisphère, émergent des observations avec des caractéristiques distinctes. La première étape dans la description de ces provinces est de définir une délimitation précise. Or, ce n'est pas une tâche aisée, car la transition entre les deux provinces est très hétérogène et a été retravaillée par différents processus (érosion, impacts, tectonique). Neumann et al. (2004) définissent la limite entre ces deux unités à l'aide d'un critère d'épaisseur de croûte : les Hauts Plateaux de l'hémisphère sud ont une croûte d'épaisseur supérieure à 40 km et les Basses Plaines de l'hémisphère nord des épaisseurs inférieures à 40 km, en comptant les bassins d'impact Argyre et Hellas dans les Hauts Plateaux. Cette limite a une forme complexe et sinueuse et comprend dans les Hautes Terres le dôme volcanique de Tharsis. Les observations tectoniques (Andrews-Hanna et al., 2008b) et d'anomalies dans le champ de gravité (Phillips et al., 2001) pointent vers une mise en place de Tharsis après la formation de la dichotomie. Andrews-Hanna et al. (2008a) proposent une limite de la dichotomie déterminée suivant le maximum du gradient d'épaisseur de croûte après avoir retiré la contribution de Tharsis sur l'épaisseur crustale. Cette méthode permet de distinguer une limite de la dichotomie sous et au travers du dôme de Tharsis. Néanmoins, la limite de la dichotomie dans la région de Arabia Terra n'est pas claire, la topographie et l'épaisseur de croûte y sont intermédiaires entre les Hauts Plateaux et

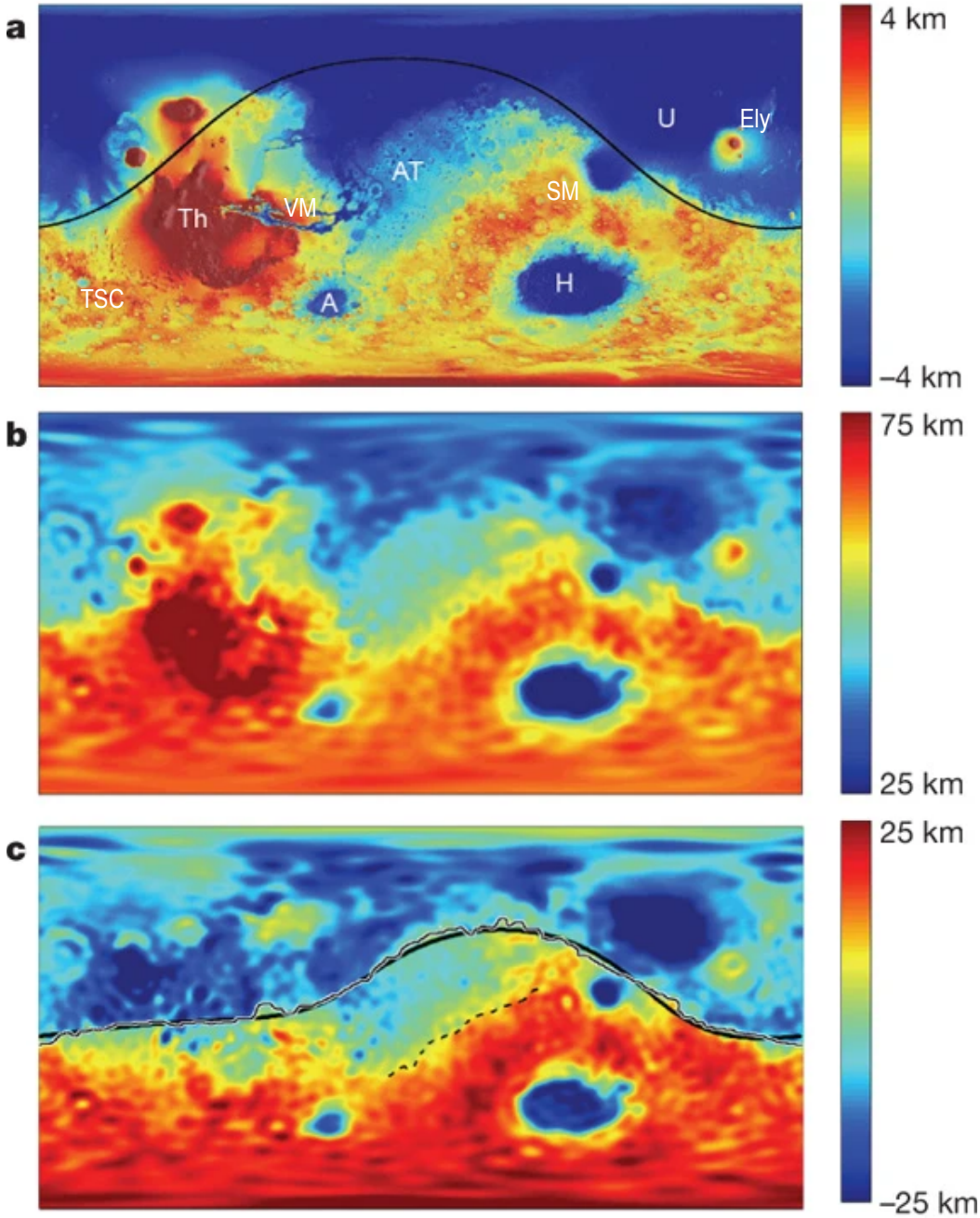

FIGURE 1.1 – (a) Topographie (Smith et al., 2001) et (b) épaisseur de la croûte martienne (projection cylindrique, Neumann et al. 2008). Les principales provinces indiquées en (a) comprennent Tharsis (Th), Arabia Terra (AT), Hellas (H), Argyre (A) et Utopia (U), Elysium (Ely), Syrtis Major (SM), Terra Sirenum Cimmeria (TSC), Valles Marineris (VM) ainsi que le contour du bassin Borealis proposé par Wilhelms and Squyres (1984) (ligne continue). (c) Perturbation modélisée de l'épaisseur de la croûte (racine isostatique), montrant la continuation de la limite de dichotomie sous Tharsis. La limite de dichotomie observée (ligne fine) est comparée à la meilleure ellipse (ligne en gras). La rupture de pente séparant Arabia Terra des hautes terres est représentée par une ligne en pointillés. Figure issue de Andrews-Hanna et al. (2008a)

les Basses Plaines du nord (Figure 1.1a). Arabia Terra présente des anomalies magnétiques de forte intensité, comme dans le reste des Hauts Plateaux, ce qui justifie que la région y soit inclue. Dans cette conformation, la limite de la dichotomie de Andrews-Hanna et al. (2008a) est très proche d'une ellipse de 10 600 × 8 500 km^2 centrée dans l'hémisphère nord (67°N - 208°E), la province des Basses Plaines représentant 42% de la surface de Mars.

Âge de la surface et de la dichotomie martienne

La surface martienne est ancienne et son échelle des temps géologiques est divisée en trois périodes stratigraphiques : le Noachien, l'Hespérien et l'Amazonien (Tanaka, 1986). L'échelle des temps géologiques selon Hartmann and Neukum (2001) donne des estimations d'âge absolu de ces périodes. Le Noachien s'étendrait du début de l'histoire de Mars il y a approximativement 4.5 Ga jusqu'à 3.7 Ga. La transition entre le Noachien et l'Hespérien est marquée par un changement global dans le registre sédimentaire, avec un registre Noachien composé majoritairement de phyllosilicates et un registre Hespérien où les dépôts de sulfates deviennent majoritaires. Ce changement est attribué soit à un changement climatique, soit à un large dégazage de soufre volcanique (Bibring et al., 2006). La transition vers l'Amazonien est moins nette avec un âge estimé entre 3.2 et 2 Ga. La dichotomie martienne est aussi présente dans les âges des surfaces, les Hauts Plateaux ont des âges Noachien - Hespérien alors que les Basses Plaines des âges Hespérien - Amazonien (Figure 1.2, Tanaka et al. 2014).

L'âge de la dichotomie est relativement peu contraint, mais il s'agit de l'une des caractéristiques les plus anciennes de la surface martienne, qui affecte la majorité des formations géologiques (Andrews-Hanna et al., 2008a; Di Achille and Hynek, 2010; Andrews-Hanna, 2012). Gurgurewicz et al. (2022) ont détecté une importante zone de cisaillement dans la région de Valles Marineris, proche de la dichotomie, âgée du début du Noachien. La dichotomie aurait alors un âge compris entre 4.3 et 4.5 Ga, bien plus ancien que l'âge de la surface des Basses Plaines (≈ 3.7 - 3.2 Ga). D'autre part, des indices de mouvement tectoniques le long de la limite de la dichotomie donne un âge de 3.7 Ga pour la formation de la dichotomie (McGill and Dimitriou, 1990). Avec cet âge plus récent, la dichotomie serait contemporaine à la formation de la surface des Basses Plaines.

1.1.3 Trois unités géologiques principales

Hauts Plateaux

Les Hauts Plateaux martiens forment une province géologique très cratérisée et avec une topographie irrégulière : la rugosité de surface y varie de 2 à 25 m (Garvin et al., 1999). Les cratères sont en grande partie des cratères d'impacts et des formations volcaniques dans une moindre mesure. Ce nombre important de cratères d'impact est caractéristique d'une surface ancienne. L'âge des Hauts plateaux est majoritairement

Noachien avec quelques provinces Hespériennes vers Syrtis Major (Figure 1.2a-b). La province comporte un grand nombre d'édifices volcaniques de relativement petite taille, entre 50 et 100 km de rayon et entre 2 et 3 km de haut, principalement situés au sud de Tharsis (Xiao et al., 2012). Ces volcans sont de type bouclier et représentatifs du volcanisme du début du Noachien. Des structures de types super-volcans, avec une faible topographie et une grande superficie, ont été détectées dans la région de Arabia Terra. Ces volcans seraient de type explosif, ce qui serait en accord avec l'observation de dépôts pyroclastiques volumineux dans la région (Brož et al., 2021). Le volcanisme explosif est moins courant que l'effusif, mais il est caractéristique des Hauts Plateaux. Les patera (caldéra extra-terrestre) de Hadriacuse et Tyrrhenus Montes sont celles des deux principaux volcans explosifs martiens, au nord-est du bassin d'Hellas (Williams et al., 2007, 2008). Les eaux souterraines et/ou les éléments volatils présents dans le liquide magmatique seraient responsables du caractère explosif de ces volcans (Brož et al., 2021). De manière plus générale, le volcanisme explosif a été important au début de l'Héspérien avant de revenir vers un volcanisme plus effusif au début de l'Amazonien (Robbins et al., 2011) ; le rôle de ce type de volcanisme sur le climat de L'Hespérien serait crucial (Brož et al., 2021). Les observations d'émissivité thermiques par l'instrument THEMIS (Thermal Emission Imaging System) renseignent sur la consolidation des roches de surface. Bandfield et al. (2013) ont déterminé par cette méthode que la surface des Hauts Plateaux était formée de fines particules peu consolidées. Les volcans explosifs génèrent de grandes quantités de dépôts pyroclastiques qui, avec les éjectas d'impacts, expliquent ces observations. Cette couche peu consolidée aurait des épaisseurs variables entre 2 et 10 km selon les endroits (Robbins et al., 2011; Bandfield et al., 2013; Wieczorek et al., 2022).

Une autre caractéristique importante des Hauts Plateaux est leurs réseaux de paléo-vallées fluviatiles (Carr, 1987; Hynek et al., 2010). Les importants réseaux de vallées impliquent un climat permettant la stabilité de l'eau liquide sur Mars. Ces réseaux ont drainé d'importantes quantités de sédiments vers les Basses Plaines du nord (Hynek et al., 2010). Ces réseaux se seraient formés pendant la transition du Noachien à l'Hespérien (3.6 - 3.8 Ga) et auraient fonctionné jusqu'au début de l'Amazonien (2.5 Ga). La présence de ces réseaux de vallées et de lacs dans les Hauts Plateaux sont une des preuves les plus évidentes d'un cycle de l'eau sur le long terme sur Mars. Une autre preuve importante est la présence de phyllosilicates sur Mars (Poulet et al., 2005), ces minéraux étant formés par l'altération aqueuse des silicates (Gaudin et al., 2011). Ces minéraux d'altération sont présents dans l'ensemble des Hauts Plateaux, le long de la dichotomie et dans une moindre mesure les Basses Plaines (Carter et al., 2023). Ils sont systématiquement présents dans les terrains du Noachien avec potentiellement d'importants volumes (Carter et al., 2023). La quantité d'eau stockée dans ces minéraux pourrait être très importante et elle nécessite d'être prise en compte dans les modèles d'évolution climatique martiens (Riu et al., 2022). L'intérêt exobiologique de ces minéraux est aussi important, car ils sont des lieux privilégiés de la conservation de matière organique et de bio-signature (Quantin-Nataf et al., 2021; Anderson et al., 2022).

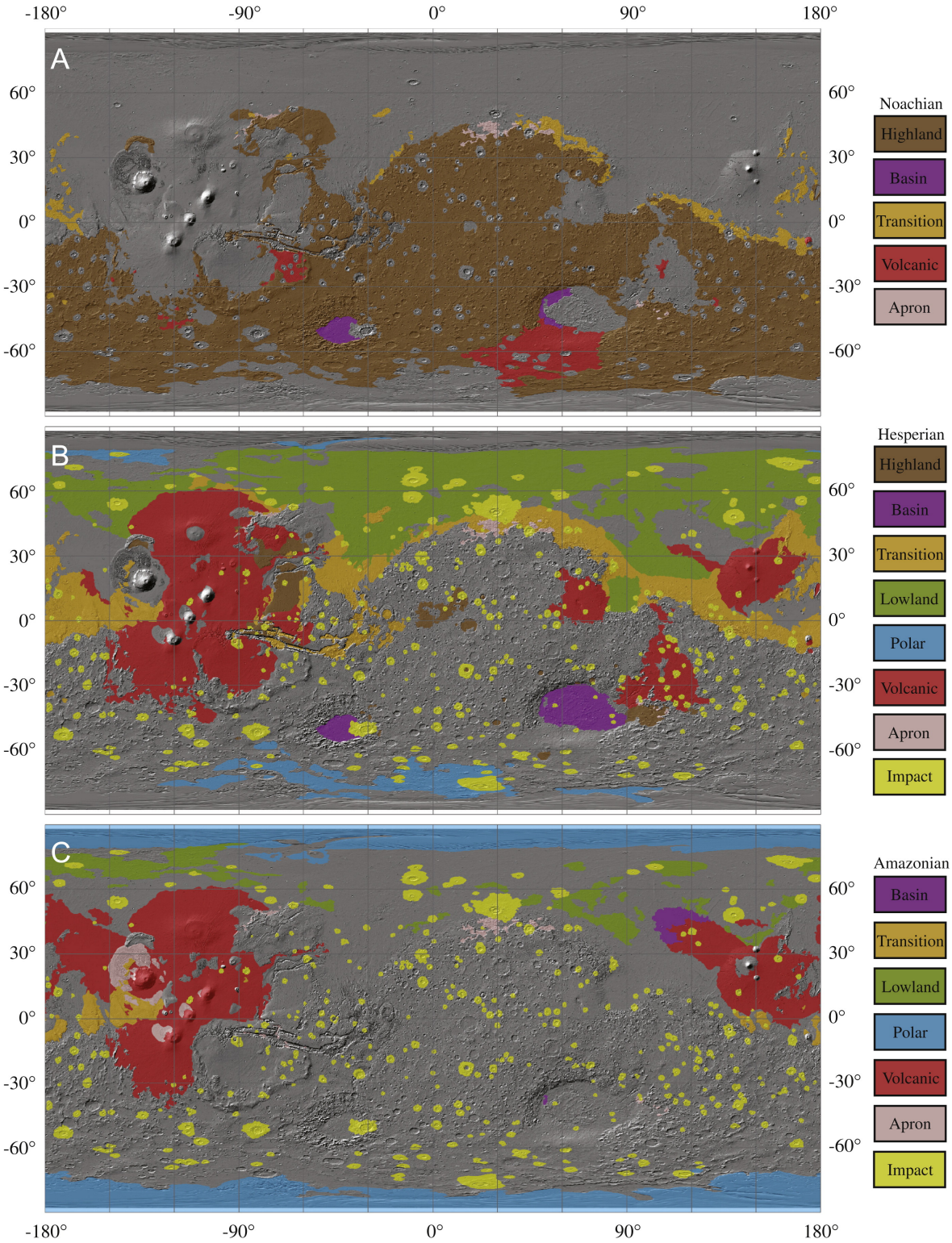

FIGURE 1.2 – Les unités de Mars sont regroupées par période : (a) Noachien, (b) Hespérien et (c) Amazonien. Certaines unités couvrent deux périodes. La carte de fond est un modèle numérique d'élévation du relief ombré de MOLA (128 pixels/deg) superposé à une mosaïque infrarouge diurne globale de THEMIS (100 m/pixel). Projection équirectangulaire, grille de 30°. Figure d'après Tanaka et al. (2014)

Basses Plaines

Les Basses Plaines forment une surface relativement plate et principalement sédimentaire, datant de la fin de l'Hespérien (Figure 1.2b). Les données MOLA montrent que la rugosité de surface est particulièrement uniforme et inférieure à 1 m (Garvin et al., 1999; Smith et al., 2001). Ce dépôt sédimentaire détritique, avec une épaisseur moyenne estimée de 100 m, recouvrirait d'anciennes plaines volcaniques ridées datées au début de l'Hespérien (Head et al., 2002; Tanaka et al., 2003). Des éjectas frais de cratères d'impacts, excavés depuis la profondeur, montrent des compositions similaires à celles de la surface des Hauts Plateaux. Cette observation est interprétée par un recouvrement sédimentaire de l'ancienne surface des Basses Plaines (Head et al., 2002; Mustard et al., 2005). La partie polaire a été recouverte par les processus glaciaires lors de l'Amazonien récent (Tanaka et al., 2003). Les plus anciennes structures des Basses Plaines datent de la fin du Noachien et du début de l'Hespérien et sont concentrées à la limite de la dichotomie (Head et al., 2002; Tanaka et al., 2003). Les observations cumulées de ces dépôts sédimentaires avec d'anciennes lignes de côtes le long de la dichotomie (Head III et al., 1999; Perron et al., 2007; Citron et al., 2018a) et de la trace d'anciens tsunamis (Rodriguez et al., 2016; Costard et al., 2017) sont utilisées comme argument pour la présence d'un océan martien à la fin de l'Hespérien dans l'hémisphère nord (Schmidt et al., 2022). Cette hypothèse est très controversée, car les modèles climatiques appliqués à Mars prédisent une instabilité d'un tel océan (Turbet and Forget, 2019) à moins d'avoir un puissant effet de serre (Schmidt et al., 2022).

Une partie des Basses Plaines est occupée par la deuxième plus grande formation volcanique martienne, Elysium (Figure 1.1A & 1.2C). Cette formation est constituée de trois volcans : Elysium Mons, le principal, et deux secondaires : Albor Tholus et Hecates Tholus. Les datations des différentes composantes de cette formation donnent des âges compris entre 3.6 Ga et 10 Ma. Elysium serait une formation plutôt ancienne avec une longue durée de vie (Pasckert et al., 2012). Horvath et al. (2021) ont révélé des coulées pyroclastiques très récentes avec un âge entre 53 et 210 milliers d'années, localisées dans Elysium Planitia. Cette région au sud de Elysium Mons contient Cerberus Fossae, une formation tectonique active en extension ou graben, qui prend la forme de fissures parallèles. Il s'agit de la formation géologique la plus active d'un point de vue sismique durant la mission InSight (Stähler et al., 2022). La récente activité volcanique et la sismicité actuelle de la région peuvent être expliqués par la présence d'un panache mantellique sous la région (Broquet and Andrews-Hanna, 2023), proposition soutenue par une anomalie de gravité.

Tharsis

Tharsis est le plus grand complexe volcanique du système solaire, il est composé de 12 volcans avec des altitudes comprises entre 3 et 21 km sur une région d'un diamètre de 5500 km. La région est souvent séparée en deux pour être incorporée aux Hauts Plateaux et aux Basses Plaines, mais c'est une province géologique à part entière qui

s'est mise en place après la formation de la dichotomie et sur sa limite (Andrews-Hanna et al., 2008a). La construction du dôme de Tharsis a débuté à la fin du Noachien (Anderson et al., 2001) avec une activité qui continue jusqu'à une époque récente (Hauber et al., 2011; Pieterek et al., 2022). La masse de Tharsis est très importante et très localisée et aurait induit un mouvement de l'axe de rotation, et donc des pôles, au cours de sa formation ("True Polar Wander"). Bouley et al. (2016) ont comparé le déplacement prédit par deux méthodes indépendantes, à partir de la composante de degré 2 du champ de gravité en l'absence de la masse de Tharsis (Matsuyama and Manga, 2010) et en utilisant la géométrie des réseaux de vallées. Il est remarquable que ces deux méthodes donnent les mêmes paléo-pôles pour Mars avec un déplacement important de l'axe de rotation de 20° par rapport à l'actuel. Dans son ancienne configuration, la dichotomie martienne est alors parallèle à l'équateur.

1.2 Géochimie martienne

La composition de Mars, de sa croûte et de son manteau est cruciale pour comprendre son évolution. Par exemple, la concentration d'éléments producteurs de chaleur détermine la quantité d'énergie à dissiper, tandis que la teneur en fer détermine la température de fusion du manteau. Pour déterminer la composition de Mars, on utilise les données obtenues par les rovers martiens, les sondes en orbite et l'étude en laboratoire des météorites martiennes. Ces données sont ensuite utilisées dans des modèles géochimiques pour reconstruire une composition globale.

1.2.1 Météorites martiennes

Les météorites martiennes sont les seuls échantillons de roches martiennes en notre possession. Ces échantillons de croûte ont été extirpés de la gravité martienne à la suite d'un impact. Les météorites martiennes ont pu être identifiées premièrement par leurs âges de cristallisation (McSween and Stolper, 1980) et ensuite via leurs compositions en gaz noble et en isotope du carbone et de l'azote qui sont identiques à celles de l'atmosphère de Mars (Bogard and Johnson, 1983). Ces météorites ont des compositions en éléments majeurs similaires, allant de ultra-mafique à mafique. Elles sont riches en pyroxène et en olivine et contiennent de la maskelynite, un feldspath formé par le choc d'un impact. Plus de 350 météorites martiennes sont enregistrées dans la base de donnée de la Meteoritical Society et sont reparties en trois principaux groupes, les Shergottites, les Nakhlites et les Chassignites (SNC). L'appartenance à chacun de ces groupes est déterminée à partir de critères géochimiques et pétrologiques (Udry et al., 2020, et ses références).

Le principal groupe est celui des shergottites avec 82% de la masse totale. Les shergottites ont une grande variété pétrologique avec des textures et des abondances minérales variables et des lithologies allant du basalte au gabbro. Elles sont subdivisées

en trois sous-groupes en fonction de leurs enrichissements en éléments traces incompatibles : enrichi, intermédiaire et appauvri. Les âges de cristallisations des shergottites s'étendent de ≈ 2.4 Ga à ≈ 150 Ma (Nyquist et al., 2001) avec une relation âge - enrichissement, les shergottites enrichies et intermédiaires étant plus récentes (Figure 1.3). Un âge de 4 Ga a aussi été proposé pour les shergottites avec les isotopes du plomb (Bouvier et al., 2009) mais un âge récent a ensuite été reconfirmé (Moser et al., 2013) et l'âge ancien relié à une contamination crustale (Bellucci et al., 2016). Le second groupe est celui des nakhlites et le troisième groupe est celui des chassignites avec en cumulé 17% de la masse totale. Les âges de cristallisation de ces deux groupes sont similaires, autour de 1.3 Ga et l'âge d'éjection de 11 Ma est identique (Figure 1.3). Ces âges similaires pointent vers un même évènement d'éjection et donc une origine géographique similaire (Nyquist et al., 2001; Cohen et al., 2017). La détermination des sources mantelliques de ces différentes météorites a montré que le manteau martien était très inhomogène isotopiquement (Blichert-Toft et al., 1999; Debaille et al., 2009; Lapen et al., 2017).

Deux météorites sortent de la classification SNC, l'orthopyroxénite ALH84001 et la brèche NWA 7034. ALH84001 est un cumulat d'orthopyroxènes avec un âge de cristallisation de 4.1 Ga soit un âge Noachien bien plus ancien que les SNCs (Lapen et al., 2010). Elle est devenue célèbre avec une importante controverse scientifique. McKay et al. (1996) ont déclaré que ALH84001 présentait un certain nombre de preuves (morphologiques et compositionnelles) d'une vie passée sur Mars. Cette thèse est hautement discutable car toutes les preuves fournies ont des explications abiotiques, cette controverse a néanmoins permis des avancées dans la définition d'une preuve de vie (Anders, 1996; Treiman, 2019). La brèche d'impact NWA 7034 et ses 15 corps parents (0.981 g au total) sont des échantillons uniques et très certainement le plus intéressant. La brèche d'impact est composée de différents fragments anguleux de roches de compositions mafiques et ultra-mafiques avec des âges de cristallisation de ≈ 4.5 Ga, ce qui en fait le plus ancien échantillon martien (Agee et al., 2013; Cassata et al., 2018). La brèche contient aussi des fragments de différentes lithologies, jamais observés auparavant, comme des fragments sédimentaires, de régolithe lithifié et surtout des fragments alcalins/felsiques. Ces fragments felsiques ont pu fournir des zircons permettant une meilleure datation des événements de solidification de l'océan magmatique et d'extraction de la croûte primordiale (Kruijer et al., 2017; Cassata et al., 2018; Bouvier et al., 2018). Ces fragments felsiques seraient les produits d'une refusion de la croûte primordiale martienne, très tôt dans son histoire (Agee et al., 2013; Humayun et al., 2013). La météorite est considérée comme représentative de la surface des Hauts Plateaux et Lagain et al. (2022) proposent le cratère de Khujirt comme sérieux candidat pour le cratère d'impact à l'origine de cette brèche, situé dans la région de Terra Sirenum Cimmeria (Figure 1.3, carte, cercle bleu).

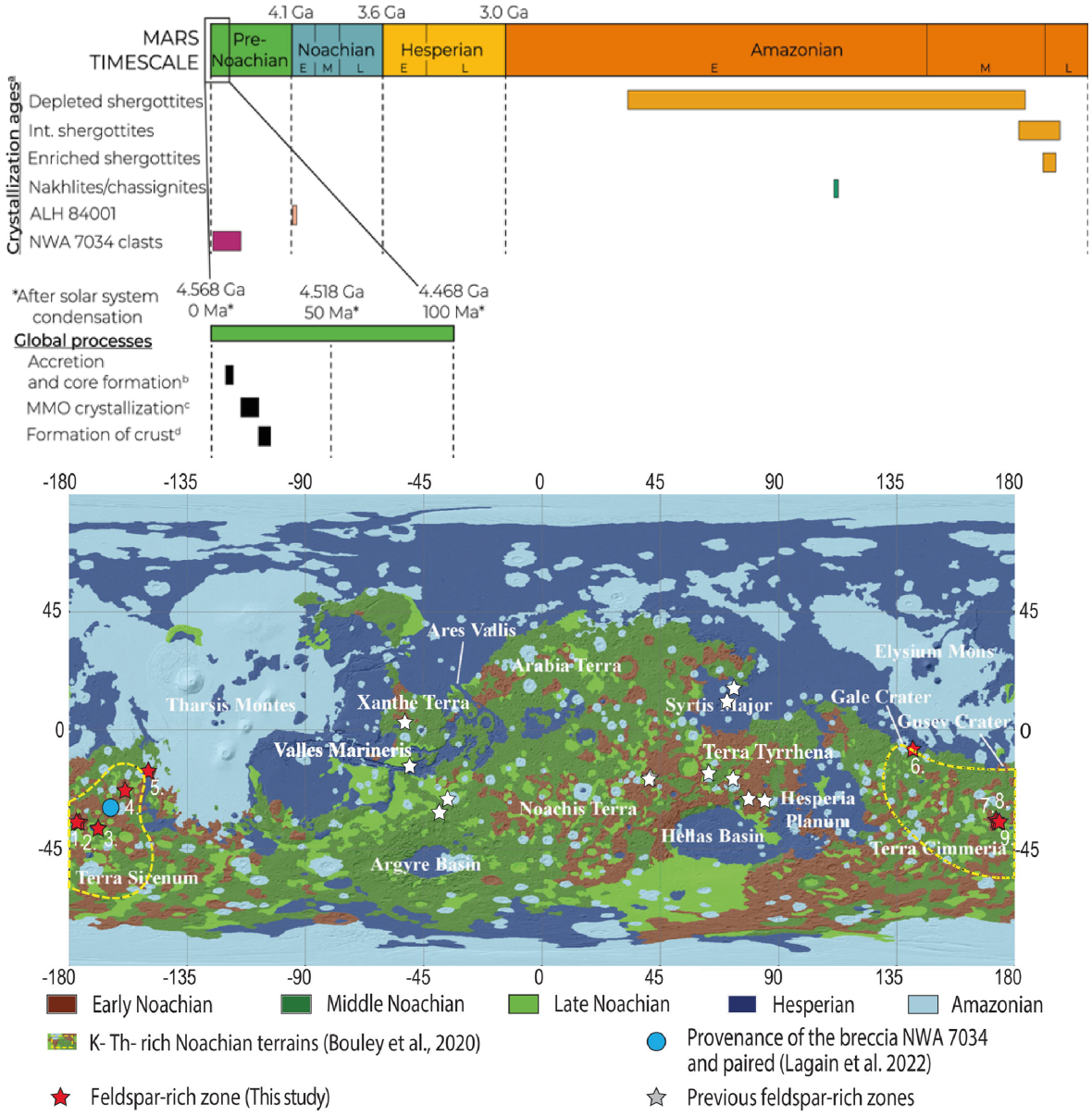

FIGURE 1.3 – **Frise chronologique** issue de Udry et al. (2020). Chronologie des principaux processus de l'histoire de Mars basée sur des études de météorites martiennes, y compris les âges de cristallisation, les âges des sources et les processus globaux. Les périodes géologiques sont tirées de la chronologie de Hartmann and Neukum (2001), les lignes plus fines représentant les différentes sous-divisions des périodes martiennes (E : early, M : mid, et L : late). Les études les plus récentes ont été utilisées dans cette figure pour chaque processus. **Carte géologique** issue de Payré et al. (2022) et modifiée d'après Tanaka et al. (2014) avec la localisation des neuf sites riches en feldspath de Payré et al. (2022). Sont également illustrés, la région riche en K-Th (Bouley et al., 2020), l'emplacement des terrains riches en feldspaths précédemment détectés par CRISM (étoiles blanches, Carter and Poulet 2013 et Wray et al. 2013) et le site d'origine de la brèche martienne Northwest Africa (NWA) 7034 et de ses météorites appariées (Lagain et al., 2022).

1.2.2 Observations orbitales et in-situ

Le spectromètre à rayons gamma (GRS) de Mars Odyssey a cartographié la surface de Mars entre les latitudes $-60°$ et $+60°$. Ces données donnent accès aux concentrations de certains éléments (Si, Fe, Ca, Al, K, Cl, S, H et Th) des premières dizaines de centimètres de la surface (Boynton et al., 2007; Newsom et al., 2007a; Karunatillake et al., 2009, 2014). Cette relativement importante pénétration lui permet d'être moins sensible à la couche de poussière qui recouvre la surface martienne (Newsom et al., 2007b), néanmoins sa résolution spatiale est faible : $\sim 400-500$ km par pixel. Les données GRS montrent une certaine uniformité de la croûte martienne pour ces éléments à cette échelle de résolution, la croûte martienne étant principalement de composition basaltique. Des zones enrichies en Th et K existent dans le nord des Basses Plaines et dans la région de Terra Sirenum Cimmeria (Figure 1.3, contour jaune).

La spectroscopie orbitale visible – infrarouge (VIR) a une bien meilleure résolution spatiale, ~ 300 m/pixel pour l'instrument OMEGA (Observatoire pour la Minéralogie, l'Eau, les Glaces et l'Activité) et ~ 20 m/pixel pour CRISM (Compact Reconnaissance Imaging Spectrometer for Mars). La pénétration n'est que de quelques micromètres seulement, les données sont donc fortement influencées par la couche de poussière. Les données de VIR renseignent sur la minéralogie de la surface, chaque minéral absorbant certaines longueurs d'ondes en particulier. Plusieurs minéraux peuvent absorber la même longueur d'onde ce qui complexifie les interprétations. La composition de la surface est celle de minéraux relativement pauvre en silice (Hamilton et al., 2001; Christensen et al., 2005) avec néanmoins des variabilités dans la composition des pyroxènes. En effet, les terrains anciens des Hauts Plateaux sont caractérisés par une forte bande d'absorption correspondant à des pyroxènes pauvres en calcium (LCP, orthopyroxène), avec une faible teneur en pyroxènes riches en calcium (HCP, clinopyroxène) (Mustard et al., 2005; Poulet et al., 2009). À l'inverse, les plaines volcaniques récentes des Basses Plaines présentent une forte contribution des HCP et une quasi-absence de LCP (Mangold et al., 2010).

Les données in-situ obtenues par les différents rovers, principalement à la limite de la dichotomie, ont confirmé une diversité pétrologique et géochimique de la croûte. Le cratère Gusev a été exploré par le rover Spirit de 2003 à 2010. Le fond du cratère est rempli d'une coulée basaltique dont l'origine n'est pas tout à fait identifiée (Squyres et al., 2006). Spirit a détecté les premiers basaltes alcalins riches en feldspath sur Mars (Arvidson et al., 2008; Squyres et al., 2006). Le rover Curiosity explore le cratère voisin de Gale, un lac daté de l'Hespérien, depuis 2012 (Deit et al., 2013). Une grande diversité minéralogique et pétrologique a été découverte dans ce cratère (Sautter et al., 2016; Cousin et al., 2017). Cette diversité est en partie due à l'histoire hydrologique du cratère, un nombre important de galets non en place et de conglomérats, regroupant différentes lithologies, sont présents à la base du Mont Sharp (Mangold et al., 2016). Une vingtaine de textures différentes ont été identifiées dont un nombre important de roches

felsiques, une première in-situ. La mission Perseverance explore le cratère Jezero depuis 2021, il s'agit aussi d'un lac daté de la fin du Noachien – début de l'Hespérien (Mangold et al., 2021; Sun et al., 2023). Deux formations géologiques volcaniques composent la base du cratère, Séítah, un cumulat d'olivine, et Máaz, une coulée volcanique mafique. Il a été proposé que Máaz soit le produit de la cristallisation fractionnée de Séítah (Udry et al., 2022), mais cela semble incompatible avec leur composition en éléments traces (Debaille et al., 2023).

1.2.3 Une composante felsique dans les Hauts Plateaux

Bien que la surface de la croûte martienne soit majoritairement basaltique, un nombre croissant d'observations vont dans le sens d'une plus grande diversité minéralogique. Christensen et al. (2005) ont été les premiers à observer une coulée de lave enrichie en silice, entre 56 et 63 % de SiO_2, à Nili Patera. Carter and Poulet (2013) et Wray et al. (2013) ont ensuite détecté des affleurements enrichis en plagioclases riches en fer (Figure 1.3, carte, étoiles bleus). Carter and Poulet (2013) donnent huit affleurements dans les Hauts Plateaux avec un cluster autour du bassin d'impact Hellas. Ils suggèrent que ces affleurements pourraient être des résidus d'une ancienne croûte anorthositique à l'image de celle présente sur la Lune. Wray et al. (2013) ont déterminé de manière indépendante trois autres sites avec des compositions riches en feldspath notamment à Nili Patera (Christensen et al., 2005). Depuis lors, ces observations se sont multipliées dans l'ensemble des Hauts Plateaux avec l'amélioration des méthodes de détection (Rogers and Nekvasil, 2015; Rogers and Farrand, 2022; Phillips et al., 2022; Payré et al., 2022). Néanmoins, cette méthode ne donne pas l'abondance en silice de ces roches et ne permet pas de conclure sur leurs degrés d'évolution entre intermédiaire et felsique (Phillips et al., 2022).

Ces découvertes depuis l'orbite ont été concomitantes avec celles de roches différenciées à Gale par le rover Curiosity. Au moins 23 échantillons avec une composition évoluée ont été étudiés par ChemCam, le LIBS (Laser-induced breakdown spectroscopy) de Curiosity (Sautter et al., 2014). Ces échantillons sont classés en trois différents groupes (Sautter et al., 2015). Le premier groupe est celui des granodiorites composées de $\simeq$ 80 % de cristaux felsiques de grande taille et $\simeq$ 20 % de cristaux mafiques (pyroxènes et olivines) avec une texture d'intrusion magmatique. La teneur en silice (SiO_2) est de $\simeq$ 64 wt% et la teneur en alcalin (Na_2O + K_2O) de $\simeq$ 10 wt%, plaçant ce groupe dans la série sub-alcaline. Le second groupe est celui des trachytes, des roches très riches en feldspath potassique avec une texture aphanitique et d'aspect vésiculaire vitreux hololeucocrate (couleur claire). La composition de ce groupe correspond à la série alcaline avec une teneur en silice (SiO_2) supérieure à 64 wt% et une teneur en alcalin (Na_2O + K_2O) supérieure à 10 wt%. Le dernier groupe est celui des trachyandésites porphyriques contenant $\simeq$ 50 % de plagioclases oligoclases (riche en sodium) dans une matrice mésostasique composée de pyroxène pauvre en calcium. Sa teneur en silice (SiO_2) est de $\simeq$ 55 wt% et la teneur en alcalin (Na_2O + K_2O) de

$\simeq$ 8 wt% ce qui correspond également à la série alcaline.

Sautter et al. (2015) soulignent les similitudes entre la composition et la pétrologie de ces trois groupes avec celles des TTG (tonalite-trondhjémite-granodiorite) qui composent 60% de la croûte continentale terrestre (Rudnick and Holland, 2005). Les différents affleurements des Haut Plateaux présentant une minéralogie évoluée peuvent appartenir à ces trois groupes, élargissant la présence d'une composante semblable aux TTG à l'échelle de tout l'hémisphère sud. Ces roches différenciées seraient alors une potentielle preuve de l'existence dans l'hémisphère sud d'une croûte proto-continentale, intermédiaire entre une croûte basaltique et continentale, ou d'une croute continentale enfouie. Udry et al. (2018) argumentent que ces roches sont chimiquement plus proches d'une suite magmatique islandaise que celle des TTG. Dans les deux cas, ces roches semblent être formées par la cristallisation fractionnée d'un protolithe mafique semblable à celui de la croûte primitive martienne (Sautter et al., 2015, 2016).

1.2.4 Modèles de composition martienne

La composition chimique globale de la partie silicatée de Mars est inconnue et doit être modélisée à partir des données existantes sur la composition de la croûte. Wänke and Dreibus (1994) ont reconstruit cette composition à partir des données de 10 SNCs en faisant une hypothèse, les abondances des éléments réfractaires sont similaires à celles des chondrites carbonées de type CI. Ce modèle prévoit un manteau martien riche en fer (FeO $\approx$ 17.9 wt%) et pauvre en eau (H_2O < 150 ppm) comparativement à la Terre (FeO $\approx$ 7.1 wt% et H_2O > 1000 ppm). Ce modèle prévoit aussi des concentrations pour les éléments producteurs de chaleur, K (305 ppm), Th (56 ppb) et U (16 ppb), avec une production actuelle de chaleur dans la partie silicatée de 2 TW. Taylor (2013) revisite le modèle de Wänke and Dreibus (1994) 20 ans plus tard avec l'ensemble des nouvelles données à sa disposition : nouvelles météorites martiennes, données GRS et isotopes de l'oxygène. L'hypothèse d'une d'abondance martienne comparable aux chondrites est réutilisée avec une composition CI revisitée. Son résultat est simple, il retrouve la même composition riche en fer (FeO $\approx$ 18.1 wt%) que le modèle précédent, mais avec une composition en eau plus importante (H_2O $\approx$ 300 ppm).

Des méthodes plus récentes proposent de reconstruire la composition martienne sans hypothèse sur les abondances (Yoshizaki and McDonough, 2020; Khan et al., 2022). Yoshizaki and McDonough (2020) utilisent des corrélations dans les ratios élémentaires des compositions martiennes pour déterminer les abondances en éléments réfractaires, méthode précédemment utilisée pour la composition terrestre (Palme and O'Neill, 2003). Le modèle résulte en une composition moins riche en fer que précédemment (FeO $\approx$ 14.7 wt%) et moins riche en eau (H_2O $\approx$ 150 ppm) mais enrichie en éléments producteurs de chaleurs, K (360 ppm), Th (67 ppb) et U (18 ppb), avec une production actuelle de chaleur dans la partie silicatée de 2.5 TW (+25% par rapport à Wänke and Dreibus 1994). Cette plus faible concentration en fer est aussi retrouvée

par Khan et al. (2022) à l'aide d'une inversion contrainte par les observations géophysiques d'InSight et les abondances cosmochimiques (FeO $\approx$ 13.7 wt%). Dans ce dernier modèle, les concentrations en eau et en éléments producteurs de chaleurs ne sont pas données.

1.3 Structure interne

La détermination de la structure interne est importante pour comprendre les mécanismes à l'origine des structures de surface. Mars est une planète tellurique, sa structure suit donc celle de la Terre avec un noyau métallique dense en son centre surplombé d'un manteau silicaté composé majoritairement d'olivine et de proxènes et de leurs polymorphes et d'une croûte silicatée en surface, moins dense que le manteau. L'observation de l'intérieur étant indirecte, un vaste panel de méthodes géophysiques sont utilisées pour le contraindre avec l'ajout récent de la sismologie Martienne grâce à la Mission InSight.

1.3.1 Modèles d'épaisseur de croûte

Gravité, anomalie de Bouguer et épaisseurs de la croûte

Le champ de gravité martien est déterminé par traçage radio des orbiteurs martiens jusqu'à un degré $l = 110$ (Konopliv et al., 2011). Ce champ peut être exprimé dans un domaine spatial, avec des coordonnées sphériques, ou dans un domaine spectral où le champ est définis comme une somme d'harmoniques sphériques. Les variations latérales du champ de gravité sont exprimé avec l'anomalie à l'air libre. Cette anomalie est obtenue en retranchant aux données une correction de l'altitude ainsi que la valeur théorique de la gravité qui dépend de la latitude, Mars n'étant pas une sphère parfaite. L'anomalie de Bouguer est ensuite obtenue en retranchant à l'anomalie à l'air libre la contribution des reliefs. La géométrie de l'anomalie de masse à l'origine de l'anomalie de Bouguer est difficile à contraindre, notamment sa position en profondeur, nécessitant des hypothèses basées sur des considérations géologiques. Dans le but d'obtenir l'épaisseur de la croûte, l'anomalie de Bouguer est considéré comme étant entièrement due au relief de l'interface croûte manteau. Il faut ensuite définir une épaisseur moyenne de la croûte ou un point d'ancrage, c'est-à-dire une position à laquelle l'épaisseur de la croûte est connue de manière indépendante. Pour un contraste de densité à l'interface croûte-manteau et en considérant le domaine spectral, il est alors possible de calculer l'épaisseur de la croûte à partir de l'anomalie de Bouguer (Wieczorek and Phillips, 1997). Une carte de l'épaisseur de la croûte peut être alors reconstruite, ce type de carte est appelé modèle d'épaisseur de croûte.

Une autre approche est de considérer que la topographie est expliquée par un mécanisme, par exemple un équilibre isostatique ; on peut ainsi écrire une relation entre topographie et gravité. Le ratio gravité sur topographie dans le domaine spatial peut alors

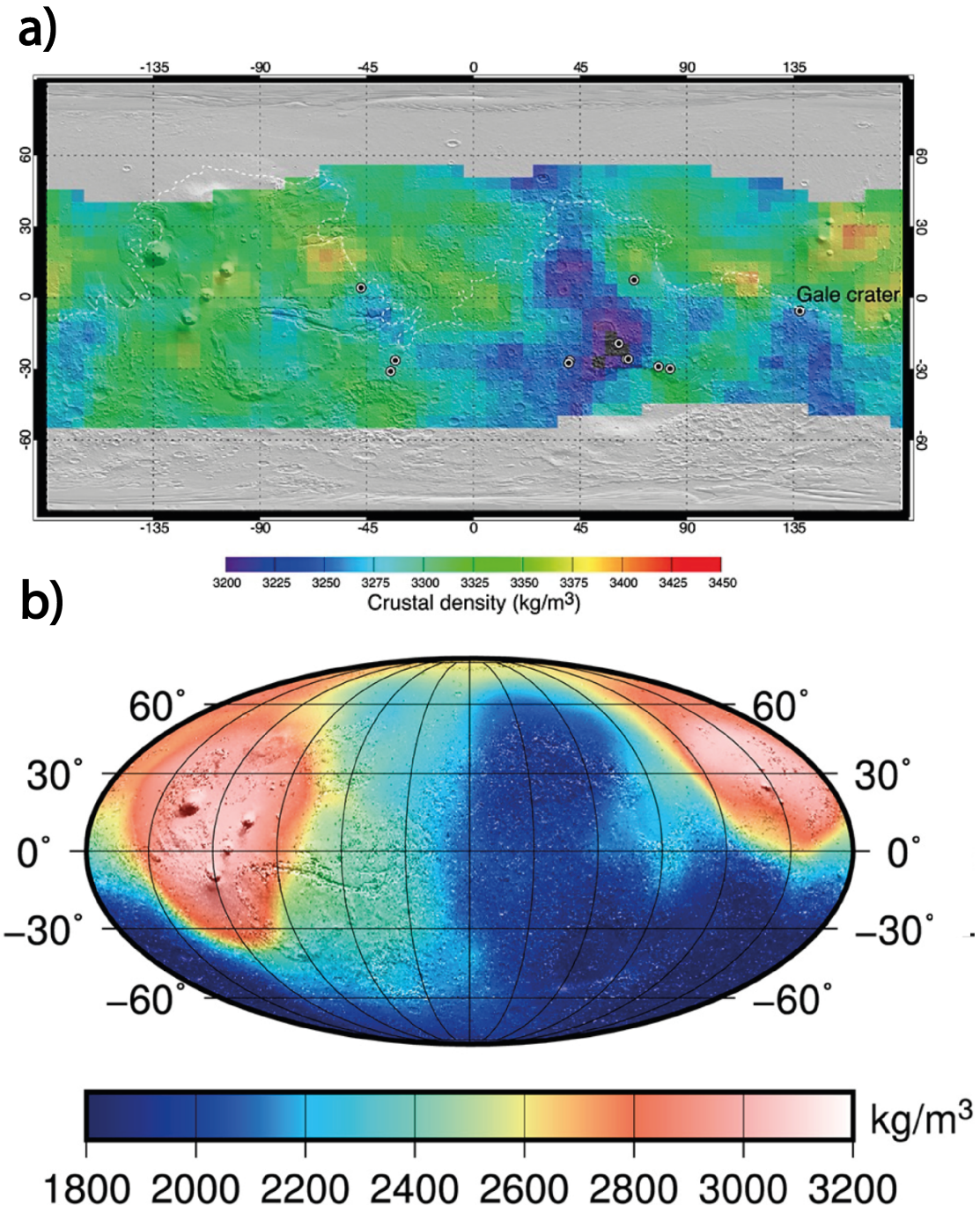

FIGURE 1.4 – Carte de densité crustale obtenue par deux méthodes différentes. (a) Carte de densité crustale hors porosité de Baratoux et al. (2014) obtenue à l'aide des données GRS et des compositions et densités des météorites martiennes, la plage de valeur est comprise entre 3200 et 3450 kg m^{-3} (b) Carte de densité crustale de Goossens et al. (2017) obtenue à partir de l'admittance, la plage de valeur est comprise entre 1800 et 3200 kg m^{-3}.

donner des informations sur des paramètres du modèle comme la densité et l'épaisseur de croûte moyenne (Wieczorek and Zuber, 2004). Cette méthode est principalement sensible aux grandes longueurs d'onde et nécessite que la relation topographie – gravité considérée s'applique bien à ces longueurs d'ondes. Pour Mars, la composante flexurale de Tharsis doit par exemple être retirée (Phillips et al., 2001; Wieczorek and Zuber, 2004). Un exercice similaire dans le domaine spectral utilise l'admittance et la corrélation entre la gravité et la topographie à différentes longueurs d'ondes (Wieczorek, 2015; Goossens et al., 2017). L'admittance mesure la relation entre topographie et gravité et la corrélation mesure la qualité de cette relation pour expliquer les données. Cette méthode est moins sensible aux grandes longueurs d'ondes et n'a pas à considérer un unique mécanisme de compensation.

Wieczorek and Zuber (2004) ont utilisé la méthode du ratio gravité sur topographie avec une hypothèse d'une compensation isostatique pour contraindre des paramètres de la croûte martienne. Ils démontrent que l'épaisseur moyenne de la croûte doit être inférieure à 100 km et l'estiment à 57 $\pm$ 24 km en moyenne. La même année, Neumann et al. (2004) utilisent l'anomalie de Bouguer pour déterminer les variations latérales de l'épaisseur de la croûte en faisant l'hypothèse d'une épaisseur moyenne de 45 km et d'une masse volumique crustale homogène sur toute la planète et prenant des valeurs entre 2700 et 3100 kg m^{-3}. Ils estiment alors la dichotomie hémisphérique d'épaisseur de croûte à $\sim$ 30 km. Néanmoins, si la densité des Hauts Plateaux est inférieure à celle des Basses Plaines, la dichotomie d'épaisseur crustale est moins prononcée. Les modèles d'épaisseur de croûte montrent que l'épaisseur moyenne de la croûte a un minimum de 25 km (Pauer and Breuer, 2008).

Densité de la croûte martienne

Le contraste de densité à l'interface croûte-manteau est un paramètre crucial à déterminer pour obtenir l'épaisseur de la croûte martienne. La densité du manteau est assez bien contrainte par les modèles minéralogiques et varie finalement assez peu (entre 3350 et 3500 kg m^{-3}, Wieczorek et al. 2022). Le contraste de densité croûte-manteau dépend alors principalement de la densité crustale qui est beaucoup plus compliquée à contraindre. La densité de la croûte terrestre est bien connue avec une différence fondamentale entre les croûtes océanique et continentale (2900 vs 2700 kg m^{-3}). La densité de la croûte lunaire a pu être déterminée grâce aux missions Apollo et GRAIL. Sa densité moyenne est beaucoup plus faible : 2550 kg m^{-3} (Wieczorek et al., 2013). Cette faible densité s'explique par sa composition et sa porosité : il s'agit d'une croûte anorthositique peu dense avec un méga-régolite ayant une importante porosité sur près de 30 km.

La densité de la croûte martienne peut aussi être inférée à partir d'études géochimiques. L'étude de Baratoux et al. (2014) propose de reconstruire la composition de la surface martienne à partir des données GRS. Néanmoins, les données GRS ne

donnent qu'une partie de la composition de surface. À l'image de Wänke and Dreibus (1994), il est possible d'utiliser des ratios élémentaires pour remonter à la composition totale. Ces ratios élémentaires sont définis à partir des météorites martiennes et des données in-situ avec l'hypothèse qu'ils sont représentatifs de la surface martienne. La composition obtenue est ensuite utilisée dans un modèle thermodynamique pour définir l'assemblage minéralogique caractéristique de la croûte et ainsi sa densité de grain (sans porosité). Les densités obtenues sont dans une plage 3200 - 3400 kg m^{-3}, avec de fortes densités dans les provinces volcaniques récentes (Tharsys - Elysium) et des densités plus faibles dans les Hauts Plateaux (Figure 1.4a). La densité d'une roche provenant de la fusion partielle d'un manteau avec une composition primordiale (Wänke and Dreibus, 1994) est estimée entre 3100 et 3200 kg m^{-3}, plus représentative d'un volcanisme Noachien/Hespérien. L'épaisseur moyenne de croûte estimée avec ces densités par les modèles d'anomalie de Bouguer est comprise entre 65 et 110 km, soit potentiellement plus que la limite donnée par les ratios gravité/topographie (Wieczorek and Zuber, 2004). Les auteurs proposent une forte porosité et une composante felsique, à l'image de la Lune, dans l'hémisphère sud pour obtenir des densités plus faibles. Pauer and Breuer (2008) avaient notamment estimé la densité maximale des Hauts plateaux à 3020 $\pm$ 70 kg m^{-3}.

L'étude de l'admittance et de la corrélation par Goossens et al. (2017) donne une estimation de la densité crustale avec une valeur bien plus faible que précédemment proposée, 2582 $\pm$ 209 kg m^{-3} (Figure 1.4b). Leurs résultats sont aussi caractérisés par de très fortes variations latérales, les densités crustales allant de 1800 à 3200 kg m^{-3}. Les fortes densités sont associées aux provinces volcaniques récentes avec une corrélation très élevé, supérieure à 0.9 (Figure 1.4b & Goossens et al. 2017). Pour ces régions, d'où viennent la majorité des météorites martiennes, cette étude est cohérente avec les estimations de Baratoux et al. (2014) ainsi qu'avec d'autres études localisées sur les édifices volcaniques (Grott and Wieczorek, 2012). Pour les Hauts Plateaux, la corrélation est un peu moins bonne, mais les différences de densité entre les deux approches sont importantes. Néanmoins, certaines similitudes dans les variations de densités sont observables, avec des Hauts Plateaux qui semblent moins denses que les Basses Plaines (Figure 1.4). Les observations d'affleurement avec des compositions felsiques (Section 1.2.3), de roches sédimentaires ou bien l'aspect peu induré de la surface Hauts Plateaux (Section 1.1.3) sont autant de pistes pour expliquer les faibles densités des Hauts Plateaux.

1.3.2 Structure de la croûte

Sismologie de la croûte martienne

La structure locale de la croûte martienne autour de l'atterrisseur InSight a été déterminée en utilisant l'analyse des fonctions récepteurs (Lognonné et al., 2020; Knapmeyer-Endrun et al., 2021; Durán et al., 2022b; Joshi et al., 2023). Une onde sismique incidente

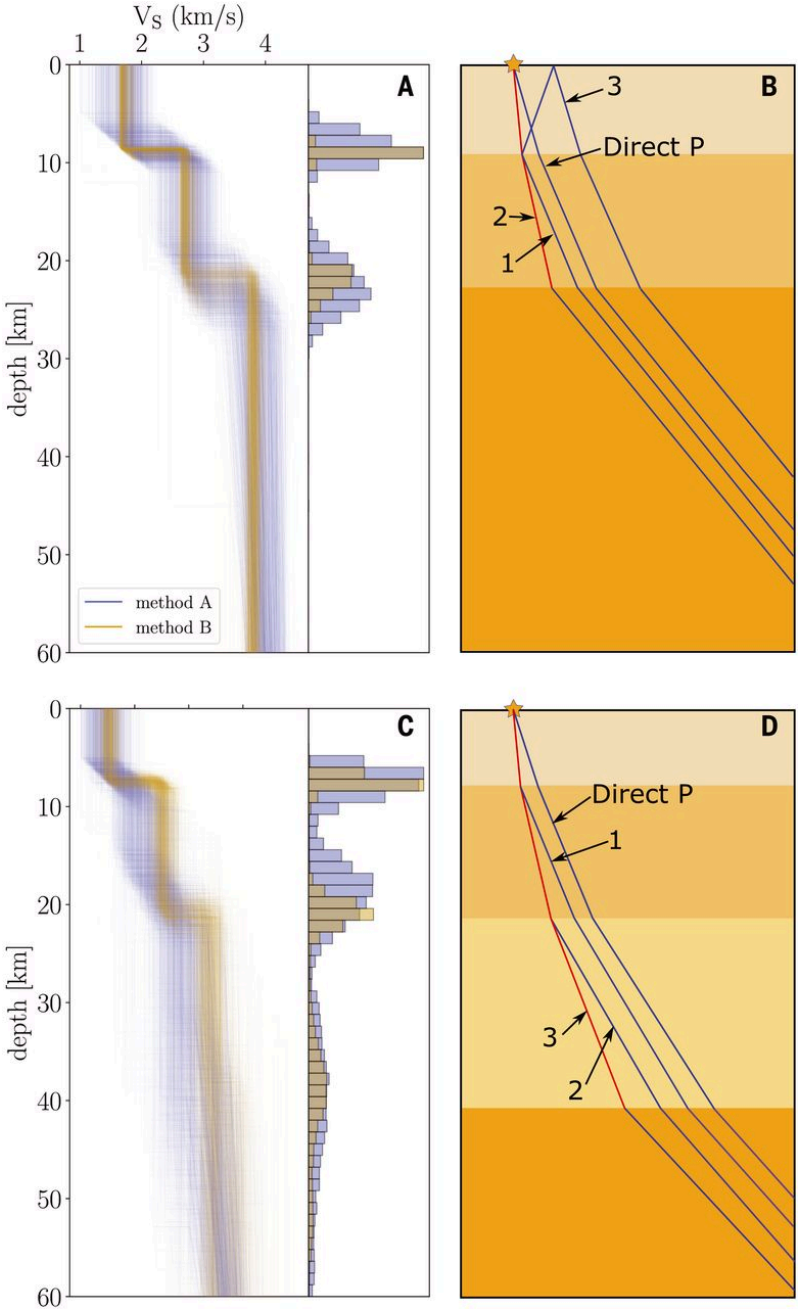

FIGURE 1.5 – Figure issue de Knapmeyer-Endrun et al. (2021), (a) Résultats de l'inversion en utilisant la méthode d'inversion des fonctions récepteurs (lignes bleues) et la méthode de l'autocorrélation (lignes brunes) et avec une paramétrisation à deux couches. (b) Schéma montrant les trajectoires des rayons des principales phases directes et converties présentes dans les données. Les lignes bleues montrent les trajectoires des phases P, tandis que les lignes rouges montrent les conversions en phases S aux interfaces sous l'atterrisseur. Les conversions directes et un multiple P sont représentés, et les étiquettes numérotées correspondent aux arrivées identifiées dans l'ordre chronologique. (c) et (d) identique à (a) et (b) mais pour l'hypothèse d'un modèle à trois couches.

sous la station sismique est réfléchie plusieurs fois sur les différentes interfaces existantes, produisant des ondes converties. L'analyse des fonctions récepteurs des ondes P et S permet de remonter aux profondeurs de ces interfaces et aux vitesses sismiques des différentes couches sous la station. Les premières analyses de Lognonné et al. (2020) et Knapmeyer-Endrun et al. (2021) utilisent respectivement deux et trois évènements sismiques originaires de Cerberus Fossae et ont permis une première détermination de la structure de la croûte sous InSight (Figure 1.5, lignes bleues). L'interface la plus proche de la surface est profonde de 8 à 11 km, délimitant une première couche à très faibles vitesses sismiques ($V_s \approx 1.7$ - 2.1 km s^{-1}). Pour les interfaces suivantes, Knapmeyer-Endrun et al. (2021) proposent soit un modèle à 2 couches, soit un modèle à 3 couches (Figure 1.5, b & d). Dans les deux modèles l'interface qui suit est à 20 $\pm$ 5 km de profondeur avec des vitesses sismiques plus élevées ($V_s \approx 2.5$ - 3 km s^{-1}). Dans le modèle à 3 couches, une troisième interface est déterminée à 39 $\pm$ 8 km de profondeur avec des vitesses sismiques très proches de celles du manteau ($V_s \approx 3.5$ - 4 km s^{-1}). La faible impédance de la dernière interface, c'est-à-dire le faible saut de vitesse sismique, la rend difficile à caractériser. Dans les deux modèles, l'interface la plus profonde est considérée être l'interface croûte-manteau. Une méthode utilisant l'autocorrélation du signal sismique donne des résultats similaires (Figure 1.5, lignes brunes).

Des études plus récentes avec des inversions plus sophistiquées et un plus grand nombre d'évènements sismiques ont permis de confirmer une structure à trois couches. Ces dernières études pointent vers une épaisseur de la croûte sous InSight entre 37 et 48 km de profondeur (Kim et al., 2021; Durán et al., 2022b; Joshi et al., 2023). D'autres méthodes donnent davantage de contraintes sur l'épaisseur et la structure de la croûte. Les ondes de Rayleigh générées par le plus fort séisme enregistré (magnitude 4.7) ont été détectées par InSight. Ces ondes de surfaces vont être sensibles à l'épaisseur de la croûte et aux vitesses sismiques le long du grand cercle passant par l'atterrisseur et la source. Kim et al. (2023b) estime ainsi l'épaisseur de la croûte le long du grand cercle à 63 km en moyenne. Le grand cercle est quasi parallèle à la limite de la dichotomie, l'incertitude sur l'azimut du cercle le fait passer ou non par Tharsis, ce qui change fortement l'interprétation qui peut en être faite. L'étude de la diffusion sismique sur ce même séisme estime une épaisseur diffusive de plus de 60 km dans les Hauts Plateaux, interprétée comme une épaisseur minimale de la croûte (Menina et al., 2023). Un large impact, éloigné d'une distance épicentrale de 146°, a permis de détecter une onde avec un rebond au point médian avec l'atterrisseur, donnant des informations sur la structure de la croûte à cet emplacement. Li et al. (2022) détectent une interface à 20 km avec cette méthode, avec un point de rebond située à la limite de la dichotomie, non loin de Tharsis. Cette interface correspond à celle de même profondeur sous InSight, l'interface moins profonde n'est pas présente et l'interface croûte-manteau a une trop faible impédance pour être détectée par cette méthode.

La structure en trois couches révélées par InSight est à ce jour encore peu comprise ; néanmoins, différentes interprétations sont proposées. Les vitesses sismiques sont sen-

sibles à deux principaux paramètres, la porosité et la composition/minéralogie des roches. Les très faibles vitesses de la première couche nécessitent une forte porosité (10-20%, Heap 2019), non remplie par de la glace, et des roches peu cimentées (Wright et al., 2022). Cette couche pourrait être formée par les éjectas des grands bassins d'impact qui l'entourent (Utopia, Hellas et Isidis, Wieczorek et al. 2022). Il existe alors un apparent contraste entre la lithologie observée à la surface, une coulée volcanique (compacte) et la couche supérieure (poreuse), mais les observations stratigraphiques autours d'InSight ont permis de contraindre l'épaisseur de la coulée à seulement 200 m (Pan et al., 2020). L'absence de détection de cette interface au point de rebond argumente dans le sens d'une structure locale (Li et al., 2022). Pour les deux couches plus profondes, il existe beaucoup moins de contraintes. La couche la plus profonde a des vitesses sismiques très proche de celle du manteau, la minéralogie de cette couche doit alors être proche de celle du manteau, c'est-à-dire ultra-mafique. Les deux couches les plus profondes pourraient aussi avoir une structure semblable au plancher océanique, une composition similaire mais un mode de dépôt et un temps de refroidissement différents (Christeson et al., 2019). La couche supérieure aurait une texture basaltique avec une certaine porosité et la couche inférieure avec la même composition mais avec une texture de gabbro (Drilleau et al., 2022). Une couche d'orthopyroxénite avec une texture gabbroïque semblable à la météorite ALH84001 pourrait aussi expliquer des vitesses sismiques légèrement plus faibles que celle d'un manteau riche en olivine (Flesch et al., 1998). La couche intermédiaire pourrait ressembler à la couche supérieure et la limite à 11 km serait une fermeture de la porosité. La déformation visqueuse des roches est un mécanisme de fermeture des pores mais son fonctionnement dépend de l'évolution thermique et de l'âge de formation des pores (Gyalay et al., 2020). Un autre mécanisme de fermeture des pores non encore étudié est le métamorphisme. Mars a une histoire hydrologique avec de l'eau liquide à sa surface et probablement un océan (Hynek et al., 2010; Schmidt et al., 2022). Ce cycle de l'eau implique une circulation d'eau en profondeur, au sein de la porosité, et permettent un métamorphisme de faible degré (Semprich et al., 2019). Ce type de métamorphisme précipite des minéraux hydratés dans la porosité pouvant entrainer sa fermeture. Ces minéraux hydraté ont pu être détectés dans les pics centraux de cratère d'impact dans les Basses Plaines du Nord (Carter et al., 2013).

Modèles d'épaisseur de croûte ancrés par la sismologie

L'épaisseur sismique sous InSight permet d'ancrer les modèles d'épaisseurs de croûte obtenus à l'aide des cartes d'anomalies de Bouguer. Avec cet ancrage, il n'est plus besoin de définir une épaisseur moyenne de croûte, les seuls paramètres restant étant les densités crustale et mantellique (Wieczorek et al., 2013; Knapmeyer-Endrun et al., 2021; Wieczorek et al., 2022). L'épaisseur moyenne de la croûte est alors estimée entre 52 et 65 km pour des densités crustales homogènes et comprises entre 2550 et 3050 kg m^{-3} et une épaisseur sous InSight de 43 km (Knapmeyer-Endrun et al., 2021; Wieczorek et al., 2022). La limite inférieure de la densité est choisie arbitrairement comme la densité de

la croûte lunaire. La densité maximale est celle où l'épaisseur minimale de la croûte tombe à 0 km dans le bassin d'Isidis (Knapmeyer-Endrun et al., 2021). Ces résultats sont en accord avec les résultats précédemment obtenus via le ratio gravité/topographie (Wieczorek and Zuber, 2004). L'amplitude de la dichotomie d'épaisseur de croûte obtenue dans ces modèles varie avec la densité crustale : plus la densité crustale est importante plus la dichotomie crustale est large.

Les modèles précédents considèrent une densité crustale homogène, or, nous avons vu qu'il existe de sérieuses preuves d'une croûte moins dense dans les Hauts Plateaux. Considérer une densité moins importante dans l'hémisphère sud réduit l'épaisseur de la croûte dans les Hauts Plateaux et diminue l'amplitude de la dichotomie (Figure 1.6). Pour une densité de 2600 kg m^{-3} dans l'hémisphère sud et 2900 kg m^{-3} dans l'hémisphère nord, la dichotomie crustale disparaît et la topographie tend vers un modèle isostatique de Pratt où la topographie est expliquée totalement par une différence de densité. Après avoir déterminé l'épaisseur moyenne le long du grand cercle des ondes de Rayleigh, Kim et al. (2023a) comparent leur résultat avec les modèles de croûte avec et sans contraste de densité crustale entre les deux hémisphères. Ils estiment une épaisseur de croûte moyenne entre 42 et 56 km et un contraste de densité inférieur à 200 kg m^{-3}.

1.3.3 Noyau martien

La taille et la composition du noyau martien ont été estimées avant la mission InSight par deux méthodes distinctes. Khan et al. (2018) inversent la masse, le moment d'inertie et la réponse aux marées solides pour déterminer la structure interne martienne et la composition martienne, notamment pour le noyau. Ils estiment un rayon du noyau entre 1730 et 1830 km, une densité entre 6.1 et 6.5 g cm^{-3} et une composition à $\sim 75.5 - 80$ wt% de fer, $\sim 5 - 6$ wt% de nickel, and $\sim 15 - 18.5$ wt% de soufre. Konopliv et al. (2020) ont utilisé les données de gravité de différentes missions orbitales pour déterminer l'oscillation de Chandler, l'oscillation de l'axe de rotation par rapport à la surface rigide. Ils déterminent avec une bonne précision une période de 206.9 $\pm$ 0.5 jours. Cette oscillation est compatible avec un rayon de noyau compris entre 1790 et 1840 km, plus grand que précédemment estimé et donc moins dense. L'étude des marées de Phobos par Pou et al. (2022) estiment un rayon du noyau similaire, de 1820 $\pm$80 km. L'instrument de traçage radio RISE de la mission InSight a déterminé une période de nutation libre du noyau de 243 $\pm$ 3.3 jours et une amplification de 0.0615 $\pm$ 0.007 pour $\approx$ 600 jours de données. Cette période d'amplification est compatible avec un rayon du noyau de 1835 $\pm$ 55 km et un facteur d'amplification non nul certifie que le noyau est totalement liquide. La taille du noyau implique des densités comprises entre 5.9 et 6.2 g cm^{-3}, encore plus faibles que précédemment. La composition du noyau nécessite alors plus d'éléments légers, 2.5 $\pm$ 0.5 wt% oxygène, 15 $\pm$ 2 wt% de soufre et 1.5 $\pm$ 0.5 wt% de carbone, en faisant l'hypothèse de 1 wt% d'hydrogène.

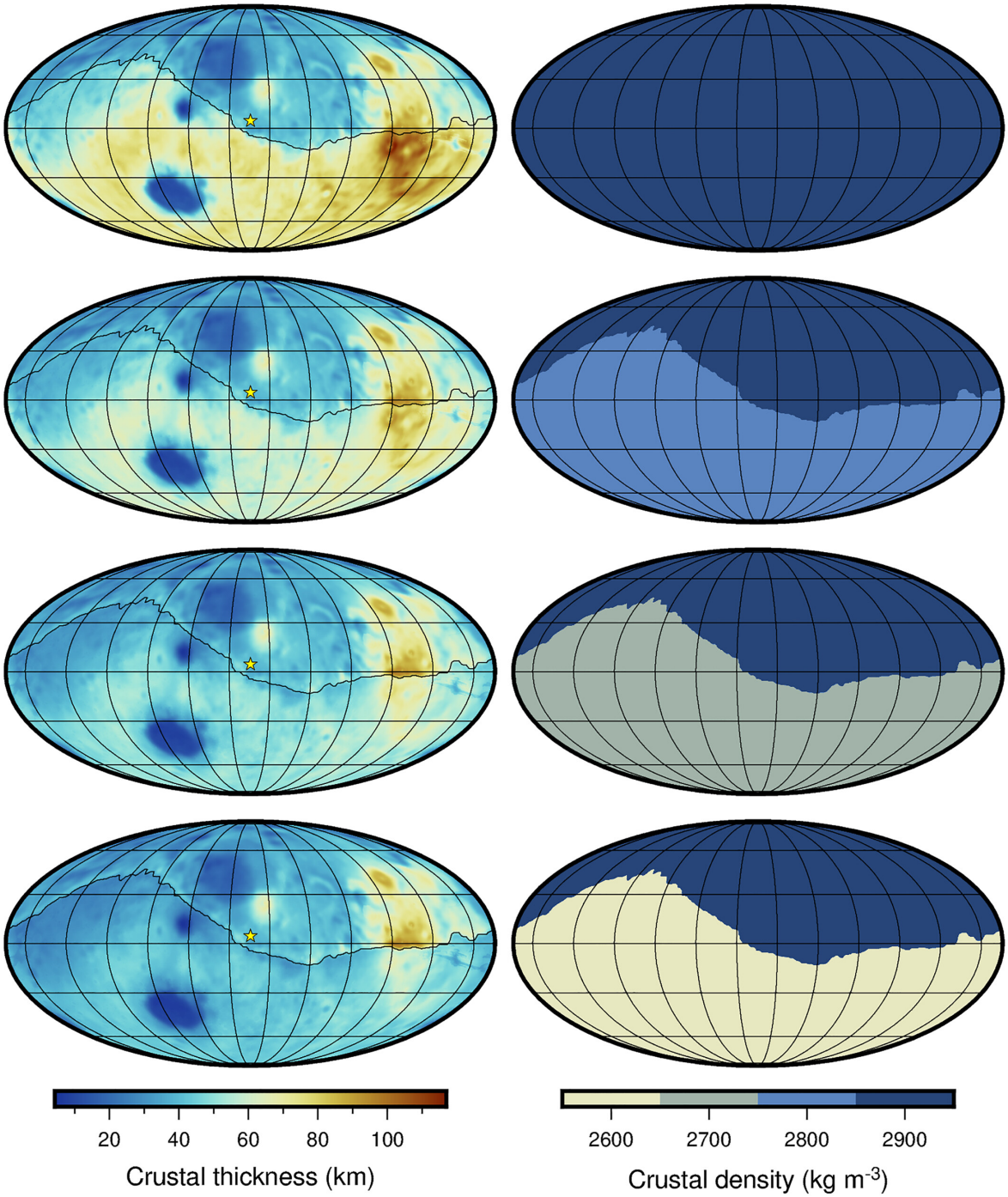

FIGURE 1.6 – Modèles d'épaisseur de croûte qui considèrent différentes densités au nord et au sud de la limite de dichotomie (Figure issue de Wieczorek et al. 2022). Pour cette série de modèles, la densité des Basses Plaines du nord est fixée à 2900 kg m^{-3}, tandis que la densité des Hauts Plateaux du sud varie (du haut vers le bas) de 2900 à 2600 kg m^{-3} par incrément de 100 kg m^{-3}. Pour tous les modèles, l'épaisseur de la croûte est contrainte à 39 km au site d'atterrissage d'InSight, et la densité du manteau et du noyau provient du modèle intérieur de Khan et al. (2022). La limite de la dichotomie (courbe noire) provient d'Andrews-Hanna et al. (2008a)

La sismologie est historiquement une méthode efficace pour déterminer la profondeur et les caractéristiques physiques, comme l'impédance, des interfaces, notamment les interfaces solide-liquide. Les ondes SH (ondes S polarisées horizontalement) ne peuvent se transmettre sous la forme d'onde P dans un liquide, contrairement aux ondes SV (polarisées verticalement). Par conséquence, Les ondes SH sont fortement réfléchies dans le manteau à l'interface noyau-manteau (liquide-solide) et arrivent au sismomètre orthogonalement à la surface. Ces ondes S réfléchies à la CMB sont appelées ScS et sont caractérisées à leurs réceptions par une polarisation linéaire et horizontale. Stähler et al. (2021) ont analysé six évènements sismiques avec un bon ratio signal sur bruit et avec des distances épicentrales compatibles avec la détection d'onde ScS, entre 27 et 38.5°. Après un filtrage de polarisation linéaire et verticale, les six évènements montrent des temps d'arrivée similaires, car à des distances similaires, pour les ondes ScS. Le rayon est ensuite calculé en utilisant des modèles de vitesses sismiques pour le manteau (Figure 1.7a, Khan et al. 2021; Stähler et al. 2021) et est estimé à 1830 $\pm$ 40 km. Ce rayon est en accord avec les estimations décrites précédemment et a été confirmé par des études ultérieures (Durán et al., 2022b; Wang and Tkalčić, 2022). Deux ondes SKS ont été détectées pour deux évènements différents. L'onde SKS est une onde S verticale convertie en onde P une première fois à l'interface manteau-noyau et retransformée en onde S à l'interface noyau-manteau avant d'atteindre le récepteur. Ces ondes ont traversé le noyau et nous renseignent sur les propriétés élastiques du noyau. La vitesse des ondes P a été estimé à 4.8-5 km s^{-1} dans le haut du noyau et la densité entre 6 et 6.3 g cm^{-3}.

Les densités nécessaires pour expliquer un noyau aussi important sont difficiles à reproduire expérimentalement et nécessitent une très grande quantité d'éléments légers (S, C, H). Une solution à ce problème serait la présence en base de manteau d'un océan magmatique basal ou couche D" (Samuel et al., 2021). En effet, les méthodes précédentes de détermination du rayon du noyau sont sensibles à une interface liquide-solide et moins ou pas du tout à un changement de composition (Stähler et al., 2021; Le Maistre et al., 2023). Une couche de magma de quelques dizaines de kilomètres d'épaisseur pourrait expliquer les importants rayons pour l'interface liquide-manteau avec des densités du noyau métallique potentiellement plus réalistes. Le Maistre et al. (2023) estiment que les résultats de RISE sur la nutation libre du noyau sont compatibles avec une telle couche jusqu'à une épaisseur de 200 km.

1.3.4 Manteau

Les modèles de composition chimiques martiens (Taylor, 2013; Yoshizaki and McDonough, 2020) peuvent être utilisés dans des modélisations thermodynamiques pour déterminer l'assemblage minéralogique à l'équilibre le long d'un profil température-pression (T, P) (Connolly, 2009). Les deux transitions minéralogiques principales du manteau terrestre se produisent à 400 km de profondeur (olivine $\rightarrow$ wadsleyite) et à

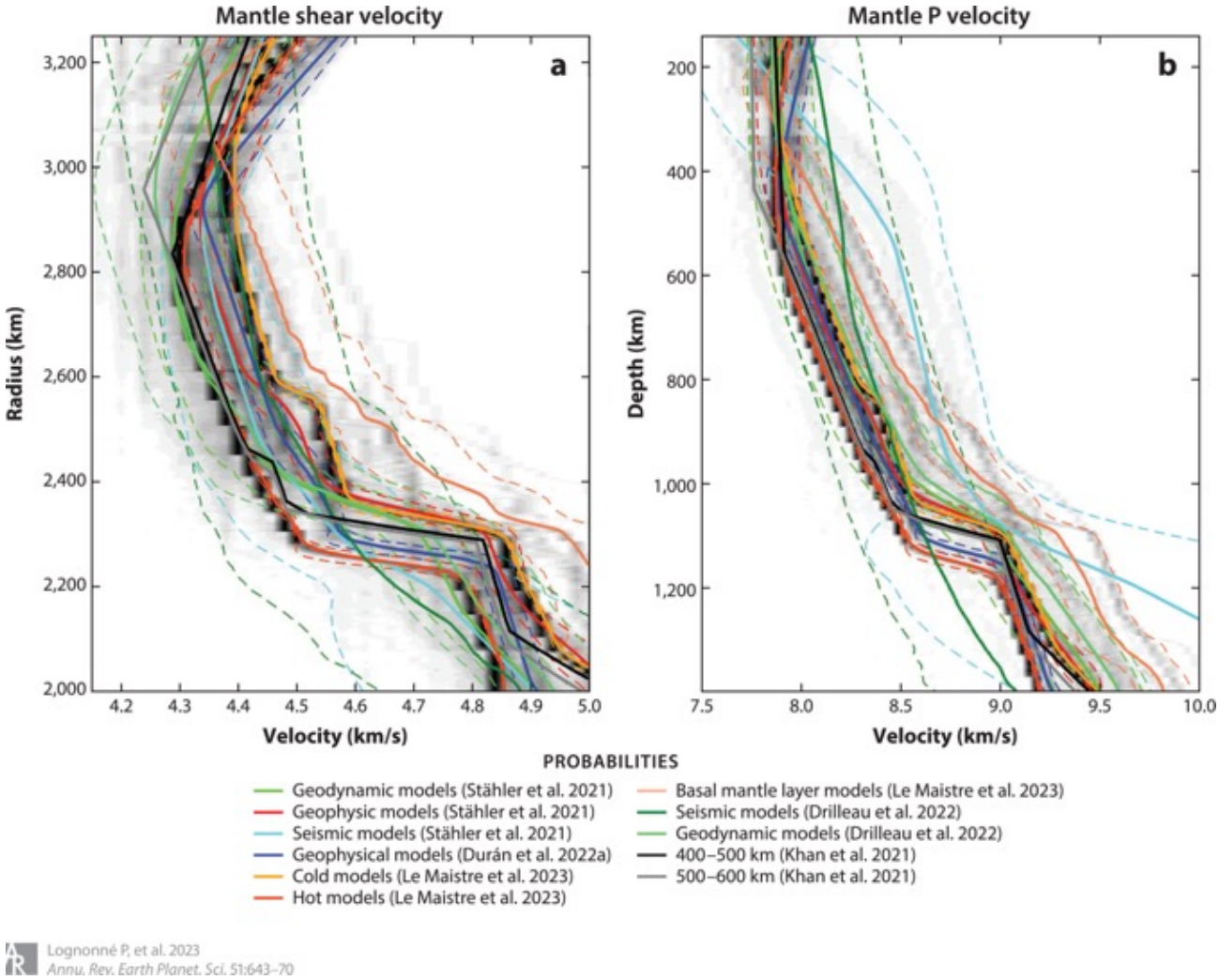

FIGURE 1.7 – Compilation des différents modèles de vitesse sismique pour le manteau obtenus à partir des inversions conjointes des phases directes (P, S) et secondaires (PP, PPP, SS, SSS, ScS) issue de Lognonné et al. (2023). De gauche à droite pour (a) les vitesses des ondes de cisaillement sismiques V_s et (b) les vitesses des ondes de compression sismiques V_p. Les références des modèles sont fournies, avec les mêmes codes de couleur dans les panneaux a et b. Pour chaque famille de modèles, la ligne continue fournit le modèle moyen, tandis que les lignes en pointillé fournissent l'incertitude $1-\sigma$. Le fond gris représente la dispersion a posteriori de ces modèles, en termes de probabilité, en supposant que chaque famille de modèles a la même probabilité. Notons qu'en dessous de 800 km de profondeur (2600 km de rayon), aucun temps de parcours des ondes P ne contraint directement les profils de vitesse des ondes P. Ces derniers sont donc indirectement contraints par les temps de parcours des ondes ScS, par le rapport V_p/V_s issu des modèles de minéralogie et de température, et par les corrélations en profondeur avec les profils V_p au-dessus de 800 km. La résolution dans la zone de transition du manteau, pour des rayons inférieurs à 2400 km, est également faible pour les ondes S, comme le montre la plus grande dispersion des modèles publiés.

660 km de profondeur (wadsleyite → bridgmanite). Ces deux transitions dépendent principalement de la pression. La gravité martienne étant $\sim 1/3$ celle de la Terre, ces transitions se font à plus fortes profondeurs (Mocquet et al., 2011). La formation de la bridgmanite est alors estimée à un rayon de 1700 $\pm$ 100 km soit un rayon inférieur au noyau liquide (noyau fer $\pm$ océan basal, Section 1.3.3). Ce changement de phase est donc très peu probable. La structure du manteau est alors définie par une lithosphère thermique conductive et une partie convective dans laquelle une zone de transition (olivine → wadsleyite) doit-être observé. La sismologie martienne permet ensuite de contraindre cette structure.

Khan et al. (2021) ont effectué l'inversion des temps d'arrivées de huit évènements sismiques martiens avec deux méthodes différentes. Une inversion sismique basée sur les vitesses des ondes P et S avec un modèle de planète à plusieurs couches et une inversion géophysique où les vitesses des ondes P et S sont reliées à l'équilibrage minéralogique et aux propriétés thermodynamiques (T, P). Ces évènements permettent d'échantillonner les 800 premiers kilomètres du manteau martien. Les profils de vitesses sismiques (S et P) obtenus par les deux méthodes sont similaires (Figure 1.7, Khan et al., 2021). Le fort gradient thermique dans la lithosphère comparé au gradient de pression, faible sur Mars, est à l'origine d'une zone de faible vitesse. En effet, le long du profil température-pression, deux effets sont en concurrence. D'une part, l'augmentation de la pression entraîne une augmentation des vitesses sismiques. D'autre part, l'augmentation de température diminue les vitesses sismiques. L'effet de cette dernière est dominant, les vitesses sismiques décroissent alors avec la profondeur dans la lithosphère thermique. Le minimum de vitesse sismique est atteint à la base de la lithosphère quand le gradient thermique diminue en devenant isentropique. La zone à faible vitesse sera plus marquée pour les ondes S car elles sont plus sensibles aux variations de températures (Figure 1.7). Une zone à faible vitesse peut générer une zone d'ombre, les séismes à une certaine distance ne sont alors pas détectés, car les raies sismiques sont déviées (Zheng et al., 2015). Cette zone d'ombre n'est pas vraiment observée dans le cas martien : des phases sismiques sont observées provenant de distances épicentrales où cet effet était attendu. Néanmoins, Khan et al. (2021); Durán et al. (2022b) ont remarqué une diminution de l'amplitude des ondes S par rapport aux ondes P entre deux distances épicentrales. Cette diminution serait la trace de cette zone d'ombre et a permis de déterminer une épaisseur pour la lithosphère thermique entre 400 et 600 km. L'absence de zone d'ombre est sans doute liée aux faibles gradients de température résultants de l'importante épaisseur de la lithosphère thermique. La température potentielle du manteau martien est comprise entre 1600 et 1700 K dans Khan et al. (2021) et entre 1650 et 1750 K dans l'étude ultérieure similaire de Durán et al. (2022a). Drilleau et al. (2021, 2022) proposent une paramétrisation d'un autre type pour obtenir la structure du manteau, l'inversion géodynamique. Cette fois, les profils de températures utilisés pour l'inversion sont issus d'un modèle géodynamique. Cette paramétrisation permet de fortement réduire la variabilité de la distribution des profils sismiques possibles. Ces inversions estiment une lithosphère épaisse, 540 $\pm$ 120 km et

une température potentielle de 1740 $\pm$ 90 K.

Le changement de phase olivine $\rightarrow$ wadsleyite au milieu du manteau génère une discontinuité sismique, un saut dans les vitesses sismiques (Figure 1.7). Ce saut est concomitant avec un gradient de vitesse sismique qui augmente significativement générant une triplication des phases sismiques. Huang et al. (2022) ont utilisé cinq évènements sismiques martiens avec une distance épicentrale compatible avec une triplication, entre 60° et 80°. Par comparaison des données avec le problème direct et en utilisant une minimisation de l'erreur, ils déterminent une profondeur de 1006 $\pm$ 40 km pour la transition. Connaissant la pression à laquelle cette transition se produit, $\approx$ 12.5 $\pm$ 0.5 GPa, on détermine pour une composition de manteau donnée, la température du changement de phase. En prenant en compte l'incertitude sur la profondeur et celle sur la composition du manteau martien, Huang et al. (2022) donne une température entre 1670 et 1892 K à la profondeur du changement de phase ce qui correspond à une température potentielle entre 1505 et 1705 K. La température du changement de phase est principalement sensible à la teneur en magnésium dans l'olivine. Moins le manteau est enrichi en fer, donc plus la teneur en magnésium des olivines est importante, plus la température du changement de phase est repoussée vers des températures plus froides. Les derniers modèles de compositions, moins riches en fer, pousseraient alors la température potentielle vers les valeurs les plus froides de la gamme.

1.4 Formation, différentiation et évolution thermique de Mars

1.4.1 Formation et Différentiation

Accrétion

Le système solaire s'est formé il y a environ 4.6 Ga par effondrement d'un nuage de gaz donnant naissance à un proto-soleil et un disque protoplanétaire. Les premiers solides connus ayant condensé à partir du disque sont les inclusions riches en calcium et aluminium (CAI, Calcium -Aluminium-rich Inclusion). La datation Pb-Pb de ces inclusions donne un âge moyen de 4568.2 Ma (Bouvier and Wadhwa, 2010) qui est classiquement considéré comme l'âge de notre système solaire. Les âges des évènements ayant eu lieu très tôt dans l'histoire du système solaire sont généralement exprimés en millions d'années après les CAI. Les premiers silicates se forment juste après, durant les trois premiers millions d'années après les CAI (Connelly et al., 2012). Les grains formés s'accrètent entre eux et grossissent en taille grâce aux forces de gravité et électromagnétique (Vigneron, 2020; Lesur et al., 2022). La taille des objets formés est de plus en plus importante, ce qui amène à la formation de corps planétaires de petites tailles, les planétésimaux. Les fortes concentrations en éléments producteurs de chaleur, notamment de courte durée de vie comme ^{26}Al permettent à ces planétésimaux de se différencier en formant un noyau et une croûte (Birnstiel et al., 2016). La chimie de ces

corps dépend de leur lieu de formation dans le disque, entrainant une grande variété dans les météorites recueillies sur Terre (Wasson and Kallemeyn, 1988). Ces météorites forment un échantillon non représentatif des blocs qui ont formé les planètes du système solaire (McDonough and Sun, 1995; Sanloup et al., 1999).

Les nombreux groupes de météorites représentent des compositions limites qui peuvent être mélangées pour obtenir la composition d'une planète. Par exemple, Sanloup et al. (1999) proposent à partir des anomalies isotopiques en oxygène (δ^{17}O et δ^{18}O) que Mars ait été formée par 45% de Chondrites à enstatite riches en fer (EH) et 55% de Chondrites ordinaires de type H (très riches en fer). Fitoussi et al. (2016) obtiennent la distribution de ces blocs ayant formé Mars à partir des anomalies isotopiques en oxygène, mais également en Cr, Ni, Ti, Mo, Ca et Sr. La distribution retenue pour Mars est 55% du corps parent des Angrites, 36% de Chondrites ordinaires H et 9 % de Chondrites carbonées CI. La composition en éléments majeurs correspondante est similaire à celle obtenue par Taylor (2013). Cette composition est compatible avec le scénario de formation planétaire du grand virement de bord ("Grand Tack"). Ce scénario est une évolution du modèle de Nice (Gomes et al., 2005) qui considère une double migration de Jupiter vers le Soleil. Ce scénario est modélisé par Walsh et al. (2011) afin d'expliquer la faible masse de Mars ou l'absence de super-Terre. En effet, la migration de Jupiter appauvrirait le disque en poussière et en petits corps à l'emplacement auquel Mars s'est formée ($\approx$ 1 U.A) et expliquerait alors sa faible masse comparée à celles de la Terre et Vénus. Néanmoins, la formation des planètes dans le disque est encore un sujet complexe et mal compris, notamment à cause du nombre de processus physiques à l'œuvre (Lesur et al., 2022).

Les impacts successifs ayant formé Mars apportent assez d'énergie ($\approx 10^{30}$ J) pour fondre l'ensemble de la planète (Wetherill, 1990; Elkins-Tanton et al., 2005). La phase siliceuse, moins dense, et la phase riche en fer, plus dense, étant immiscibles, la planète se différencie. La phase riche en fer plonge vers le centre de la planète formant le noyau alors que la phase silicatée forme un océan de magma.

Océan magmatique

La géochronométrie Hf - W des météorites martiennes pointe vers une différentiation noyau-manteau entre 7 et 13 millions d'années après les CAI (Blichert-Toft et al., 1999; Kleine et al., 2002), impliquant que l'accrétion de Mars et la formation de l'océan magmatique sont encore plus précoce (Figure 1.3). Cette différentiation est très précoce comparée à celle de la Terre (avant l'impact avec Theïa) datée à 30 Ma après les CAI (Bourdon et al., 2008). Le refroidissement et la cristallisation de l'océan magmatique sont fortement reliés à la formation et l'évolution de l'atmosphère primitive (Elkins-Tanton, 2008; Debaille et al., 2009). En effet, des volatiles comme l'eau ou le dioxyde de carbone sont des gaz à effet de serre et une atmosphère primitive riche en ces gaz ralentit considérablement le refroidissement et la cristallisation de l'océan magmatique.

Cette cristallisation et le début de l'extraction de la croûte sont datés entre 20 et 30 Ma après les CAI (Figure 1.3, Kruijer et al. 2017; Bouvier et al. 2018).

La pente du solidus du manteau martien étant plus importante que le gradient adiabatique, l'océan magmatique cristallise à partir de sa base (Elkins-Tanton et al., 2003, 2005). Des cristaux d'olivine se forment tout le long la cristallisation de l'océan magmatique. Si ces cristaux sont plus denses que le magma, ils s'accumulent en base de l'océan de magma, formant une couche qui s'épaissit, les cumulats, jusqu'à cristallisation complète de l'océan magmatique. Mais si les cristaux sont moins denses que le magma, ils flottent à une profondeur d'équilibre. Si les olivines flottent, une couche de magma stable se forme à l'interface avec le noyau lors de la cristallisation (Labrosse et al., 2007). Cette couche est enrichie en éléments incompatibles tels que les éléments producteurs de chaleur et en fer. Dans le cas de Mars, une telle couche est stable chimiquement et gravitationnellement à l'échelle des temps géologiques permettant d'expliquer la présence d'une couche de magma basal actuel comme celle proposée par Samuel et al. (2021).

Une croûte primaire anorthositique ?

Pendant la cristallisation de l'océan magmatique, les cumulats d'olivines ne sont pas les seuls à cristalliser. Des cristaux de plagioclase (pôle anorthose) peuvent se former à faible pression. Ces cristaux étant plus légers que le magma silicaté mafique, ils vont remonter jusqu'à la surface de l'océan de magma et former de l'anorthosite. Ces anorthosites vont peu à peu former une croûte primaire. C'est le scénario standard pour la formation des Hauts Plateaux lunaires (Wood et al., 1970), avec une épaisseur de 34 à 43 km pour la croûte anorthositique (Wieczorek et al., 2013). Michaut and Neufeld (2022) proposent un autre modèle de la formation d'une croûte anorthositique par l'extraction d'un liquide enrichi en composant léger de type anorthositique pendant une phase d'océan de magma boueuse. Ce mode de formation de la croûte prolonge considérablement la cristallisation de l'océan de magma. Ce modèle permet de réconcilier les différences de chimie observées dans les échantillons lunaires et les âges de ces échantillons.

Dans le cas de l'océan magmatique martien, la formation d'une croûte primaire anorthositique est suggérée pour expliquer les observations de roches felsiques dans les Hauts Plateaux martiennes, comme sur la Lune (Carter and Poulet, 2013). Des expériences de fusion, pour une composition martienne, menées par Collinet et al. (2015), montrent que le plagioclase est stable à pression inférieure à $\sim$ 1 GPa et pour des températures correspondant à une fraction fondue inférieure à $\sim$ 15%. Ces expériences vont à l'encontre de l'hypothèse d'une croûte de flottaison pour Mars, les cristaux de plagioclase se formant à une fraction fondue inférieure à celle de la transition rhéologique. L'hypothèse d'une croûte anorthositique formée par extraction de liquide n'a pas été testée dans le cadre de l'océan de magma martien pour le moment.

1.4.2 Évolution thermique et Convection solide

De l'océan de magma au régime de couvercle stagnant

Les observations de la mission InSight sur la structure thermique du manteau et de la croûte sont en accord avec le régime de convection du manteau Martien attendu : il s'agit d'un couvercle stagnant (Knapmeyer-Endrun et al., 2021; Khan et al., 2021; Durán et al., 2022b). La viscosité des roches, c'est-à-dire leur capacité à se déformer, varie sur une dizaine d'ordres de grandeur entre leur point de fusion, le solidus $\sim$ 1400 K à 0 GPa, et la température à la surface des planètes, $\sim$ 300 K. Les roches proches de la surface sont trop visqueuses pour pouvoir participer à la convection mantellique, un couvercle rigide et conductif se développe, un couvercle stagnant (Solomatov, 1995; Solomatov and Moresi, 1997). Davaille and Jaupart (1993) ont pu montrer avec des expériences analogiques que la base du couvercle est une limite thermique et rhéologique, donnant un critère pour délimiter la partie convective et la partie rigide. La viscosité au sein du couvercle stagnant varie sur plusieurs ordres de grandeur alors qu'elle varie peu dans la partie convective. Un régime en couvercle stagnant peut être alors modélisé par un manteau isovisqueux surplombé d'une couche conductive isolante (Davaille and Jaupart, 1993; Grasset and Parmentier, 1998). La planète refroidit alors par l'épaississement de la couche conductive et dans une moindre mesure par la diminution en température de la partie convective. Les conditions initiales du couvercle, la température du manteau convectif et l'épaisseur du couvercle, dépendent de la transition entre un régime d'océan magmatique liquide et la convection solide.

Lors de la cristallisation de l'océan magmatique, la couche limite supérieure se refroidit de plus en plus car le flux de chaleur provenant de l'océan diminue et elle commence alors à cristalliser. Les roches formées présentent de fortes viscosités formant un couvercle rigide, stagnant et conducteur à la surface (Michaut and Neufeld, 2022; Watson et al., 2022). Ce couvercle conducteur isole la partie convective du manteau encore partiellement fondu qu'il surplombe. En cristallisant, la viscosité du manteau augmente rapidement, la viscosité des roches étant $\approx$ 20 ordres de grandeur plus importante que la viscosité du magma. Plus les taux de fusion baissent, plus la viscosité apparente augmente et plus la vigueur de la convection et le flux de chaleur associé diminuent. La diminution du flux permet à la surface de se refroidir et au couvercle de croître en épaisseur. Le manteau passe d'une rhéologie gouvernée par le magma avec des cristaux en suspension à une rhéologie gouvernée par une matrice solide avec une porosité formée par la fusion partielle. Cette transition dite rhéologique se déroule à une fraction fondue comprise entre 30 et 40%. Une fois la transition dépassée, le refroidissement est beaucoup plus lent, permettant de maintenir une couche partiellement fondue sous le couvercle. Cette couche est de l'ordre d'une centaine de kilomètres d'épaisseur et peut être maintenue pendant plusieurs centaines de millions d'années (Breuer and Spohn, 2006).

Le magma présent dans cette couche partiellement fondue évolue en composition à

mesure que le taux de fusion diminue, s'enrichissant en éléments tels que le silicium, le fer et le calcium. Les éléments producteurs de chaleur (K, U et Th) sont très incompatibles et le magma est très enrichi en ces éléments (10 à 30 fois plus que le résidu). Ce magma mafique est moins dense que le manteau, il a donc une flottabilité positive ce qui l'amène à être extrait du manteau vers la surface. En se refroidissant en surface, ce magma mafique enrichi en éléments producteurs de chaleur forme la croûte basaltique, expliquant les fortes concentrations en K-Th de la surface martienne. La dynamique de ce manteau partiellement fondu détermine la croissance de la croûte et l'appauvrissement du manteau en éléments producteurs de chaleur. L'approche la plus physique de ce problème est de considérer un écoulement biphasique comme Boukaré and Ricard (2017) en considérant la compaction de la matrice solide. Ogawa and Yanagisawa (2012a) ont modélisé l'évolution d'un manteau avec une couche partiellement fondue tenant compte d'une dynamique du magma au sein de la matrice solide dans une géométrie cartésienne. Ils montrent que la croûte s'extrait bien à partir de cette couche partiellement fondue et que l'effet de la déshydratation est important dans la dynamique. Néanmoins, ce modèle ne résout pas explicitement un écoulement biphasique qui est un défi de modélisation, c'est pourquoi la majorité des modèles dynamiques du manteau considèrent une convection purement solide où le magma n'a pas ou peu d'effet sur la dynamique (Keller and Tackley, 2009; Šrámek and Zhong, 2012; Plesa and Breuer, 2014).

Une fois la croûte extraite et le manteau quasi complètement cristallisé, le meilleur modèle d'évolution pour Mars est une convection en couvercle stagnant (Solomatov, 1995; Solomatov and Moresi, 1997). Le couvercle conductif est composé d'une partie crustale en surface et d'une partie mantellique. Ce couvercle conductif et isolant surplombe un manteau convectif avec deux couches limites thermiques inférieure et supérieure et dont le profil de température moyen suit un gradient de température isentropique (à entropie constante). Ce manteau refroidit principalement par épaississement du couvercle au cours du temps et seulement ensuite par la baisse de la température moyenne du manteau convectif. Les paramètres principaux contrôlant l'évolution thermique sont la rhéologie du manteau (principalement la viscosité) (Breuer and Spohn, 2006; Plesa et al., 2015) et la distribution des éléments radioactifs entre la croûte et le manteau (Thiriet et al., 2018).

Observation sur l'évolution thermique

Les observations permettant de contraindre l'évolution thermique martienne sont peu nombreuses, notamment du fait du manque d'échantillons anciens à notre disposition. Les échantillons nous renseignent sur l'âge de début de construction de la croûte, qui semble être de 20 à 30 Ma après les CAI (Kruijer et al., 2017; Bouvier et al., 2018) et permettent de déterminer un âge de départ des modèles d'évolution thermique. L'âge des météorites martiennes les plus récentes témoigne d'un volcanisme qui a persisté jusqu'à notre époque. Le volcanisme martien se déroule sur 4,5 milliards d'années, mais le

volume de magma produit diminue avec le temps (Tanaka et al., 2014; Baratoux et al., 2013). Les observations actuelles sur les épaisseurs crustales, ainsi que sur l'état thermique du manteau renseignent sur un état final, mais différentes évolutions thermiques peuvent produire les mêmes états finaux. Pour distinguer les différentes évolutions thermiques, deux principales observations indirectes fournissent des contraintes sur l'état thermique passé : les épaisseurs élastiques et la chimie de la croûte.

L'épaisseur élastique de la lithosphère définit la profondeur jusqu'à laquelle une contrainte est supportée par déformation élastique, au-delà la contrainte est accommodée par la déformation visqueuse. La rhéologie dépend fortement de la température et la transition se produit à une température située entre 700 et 850 K (Caldwell and Turcotte, 1979). L'épaisseur élastique permet ainsi de déterminer une température à une certaine profondeur, ce qui est un bon indicateur du gradient de température et du flux de chaleur au sein de la lithosphère. L'épaisseur élastique sous les grands édifices peut être déterminée à partir des données gravimétriques. En effet, lorsque l'édifice se construit, il crée une surcharge de masse à la surface, appliquant une contrainte qui déforme la lithosphère. L'anomalie de gravité résultante dépend de l'épaisseur élastique au moment de la mise en place. Nous supposons que l'anomalie de gravité est préservée pendant le reste de l'évolution thermique. En datant la formation de l'édifice, nous obtenons alors une estimation du profil thermique et du flux de chaleur en un point donné de la surface de Mars et au moment de la charge. Par exemple, les études au niveau de différents édifices volcaniques permettent de déterminer un certain nombre d'épaisseurs élastiques (McGovern et al., 2004; Hoogenboom and Smrekar, 2006; Grott and Wieczorek, 2012), mais avec de grandes incertitudes quant à leur âge (Grott et al., 2013). Les épaisseurs élastiques actuelles sous les calottes polaires sont déterminées notamment grâce aux observations de l'instrument *Shallow Radar* de Mars Reconnaissance Orbiter (Phillips et al., 2008; Wieczorek, 2008; Broquet et al., 2021). Sous la calotte nord, l'épaisseur élastique calculée est entre $\approx$ 330 et 450 km alors qu'elle n'est qu'entre $\approx$ 150 et 360 km sous celle au sud. Les épaisseurs élastiques sont plus faibles au Noachien et augmentent jusqu'à aujourd'hui, confirmant l'idée d'une planète en couvercle stagnant, voyant son couvercle s'épaissir avec le temps.

Les observations de spectroscopie orbitale, infrarouge et gamma, ainsi que celles des différents rovers martiens, donnent un aperçu de la chimie des roches de la surface martienne (Taylor et al., 2006; Mangold et al., 2010; Baratoux et al., 2013; Sautter et al., 2016). La composition des roches basaltiques est directement liée aux conditions de pression et de température du manteau au moment de l'extraction du magma parent, en supposant un équilibre chimique avec le manteau et l'absence d'assimilation de la croûte au cours de l'ascension vers la surface. Une datation des roches permet ensuite de relier ces conditions à une époque géologique. Par exemple, Baratoux et al. (2013) prennent pour proxies les pyroxènes riches en calcium (HCP, High Calcium Pyroxene) et pauvres en calcium (LCP, Low Calcium Pyroxene). Plus un basalte est riche en LCP, plus il a été formé à une fraction fondue importante, car le calcium

est un élément avec un coefficient de partage inférieur à 1. Les terrains Noachien sont caractérisés par des roches riches en LCP alors que les terrains Héspérien le sont par des roches riches en HCP. À l'aide de pMELT, un modèle thermodynamique, Baratoux et al. (2013) calculent, en fonction de la pression et de la température potentielle de ce manteau, les abondances des deux types de pyroxènes dans une roche formée à partir d'un liquide magmatique en équilibre avec un manteau de composition martienne. Leurs résultats donnent des estimations des températures potentielles du manteau pendant les différentes périodes géologiques martiennes et montrent un volcanisme présent depuis le début du Noachien lié à un refroidissement régulier du manteau. Néanmoins, ces résultats sont fortement dépendants du modèle thermodynamique qui est adapté à des compositions terrestres. Collinet et al. (2021) ont développé un modèle thermodynamique qui utilise des données d'expériences avec une composition martienne pour modéliser des compositions de magma. Les températures potentiels calculés sont plus froides que celles précédemment calculés.

Le champ magnétique crustal détecté dans les Hauts Plateaux est généralement attribué à une géodynamo active à un stade très précoce de l'histoire martienne (Langlais et al., 2019). Dans ce cas, la dynamique du noyau et du manteau doit permettre à cette géodynamo de se développer. Une telle géodynamo peut être générée par une surchauffe initiale du noyau impliquant un flux initial important à l'interface noyau-manteau (Hauck and Phillips, 2002; Breuer and Spohn, 2003; Williams and Nimmo, 2004; Ke and Solomatov, 2009; Yan et al., 2023). Cependant, des observations récentes indiquent une dynamo encore active il y a 3.7 Ga, avec un arrêt possible entre ces deux périodes qui est difficile à concilier avec les modèles (Mittelholz et al., 2020). La dissipation des forces de marée et leurs interactions avec les orbites de Phobos et Déimos sont également utilisées comme une contrainte sur l'évolution thermique martienne (Mignard, 1981; Samuel et al., 2019). La dissipation des forces de marée dépend de la rhéologie de l'intérieur de Mars et donc de son état thermique. L'absence de contraintes sur l'âge des lunes et sur leurs évolutions orbitales est le principal défaut de cette approche.

Modélisation de l'évolution thermique

L'approche classique pour modéliser l'évolution thermique à l'échelle d'une planète est de résoudre les équations de conservation, de la masse, de l'énergie et de la quantité de mouvement. Cette approche permet d'obtenir dans la géométrie souhaitée les champs de vitesse, de température et de composition (Zhong, 2009; Keller and Tackley, 2009; Plesa and Breuer, 2014). Pour des cas simples isovisqueux cette approche fonctionne bien, mais la viscosité des roches dépend fortement de la température et, dans une moindre mesure, de la pression et de la composition. Par exemple, la viscosité est fortement modifiée par le contenu en eau d'une roche, une roche déshydratée pouvant avoir une viscosité jusqu'à 100 fois plus importante qu'une roche hydraté (Karato and Wu, 1993). Ces fortes variations de viscosité augmentent considérablement la

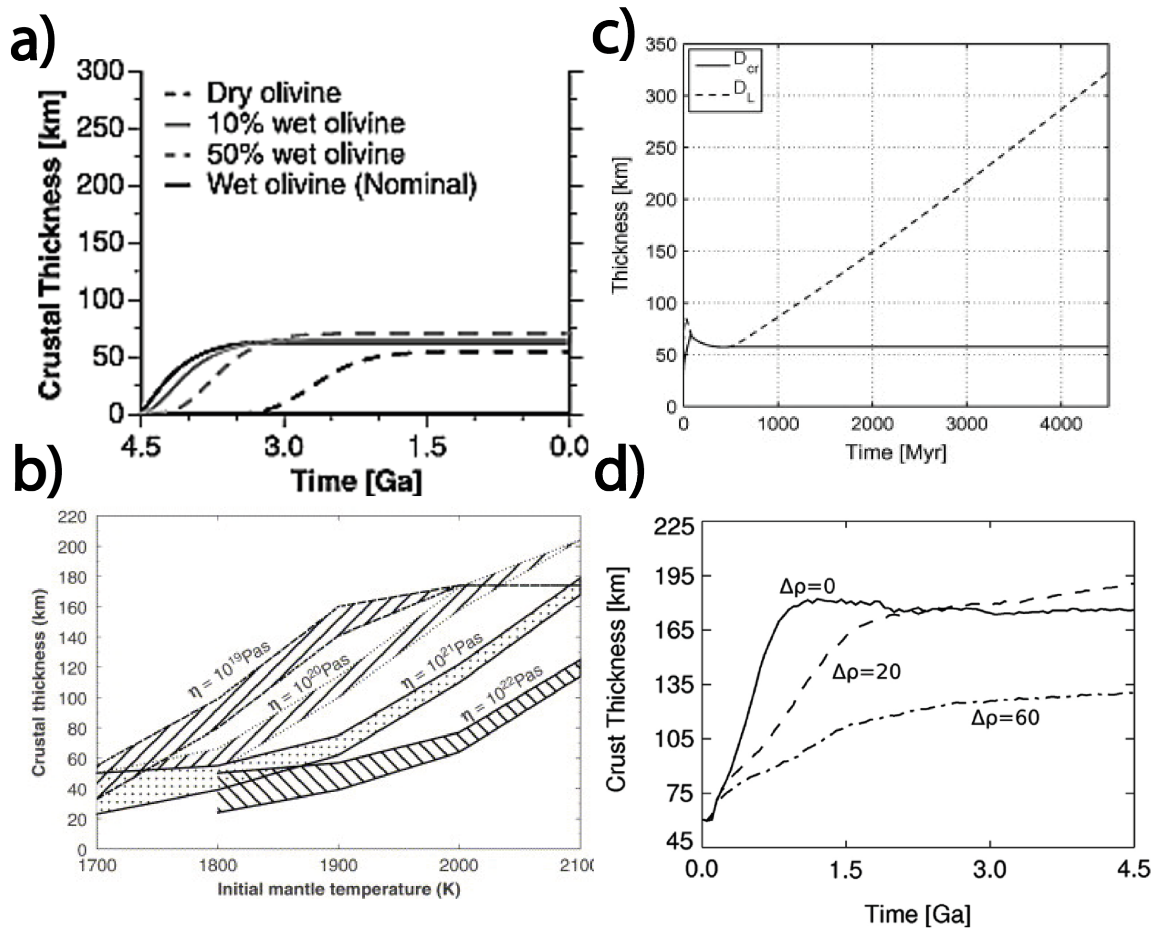

FIGURE 1.8 – Épaisseurs de croûtes obtenues par différentes études et différents types de modèles. (a) Hauck and Phillips (2002) Évolution de l'épaisseur de la croûte pour des manteaux plus ou moins riches en eau. La teneur en eau réduit la viscosité et retarde l'extraction de la croûte. (b) Breuer and Spohn (2006) Épaisseurs de croûte finales en fonction de la viscosité et de la température initiale du manteau. À viscosité constante, l'épaisseur de croûte augmente quand la température initiale augmente et à température initiale constante, l'épaisseur de croûte augmente en diminuant la viscosité. (c) Morschhauser et al. (2011) Exemple d'une évolution thermique où la croûte (ligne pleine) devient aussi épaisse que la lithosphère (ligne pointillée) et est érodée thermiquement (d) Plesa and Breuer (2014) Évolution de l'épaisseur moyenne de la croûte dans un modèle en géométrie 2D cylindrique pour différents contrastes de densité entre les résidus et le manteau fertile. Dans tous les cas proposés, les croûtes sont beaucoup plus épaisses qu'attendues.

complexité et le temps de calcul des modèles de convection. Les modèles d'évolution thermique paramétrés sont une alternative avec une physique plus simple, mais un temps de calcul considérablement plus court. Ce type de modèle considère un manteau convectif bien mélangé où l'on néglige les variations latérales et qui est surplombé par un couvercle conducteur. Le manteau convectif est alors décrit par une température moyenne dont l'évolution temporelle peut être obtenue par simple conservation de la chaleur. L'évolution temporelle de l'épaisseur du couvercle est obtenue par un bilan entre le flux convectif du manteau, déterminé par la théorie de la couche limite, et le flux conductif à la base du couvercle calculé avec l'équation de la chaleur en symétrie sphérique. Ce modèle nécessite de définir des lois d'échelle reliant par exemple le nombre de Rayleigh, la vigueur de la convection, avec le nombre de Nusselt, l'efficacité du refroidissement convectif (Solomatov, 1995). Ces lois d'échelle peuvent être obtenues soit par des expériences de laboratoires analogiques (Davaille and Jaupart, 1993, 1994) soit des expériences numériques (Grasset and Parmentier, 1998; Sotin and Labrosse, 1999; Dumoulin et al., 1999; Deschamps and Sotin, 2001; Thiriet et al., 2019).

L'extraction de la croûte et son interaction avec l'évolution thermique ont été principalement étudiées dans des modèles paramétriques (Hauck and Phillips, 2002; Breuer and Spohn, 2006; Morschhauser et al., 2011). Hauck and Phillips (2002) montrent qu'une faible viscosité est nécessaire pour expliquer les vitesses de croissance et les épaisseurs de croûtes attendues (Figure 1.8a). Ces faibles viscosités résulteraient d'un manteau mouillé, c'est-à-dire enrichi en eau. Breuer and Spohn (2006) ont amélioré le précédent modèle en considérant une vitesse d'extraction reliée à la vigueur de la convection plutôt qu'une extraction totale du magma formé. Contrairement à l'étude précédente, ils montrent que de plus fortes viscosités peuvent aussi expliquer les épaisseurs de croûte à condition d'avoir un manteau initialement plus chaud (Figure 1.8b). Morschhauser et al. (2011) montrent que certains modèles d'évolution thermique impliquent un recyclage de la croûte par délamination thermique (Figure 1.8c). Aucune observation ne soutient ce processus dans le cas de Mars, ces évolutions thermiques seraient alors à exclure. Ils montrent également le rôle de l'eau et de la déshydratation du manteau, notamment pour la croissance de l'épaisseur du couvercle conducteur. La prise en compte d'une viscosité dépendante de la teneur en eau du manteau aide à obtenir les épaisseurs élastiques observées. Plesa and Breuer (2014) explorent l'extraction de la croûte et la déshydratation du manteau dans un modèle de convection 2D dans le cas d'une planète en couvercle stagnant. L'augmentation de la viscosité et de la densité due à la formation de résidu appauvri en éléments légers et en eau joue un rôle important et complexe dans la dynamique du manteau. Néanmoins, à l'image des autres modèles prenant en compte l'extraction de la croûte en 2D et 3D (Keller and Tackley, 2009; Golabek et al., 2011; Šrámek and Zhong, 2012), les épaisseurs de croûtes obtenues, entre 100 et 200 km, sont trop grandes pour Mars (Figure 1.8d).

Les épaisseurs élastiques présentent des différences importantes entre les deux hémisphères (Grott et al., 2013). Pour étudier ces différences, Thiriet et al. (2018) ont

développé un modèle paramétrique avec une géométrie asymétrique, dans lequel deux hémisphères différents sont couplés avec le même manteau convectif. Ce modèle permet d'étudier d'éventuelles différences à l'échelle hémisphérique dans la structure de la lithosphère. Ils ont pu mettre en évidence que la dichotomie martienne d'épaisseur de croûte se prolonge en profondeur avec des lithosphères d'épaisseurs différentes entre les deux hémisphères. Ils expliquent les épaisseurs élastiques observées par une répartition différente des éléments producteurs de chaleur entre les deux hémisphères, avec 55% du total des éléments dans la croûte (dont 12 à 14% du total dans le nord et 43 à 51% dans le sud) et de 35 à 45% dans le manteau. Le surplus de chauffage dans l'hémisphère sud isole thermiquement l'hémisphère durant l'évolution thermique, ralentissant la croissance de la lithosphère thermique et donc de l'épaisseur élastique. Avec les nouvelles contraintes d'InSight, ce modèle a permis de déterminer que pour obtenir de la fusion actuelle sous Tharsis, 55 à 70 % du total des éléments producteurs de chaleur doivent être contenus dans la croûte (Knapmeyer-Endrun et al., 2021)

1.5 Formation de la dichotomie, évènement crucial de l'Histoire Martienne

Les épaisseurs de croûtes martiennes sont réparties de manière quasi bimodale entre les plaines de l'hémisphère nord et les Hauts Plateaux de l'hémisphère sud (Andrews-Hanna et al., 2008a; Bouley et al., 2020). Le mécanisme à l'origine de la formation de cette dichotomie est l'un des débats majeurs concernant l'évolution martienne. Avec un âge compris entre 4.5 et 3.7 milliards d'années, la dichotomie est une des plus anciennes caractéristiques de la surface martienne (Solomon et al., 2005; McGill and Dimitriou, 1990; Gurgurewicz et al., 2022). L'apparition de celle-ci est contemporaine voire plus ancienne que les Hauts plateaux alors que les Basses Plaines semblent plus récentes que la formation de la dichotomie. La jeunesse de la surface des Basses Plaines est probablement plus une conséquence tardive de la dichotomie que relative à sa formation (Figure 1.2, Tanaka et al. 2014). En effet, en prenant en compte les cratères d'impacts enfouis sous la surface de Mars, Watters et al. (2006) concluent que les Basses Plaines sont au moins aussi anciennes que les Hauts Plateaux. La présence d'un océan circumpolaire (Di Achille and Hynek, 2010; Citron et al., 2018a; Schmidt et al., 2022) est une piste sérieuse pour expliquer cette surface plus jeune par la formation de dépôts sédimentaires, enfouissant une partie des bassins d'impacts et diminuant le nombre de nouveaux cratères d'impact. Le mécanisme étant ancien, les traces qu'il a laissées à l'intérieur et en surface de Mars sont rares et dégradées et peuvent se confondre avec d'autres processus passés.

La Terre présente également une distribution bimodale des épaisseurs de croûte, avec des croûtes continentales épaisses et des croûtes océaniques plus fines. Cette distribution est une conséquence de la tectonique des plaques, or Mars ne présente pas de tectonique des plaques. D'autres mécanismes ont donc été proposés pour expliquer

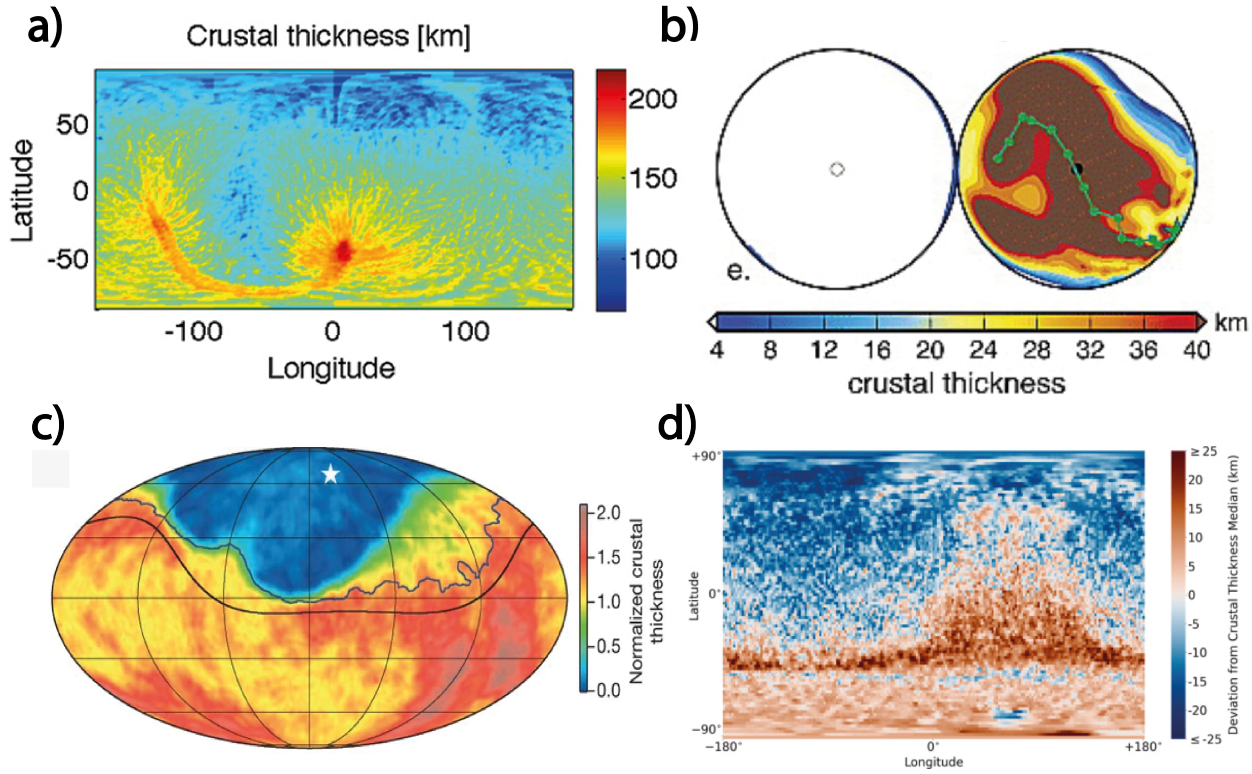

FIGURE 1.9 – Cartes d'épaisseurs crustales obtenues par différents mécanismes de formation de la dichotomie martienne. (a) Convection de degré 1 avec extraction de croûte par Keller and Tackley (2009), l'échelle est en km. (b) Migration du panache de Tharsis par Šrámek and Zhong (2012) où l'échelle de couleur, saturée à 40 km, représente la croûte formée par le panache et la ligne verte représente le chemin du cœur du panache qui termine sa course au niveau de l'étoile verte. (c) Bassin d'impact résultant des modélisations de Marinova et al. (2008), la ligne noire représente une limite de la dichotomie par Andrews-Hanna et al. (2008a) et la ligne bleue est la limite d'excavation. (d) Modèle d'épaisseur de croûte de Ballantyne et al. (2023), l'échelle est la différence entre l'épaisseur de croûte calculée et l'épaisseur médiane de Bouley et al. (2020)

ces épaisseurs de croûte différentes. Les mécanismes proposés pour la formation de la dichotomie martienne se séparent en deux familles. D'un côté les processus endogènes avec majoritairement des modes de convection de degré 1, et de l'autre des processus exogènes, principalement un impact géant.

1.5.1 Une origine endogénique

La croûte se forme classiquement par extraction d'un magma formé par fusion partielle du manteau. Plus la fusion partielle et importante, plus il est possible d'extraire d'importants volumes de magmas. Une variation dans le taux de fusion du manteau à l'échelle hémisphérique induirait une différence dans le taux d'extraction de la croûte

et pourrait donc expliquer la formation d'une croûte plus épaisse dans un hémisphère. L'ensemble des modèles proposant une origine endogénique se basent sur cette idée. Ces modèles proposent alors un mécanisme pour expliquer la formation de variations de températures et donc de taux de fusion à l'échelle hémisphérique. Ces mécanismes ont préférentiellement lieu lors de la cristallisation de l'océan magmatique ou après dans une phase de convection solide. En effet, les faibles viscosités d'un océan magmatique vont avoir tendances à l'homogénéiser tant qu'il n'a pas commencé à cristalliser.

Convection mantellique de degré 1

La convection mantellique peut prendre la forme d'un panache hémisphérique ascendant chaud dans un hémisphère tandis que le panache froid descendant occupe le second hémisphère. Ce mode de convection induit une forte différence de température entre les deux hémisphères. Cette forme de convection est appelée une convection de degré 1. La convection mantellique de degré 1 est un des mécanismes proposés pour former des différences de taux de fusion à l'échelle hémisphérique. Cette forme de convection a été proposée pour la Terre où elle serait induite par la présence d'un changement de phase spinelle-pérovskite. Ce changement de phase est endothermique, c'est-à-dire qu'il nécessite un apport de chaleur ce qui favorise la convection à grande longueur d'ondes (Tackley et al., 1993). Dans le cas de Mars, cette transition peut avoir lieu à 1700-1800 km de profondeur, ce qui supérieur à la profondeur de l'interface manteau-noyau (Stähler et al., 2021; Le Maistre et al., 2023). De plus, Roberts and Zhong (2006) montrent que le temps de développement d'un mode de convection de degré 1 par un changement de phase est supérieur à 5 Ga et donc trop long vis-à-vis de l'âge de la dichotomie martienne, formée en moins d'un milliard d'années (Solomon et al., 2005; McGill and Dimitriou, 1990). Le changement de phase endothermique n'est donc pas une origine possible pour une convection de degré 1 dans le manteau martien.

D'autre part, Zhong and Zuber (2001) démontrent qu'un manteau stratifié en viscosité développe principalement une convection de degré 1. Ce résultat est obtenu par une analyse de stabilité de Rayleigh-Taylor avec un contraste de viscosité entre le manteau inférieur et supérieur de 100. Roberts and Zhong (2006) ont étudié le déclenchement de la convection dans un manteau 3D à géométrie sphérique et avec une viscosité qui dépend de la température et de la pression. Dans cette configuration, le contraste de viscosité nécessaire pour former un degré 1 est de 25. Le temps de développement d'un degré 1 par ce mécanisme est autour de 100 millions d'années et dépend du nombre de Rayleigh et donc de la viscosité du manteau. Ce temps de formation d'un degré 1 est lui compatible avec l'âge proposé pour la dichotomie. Ces résultats sont cohérents avec l'étude similaire produite par Yoshida and Kageyama (2006). Keller and Tackley (2009) ajoutent à ce mécanisme une paramétrisation de l'extraction de la croûte ce qui permet d'obtenir la répartition des épaisseurs crustales à la surface résultante de ce mécanisme (Figure 1.9a). Une structure linéaire, similaire à une ride océanique, se forme en surface et la répartition des épaisseurs de croûte présente une dichotomie

nord/sud.

La formation de la dichotomie martienne par une convection mantellique de degré 1 a une faiblesse importante, les épaisseurs de crustales ne suivent pas une distribution quasi bimodale comme c'est le cas pour Mars. La production de magma est plus importante au centre du panache, plus chaud, et moindre sur les bords, plus froid. On observe alors une distribution des épaisseurs de croûte avec un maximum qui correspond au centre du panache et une croûte de moins en moins épaisse en s'écartant du centre (Figure 1.9a).

Degré 1 lors de la cristallisation de l'océan magmatique

Un champ de température de degré 1 peut aussi être hérité de l'océan magmatique et être préservé jusqu'à la formation de la croûte. Une cristallisation lente de l'océan de magma induit un fractionnement des éléments entre les cumulats et le liquide résiduel (Elkins-Tanton et al., 2003). Cette cristallisation fractionnée forme des cumulats riches en éléments compatibles comme le Magnésium et le liquide s'enrichit petit à petit en éléments incompatibles tels que le Fer. La cristallisation de l'océan se fait de l'interface Noyau-Manteau vers la surface. Les cumulats formés sont de plus en plus riches en fer et donc de plus en plus denses alors que le rayon augmente. Ce scénario aboutit à un profil de densité gravitationnellement instable, le manteau est plus dense vers la surface et moins dense vers le noyau créant une instabilité de Rayleigh-Taylor. Cette instabilité pourrait induire un panache de degré 1 le temps du retournement du manteau (Elkins-Tanton et al., 2003, 2005). Cette hypothèse est supportée par des indices isotopiques dans les SNC mais seulement si l'océan de magma se solidifie après 100 millions d'années (Debaille et al., 2009).

Le scénario d'une formation de la dichotomie par un retournement du manteau rencontre néanmoins certaines difficultés importantes. Le retournement du manteau renverse le profil de densité, les matériaux denses se retrouvent en bas et les moins denses en haut, ce qui est une stratification très stable. Dans cette configuration, la convection s'arrête au bout d'1 milliard d'années (Tosi et al., 2013b; Plesa et al., 2014) alors que l'activité volcanique récente sur Mars (Neukum et al., 2004; Hauber et al., 2011; Horvath et al., 2021; Stähler et al., 2022), indique une convection mantellique tout le long de l'histoire thermique martienne. La plus récente datation de l'âge de cristallisation de l'océan magmatique pointe vers une solidification très rapide en 20 Ma après la formation du système solaire (Bouvier et al., 2018), ce qui n'est pas en accord avec le critère isotopique nécessitant un refroidissement en 100 Ma (Debaille et al., 2009). Les conditions de formation d'une instabilité de Rayleigh-Taylor, c'est-à-dire un manteau isovisqueux avec un profil de densité instable, ne semblent pas non plus réunies. Un manteau isovisqueux comme supposé par Elkins-Tanton et al. (2003, 2005) n'est pas réaliste, une large partie du manteau serait trop visqueuse et ne pourrait pas participer au retournement total du manteau. La stratification du manteau suppose une absence

de convection et de mélange dans les cumulats avant le retournement. Or, d'après, Morison et al. (2019) la convection dans les cumulats commence avant la cristallisation complète du manteau. Les cumulats se mélangeant alors au fur et à mesure de leur cristallisation, la formation d'un gradient de composition n'est pas stable dans le temps.

Néanmoins, cette convection dans les cumulats peut préférentiellement former une anomalie de température de degré 1 en particulier à cause du changement de phase se produisant à l'interface cumulats/océan de magma et permettant l'échange de matière (Morison et al., 2019). Cette condition aux limites impose une forme très spécifique pour la convection. Les cumulats cristallisent dans un hémisphère à l'interface avec l'océan et contournent le noyau pour venir refondre à l'interface avec l'océan dans l'hémisphère opposé. Le mouvement de la matière suit une translation hémisphérique. La différence dans le champ de température s'explique par la libération ou la consommation d'énergie latente aux interfaces, l'hémisphère dans lequel les cumulats fondent est donc plus chaud.

Watson et al. (2022) se sont intéressés à l'épaississement du couvercle conducteur d'un océan de magma dans sa phase partiellement cristallisé où les cristaux sont toujours en suspension. La dépendance en pression de la viscosité causée par un taux de fusion variable sous ce couvercle induit une instabilité dans la croissance du couvercle conducteur et l'analyse de stabilité linéaire démontre que la perturbation de degré 1 se développe préférentiellement. Ces deux dernières études (Morison et al., 2019; Watson et al., 2022) ne comportent ni d'évolution thermique qui permettrait de démontrer la stabilité de cette anomalie de degré 1 tout le long de la cristallisation de l'océan magmatique, ni d'extraction de la croûte permettant d'étudier la formation ou non d'une dichotomie crustale. Néanmoins, si cette anomalie est conservée, elle pourrait générer une différence dans le volume de croûte extrait à l'échelle hémisphérique.

Migration de Tharsis

Le dernier mécanisme endogénique propose de relier la formation des Hauts Plateaux et la formation du dôme de Tharsis. En se basant sur la formation d'un panache hémisphérique par contraste de viscosité, Zhong (2009) émet l'hypothèse que l'extraction du magma depuis le panache ascendant associé à une "quille" lithosphérique se rigidifiant entraînant des variations latérales de viscosité qui enclenchent un champ de vitesse toroïdal dans le manteau. Ce champ permet la migration du panache ascendant et permettrait d'expliquer la migration de Tharsis au cours du temps (Johnson and Phillips, 2005) et la formation des Hauts Plateaux. Pour confirmer cette hypothèse, Šrámek and Zhong (2012) ont implémenté dans un modèle de convection 3D similaire à Zhong (2009) une paramétrisation de la fusion du manteau et de l'extraction de la croûte. La viscosité du résidu augmente avec son degré d'extraction avec un contraste maximum de 200. Šrámek and Zhong (2012) montrent que l'extraction de la croûte est

suffisante pour former la "quille" lithosphérique nécessaire à la migration du panache de Tharsis. Dans les cas où la migration du panache parcours l'entièreté d'un hémisphère sud, cela résulte en la formation d'une croûte présentant une distribution quasi bimodale des épaisseurs (Figure 1.9b). Ce mécanisme prédit une relation âge-distance à Tharsis pour les terrains de l'hémisphère sud, plus le terrain est éloigné de Tharsis plus il doit être ancien. cette prédiction n'est pas corroboré par les observations, par exemple la région la plus ancienne des Hauts Plateaux, Terra Sirenum-Cimmeria se trouve proche de Tharsis (Figure 1.2).

1.5.2 Une origine exogénique

Les impacts géants

L'origine exogénique de la dichotomie martienne est l'hypothèse la plus largement répandue dans la communauté. La différence d'épaisseur de croûte serait la conséquence d'un ou plusieurs impacts géants dans un hémisphère. Les planètes du système solaire sont formées par accrétion de poussière du disque proto-planétaire et impacts de planétésimaux. Les datations pour Mars pointent vers une formation et une cristallisation très tôt de la planète, 20 Ma après les CAI (Bouvier et al., 2018). La fréquence des impacts décroît exponentiellement avec le temps et cette décroissance est d'autant plus rapide que la taille de l'impacteur considéré est grande (Morbidelli et al., 2018). Il est donc très probable que Mars ait pu être frappée par un ou plusieurs grands impacts au début de son histoire et sa surface parsemée de très larges cratères d'impact en est une bonne démonstration. Frey and Schultz (1988) ont proposé que la dichotomie se soit formée par une série d'impacts de la taille d'Utopia et concentrée dans l'hémisphère nord. Un tel évènement semble peu probable et n'est pas étayé par des observations géologiques (McGill and Dimitriou, 1990).

Le scénario privilégié est celui d'un impact géant modifiant l'épaisseur de croûte en surface à l'échelle d'un hémisphère (Wilhelms and Squyres, 1984; Marinova et al., 2008; Andrews-Hanna et al., 2008a) et qui aurait formé les lunes martiennes Phobos et Déimos (Marinova et al., 2008; Rosenblatt et al., 2016). Cette hypothèse suit un schéma similaire à l'impact géant qui aurait formé le système binaire Terre-Lune (Canup, 2012). Un impact de Mars avec un corps de plusieurs centaines de kilomètres de rayon, comme envisagé, serait un évènement tellement extrême qu'il pourrait détruire partiellement la planète (Wilhelms and Squyres, 1984; Nimmo and Tanaka, 2005) ou tout du moins reformer un océan magmatique global et effacer toute trace de la collision en surface comme ce fut le cas pour la Terre (Tonks and Melosh, 1993). Le défi d'un tel scénario est donc d'expliquer la formation d'une dichotomie encore observable à l'échelle hémisphérique aujourd'hui. Un tel impact libère assez d'énergie cinétique au minimum pour former un océan de magma local en lieu et place de l'impact. Ensuite, les différents scénarios divergent sur les conséquences de la formation de cet océan de magma local. L'impact excave la croûte existante, mais produit aussi une large quantité de magma qui remonte en surface et reforme de la croûte. Si le résultat de cet

impact est une croûte plus fine dans l'hémisphère impacté, c'est-à-dire que le volume de croûte excavé est supérieur au volume produit par l'océan de magma local, l'impact sera préférentiellement situé dans l'hémisphère nord. Au contraire, si la croûte résultante est plus épaisse, le volume de croûte nouvellement formé est supérieur au volume de croûte excavé, alors l'impact sera placé plus tôt dans l'hémisphère sud.

Impact dans l'hémisphère nord

L'idée d'un impact géant dans l'hémisphère nord est ancienne (Wilhelms and Squyres, 1984; Frey and Schultz, 1988) et a fait l'objet d'un nombre important d'études (Nimmo et al., 2008; Marinova et al., 2008, 2011). Les Basses Plaines forment un bassin elliptique, le bassin boréal, de 10 600 km par 8500 km, avec une transition de la topographie vers les Hauts Plateaux très nette, c'est-à-dire avec une forte pente (Andrews-Hanna et al., 2008a). Cette forme spécifique se rapproche de celui des impacts géants observés dans le système solaire, comme le bassin d'impact d'Aitken au pôle Sud de la Lune (Ohtake et al., 2014).

Marinova et al. (2008) ont été les premiers à présenter un modèle dynamique d'un tel impact pour Mars à l'aide d'un modèle dit SPH. Pour des évènements aussi catastrophiques, les modèles d'évolution planétaire classiques, c'est-à-dire de la physique des milieux continus avec une description eulérienne, sont peu adaptés. On utilise alors des modèles suivant l'hydrodynamique des particules lissées, ou "smoothed particule hydrodynamics" (SPH) en anglais, la physique des milieux continus suit une description lagrangienne. La matière est représentée par des masses ponctuelles dont les caractéristiques sont obtenues par lissage avec les particules voisines selon une longueur définie. Toutes les particules suivent des règles physiques similaires (rhéologie, gravité, changement d'état). Le modèle SPH de Marinova et al. (2008, 2011) utilise les équations d'état de Tillotson (1962) et la conservation de la masse, du moment cinétique et de l'énergie définissent pour chaque particule une énergie interne et une densité. La quantité de magma produit par l'impact est obtenue à l'aide d'un critère énergétique, si l'énergie d'une particule dépasse une valeur elle est considérée comme fondue (Marinova et al., 2011). Le magma présent à une pression inférieure à 7.4 GPa est extrait pour former la nouvelle croûte.

L'impact est ensuite modélisé entre un corps de la taille de Mars et un impacteur dont la taille, la vitesse d'impact et l'angle d'impact peuvent varier. L'énergie relâchée lors de l'impact dépend des paramètres de l'impact et détermine, avec l'angle d'impact, la forme du bassin. Des impacts trop énergétiques produisent des formes non observées comme une dislocation de la croûte à l'antipode de l'impact ou la production de grande quantité de magma allant jusqu'à la disparition du bassin. Un angle d'impact plus large augmente l'ellipticité et diminue la production de magma, mais produit une forme d'anneau épaissi autour du bassin qui, elle non plus, n'est pas observée. Marinova et al. (2008) proposent une gamme de paramètres, un "sweet spot", où l'ellipticité

des Basses Plaines est obtenue sans épaississement annulaire, ni effet antipodal et avec une formation d'un bassin. Selon leurs modélisations, l'impacteur doit avoir une taille comprise entre 800 et 1350 km de rayon, une énergie d'impact entre 3 et 6×10^{19} J, une vitesse entre 6 et 10 km s^{-1} et un angle d'impact entre 30 et 60°. Un tel impact permet d'excaver suffisamment de croûte tout en conservant une grande partie du magma en profondeur et donc de former un bassin elliptique d'une forme similaire au bassin Boréal (Figure 1.9c). La probabilité d'obtenir un impacteur de cette taille diminue très vite avec l'âge du système solaire, le modèle de Morbidelli et al. (2018) suggère un impact avant -4.5 Ga. La dichotomie est dans ce scénario très ancienne et les différents évènements de l'histoire martienne ultérieurs à cet impact expliqueraient le peu de traces laissées jusqu'à aujourd'hui.

Citron et al. (2018b) proposent un autre scénario pour un impact géant dans l'hémisphère nord. L'impact dans l'hémisphère nord pourrait induire une faible différence d'épaisseur de croûte et de composition entre les deux hémisphères. La croûte nouvellement formée par l'impact dans l'hémisphère nord serait moins enrichie en éléments producteurs de chaleur car elle se serait formée dans un manteau déjà appauvri par une extraction initiale de croûte. La croûte plus épaisse et avec un chauffage interne plus élevé dans l'un des hémisphères a un effet isolant et promeut la formation d'une convection de degré 1 avec un panache ascendant dans l'hémisphère sud. Ce panache viendrait épaissir la croûte dans l'hémisphère sud et se stabiliserait à la limite de la dichotomie pour former le dôme de Tharsis. Ce scénario n'a pas besoin de préserver des reliefs dû à l'impact et permet d'enclencher une convection de degré 1 sans imposer un saut de viscosité dans le manteau.

Impact dans l'hémisphère sud

La formation d'un océan de magma local à l'échelle d'un hémisphère peut produire de larges volumes de croûte (Reese and Solomatov, 2006). Un océan de magma localisé dans l'hémisphère sud peut être créé par un impact géant et résulter en la formation d'une province de croûte épaisse comme les Hauts Plateaux. Reese et al. (2010) proposent un scénario où l'impact géant apporte assez d'énergie au manteau et au noyau pour enclencher une géodynamo tôt dans l'histoire martienne, simultanément à la formation des Hauts Plateaux. La concomitance entre la formation des Hauts Plateaux et l'activation d'une dynamo expliquerait les fortes anomalies magnétiques crustales présentes dans les Hauts Plateaux. Néanmoins, ces études ne simulent pas l'impact en lui-même, mais seulement le refroidissement de l'océan magmatique local avec un modèle analytique, ne prenant pas en compte le volcanisme plus tardif qui découle de l'anomalie de température produite par l'impact.

Golabek et al. (2011) modélisent en deux étapes les conséquences d'un impact ayant formé un océan de magma local. Premièrement, ils modélisent la formation du noyau et la cristallisation de l'océan magmatique avec un premier code adapté (I2ELVIS, Gerya

and Yuen 2007) qui permet de calculer l'épaisseur de croûte formée par l'océan magmatique et l'impact ainsi qu'un champ de température réaliste. Ces sorties sont ensuite utilisées en entrée d'un code de convection classique (STAGYY, Tackley 2008) pour étudier l'évolution thermique et le volcanisme postérieur à l'impact. Ils montrent ainsi que ce scénario permet la formation d'une différence d'épaisseur de croûte à l'échelle hémisphérique dans un cas en 2D et Leone et al. (2014) généralisent ce scénario à une géométrie 3D.

La récente étude de Ballantyne et al. (2023) revisite les modèles SPH dans le but de départager les théories d'impact géant entre celles le plaçant dans l'hémisphère nord et celles dans l'hémisphère sud. Le scénario d'un impact dans l'hémisphère nord ayant excavé plus de croûte qu'il n'en forme n'est plus retrouvé dans cette étude. Les auteurs attribuent la différence entre les résultats de Marinova et al. (2008, 2011) et les leurs aux différences entre les modèles utilisés. En effet, cette récente étude utilise des équations d'état plus sophistiquées et inclut la résistance des matériaux, contrairement au modèle précédent où le matériau est considéré comme un fluide. De plus, l'utilisation d'un solidus pour le calcul du taux de fusion et une paramétrisation plus réaliste de l'extraction de croûte résultent en des volumes de croûtes formées plus importants dans le modèle le plus récent. La théorie d'un impact géant dans l'hémisphère nord est donc fortement remise en question par cette étude et les auteurs pointent vers un impact dans l'hémisphère sud très tôt dans l'histoire martienne. Leurs résultats suggèrent un rayon d'impacteur, une vitesse d'impact et un angle d'impact plus petits que les études précédentes (Marinova et al., 2008, 2011; Golabek et al., 2018).

1.5.3 Discussion

Une origine endogénique par l'apparition d'un degré 1 a pour principale critique son incapacité à former une distribution quasi bimodale des épaisseurs de croûte. La migration du panache au cours du temps, comme proposée par Šrámek and Zhong (2012), ne répond qu'en partie à cette critique, la migration de Tharsis sur une aussi grande distance n'est pas étayée par les observations. Le contraste de viscosité nécessaire pour enclencher le degré 1 est aussi pour le moment assez spéculatif. Un degré 1 hérité de l'océan magmatique est aussi possible à l'aide de plusieurs mécanismes (Morison et al., 2019; Watson et al., 2022). Néanmoins, ces mécanismes n'ont pas été testés pour ce qui est de l'extraction de la croûte et la formation d'une dichotomie d'épaisseur crustale. Cela nécessite un modèle de cristallisation de l'océan magmatique prenant en compte un écoulement biphasique avec l'extraction de la croûte à l'image du modèle en géométrie cartésienne de Ogawa and Yanagisawa (2012a).

L'origine exogénique la plus robuste à ce jour est un scénario d'un impact géant dans l'hémisphère sud ayant entraîné la formation d'un océan de magma local. La difficulté d'obtenir un bassin d'impact à l'échelle hémisphérique ayant les mêmes caractéristiques que le bassin boréal explique ce changement. Un tel impact est un défi de modélisation,

car il implique des phénomènes physiques qui ont des temps caractéristiques très différents, l'impact avec quelques heures/jours, l'océan de magma de quelques milliers à quelques millions d'années et l'évolution thermique sur les 4.5 Ga jusqu'à aujourd'hui. Ces trois temps caractéristiques nécessitent trois modèles différents. Si des efforts ont été faits pour coupler des modèles deux par deux (Golabek et al., 2011; Leone et al., 2014; Golabek et al., 2018), la modélisation du processus dans son intégralité est un travail en cours (Cheng et al., 2022). Néanmoins, il y a un manque d'observation en faveur d'un impact dans l'hémisphère sud comme des traces isotopiques dans les échantillons martiens, comme des anomalies positives en éléments sidérophiles. Il est à noter que l'étude de Roberts and Arkani-Hamed (2014) montrant qu'un impact géant provoquerait l'arrêt de la convection dans le noyau pendant quelques centaines de millions d'années et expliquerait l'arrêt supposé de la géodynamo martienne. L'impacteur considéré dans l'étude est grand ($\approx$ 1000 km) et la probabilité d'un tel impact est faible (Morbidelli et al., 2018). Les modèles comprenant la formation de croûte pendant et après l'impact dans le sud prévoient systématiquement des dichotomies bien plus larges que celle attendue pour Mars (Golabek et al., 2011; Leone et al., 2014; Golabek et al., 2018; Cheng et al., 2022; Ballantyne et al., 2023).

La majorité des mécanismes proposés pour la formation de la dichotomie martienne se concentre sur la formation d'une différence d'épaisseur de croûte à l'échelle hémisphérique. La dichotomie entre les Hauts Plateaux et les Basses Plaines relative aux différences de composition des roches, et potentiellement de densité, n'est pas expliquée par ces mécanismes. Les faibles densités dans l'hémisphère sud sont parfois reliées à la présence d'une couche de méga-régolithe formée par les éjectas des différents grands impacts, dont l'impact qui aurait formé le bassin boréal (Wieczorek et al., 2022). Les conséquences de la formation de la dichotomie et l'évolution thermique ultérieure sont peu étudiées (Šrámek and Zhong, 2012; Marinova et al., 2011; Ballantyne et al., 2023) et quand elles le sont, les prévisions du modèle ne correspondent pas aux observations sur la structure thermique et l'épaisseur de la croûte martienne (Golabek et al., 2011; Cheng et al., 2022).

1.6 Problématique

Nos connaissances de la structure et de l'évolution martiennes se sont considérablement améliorées avec l'ère de l'exploration spatiale et notamment avec la mission InSight, mais certaines questions sur l'évolution thermique martienne restent en suspens :

Quel mécanisme pour la formation de la dichotomie martienne ? Les mécanismes proposés pour la formation de la dichotomie martienne ne parviennent pas à expliquer les observations de manière satisfaisante. Le modèle standard de l'impact géant dans l'hémisphère nord est de plus en plus difficile à justifier (Ballantyne et al., 2023). Un impact dans le sud semble la piste privilégiée par les études récentes, mais

sa capacité à reproduire la dichotomie martienne observée reste néanmoins à démontrer (Golabek et al., 2011). Les origines internes sont essentiellement basées sur des panaches hémisphériques, qui ne permettent pas la formation d'une dichotomie quasi bimodale (Šrámek and Zhong, 2012). La possibilité d'un héritage d'une anomalie de température hémisphérique provenant de l'océan magmatique reste à démontrer (Morison et al., 2019; Watson et al., 2022).

Comment concilier l'épaisseur de la croûte et la structure thermique du manteau dans un modèle d'évolution thermique ? Les nouvelles contraintes de la mission InSight pointent vers une croûte relativement épaisse et un manteau plutôt froid (Knapmeyer-Endrun et al., 2021; Stähler et al., 2021; Khan et al., 2021; Huang et al., 2022). Les modèles d'évolution thermique doivent reproduire ces observations tout en permettant un volcanisme tout le long de l'histoire martienne.

Quel est l'effet de la dichotomie et de sa formation sur l'évolution thermique ? La dichotomie d'épaisseur crustale martienne résulte en deux hémisphères avec des états thermiques très différents (Thiriet, 2018). L'impact sur l'évolution thermique d'une telle différence par rapport au cas homogène est encore peu décrit.

Comment la dichotomie de l'épaisseur de la croûte peut-elle être reliée aux autres caractéristiques de la dichotomie (densité, minéralogie) ? La différence de topographie liée à la différence d'épaisseur de la croûte est la principale caractéristique de la dichotomie, mais ce n'est pas la seule. La présence de roches felsiques uniquement dans les Hauts Plateaux (Sautter et al., 2015) et les faibles densités apparentes des Hauts Plateaux (Goossens et al., 2017) sont également des caractéristiques importantes pour comprendre l'histoire martienne. Est-ce que ces caractéristiques ont une ou plusieurs relations de cause à effet ?

C'est à la lumière des nouvelles contraintes de la mission InSight de la NASA et dans le but de répondre à ces questions que j'ai, avec mes encadrants, poursuivi ma thèse et rédigé ce manuscrit. Le Chapitre 2 décrit le modèle d'évolution thermique que j'ai développé dans le cadre de cette thèse. Le Chapitre 3 décrit le nouveau mécanisme que nous avons démontré pour la formation de la dichotomie martienne. Le Chapitre 4 étudie l'impact d'une dichotomie crustale hémisphérique sur l'évolution thermique de Mars. Le Chapitre 5 propose une origine pour la formation des roches felsiques sur Mars qui explique également leur distribution spatiale.

Chapitre 2

An Asymmetric parameterised thermal evolution model of Mars

2.1 Introduction

The aim of this thesis is to study the formation of Martian hemispheric differences (crust thickness, thermal structure, etc.) by modelling its thermal evolution and the extraction of its crust. This chapter describes the type of model we have chosen and the improvements we have made to it. Although 3-D convection models can provide a full description of the temperature field over time as well as of the convection pattern (Šrámek and Zhong, 2012; Plesa et al., 2015), they are numerically very time-consuming and do not yet allow to account for realistic 3-D segregation of melt from the mantle. Since our goal is to study crust formation by melt extraction, we use a parameterised model for a stagnant lid (Breuer and Spohn, 2006) which considers a well-mixed convective mantle topped by a conductive thermal lithosphere (composed of a rigid lid and a mobile boundary layer), where heat is transported by conduction. We assume a well-mixed mantle characterised by a temperature at its top and an isentropic temperature profile. We neglect the lateral temperature variations that naturally arise in convection flows (Roberts and Zhong, 2006). In order to study the differences at the hemispheric scale in the lid, we use an asymmetric parametric model as developed by Thiriet et al. (2018). This model is characterised by a lid which is split into two hemispheres with different temperature profiles $T(r,t)^{\mathrm{N/S}}$, lid thicknesses $D_l^{\mathrm{N/S}}$, crust thicknesses $D_{cr}^{\mathrm{N/S}}$ and crust enrichments compared to bulk silicate Mars $\Lambda_{cr}^{\mathrm{N/S}}$, where the subscripts N/S refer to values for the Northern (N) or Southern Hemisphere (S), respectively (Figure 2.1).

2.2 Thermal modelling

Parameterised convective heat flow

The viscosity of planetary mantle rocks is strongly temperature-dependent and also varies with pressure. Because of the large temperature dependence of the viscosity, a rigid and stagnant lid develops at the top of the convective mantle, where heat is transported by conduction and which encompasses a large range of viscosity variations. We use an Arrhenius law to describe the temperature and pressure dependency of the viscosity :

$$\eta(T,P) = \eta_0 \exp\left(\frac{A+PV}{RT} - \frac{A+P_0V}{RT_0}\right), \tag{2.1}$$

where T is temperature, P pressure, η_0 is a reference viscosity at the reference temperature $T_0 = 1600$ K and pressure $P_0 = 3$ GPa, R is the gas constant, A the activation energy and V the activation volume. The mantle viscosity may also depend on its water content and melt fraction. However, for simplicity, we neglect them and we will discuss their potential effects later in the manuscript. (see Section 3.6 & 4.6). The viscosity also depends on the deformation mechanism, which depends on the grain size that is poorly constrained and may vary depending on local conditions. As an example, for diffusion creep in a dry peridotite the activation energy is 300 kJ mol^{-1} and the activation volume is $V = 6$ cm^3 (Karato and Wu, 1993). We evaluate, throughout the manuscript, how these values affect our results (Section 3.5.2 & 4.5).

We follow the approach of Davaille and Jaupart (1993) and parameterise the heat flow out of the well-mixed convective mantle as a function of a rheological temperature scale T_ν :

$$T_\nu = -\eta(T_m)\left(\left.\frac{\mathrm{d}\eta}{\mathrm{d}T}\right|_{T_m}\right)^{-1} = \frac{RT_m^2}{A}, \tag{2.2}$$

where T_m is the temperature at the top of the convective mantle and corresponds to the well-mixed interior temperature. Below the rigid lid, the unstable boundary layer is characterised by a temperature contrast of (Davaille and Jaupart, 1993) :

$$T_m - T_l = a_{rh} T_\nu, \tag{2.3}$$

where T_l is the temperature at the base of the lid (Figure 2.1), and a_{rh} a dimensionless coefficient taken equal to 2.54 for Mars (Thiriet et al. 2019, Table 2.1). Following Grott and Breuer (2008) and Thiriet et al. (2018, 2019), the mantle is divided into a stagnant lid and a convective mantle characterised by a top and bottom thermal boundary layers which concentrate temperature variations (Figure 2.1). Because of internal heating and of the temperature and pressure dependence of the viscosity, these two thermal boundary layers are not symmetric and the upper one is considerably thicker. Their average thicknesses are well described by the boundary layer stability analysis as given by Turcotte and Schubert (2002) :

$$\delta_{u/c} = d\left(\frac{Ra^{u/c}_{crit}}{Ra^{u/c}}\right)^{\beta}, \tag{2.4}$$

where the superscripts u, c stand for the upper and bottom boundary layer respectively, Ra_{crit} is the critical Rayleigh number, the convective height is given by $d = R_l - R_c$, with R_l the radius at the lid base and R_c the core radius (Figure 2.1). We use $\beta^c = 1/3$ for the lower boundary layer and $\beta^u = 0.335$ for the upper one (Thiriet et al., 2019). The Rayleigh number characteristic of the upper/lower boundary layer $Ra^{u/c}$ is given by :

$$Ra^{u/c} = \frac{\alpha\rho_m g^{u/c}\Delta T^{u/c} d^3}{\kappa_m \eta^{u/c}}, \tag{2.5}$$

where α is the thermal expansion coefficient, ρ_m mantle density, κ_m mantle diffusivity, g gravity, ΔT the temperature jump across the boundary layer, η the viscosity. For the lower boundary, we use $\Delta T^c = |T_b - T_c|$ with T_c the core-mantle boundary (CMB) temperature and T_b the temperature at the top of the lower boundary layer which can be larger than T_c early in the planet history ; the viscosity η^c is estimated at the temperature $(T_b + T_c)/2$ and pressure P^c characteristic of the CMB. For the upper boundary layer, we use $\Delta T^u = T_m - T_l$ and the viscosity η^u is estimated at the temperature T_m and pressure at the lid base. Since the lid thickness, and hence the radius and pressure at the lid base, may be different between both hemispheres, the thickness of the upper boundary layer and the Rayleigh number Ra^u may also differ between North and South. As in Thiriet et al. (2019), we use a constant critical Rayleigh number $Ra^u_{crit} = 450$ for the upper boundary layer and the formulation of Deschamps and Sotin (2001) for the critical Rayleigh number of the lower boundary layer :

$$Ra^c_{\text{crit}} = 0.28 Ra_\theta^{0.21}, \tag{2.6}$$

where the internal Rayleigh number Ra_θ is given by $Ra_\theta = \frac{\alpha\rho_m g_u \Delta T_\theta d_\theta^3}{\kappa\eta_\theta}$ with $d_\theta = R_p - R_c$, η_θ estimated at the temperature T_m and pressure $\bar{P_m}$ at the average radius of the lid base $\bar{R_l} + \bar{\delta_u}$. The bar symbol ($\bar{x}$) refers to north-south averaged values (see Section 2.7). We use $\Delta T_\theta = (T_m - T_{surf}) + (T_c - T_b)$. If $T_c < T_b$, then we use $\Delta T_\theta = (T_m - T_{surf})$.

The parameterised heat flux from the convective mantle into the lid and from the core into the mantle are then respectively given by :

$$q^{\text{N/S}}_{cm} = k_m \frac{T_m - T_l}{\delta^{u,\text{N/S}}}, \tag{2.7}$$

$$q_c = k_m \frac{T_c - T_b}{\delta^c}. \tag{2.8}$$

where k_m is the mantle conductivity, and δ^c, T_c, T_b, T_m and T_l are the same for both hemispheres as the mantle and core are assumed to be well-mixed, $\delta^{u,\text{N/S}}$ is hemisphere-dependent through its dependence on the viscosity at the top of the mantle ($V \neq 0$) and

on the convective height $d^{\mathrm{N/S}}$. Within the well-mixed convective part of the mantle, the temperature profile is adiabatic ; we use an isentropic formulation (Jaupart et al., 2015) to describe the radial dependence of the temperature and to relate the temperature at the top of the lower boundary T_b to the temperature at the top of the well-mixed convective mantle T_m (Grott and Breuer, 2008; Thiriet et al., 2019) :

$$T_b = T_m + \frac{\alpha g T_m}{C_m}(\bar{d} - \bar{\delta^u} - \delta^c). \tag{2.9}$$

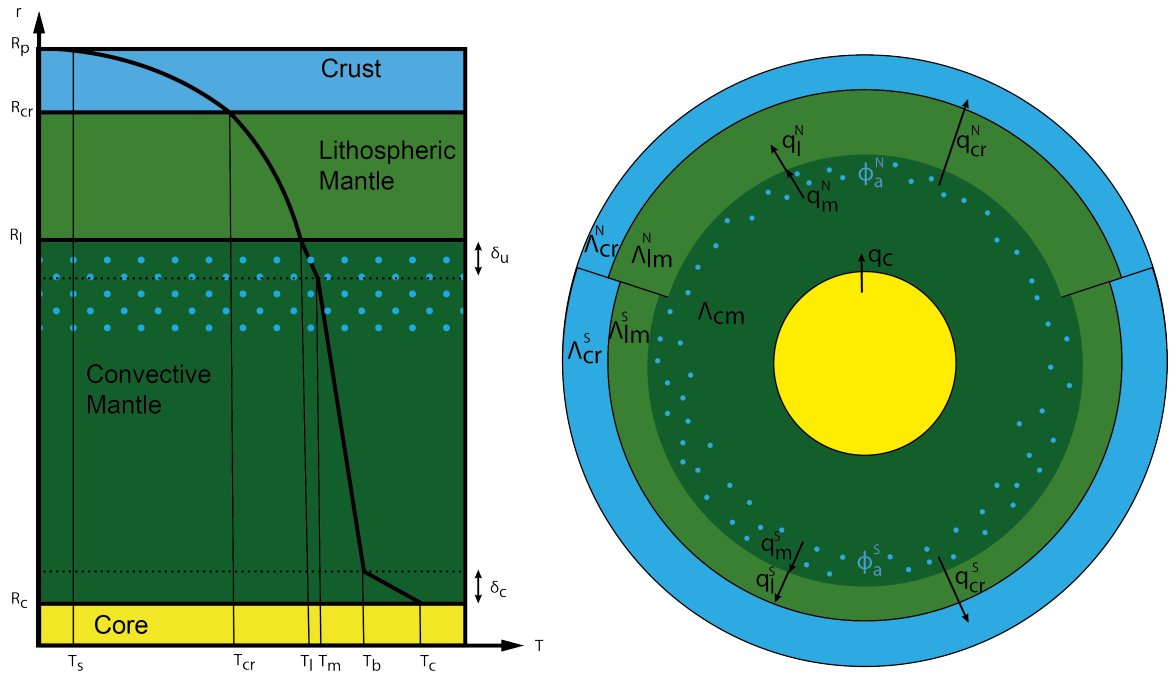

FIGURE 2.1 – Left : Parameterised model for one hemisphere with 4 different layers : the core, the convective mantle, the lithospheric mantle and the crust. A characteristic temperature profile is indicated in black line with the associated temperature at each interface. Blue dots represent melting and dotted lines the thermal boundary layer thicknesses (δ_u, δ_c). Right : bi-hemispherical parameterised model with 5 different reservoirs characterised by different HPE enrichments and enrichment factors Λ : the northern and southern crusts ($\Lambda_{cr}^{\mathrm{N/S}}$), the northern and southern lithospheric mantles ($\Lambda_{lm}^{\mathrm{N/S}}$) and the convective mantle (Λ_{cm}).

2.3 Mantle melting and crust extraction

2.3.1 Mantle melting

The mantle mineralogy is dominated by solid solutions of olivine and pyroxene with an additional aluminous phase and hence, the melting of mantle rocks is temperature, pressure, and composition-dependent. Here, we use the solidus of Ruedas and Breuer (2017) for a fertile K-free peridotite that is based on the composition of Wänke

and Dreibus (1994). As in Morschhauser et al. (2011) and Thiriet et al. (2018), we also consider the progressive increase in mantle solidus temperature caused by mantle depletion due to crust extraction through an additional term assumed to be linearly proportional to the crustal thickness D_{cr} :

$$T_{\rm sol}(P, D_{cr}) = 1340 + 130.4P - 6.38P^2 + 0.119P^3 + \frac{D_{cr}}{D_{\rm ref}}\Delta T_{sol}, \tag{2.10}$$

where P is the pressure in GPa (see Table 2.1 for parameter values). The Martian crust amounts to $\sim$ 5 to 7% of the volume of the bulk silicate part of the planet (See Section 3.4.2), which corresponds to a solidus temperature increase of 40 to 50 K after crust extraction. No experiment have been conducted to determine the martian liquidus, therefore we follow Breuer and Spohn (2006) and use the liquidus of Takahashi (1990) for a dry terrestrial peridotite :

$$T_{\rm liq}(P) = 2035 + 57.46P - 3.487P^2 + 0.0769P^3. \tag{2.11}$$

For simplicity, the melt fraction is usually considered to be a linear function of temperature over the melting interval, implying constant melt productivity at a given pressure (Morschhauser et al., 2011; Samuel et al., 2019). However, the melt productivity at constant pressure in peridotite $\left(\frac{{\rm d}\phi}{{\rm d}T}\right)_P$ has been shown to be highly variable between 0 and 20% melt fraction because it is affected by a phase exhaustion (Hirschmann et al., 1999; Robinson et al., 1998). Near-solidus productivity is very small and it increases continuously with increasing melt fraction up to clinopyroxene exhaustion (Baker and Stolper, 1994), which occurs around 15-20% melt in a fertile peridotite. After Cpx exhaustion, melt productivity drops to an almost constant value for melt fractions between $\sim$20-30% (Hirschmann et al., 1999). Since we are interested in the mechanism of crust formation by melting and melt extraction from initially fertile material, with melt fraction spanning the range 0-30%, it is important to account for non-constant melt productivity.

We consider that clinopyroxene exhaustion occurs at the melt fraction $\phi_t = 0.17$. For $\phi \geq \phi_t$, the melt fraction is a linear function of temperature over the melting interval :

$$\phi_l(T, r) = (T(r) - T_{sol}(r))/(T_{liq}(r) - T_{sol}(r)). \tag{2.12}$$

Below ϕ_t, the melt fraction is taken to vary non-linearly with temperature and is computed from a degree-six polynomial written as a function of $\phi_l(T, r)/\phi_t$. With such a parameterisation, melt productivity is indeed low near the solidus but largely increases before clinopyroxene exhaustion to then drop to a constant value (Figure 2.2). Note that Katz et al. (2003) propose a parametrisation of the mantle melt fraction that gives a similar evolution (Figure 2.2). In the end, the melt fraction is computed from :

$$\Phi(T, r) = \min\left[\phi_l = \frac{T(r) - T_{sol}(r)}{T_{liq}(r) - T_{sol}(r)}; \phi_{nl} = \sum_{i=1}^{6} a_i \left(\frac{\phi_l}{\phi_t}\right)^i\right] \text{ for } T_{sol}(r) < T(r) < T_{liq}(r), \tag{2.13}$$

where the different coefficients a_i of the degree-6 polynomial are obtained by matching the dry case of Hirschmann et al. (1999), Figure 8, and are given in the caption of Figure 2.2.

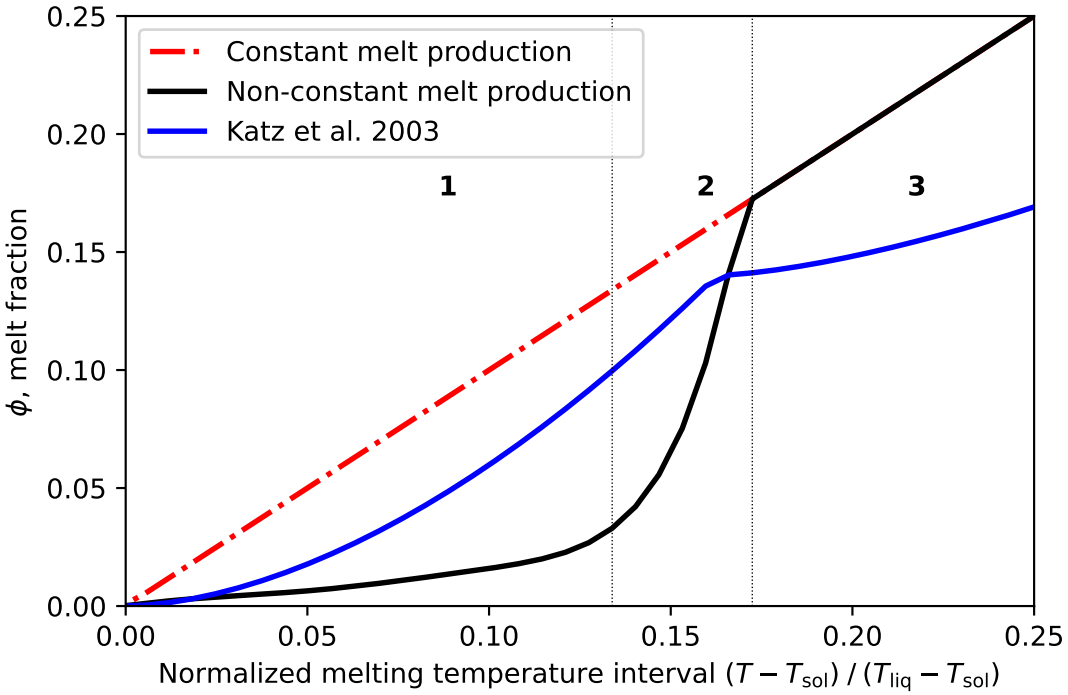

FIGURE 2.2 – Melt fraction as a function of the temperature difference from the solidus $\phi_l = \frac{T-T_{sol}}{T_{liq}-T_{sol}}$ for three different parametrisations : linear (dash-dotted red line), and non-linear, from Katz et al. (2003) in blue solid line, or adapted from Hirschmann et al. (1999) (Equation 2.13) in black solid line. The non-constant melt production parametrisation shows three different phases of melt production : (1) a low productivity near the solidus, (2) an increasingly high productivity below Cpx exhaustion at 17% melt fraction, and (3) a constant melt production after Cpx exhaustion. The coefficient a_i of the polynomial are as follows : $a_0 = 0$, $a_1 = 0.035$, $a_2 = -0.048$, $a_3 = -0.3305$, $a_4 = 1.9763$, $a_5 = -3.3423$, $a_6 = 1.8814$.

The average melt fraction ϕ_a over the partially melted volume of the mantle V_ϕ is :

$$\phi_a^{\mathrm{N/S}} = \frac{1}{V_\phi^{\mathrm{N/S}}} \int_{V_\phi} \Phi(T, r)^{\mathrm{N/S}} \mathrm{d}V. \tag{2.14}$$

However, extraction of the melt is only possible if the melt is interconnected, which occurs if the melt fraction is larger than a critical value ϕ_c that is equal to a few percent (Miller et al., 2014) (Table 2.1). To account for this we define an "effective average melt fraction" (ϕ_{eff}) which is the fraction of interconnected fluid over the partially melted volume of the mantle :

$$\phi_{\text{eff}}^{\text{N/S}} = \frac{1}{V_\phi^{N/S}} \int_{V_\phi} \Phi^i(r)^{N/S} \mathrm{d}V, \tag{2.15}$$

where $\Phi^i(r)^{N/S} = \Phi(T,r)^{N/S}$ if $\Phi(T,r)^{N/S} \geq \phi_c$, else $\Phi^i(T,r)^{N/S} = 0$.

2.3.2 Crust extraction

Mantle melts are positively buoyant relative to the surrounding mantle rocks and rise through the convective and lithospheric mantle to reach the crust and increase its thickness. The rate of crustal growth is given by :

$$\frac{\mathrm{d}D_{cr}^{\text{N/S}}}{\mathrm{d}t} = w^{\text{N/S}} \left(\frac{R_l^{\text{N/S}}}{R_{cr}^{\text{N/S}}} \right)^2, \tag{2.16}$$

where $w^{N/S}$ is the melt output velocity at the lid radius $R_l^{N/S}$ and $R_{cr}^{N/S}$ is the radius where the liquid is injected into the crust. In contrast to Breuer and Spohn (2006); Morschhauser et al. (2011) and Samuel et al. (2019), we do not consider that melt is extracted from the mantle at a rate set by the vigour of convection but at a percolation velocity (Richter and McKenzie, 1984; McKenzie, 1985; Bercovici et al., 2001) :

$$w^{\text{N/S}} = \frac{k_\phi^{\text{N/S}} \Delta\rho g_u}{\eta_{\text{liq}}} (1 - \phi_{\text{eff}}), \tag{2.17}$$

where k_ϕ is the permeability of the host rock that is a function of the melt fraction ϕ, η_{liq} the melt viscosity, $\Delta\rho = \rho_m - \rho_{\text{liq}}$ the density difference between the host rock and the melt. We account for melt compressibility and parameterise the melt density to evolve linearly with pressure :

$$\rho_{\text{liq}}^{\text{N/S}} = \rho_{\text{liq}}^0 (1 + \chi P_m^{\text{N/S}}), \tag{2.18}$$

where ρ_{liq}^0 is the melt density at 0 GPa and χ is the coefficient of isothermal compressibility ($\chi \sim 0.04$ GPa^{-1}). The density of the melt becomes larger than the mantle density at a pressure close to $P_{\max} = 7.4$ GPa as in Suzuki and Ohtani (2003), if $\Delta\rho$ becomes zero or negative, the extraction rate falls to zero.

The host rock permeability k_ϕ evolves as Richter and McKenzie (1984); McKenzie (1985) :

$$k_\phi^{\text{N/S}} = k_0 \left(\phi_{\text{eff}}^{\text{N/S}} \right)^3, \tag{2.19}$$

where k_0 is a reference permeability which may vary over several orders of magnitude, typically between 10^{-12} and 10^{-7} m^2 depending on the grain size (Miller et al., 2014).

However, the melt extraction rate is limited by the rate of melt supply, which depends on the convection velocity. We thus consider that the melt extraction rate w cannot be larger than the characteristic convection velocity, given by the thermal boundary layer theory, times the effective melt fraction (Morschhauser et al., 2011; Samuel et al., 2019) :

$$w_{\max}^{\mathrm{N/S}} = \frac{\kappa_m}{\bar{R}_l - R_c} \left(\frac{Ra_u^{\mathrm{N/S}}}{Ra_u^{\delta}} \right)^{2\beta_u} \phi_{\mathrm{eff}}^{\mathrm{N/S}}. \tag{2.20}$$

This limit is however only reached for the highest values of the reference permeability and at large melt fractions. For instance, using $Ra = 10^8$, the convection velocity is $\sim 7 \times 10^{-9}$ m s^{-1}. To get a similar extraction rate with a melt fraction of 10%, k_0 must be equal to 5×10^{-9} m^2, which is large. Thus, in most cases, melt extraction occurs at the Darcy velocity (2.17). This generally leads to smaller extraction rates compared to previous considerations ; it implies that the remaining liquid is entrained by convection with the solid matrix and crystallizes at depth.

As in Morschhauser et al. (2011), we account for the heat flux due to melt extraction at temperature T_m from the convective mantle :

$$q_{cr}^{\mathrm{N/S}} = w^{\mathrm{N/S}} \rho_{cr} (L + C_{cr}(T_m - T_l)), \tag{2.21}$$

with C_{cr} the crust heat capacity of the crust.

2.4 Lid advection, Magma heating and crustal melting

2.4.1 Downward advection due to crust growth

While the injection of magma heats up the crust, the growth of the crust leads to a downward advection of the underlying lid through the addition of new crustal material. It limits the heating caused by magmatism by bringing colder material downwards. This effect is generally neglected in parameterised thermal evolution studies (Breuer and Spohn, 2006; Morschhauser et al., 2011; Samuel et al., 2019). Foley and Smye (2018) argued that it is likely negligible as the Péclet number ($\frac{D_l w}{\kappa}$) is less than one. In Chapter 3, which will focus on crustal extraction dichotomy formation, advection is neglected but it is taken into account in Chapters 4 and 5. In Section 3.6 we will discuss the relevance of neglecting advection for Martian thermal evolution. How the intrusive magma distributes below, within or above the crust determines the downward advection process as well as the heating caused by the intrusion (Figure 2.3). We consider that a fraction of magma ($\boldsymbol{f_{\mathrm{mag}}}$) is deposited as magmatic intrusions at depth while the rest ($1 - \boldsymbol{f_{\mathrm{mag}}}$) erupts at the surface. The intrusive fraction is then divided into a basal component noted as "basal magmatism" (f_{base}) while the rest distributes over the bulk of the crust as "crustal intrusions" ($1 - f_{\mathrm{base}}$). Volcanism induces crust growth from the surface, causing downward advection of the entire crust and lid. Whereas deposition at the base of the crust as basal magmatism will only cause downward advection of the underlying lithospheric mantle. Crustal magmatism over the whole crust volume generates a downward advection flow with a vertical velocity $u(r)$ that increases with depth in the crust. The advection velocity caused by volcanism and magmatism ($u(r)$)

TABLE 2.1 – Parameter values and description for our reference case

Parameter	Description	Value	Unit
R_p	Planet radius	3390	km
R_c	Core radius	1825	km
f	lowlands area fraction	0.4	
ρ_c	Core density	6200	kg m^{-3}
ρ_p	Primordial mantle density	3472	kg m^{-3}
ρ_{cr}	Crustal density	2900	kg m^{-3}
k_{cr}	Crustal thermal conductivity	3	W m^{-1} K^{-1}
k_m	Mantle thermal conductivity	4	W m^{-1} K^{-1}
C_c	Core Heat capacity	840	J K^{-1} kg^{-1}
C_{cr}	Crust Heat capacity	1000	J K^{-1} kg^{-1}
C_m	Mantle Heat capacity	1142	J K^{-1} kg^{-1}
α_m	Thermal expansion coefficient	2.5×10^{-5}	K^{-1}
L	Latent Heat of crystallization	5×10^5	J kg^{-1}
D_i	Partition coefficient	0.01	
ρ^0_{liq}	Magma density at 0 GPa	2600	kg m^{-3}
χ	isothermal compressibility	0.04	GPa^{-1}
f_{mag}	Magmatism fraction	0.5	
f_{base}	Basal magmatism fraction	0.5	
g_u	Surface gravity	3.7	m s^{-2}
g_c	Core-Mantle boundary gravity	3.4	m s^{-2}
ϵ_c	Ratio of the mean to upper core temperature	1.1	
P_0	Reference pressure	3	GPa
T_0	Reference temperature	1600	K
A	Activation energy	300	kJ mol^{-1}
a_{rh}	Rheological coefficient	2.54	
R	Gas constant	8.314462	J mol^{-1} K^{-1}
η_0	Reference viscosity	10^{19} to 10^{22}	Pa s
V	Activation volume	3×10^{-6}	m^3
β_u	Upper boundary layer exponent	0.335	
β_c	Lower boundary layer exponent	1/3	
Ra^u_{crit}	Upper critical Rayleigh number	450	
k_0	Mantle reference permeability	10^{-12} to 10^{-7}	m^2
η_l	Melt viscosity	1	Pa s
ϕ_c	Critical melt fraction	0.02	
D_{ref}	Crust thickness corresponding to 20% of silicate volume	191	km
ΔT_{sol}	Increase in solidus for a crust thickness of D_{ref}	150	K
$X^p_{H_2O}$	Primordial mantle water content	0.1	$\%wt$ H_2O
D^0_l	initial lid thickness	50	km
D^0_{cr}	initial crust thickness	4	km
T_s	Surface Temperature	200	K
T^0_m	Initial upper mantle temperature	1700	K
ΔT^0_c	Initial superheating of the core	100	K
Λ^0_{cr}	Initial enrichment of the crust	10	
ΔD^0_l	Initial N-S difference in lid thickness	2	km

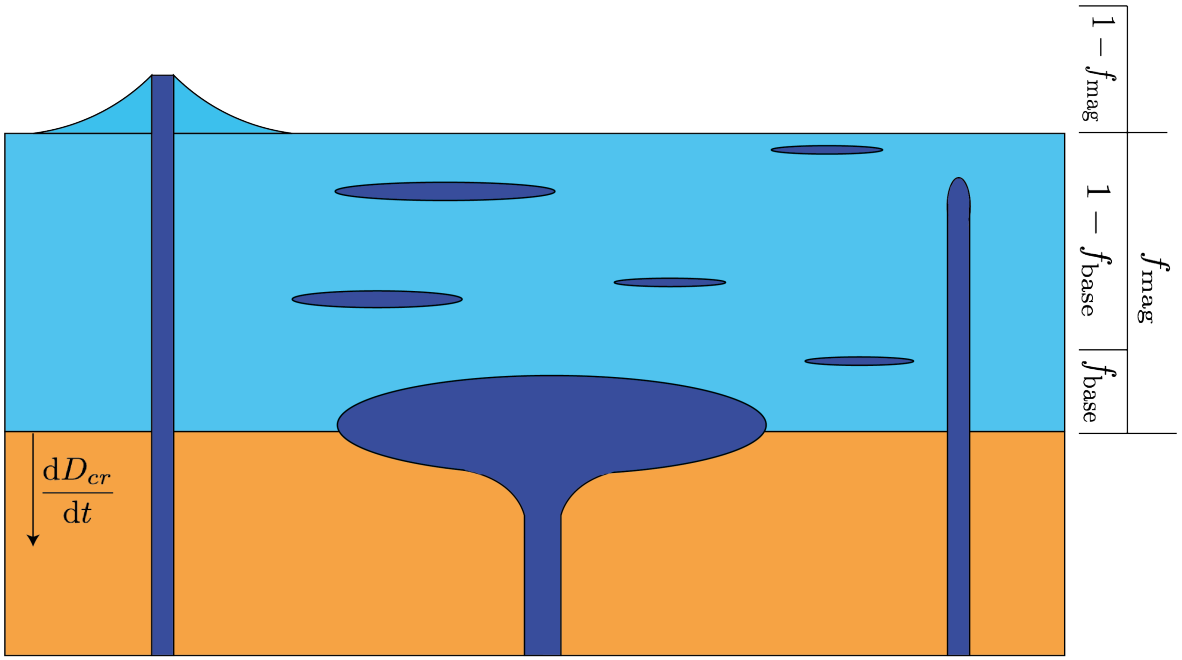

FIGURE 2.3 – The crust grows at a rate $\frac{\mathrm{d}D_{cr}}{\mathrm{d}t}$ but magma can (i) erupt at the surface (fraction $(1 - f_{\text{mag}})$ of the incoming magma) or (ii) intrude within the crust as crustal intrusion (fraction f_{mag} of the incoming magma) or just below the crust as basal magmatism (fraction $(1 - f_{\text{base}}) \times f_{\text{mag}}$ of the incoming magma). The fraction that erupts at the surface cools down instantaneously while the fraction intruding below or within releases heat to the surroundings.

is obtained by volume conservation. Two general equations for this advection velocity, one for the crust and one for the lithospheric mantle, are then obtained :

$$u(r > R_{cr}) = (1 - \boldsymbol{f_{\text{mag}}}) \times w \left(\frac{R_l}{r}\right)^2 + (1 - f_{\text{base}}) \times \boldsymbol{f_{\text{mag}}} \times w \frac{R_l^2}{r^2} \frac{R_p^3 - r^3}{R_p^3 - R_{cr}^3}, \quad (2.22)$$

$$u(r \leq R_{cr}) = w \times \left(\frac{R_l}{r}\right)^2, \quad (2.23)$$

where w is the percolation rate (Equation 2.17) at the radius of the base of the lid R_l, R_p is the radius of Mars and R_{cr} the radius of the crust-mantle boundary.

2.4.2 Magma heating

The magma extracted and deposited in the crust is hotter than the surrounding crust. Magma cooling to the temperature of the crust releases heat to its surrounding, increasing the temperature of the crust. We neglect heat loss during magma ascent from the base of the lid to the crust and thus assume that the magma reaches the crust at the temperature T_l. This heat supply is expressed as a heat source term, that depends on how the magma is distributed in the crust (Figure 2.3). We neglect

the effect of heat released at the surface by volcanism as it is almost instantaneously evacuated. The amount of energy released is then dependent on the fractions of bulk intrusive and basal magmatism as well as on the temperature of the crust, the colder the crust, the more energy being released. This gives an internal heating term which is temperature-dependent :

$$H_{\rm mag}^{\rm N/S}(r > Rcr) = w^{\rm N/S}\frac{A_{cm}^{\rm N/S}}{V_{cr}^{\rm N/S}}\rho_{cr}\Big[L + C_{cr}\Big(T_l - T(r)\Big)\Big]f_{\rm mag}(1 - f_{\rm base}), \tag{2.24}$$

$$H_{\rm mag}^{\rm N/S}(R_{cr}) = w^{\rm N/S}A_{cm}^{\rm N/S}\rho_{cr}\Big[L + C_{cr}\Big(T_l - T_{cr}\Big)\Big]f_{\rm mag}\left(\frac{(1 - f_{\rm base})}{V_{cr}^{\rm N/S}} + \frac{f_{\rm base}}{dV_{cr}}\right), \tag{2.25}$$

where the crust-mantle boundary is at temperature T_{cr}, A_{cm} is the area corresponding to the radius R_l and dV_{cr} the volume at the base of the crust heated by crustal base magmatism.

2.4.3 Crustal melting

The crust may reach its melting point during the thermal evolution. A characteristic solidus for the Martian crust has not yet been determined experimentally, especially since the composition of the Martian crust which still remains unknown. Nevertheless, in the absence of such data, we can rely on existing experiments on terrestrial basaltic analogues and propose an approximate solidus.

For the Earth, the solidus of rocks with basaltic compositions has been determined for subduction settings where the rocks are often altered and/or enriched in water. Indeed, the solidus of mafic rocks is strongly modified by the addition of water (Peacock et al., 1994). The water composition of the Martian primordial mantle (1 to 1000 ppm, Mysen et al. 1998 Johnson et al. 1991) is not sufficient to significantly affect the melting temperature of the mantle of Mars. Still, as water behaves as an incompatible element, the Martian crust may be enriched compared to the mantle. As water and heat-producing elements share similar partition coefficients (Aubaud et al., 2004), the crust of Mars may be similarly enriched in water and heat-producing elements, i.e. 10 to 15 times more enriched (Thiriet et al., 2018). But, even in this case, the water enrichment of the Martian crust (0.1 to 1.5%) is much lower than that considered for terrestrial basalt ($\simeq 2 - 3\%$ Peacock et al. 1994) ; such a water concentration is however close to that for a terrestrial water-rich mantle (Katz et al., 2003). Basaltic rocks are chemically and mineralogically relatively similar to mantle rocks, so it seems reasonable to consider a similar parametrisation for the solidus of a basaltic crust than for a mantle solidus.

We thus use a similar parametrisation as Katz et al. (2003) to define a crustal solidus as a function of the water content of the melt fraction (X_{H_2O}) and of the pressure (P, GPa), with a classical slope of 100 K GPa^{-1} :

$$T_{\rm sol}^{\rm cr}(P, X_{H_2O}) = T_{\rm sol}^{\rm cr\,0} + 100P - \Delta T(X_{H_2O}), \tag{2.26}$$

where $T_{\rm sol}^{\rm cr}$ is expressed in Kelvin. $T_{\rm sol}^{\rm cr\,0}$ is the crust solidus temperature at zero pressure, and is defined as $T_{\rm sol}^{\rm cr}(P = 0) = T_{\rm sol}^{\rm Earth} - \Delta T_{\rm Fe}$, where $T_{\rm sol}^{\rm Earth}$ is the typical solidus temperature for a terrestrial basalt (1323 K, Peacock et al. (1994)) and $\Delta T_{\rm Fe}$ is a correction for different $\#Mg$ between the Earth and Mars. As Collinet et al. (2015) gives a difference between the solidus of the Martian and Earth mantle of 50K, we decided to extrapolate this difference to our crustal solidus. $\Delta T(X_{H_2O})$ is the solidus temperature decrease caused by the addition of water in the melt, which we express as a power law, a function of the water content in the melt, expressed in %wt :

$$\Delta T(X_{H_2O}) = K X_{\rm H_2O}^{\gamma}, \tag{2.27}$$

where we use $K = 43$ K %wt$^{-\gamma}$ and $\gamma = 0.75$ as taken in Katz et al. (2003) for the terrestrial mantle solidus. The water content in the melt is obtained assuming a chemical equilibrium :

$$X_{\rm H_2O} = \frac{\Lambda_{cr}^{N/S} X_{\rm H_2O}^{p}}{D_i + \phi_{\rm min}(1 - D_i)}, \tag{2.28}$$

with $X_{H_2O}^{p}$ the water content of the bulk silicate part of Mars primordial mantle, $\Lambda_{cr}^{N/S}$ the crustal enrichment in water. As water and heat-producing elements share the same partition coefficient D_i, we assume that they distribute in the same way between the crust and the mantle and hence that the crustal enrichment in water is the same as the crustal enrichment in heat-producing elements (Aubaud et al., 2004). $\phi_{\rm min}$ is the minimum melt fraction at which the solidus is calculated. Here, we are interested in the temperature at which the melt fraction is higher than zero, and especially higher than 0.02 at which segregated grain boundaries becomes interconnected. As the melt becomes saturated in water, the decrease in solidus temperature associated with the addition of water stops :

$$\Delta T(X_{\rm H_2O} > X_{H_2O}^{\rm sat}) = \Delta T(X_{\rm H_2O}^{\rm sat}), \tag{2.29}$$

where $X_{H_2O}^{\rm sat}$ is the maximum water content in the melt, which depends on pressure following :

$$X_{\rm H_2O}^{\rm sat} = 12P^{0.6} + P, \quad \%\text{wt}, \tag{2.30}$$

where P is expressed in GPa (Katz et al., 2003). The resulting solidus is shown on Figure 2.4, it decreases with pressure following the water-saturated solidus down to a depth that depends on the enrichment in water of the crust. The curves obtained are quite similar to those described in Peacock et al. (1994). The water contents proposed by Taylor (2013) (i.e. 300 ± 150 ppm) are sufficient to obtain significantly lower solidus temperature than the anhydrous one.

To calculate the crustal melt fraction, we assume a constant melt production between the solidus and liquidus temperatures to which is added the minimum melt fraction (2%). The melt fraction in the crust can then be written as a linear function of

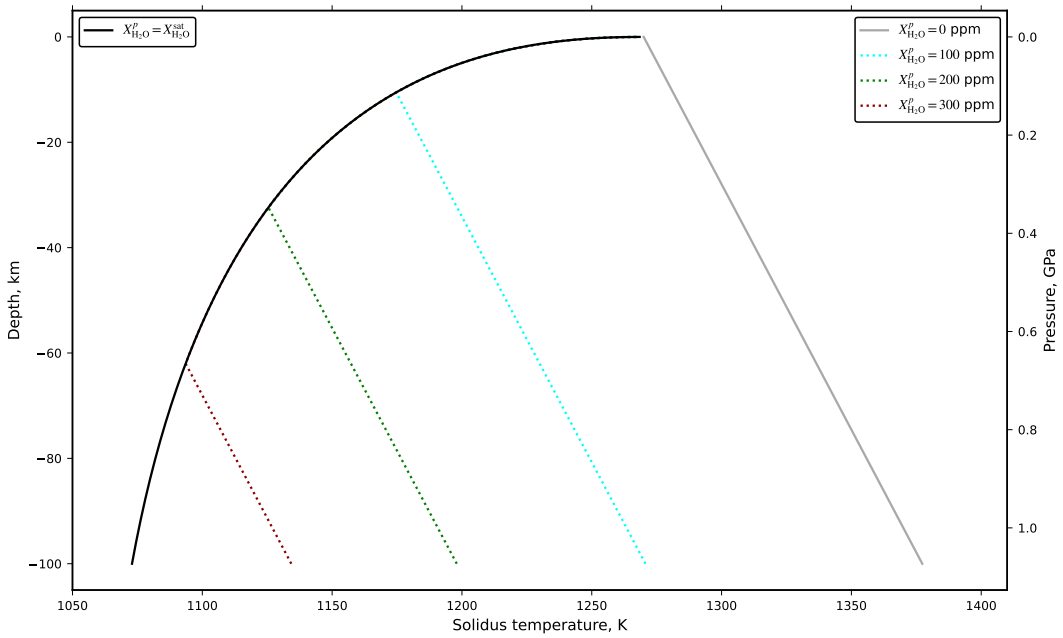

FIGURE 2.4 – Crustal solidus temperature T^{cr}_{sol} as a function of depth. The dotted curves represent the crust solidus for increasing values of water content $X^p_{H_2O}$ from 0 ppm to 300 ppm in 100 ppm increments. The black solidus curve is the solidus at water saturation ($X_{H_2O} = X^{sat}_{H_2O}$). The grey solid curve is the anhydrous solidus. The pressure at 100 km depth is 1.07 GPa using a crustal density of 2900 kg.m^{-3} and a gravity of 3.7 m^2.s^{-1}.

the temperature :

$$\phi^{cr}(r) = \frac{T(r) - T^{cr}_{sol}(r)}{T^{cr}_{liq}(r) - T^{cr}_{sol}(r)} + \phi_{min}, \tag{2.31}$$

where $T^{cr}_{liq}(r)$ is the crustal liquidus, expressed in Kelvins, that is approximated from the addition of a constant to the anhydrous solidus :

$$T^{cr}_{liq}(r) = T^{cr^0}_{sol} + 100P + 330. \tag{2.32}$$

.

Melting is not considered in chapter 3 because we are mainly interested in the growth of the crust and not its thermal state, unlike in the following chapters. The effect of adding crustal melting on our results is discussed in Section 3.6.

2.5 Radioactive heat production and HPE distribution

Because heat-producing elements (HPEs) are lithophile and incompatible elements, their concentration differs among the different layers of the planet : while the crust, mainly formed by mantle melt extraction, is enriched in HPEs, their concentrations in the core is negligible. Here, we assume that the four major heat-producing elements

(^{40}K, ^{232}Th,^{235}U, ^{238}U) are characterised by the same solid-liquid partition coefficient D_i and hence each reservoir j is characterised by a single enrichment factor Λ_j :

$$\Lambda_j = \frac{[\mathrm{HPE}]_j}{[\mathrm{HPE}]_{\mathrm{MBS}}}, \tag{2.33}$$

where $[\mathrm{HPE}]_j$ is the element concentration in the reservoir j and $[\mathrm{HPE}]_{\mathrm{MBS}}$ the element concentration in the bulk silicate part of Mars, or primitive mantle (Figure 2.1). We use the geochemical model of Wänke and Dreibus (1994) for the present-day HPEs concentration in the bulk silicate Mars.

During melting, HPEs partition in between the melt and residual rock according to their partition coefficient D_i :

$$D_i = \frac{[\mathrm{HPE}]_{\mathrm{melt}}}{[\mathrm{HPE}]_{\mathrm{residual}}}. \tag{2.34}$$

The convective mantle melt fraction varies only slowly with time, we assume chemical equilibrium ; the melt enrichment factor is thus given by :

$$\Lambda_{liq}^{\mathrm{N/S}} = \frac{\Lambda_{cm}}{\phi_a^{\mathrm{N/S}} + (1 - \phi_a^{\mathrm{N/S}})D_i}. \tag{2.35}$$

Melt and HPE extraction deplete the mantle that is assumed to be well-mixed and homogeneous. However, this is not the case for the lithospheric mantle which is stagnant and grows during crust extraction as the mantle becomes progressively more depleted. We follow the bulk HPE enrichment of the five different reservoirs using mass balance. The mass variation $\mathrm{d}m$ in heat producing element in a reservoir j, given by $\mathrm{d}m = \mathrm{d}(\rho_j V_j \Lambda_j [HPE]_{\mathrm{MBS}})$, is due to a mass flux from a reservoir k to a reservoir j ($\dot{m}_j^k$), expressed as $\dot{m}_j^k = \pm\ \rho_{\mathrm{j}} \Lambda_k^j [HPE]_{\mathrm{MBS}} \mathrm{d}V_j^k$. Accounting for all possible fluxes ($\mathrm{d}m_j = \sum^k \dot{m}_j^k$), we obtain :

$$\mathrm{d}(\Lambda_{cr} V_{cr}) = \Lambda_{liq} \mathrm{d}V_{cr}, \tag{2.36a}$$

$$\mathrm{d}(\Lambda_{lm} V_{lm}) = \Lambda_{cm} \mathrm{d}V_{lm}, \tag{2.36b}$$

$$\rho_m\, \mathrm{d}(\Lambda_{cm} V_{cm}) = -\rho_{cr} \Lambda_{liq} \mathrm{d}V_{cr}, \tag{2.36c}$$

where Λ_{cr} is the northern or southern crustal enrichment, Λ_{lm} is the northern or southern lithospheric mantle enrichment and Λ_{cm} the convective mantle enrichment.

The volumetric heat production $H_j(t)$ in the reservoir j is given by the sum of the four contributions :

$$H_j(t) = \Lambda_j \rho_j \sum_{i=1}^{N_e} J^i \left[\mathrm{HPE}^i\right]_{\mathrm{MBS}} \exp(-\lambda_i t), \tag{2.37}$$

where J^i, in W kg^{-1}, is the power produced by the decay of 1 kg of an element i, λ_i the decay constant of that element (Ruedas, 2017), ρ_j the reservoir density and t is time (with $t = 0$ at present-day and negative in the past).

Early in the thermal evolution, the crust extraction rate may be limited by the lid growth rate such that the lid is entirely made of crustal material. If the lid thickness (and hence potentially the crust thickness) decreases, HPEs from the lid and/or crust are recycled back into the mantle. However, a recent study by Batra and Foley (2021) shows that a buoyant crust could resist entrainment by the convective mantle, which would then reduce the mantle heat flow and thicken the lid because HPEs are not remixed in the mantle.

Finally, in order to ensure mass conservation of the bulk silicate part of Mars, the mantle density ρ_m is taken to increase as the crustal volume V_{cr} increases :

$$\rho_m = \frac{(V_p \rho_p - V_{cr} \rho_{cr})}{V_m}, \tag{2.38}$$

where $M_p = V_p \rho_p$ is the mass of the primordial mantle.

2.6 Thermal evolution

2.6.1 Heat conservation in the core and mantle

We follow Grott and Breuer (2008); Morschhauser et al. (2011) and Thiriet et al. (2018), and use the conservation of heat in the mantle and core to calculate the evolution of the temperature at the top of the convective mantle T_m accounting for heat fluxes at the interfaces, as well as, in the mantle case, radioactive heating, latent heat of melting and heat removal by melt extraction :

$$\rho_m C_m V_{cm} \epsilon_m (St + 1) \frac{\mathrm{d}T_m}{\mathrm{d}t} = -\sum^{N/S} \left(q_{cr}^{\mathrm{N/S}} + q_{cm}^{\mathrm{N/S}} \right) A_{cm}^{\mathrm{N/S}} + q_c A_c + H_{cm} V_{cm}, \tag{2.39}$$

where ρ_m is the mantle density, V_{cm} is the convective mantle volume, ϵ_m the ratio between $\bar{T}_{cm}$, the mean temperature of the convective mantle, computed at each iteration, and T_m the temperature at the top of the convective mantle, C_m the mantle heat capacity, $q_m^{\mathrm{N/S}}$ is the convective heat flux in each hemisphere (Section 2.2, Equation 2.7), $q_{cr}^{\mathrm{N/S}}$ the heat flux out of the mantle due to crust extraction (Section 2.3.2, Equation 2.17), q_c the core-mantle boundary heat flux (Section 2.2, Equation 2.8), H_{cm} the heat production in the convective mantle (See Section 2.5, Equation 2.37). $A_{cm}^{\mathrm{N/S}}$ is the area of the interface between the lid and the convective mantle in each hemisphere and A_c is the surface of the CMB as described in Equation 2.44. As in Breuer and Spohn (2006), the time-dependent Stefan number St is defined as the ratio between latent heat released by melting and the sensible heat lost by the convective mantle :

$$St = \frac{L}{C_m} \frac{V_\phi}{V_{cm}} \frac{\mathrm{d}\phi_a}{\mathrm{d}T_m}, \tag{2.40}$$

where $\frac{\mathrm{d}\phi_a}{\mathrm{d}T_m}$ is the average melt production over the volume of the convective mantle and V_ϕ is the volume of mantle rocks that is above the solidus temperature.

Similarly, heat conservation in the core gives :

$$\rho_c C_c V_c \epsilon_c \frac{\mathrm{d}T_c}{\mathrm{d}t} = -q_c A_c, \tag{2.41}$$

with ρ_c the core density, C_c the core heat capacity, V_c the core volume, ϵ_c the ratio between $\bar{T}_c$, the mean temperature, and T_c taken as 1.1 (Stevenson et al., 1983).

2.6.2 Growth of the lid

As the planet cools, the lid thickness grows and its growth rate $\frac{\mathrm{d}D_l}{\mathrm{d}t}$ is determined from a Stefan-like equation which considers the balance, at the lid base, between the heat flow from the convective mantle and the conductive heat flow (Grott and Breuer, 2008; Morschhauser et al., 2011) :

$$\rho_m \left(C_m (T_m - T_l) + L\phi_a^{N/S} \right) \left(\frac{\mathrm{d}D_l^{N/S}}{\mathrm{d}t} - w^{\mathrm{N/S}} \right) = -q_{cm}^{N/S} - k_m \left. \frac{\mathrm{d}T}{\mathrm{d}r} \right|_{r=R_l}^{N/S}, \tag{2.42}$$

where $\phi_a^{N/S}$ is the average melt fraction (see Section 2.3.1), L is the latent heat of mantle melting and $w^{\mathrm{N/S}}$ is the percolation velocity (Equation 2.17) which is equal to the downward advection velocity caused by the thickening of the crust.

2.6.3 Conservation of heat in the conductive lid

We solve for the diffusion equation in spherical geometry over the lid thickness accounting for heat brought by magmatism H_{mag}, downward advection caused by crust growth at velocity $u(r)$ and crustal melting :

$$\left(\rho(r) C(r) + \frac{L a_m}{\Delta T_{\mathrm{l-s}}} \right) \frac{\partial T(r)}{\partial t} + u(r) \frac{\partial T(r)}{\partial r} = \frac{1}{r^2} \frac{\partial}{\partial r} \left(r^2 k(r) \frac{\partial T(r)}{\partial r} \right) + H(r,t) + H_{\mathrm{mag}}(r, T(r)), \tag{2.43}$$

where $k(r)$ is thermal conductivity, equal to k_{cr} in the crust and k_m in the mantle, $C(r)$ is the heat capacity, equal to C_m in the mantle and C_{cr} in the crust and $\rho(r)$ is the density, equal to ρ_{cr} in the crust and ρ_m in the mantle. We assume the crustal melt fraction in the crust to be low enough to neglect any change in the thermodynamic parameters of the crust caused by melting (thermal conductivity k_{cr}, density ρ_{cr}, heat capacity C_{cr}) and, for the sake of simplicity, we neglect upward melt segregation in the crust. Crustal melting is then added to the heat equation with a heat sink term that depends on the latent energy of melting (L) and secular cooling. L is the latent energy of melting in the crust (J m^{-3}) and we assume it's the same as in the mantle. a_m is 1 if the melt fraction is non-zero and 0 if the melt fraction is zero. $\Delta T_{\mathrm{l-s}} = T_{\mathrm{liq}}(r) - T_{\mathrm{sol}}(r)$ is the difference between the liquidus and solidus of the crust (Equations 2.26 & 2.32) or the mantle (Equations 2.10 & 2.11). Downward advection depends on the advection velocity $u(r)$ (Section 2.4.1) and temperature gradient ($\frac{\partial T(r)}{\partial r}$). Magmatism provides a heating term (H_{mag}) that depends on crustal temperatures and the fraction of basal and crustal intrusive magmatism (Section 2.4.2) and is zero in the lithospheric mantle.

2.6.4 Geometry

The following equations give the volume and basal area of the crust (V_{cr}, A_{cr}), lithospheric mantle (V_{lm}, A_{lm}) and convective mantle (V_{cm}, A_{cm}) as a function of f, the surface fraction of the northern lowlands, that is either taken equal to 0.4, to account for the two different provinces (North and South) (Andrews-Hanna et al., 2008a), or equal to 0 (or 1), for a radially symmetric evolution :

$$V_{cr} = \frac{4}{3}\pi(R_p^3 - fR_{cr}^{N\,3} - (1-f)R_{cr}^{S\,3}), \tag{2.44a}$$

$$V_{lm} = \frac{4}{3}\pi\left(f(R_{cr}^{N\,3} - R_l^{N\,3}) + (1-f)(R_{cr}^{S\,3} - R_l^{S\,3})\right), \tag{2.44b}$$

$$V_{cm} = \frac{4}{3}\pi(fR_l^{N\,3} + (1-f)(R_l^{S\,3} - R_c^3)), \tag{2.44c}$$

$$A_j = 4\pi\left(fR_j^{N\,2} + (1-f)R_j^{S\,2}\right) = A_j^N + A_j^S. \tag{2.44d}$$

North-South averages radius are indicated by the radius denoted by a bar symbol ($\bar{R}$). The average radius is defined as the radius of the sphere whose volume is equivalent to the sum of the North and South volumes :

$$\bar{R} = \left(fR_N^3 + (1-f)R_S^3\right)^{1/3}, \tag{2.45}$$

where R_N is the radius of the Northern Hemisphere and R_S is the radius of the Southern Hemisphere. The corresponding average thicknesses are obtained by taking the difference between the radius of the planet $\bar{D} = R_p - \bar{R}$ (crustal thickness, lid thickness, thermal lithosphere thickness) or the radius of the core $\bar{d} = \bar{R} - R_c$ (convective heigh, Equation 2.5).

2.7 Dimensionless numbers and critical parameters of the model

In the end, our system is mainly controlled by main dimensionless numbers. The Rayleigh number Ra determines the vigour of the convection and the cooling rate of the convecting mantle. Since it controls the thickness of the upper thermal boundary layer, Ra also strongly influences the melt fraction ; it mostly depends on mantle rock viscosity, and hence on the reference viscosity value η_0 (Section 2.2). A second important dimensionless number, noted Da corresponds to the ratio between between a characteristic time for conduction ($\tau^\kappa = R_p^2/\kappa_m$) and a characteristic time for crust extraction ($\tau^w = R_p\eta_l/k_0\Delta\rho g$) :

$$Da = \frac{\tau^\kappa}{\tau^w} = \frac{R_p k_0 \Delta\rho g}{\kappa_m \eta_l}. \tag{2.46}$$

The value of Da is mostly determined by that of the reference permeability k_0 (Section 2.3.2).

2.8 Numerical Resolution

Our physical model is solved numerically. The time-dependent equations (Equations 2.39, 2.41, 2.42 and 2.16) form a system of four first-order differential equations solved using a Runge-Kutta method of order 4. The diffusion equation in the lid (2.43) is solved using a finite volume method in spherical geometry and an implicit Euler scheme in time. Equations (2.36a-c) are solved explicitly at the end of each time step. We verify that secular cooling corresponds to the balance between surface cooling and heat production to ensure energy conservation and that bulk heat production is conserved as well. Appendix A gives more information on the numerical calculation.

Chapitre 3

A positive feedback mechanism between crustal thickness and melt extraction

This chapter was the subject of a paper published at the end of November 2022 in JGR Planets (Bonnet Gibet et al., 2022).

3.1 Introduction

The Martian surface is characterised by a dichotomy in elevation, crustal thickness, and morphology between the northern lowlands and southern highlands (Watters et al., 2007; Platz et al., 2013). The highlands are highly cratered and incised by many old river valleys (Tanaka et al., 2014). The oldest terrains outcrop in the Southern Hemisphere (Platz et al., 2013) which also concentrates observations of volcanic constructs and felsic rocks (Carter and Poulet, 2013; Wray et al., 2013). In contrast, the upper portion of the lowlands crust is made of vast and smooth basaltic plains and sedimentary deposits derived from the erosion of the highlands (Platz et al., 2013; Tanaka et al., 2014). The dichotomy is perhaps the most evident feature of the crust (Figure 3.1). Superposed on the dichotomy boundary is the Tharsis bulge, whose origin may (Andrews-Hanna et al., 2008a), or may not (Neumann et al., 2004), be related to it. Prior to the InSight mission, inversion of gravity and topography data were used to constrain the crustal thickness of Mars and its lateral variations, though these models depended on assumptions such as crustal density and minimum crustal thickness (Neumann et al., 2004; Wieczorek and Zuber, 2004)

The NASA InSight (Banerdt et al., 2020) mission has allowed recording for the first time the seismic activity of Mars with the deployment, early 2019, of the seismometer SEIS (Seismic Experiment for Interior Structure) in Elysium Planitia (Lognonné et al., 2020). From P and PP receiver function analyses of teleseismic events recorded by the seismometer, subsurface interfaces, including the crust-mantle interface or the Mohorovičić discontinuity, commonly referred to as the Moho, have been detected below the station (Knapmeyer-Endrun et al., 2021; Kim et al., 2021; Durán et al., 2022b).

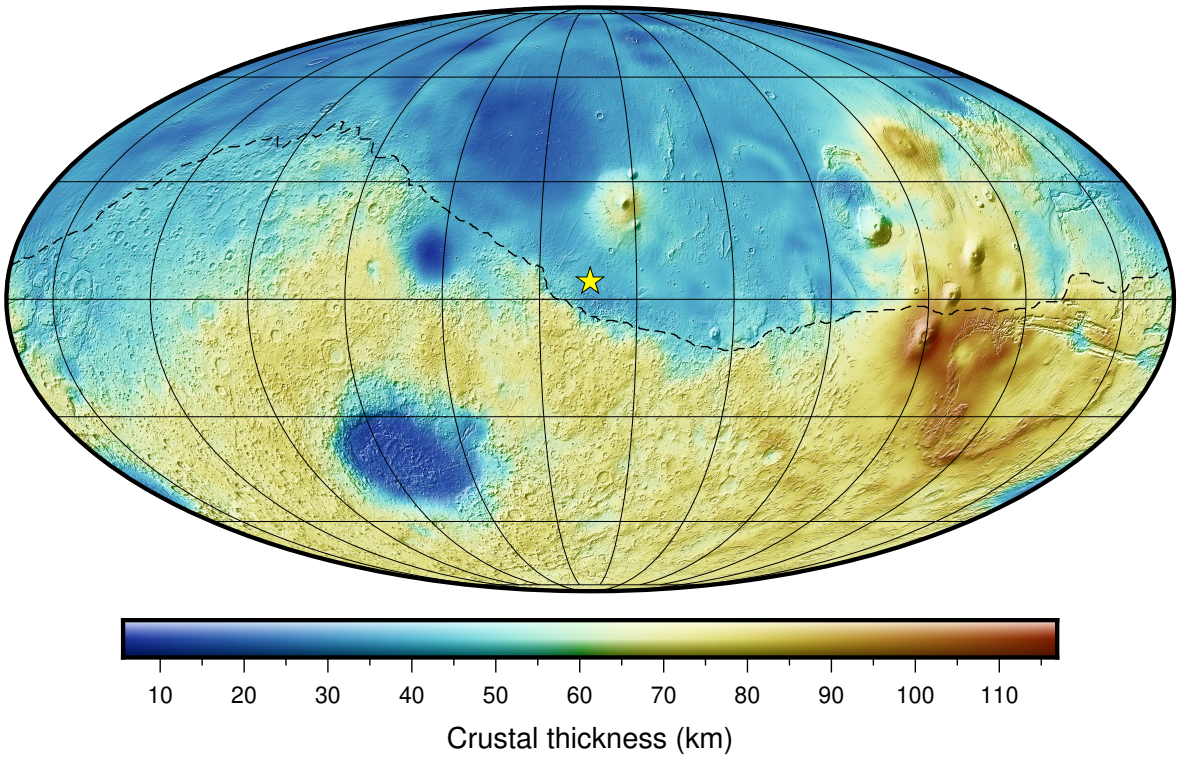

FIGURE 3.1 – Thickness of the crust of Mars using a crustal density of 2900 kg m^{-3}. For this model, the mantle density profile is that of (Khan et al., 2021) and the crustal thickness at the Insight landing site (yellow star) is 39 km (Knapmeyer-Endrun et al., 2021). The dashed line represents the dichotomy boundary from (Andrews-Hanna et al., 2008a). This map is presented in a Mollweide projection with a central meridian of 136°E longitude.

This local seismological constraint on the Martian crustal thickness provided a critical anchor point that is necessary for crustal studies that rely on topography and gravity data (Knapmeyer-Endrun et al., 2021). Following this detection, the Martian crust thickness and its lateral variations have been revealed (Knapmeyer-Endrun et al., 2021; Wieczorek et al., 2022) (see Section 3.4.2). A similar procedure was used on the Moon with receiver function and travel-time data analyses in order to estimate the local crustal thickness beneath the Apollo seismic stations (Vinnik et al., 2001; Lognonné et al., 2003) and to anchor global crustal thickness models based on gravity and topography data (Wieczorek et al., 2013).

The mechanism at the origin of the crustal dichotomy is one of the major debates concerning Mars' evolution (Watters et al., 2007). With an age between 4.5 and 3.7 Gyr, the dichotomy appears to be one of the oldest features of Mars (McGill and Dimitriou, 1990; Solomon et al., 2005). The formation of the dichotomy appears older than the northern lowlands but contemporary to the southern highlands. The younger surface of the Northern Hemisphere is then probably a late consequence of the dichotomy rather than related to its formation mechanism.

As planetary crusts grow by extraction of buoyant mantle melts, the dichotomy could have originated during crust growth due to laterally variable mantle melt fractions. A degree-one mantle convection pattern with a hot ascending mantle plume in the South and a cold downwelling in the North can generate such a spatially variable mantle melt fraction. A degree-one mantle convection may be favoured by a radial stratification in viscosity in the mantle (Zhong and Zuber, 2001; Yoshida and Kageyama, 2006; Šrámek and Zhong, 2010). (Zhong, 2009) linked this degree-one to the presence of Tharsis. He proposed that melt extraction from the ascending plume and associated stiffening of the lithospheric keel could have generated a lateral viscosity variation that could in turn have triggered a toroidal velocity field inducing plume migration and explaining the location of Tharsis, straddling the dichotomy. In this study, the lithospheric keel was prescribed, extending over one hemisphere. (Šrámek and Zhong, 2012) lately parameterised partial melting and melt extraction in a 3D convection model to demonstrate that the associated lithosphere stiffening and crustal thickening were large enough to produce the observed dichotomy. The formation of the highlands by migration of the Tharsis plume would require several hundred million years and would imply an age-distance to Tharsis relationship for the highlands which is not obvious. Recently, (Morison et al., 2019) showed that a degree-one mode of mantle convection could also be generated during magma ocean solidification by melting and freezing at the boundary between the solid cumulates and the liquid ; but they did not investigate its consequences on crust formation.

The dichotomy may also result from the reprocessing of the crust after its main extraction phase through one or more impacts, which were frequent in the early times of the Solar System. A large impact in the Northern Hemisphere is currently the most popular explanation for the topographic depression in the North (Marinova et al., 2008). This impact could potentially explain the formation of the Martian moons Phobos and Deimos (Marinova et al., 2008) and possibly the cessation of the Martian geodynamo (Roberts and Arkani-Hamed, 2014). But, while a large impact event may help explain many features of the Martian surface, its real consequences on the structure and evolution of the crust are difficult to quantify and remain partly speculative given the ancient age of this event. The amount of kinetic energy released by a large impact could have significantly raised the mantle temperature (Roberts and Arkani-Hamed, 2014) inducing such a large amount of melt that the very evidence for an impact basin - i.e. the dichotomy - could have been eradicated (Tonks and Melosh, 1993). On another hand, (Marinova et al., 2011) used a smoothed particle hydrodynamics (SPH) model to argue that, depending on the impact characteristics, a significant fraction of the melt could have sequestered at depth without contributing to resetting the planetary surface. The size and speed of the impactor would then point to an age of 4.5 Gyr for this impact. An early large impact in the South has also been proposed to explain the larger crustal thickness in this hemisphere (Reese et al., 2010; Golabek et al., 2011).

In one-plate planets, the convective mantle interior is well characterised by a nearly uniform temperature, where a stagnant lid develops at the top as the cold boundary layer that is too viscous to be advected away (Nataf and Richter, 1982; Solomatov, 1995). The lid base is set by the mantle rheology which mainly depends on its temperature (Davaille and Jaupart, 1993). As a result, in a stagnant lid regime, the thermal structure of the crust largely influences the thickness of the thermal lithosphere and hence the amount of partial melt that is generated in the mantle below (Thiriet et al., 2018; Knapmeyer-Endrun et al., 2021) because mantle upwellings decompress down to pressures corresponding to the base of the lid. Here, we propose that the Martian dichotomy could have resulted from an instability in crustal growth. Indeed, since the crust is enriched in incompatible heat-producing elements (HPEs), the lid of a one-plate planet is thinner where the crust is thicker (Thiriet et al., 2018) and the pressure at its base is lower. Because the solidus temperature decreases more rapidly than the adiabat as pressure decreases, more melt is generated in the mantle below regions of thicker crust. As the melt extraction rate increases with melt fraction (McKenzie, 1985; Katz et al., 2022), there exists a positive feedback between crustal growth and crustal thickness on stagnant lid planets (Figure 3.2).

Here, we first demonstrate, using a simple analytical model, that larger wavelength perturbations, i.e. hemispherical perturbations, grow faster because smaller wavelengths are more attenuated by lateral thermal diffusion. We then develop a bi-hemispherical parameterised thermal evolution model to show that this positive feedback mechanism can indeed generate a significant dichotomy in crustal thickness from initially small thermal perturbations, and this despite the cooling of the planet. We finally investigate the different types of thermal and crustal extraction histories that are able to reproduce the range of Martian crustal thicknesses as deduced from the InSight mission.

3.2 Study of the instability for a simplified setup

Before developing a more complex thermal evolution model to study the differential growth of the crust in the Northern and Southern hemispheres of Mars, we first use a simplified toy model along with a linear stability analysis to study the growth of a thermal perturbation as a function of its wavelength. We demonstrate that lateral thermal perturbations of larger wavelengths grow faster because lateral thermal diffusion attenuates more easily the smaller wavelengths.

Here, we study the thermal evolution of a lid that becomes progressively enriched in heat-producing elements as melts, which concentrate incompatible and heat-producing elements, are extracted from the mantle below and redistributed within this lid. In particular, we follow the temperature at the base of the lid $T_b(t)$, assumed to be above

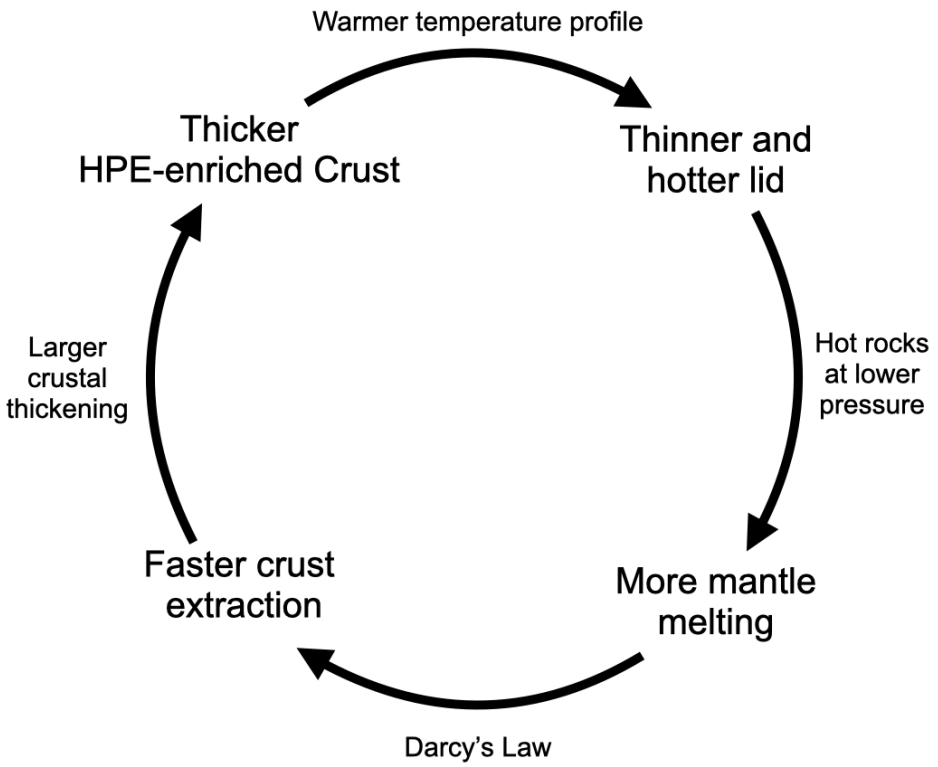

FIGURE 3.2 – Conceptual diagram of the positive feedback of crust thickness on melt extraction. 1-The crust is enriched in heat-producing elements leading to larger temperature gradients in the crust than in the mantle. 2- If the crust is locally thicker, the transition temperature between the convective mantle and the lid (T_l, Equation 2.3) is expected to be reached at shallower depths, i.e. a thinner lid. 3-The convective mantle with a temperature Tm rises to lower pressures where the lid is thinner. The mantle melt rate is therefore higher because the solidus temperature increases strongly with pressure (Equation 2.10). 4- According to Darcy's law, the increase in melt creates more porosity which increases its extraction rate. Therefore, it is expected that there will be more crustal thickening where the crust is already thick.

the solidus temperature T_{sol}, as well as the instantaneous melt fraction $\phi(t)$, which is taken to be a linear function of temperature over the melting interval $T_{liq} - T_{sol}$:

$$\phi(t) = \frac{T_b(t) - T_{sol}}{T_{liq} - T_{sol}}. \tag{3.1}$$

In this simplified model, we assume that, although enriched melts are deposited in the lid, the lid thickness $D_l = R_p - R_l$ remains constant, where R_p is the mean planetary radius and R_l the radius at the lid base. Hence, we neglect planetary cooling. The volumetric heat production in the lid $H(\theta, \varphi, t)$ evolves with time and is assumed to be radially homogeneous (i.e. the extracted melt is distributed evenly across the lid thickness, and we do not consider a chemically distinct crust). We finally assume a linear relationship between the melt extraction rate, and hence the enrichment rate of the lid in heat-producing elements $\dot{H}$, and the melt fraction ϕ at the base of the lid :

$$\dot{H}(t) = \alpha\phi(t) = \gamma T_b(t) - b, \tag{3.2}$$

where α is the rate of increase in heat production with time of the lid in W m^{-3} s^{-1} ; which could be estimated from $\alpha \approx vH_{\text{liq}}/D_l$, with v a characteristic melt extraction velocity and H_{liq} the melt heat production. The constants $\gamma = \frac{\alpha}{(T_{liq} - T_{sol})}$ and $b = \frac{\alpha T_{sol}}{(T_{liq} - T_{sol})}$ are also positive.

We solve for 3D diffusion of heat in the lid assuming, for this specific toy model, a steady-state, a constant heat flux q^0_{cm} from the underlying convective mantle and a constant temperature $T(R_p)$ at the surface :

$$\vec{\nabla}^2 T(r, \theta, \varphi, t) = -\frac{H(\theta, \varphi, t)}{k}, \tag{3.3}$$

with k the thermal conductivity. Our background state is such that the zero-order heat production $H^0(t)$ is laterally constant, and the zero-order background temperature field $T^0(r)$ is straightforward to obtain from (3.3) and boundary conditions. We now add small lateral perturbations in heat production and temperature to this background state :

$$H(\theta, \varphi, t) = H^0(t) + \epsilon H^1 Y_{lm}(\theta, \varphi) e^{\lambda t}, \tag{3.4}$$

$$T(r, \theta, \varphi, t) = T^0(r, t) + \epsilon T^1(r) Y_{lm}(\theta, \varphi) e^{\lambda t}, \tag{3.5}$$

where $\epsilon \ll 1$, $Y_{lm}(\theta, \varphi)$ are the spherical harmonic functions of degree l and order m, θ the colatitude, φ the longitude, $\lambda(l)$ the perturbation growth rate and t time. Injecting (3.4) and (3.5) into (3.3) and (3.2), we derive the following relations for first-order perturbations in ϵ :

$$\frac{1}{r^2}\frac{\partial}{\partial r}\left(r^2 \frac{\partial T^1(r)}{\partial r}\right) - \frac{T^1(r)}{r^2} l(l+1) = -\frac{H^1}{k}, \tag{3.6}$$

$$\lambda(l) H^1 = \gamma T^1(R_l), \tag{3.7}$$

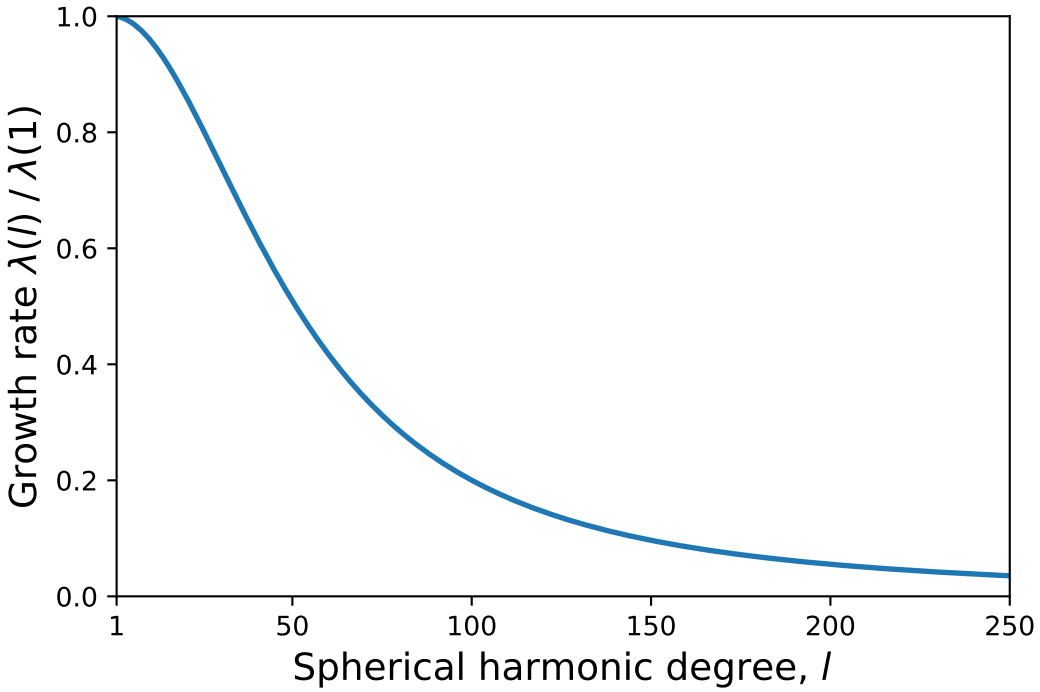

FIGURE 3.3 – Growth rate λ given by (3.8) and normalised by the growth rate for $l = 1$ as a function of spherical harmonic degree. We use $k = 3$ W m^{-1} K^{-1}, $R_p = 3390$ km, $R_l = 3290$ km.

with the boundary conditions $T^1(R_p) = 0$ and $k \left.\frac{dT^1}{dr}\right|_{r=R_l} = 0$. This finally gives a general solution for $l \neq 2$ and a particular solution for $l = 2$ (as the denominator of B_l and C_l is equal to zero in this case, i.e. $6 - l(l+1) = 0$ in (3.8a)) :

$$\forall\, l \neq 2 \qquad \begin{aligned} \frac{\lambda(l)}{\gamma} &= C_l R_l^l + B_l R_l^{-(l+1)} - \frac{R_l^2}{k}(6 - l(l+1))^{-1}, \\ B_l &= \frac{1}{k(6 - l(l+1))} \times \frac{l R_p^{2-l} R_l^{l-1} - 2R_l}{l R_p^{-(2l+1)} R_l^{l-1} + (l+1) R_l^{-(l+2)}}, \\ C_l &= \frac{R_p^{2-l}}{k(6 - l(l+1))} - B_l R_p^{-(2l+1)}, \end{aligned} \tag{3.8a}$$

$$\begin{aligned} \frac{\lambda(2)}{\beta} &= -\frac{R_l^2}{5k} \ln R_l + \frac{B_2}{R_l^3} + C_2 R_l^2, \\ B_2 &= \frac{R_l}{5k} \times \frac{2\, ln R_p - 2 \ln R_l - 1}{2 R_l R_p^{-5} + 3 R_l^{-4}}, \\ C_2 &= \frac{\ln R_p}{5k} - \frac{B_2}{R_p^5}. \end{aligned} \tag{3.8b}$$

Our solution shows that the growth rate is positive for all wavelengths. This means that perturbations of all wavelengths grow, and no wavelengths are damped (Figure 3.3). However, since lateral heat diffusion tends to attenuate smaller wavelengths

more, the larger the wavelength (the smaller l), the larger the growth rate λ of the perturbation is (Figure 3.3). Therefore, longer wavelength perturbations grow faster and are favoured by this feedback mechanism. The largest growth rate occurs for spherical harmonic degree 1, though the growth rates are not too different for the first few degrees. In order to study if the growth over time of a thermal perturbation is sufficient to induce a significant crustal dichotomy despite planetary cooling, which tends to damp crustal growth and hence this mechanism, we restrict our study to the case of a hemispherical perturbation ($l = 1$), which grows the fastest, and use a more complex thermal evolution model.

3.3 Model

In this chapter, we use the parameterised thermal evolution model described in Chapter 2, where we consider two different hemispheres, North and South, with a Northern Hemisphere making a fraction $f = 0.4$ of the surface of Mars. Hence, we here impose a degree one. However, since we are interested in crustal growth only, we neglect the advection of heat caused by crustal growth, i.e. $u(r) = 0$ in the heat conservation equation for the lid (Equation 2.40). Since the characteristic Péclet number ($Pe = \frac{D_l w}{\kappa}$) is lower than 1 during the thermal evolution of the planet (Foley and Smye, 2018) so the effect of downward advection of cold material caused by crustal growth on the global cooling may be neglected. We neglect also crustal melting, i.e. $a_m = 0$ in the term $\frac{La_m}{\Delta T_{\mathrm{l-s}}}$ in the same equation (Equation 2.43), which has a negligible effect on the thermal budget in the lid. For simplicity, we assume a homogeneous distribution of the melts extracted from the mantle in the volume of the crust volume as crustal intrusions, i.e. $f_{\mathrm{mag}} = 1$ and $f_{\mathrm{base}} = 0$. The density of the magma (Equation 2.18) is calculated here differently only in this chapter. The melt density evolves also linearly with the pressure ($P_m^{\mathrm{N/S}}$) but between the density of the crust and that of the mantle, following a slope of $\frac{\rho_m - \rho_{cr}}{P_{\max}}$. Using one or the other expression for the melt density does not affect our results.

3.4 Initial Parameters, Reference case and Crustal Thickness Constraints

3.4.1 Initial state

The initial state is described by a temperature at the top of the mantle T_m^0, a CMB temperature T_c^0, a lid thickness D_l^0, a crustal thickness D_{cr}^0 and a crustal enrichment Λ_{cr}^0. Since our goal is to examine whether this model may be able to produce the observed dichotomy in crustal thickness, we start with the smallest possible value for the initial crustal thickness in light of our numerical constraints, which is set to $D_{cr}^0 = 4$ km in both the North and South. This represents $\sim 10\%$ of the minimum final northern crust thickness (Section 3.4.2). A thicker crust, formed after an initial phase during

magma ocean solidification, might have been present initially (Wieczorek et al., 2022). However, the start of our model represents the late, mushy, stage of a magma ocean phase, when the rheological transition to solid-like convection has been reached. The model thus accounts for the formation of a primary crust by extraction of melts from an enriched mushy mantle (Michaut and Neufeld, 2022). It does not account for the formation of a large initial plagioclase flotation crust as proposed for the Moon ; but, given the higher gravity of Mars and larger water content, this would be less likely. Because the initial crust is so thin, the initial crustal enrichment has a low impact on the subsequent thermal evolution and we use a classical value of $\Lambda_{cr}^0 = 10$, equivalent to 560 ppb of ^{232}Th at present-day (Thiriet et al., 2018; Knapmeyer-Endrun et al., 2021).

We use values of T_m^0 and D_l^0 such that the mantle has just reached the rheological transition to solid-like convection in the mantle, i.e. such that the maximum mantle melt fraction (2.13) is between 0.3 and 0.4 initially (Salvador et al., 2017). The average melt fraction over the molten volume $\Phi_a^{\mathrm{N/S}}$ (2.14) is then less than $\sim 20\%$. Following (Knapmeyer-Endrun et al., 2021) and (Drilleau et al., 2021), we explore the range $1650 - 1750$ K for T_m^0, and therefore the range 50 ± 10 km for D_l^0. The core is considered to be superheated by ΔT_c^0 due to core formation and associated dissipation in gravitational potential energy. The initial CMB temperature is thus given by :

$$T_c^0 = T_m^0 + \frac{\alpha g T_m^0}{C_m}(R_l^0 - R_c) + \Delta T_c^0. \tag{3.9}$$

To trigger the instability, we impose an initial small perturbation to the symmetrical base state. In our reference case, this perturbation is an initial N/S difference in lid thickness ($\Delta {D_l}^0 = D_l^{N\,0} - D_l^{S\,0}$) of 2 km, (i.e. 4% of the mean lid thickness). We also explore smaller perturbations (down to 2% of the lid thickness) as well as the case of a perturbation in crustal thickness ($\Delta {D_{cr}}^0 = D_{cr}^{S\,0} - D_{cr}^{N\,0}$), which is equivalent to a perturbation in total HPE content in the lid (Section 3.5.2).

The initial time is equal to -4.5 Gyr. Parameter values for our reference case are given in Table 2.1.

3.4.2 Present-day crustal thickness of Mars from topography and gravity data

The Bouguer gravity anomaly can be inverted to provide the relief along the crust-mantle interface, and hence the crust thickness. These inversions depend upon the crustal density, upper mantle density profile and the local value of the crustal thickness at the InSight landing site (Wieczorek et al., 2022). Using receiver function methods on direct P-waves of teleseismic events recorded by the InSight seismometer, (Knapmeyer-Endrun et al., 2021) determined two possible crustal structures below the landing site : either the crust is thin and made of 2 layers, or it is thicker and made of 3 layers. The 3-layer, thicker, crustal model seems more consistent with thermal evolution models

(Knapmeyer-Endrun et al., 2021) as well as PP receiver function analyses (Kim et al., 2021).

We thus compare our final crustal thicknesses in the North and South, as well as their differences, with that obtained from the inversion of gravity and topography data that consider a thick crustal structure below the InSight landing site as well as the same density for the North and South. We use the dichotomy boundary of (Andrews-Hanna et al., 2008a) to calculate the surface average crustal thickness in the North and South. The boundary effectively cuts the Tharsis province in half, with half of Tharsis being located in the northern lowlands, and the other half in the southern highlands. For the sake of consistency, we compare the results of our model with Bouguer anomaly's inversions that consider the same crustal density as in our calculations ($\rho_{cr} = 2900$ kg m^{-3}, Table 2.1). With these considerations, the average northern crustal thickness D_{cr}^{N} is between 39.8 and 54.5 km, the average southern crustal thickness D_{cr}^{S} is between 57.9 and 82.4 km, and the average amplitude of the N/S dichotomy $\Delta D_{cr} = D_{cr}^{S} - D_{cr}^{N}$ ranges between 18.1 and 28.0 km. the average thickness of the crust is between 50.7 and 71.2 and corresponds to 5 to 7% of the silicate volume.

3.5 Results

We first describe results corresponding to a reference set of calculations for parameter values (Table 2.1), varying only the reference permeability (k_0) and the reference viscosity (η_0). We then study the effects of the other model parameters by comparing to our reference case.

3.5.1 Reference simulations

Two extreme cases of evolution

The final range of differences in crustal thickness between the Northern and Southern hemispheres obtained for our set of reference calculations is large, from no crustal dichotomy (dashed lines, Figure 3.4) to a difference of $\sim$ 80 km (solid lines, Figure 3.4).

Generally, melt formation occurs in two phases which could potentially result in two phases of crust extraction depending on the amplitude of melting (Figure 3.4d). The initial phase of melting occurs within the first $\sim$100 Myr of evolution and mostly depends on the initial conditions and mantle viscosity, with smaller viscosities leading to thinner boundary layers and larger melt fractions. The peak of the second phase of melting occurs between $\sim$500 Myr and 1 Gyr after the start of the simulation and is caused by the temperature increase in the convective mantle (Figure 3.4a) associated to the combined effect of the blanketing of the lid (Figure 3.4b), which grows in thickness, and radiogenic decay in the mantle. The amplitude of melting during this second phase mostly depends on model parameters and is not sensitive to the initial conditions : it is enhanced if melts and heat-producing elements are preserved in the

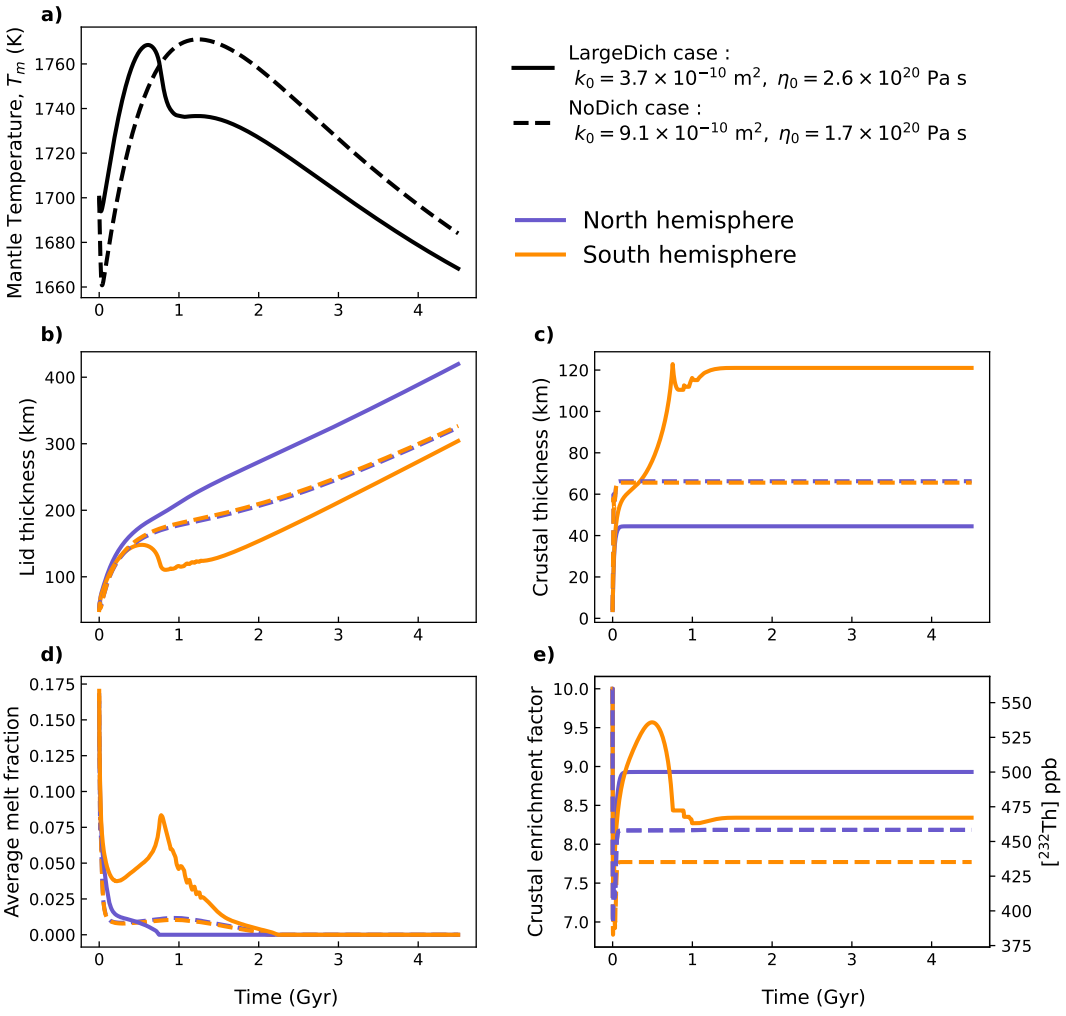

FIGURE 3.4 – Thermal evolution over 4.5 Gyr for two different calculations. (a) Evolution of the mantle temperature T_m, (b) evolution the lid thickness $D_l^{N/S}$, (c) evolution of the crustal thickness $D_{cr}^{N/S}$, (d) evolution of the average melt fraction below each lid $\phi_{\mathrm{a}}^{N/S}$, (e) evolution of the crustal enrichment factor $\Lambda_{cr}^{N/S}$. Blue lines, evolution for the Northern Hemisphere, orange lines, evolution for the Southern Hemisphere. Dashed lines, NoDich case with $\eta_0 = 1.6 \times 10^{20}$ Pa s and $k_0 = 9.1 \times 10^{-10}$ m^2, solid lines, LargeDich case : $\eta_0 = 2.6 \times 10^{20}$ Pa s and $k_0 = 3.7 \times 10^{-11}$ m^2.

convective mantle. If, during this second melting phase, the melt fraction exceeds the critical melt fraction, then a late, second phase of crustal extraction can occur, more frequently in regions of thick crusts, such as in the Southern hemisphere. Note for instance the increase in crustal growth rate in the South only, at $\sim$ 300 Myr, in the LargeDich case on Figure 3.4c that is associated with the increase in melt fraction in the South at the same time (Figure 3.4d).

The case with no significant difference in crustal thickness (NoDich case) is obtained at rather low viscosity $\eta_0 = 1.6 \times 10^{20}$ Pa s and high permeability of $k_0 = 9.1 \times 10^{-10}$ m^2. Initially, in both hemispheres, crust growth is limited by lid growth resulting in the northern crust being thicker than the southern one because of the imposed initial difference in lid thickness ΔD_l^0. No second phase of crustal extraction occurs because the melt fraction remains below the critical melt fraction during the second melting phase, which peaks at $t \sim 1$ Gyr in this case (3.4c,d), and the difference in crustal thickness remains similar to the imposed initial difference in lid thickness (which is 2 km).

A large dichotomy occurs for a slightly higher viscosity ($\eta_0 = 2.55 \times 10^{20}$ Pa s) and lower permeability ($k_0 = 3.7 \times 10^{-11}$ m^2) and is referred to as the LargeDich case (solid lines on Figure 3.4). For a higher reference viscosity, the upper thermal boundary is thicker and the initial melt fraction smaller, the lid also grows more quickly on average. This, together with the lower reference permeability, results in a smaller initial crustal extraction phase than in the NoDich case. The lid does not limit crustal growth during the first extraction phase, allowing the initial perturbation to grow. The higher initial melt fraction in the Southern Hemisphere, caused by the initial perturbation, results in a larger initial crustal extraction there. The larger crustal growth in the South is then enhanced during the second melting phase associated with the rise in mantle temperature after $\sim$ 200 Myr ; it implies a larger addition of heat from HPEs and melts which decreases the conductive heat flux at the lid base, compensating for the decrease in the convective heat flux and stopping lid growth in the South (Figure 3.4d at $t \sim 300$ Myr). With continued melt extraction in the South, the crustal temperatures rise further, increasing the melt fraction at the lid base and finally inducing a thinning of the lid at $t \sim 500$ Myr. Cooling of the planet by convection manifests in the North, with a large increase in lid thickness, and by an effective cooling of the mantle (Figure 3.4a-b). These two extreme cases do not match InSight constraints on crustal thickness (Section 3.4.2).

Systematic exploration of the effects of η_0, k_0

We now describe a systematic exploration of the effects of the main controlling parameters of our model η_0 and k_0 (Figure 3.5). Generally, a lower viscosity induces a thinner boundary layer, resulting in higher melt fraction and crustal extraction rate and hence in a larger crustal thickness (Figure 3.5a-b). A lower reference viscosity η_0 also leads to a higher convective heat flux (2.7) which tends to induce colder present-day mantle temperatures (Figure 3.5d).

The crustal extraction rate increases with the reference permeability k_0 (2.19). But the largest crustal thicknesses are obtained for low reference permeability values (Figure 3.5, bottom left of a-b) because melt extraction is an efficient way to cool the convective mantle through the removal of HPEs and sensible heat ($q_{cr}^{N/S}$, Equation 2.21). Thus, lower values of k_0 tend to preserve heat and HPEs in the convective

mantle, to induce higher mantle temperatures and prolong crustal extraction, resulting in thicker crusts.

For reference viscosity values $< 10^{20.6}$ Pa s (Figure 3.5c), the thin lid induced by the low reference viscosity initially limits crust growth in both hemispheres. Since we start with a thicker northern lid ($\Delta D_l^0 = -2$ km), this even rapidly leads to a slightly thicker crust in the North as in the NoDich case (Figure 3.4 dashed-lines). If the permeability value is sufficiently large (i.e. larger than about $\gtrsim 10^{-10.5} - 10^{-9.5}$ m^2 depending on η_0), the initially large extraction rates of melts, and associated HPEs and sensible heat, from the convective mantle, strongly limits the duration of crust formation to the very early times, preventing the growth of a dichotomy in crustal thickness as in the NoDich case. However, if the reference permeability is low ($k_0 < 10^{-9.5} - 10^{-10}$ m^2), mantle melts and HPEs are retained in the mantle, prolonging mantle cooling. In that case, the retroactive feedback mechanism applies but inversely, the northern crust is thicker, which leads to a reverse dichotomy (the northern crust is thicker than the southern one, Figure 3.5c).

A larger reference viscosity value leads to a thicker lid and to a lower mantle melt fraction due to the pressure dependence of the solidus. This tends to generate more enriched melts and hence a larger crustal enrichment factor (Figure 3.5e, for $10^{20.5} < \eta_0 < 10^{21.3}$ Pa s), in particular for large reference permeability values that strongly limit the duration of crust construction. However, large reference viscosity values also lead to smaller convective heat fluxes, prolonged mantle cooling, higher mantle temperatures and larger melt fractions. This explains the opposite behaviour for reference viscosities larger than $\eta_0 > 10^{21.5}$ Pa s where the crustal enrichment factor then tends to decrease with increasing value of η_0.

Range of η_0, k_0 matching InSight constraints on crustal thickness

Two different ranges of values for (k_0, η_0) allow to match all three constraints on crustal thickness : average North and South crustal thicknesses as well as dichotomy amplitude (Section 3.4.2), each shown as black contours on the left panels of Figure 3.5. These two ranges (intersection of all black contours) are shown as purple contours on the right panels of Figure 3.5.

The first region is at rather low viscosity ($\eta_0 \sim 10^{20.5}$ Pa s) and large permeability $k_0 > 10^{-9.5}$ m^2. The simulation EarlyDich (solid lines in Figure 3.6) well illustrates the type of thermal evolution obtained for these ranges of values. The relatively high permeability induces an early and rapid (< 100 Myr) extraction of the crust (Figure 3.6c) during the initial phase of rapid lid growth (Figure 3.6b). The early extraction of melt and heat-producing elements causes rapid cooling of the convective mantle (Figure 3.6a) which induces a rapid decrease in mantle melt fraction, stopping crustal

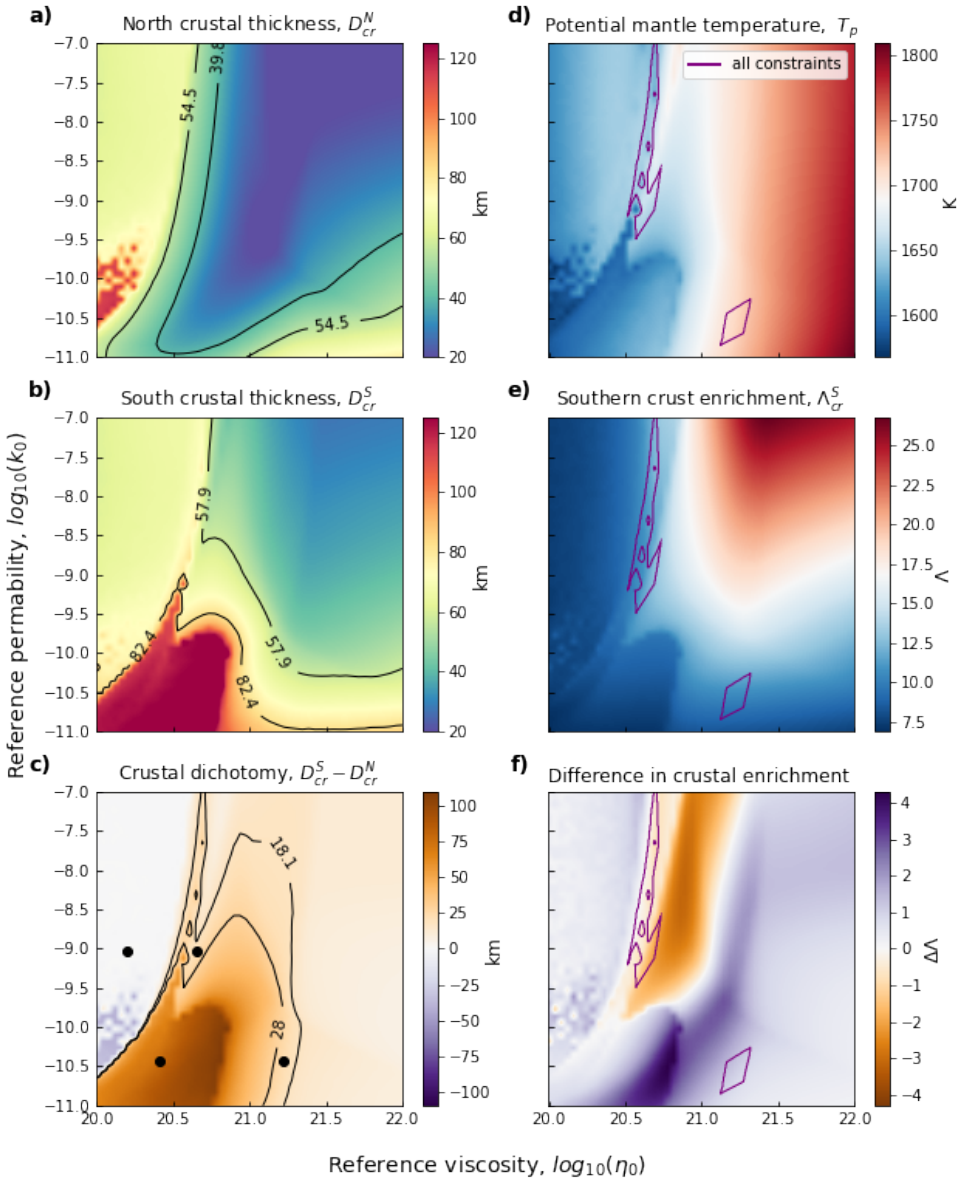

FIGURE 3.5 – Systematic exploration of (k_0, η_0) for our reference set of parameters (Table 2.1), with η_0 between 10^{20} and 10^{22} Pa s and k_0 between 10^{-11} and 10^{-7} m^2. (a) Final northern crust thickness, D_{cr}^N. (b) Final southern crust thickness D_{cr}^S. (c) Final amplitude of the crustal dichotomy $D_{cr}^N - D_{cr}^S$. (d) Present-day potential mantle temperature $T_p = T_m - \frac{\alpha g T_m}{C_m}(\bar{D}_l + \bar{\delta^u})$. (e) Present-day bulk southern crust enrichment factor Λ_{cr}^S. (f) Present-day difference in crustal enrichment $\Lambda_{cr}^N - \Lambda_{cr}^S$. The black curves on the left panels delimit the parameter space where each InSight constraint on crust thickness is met (See Section 3.4.2) and the intersection of these three spaces, i.e. the region where all 3 constraints are met, are represented by the purple curves on the right panels.

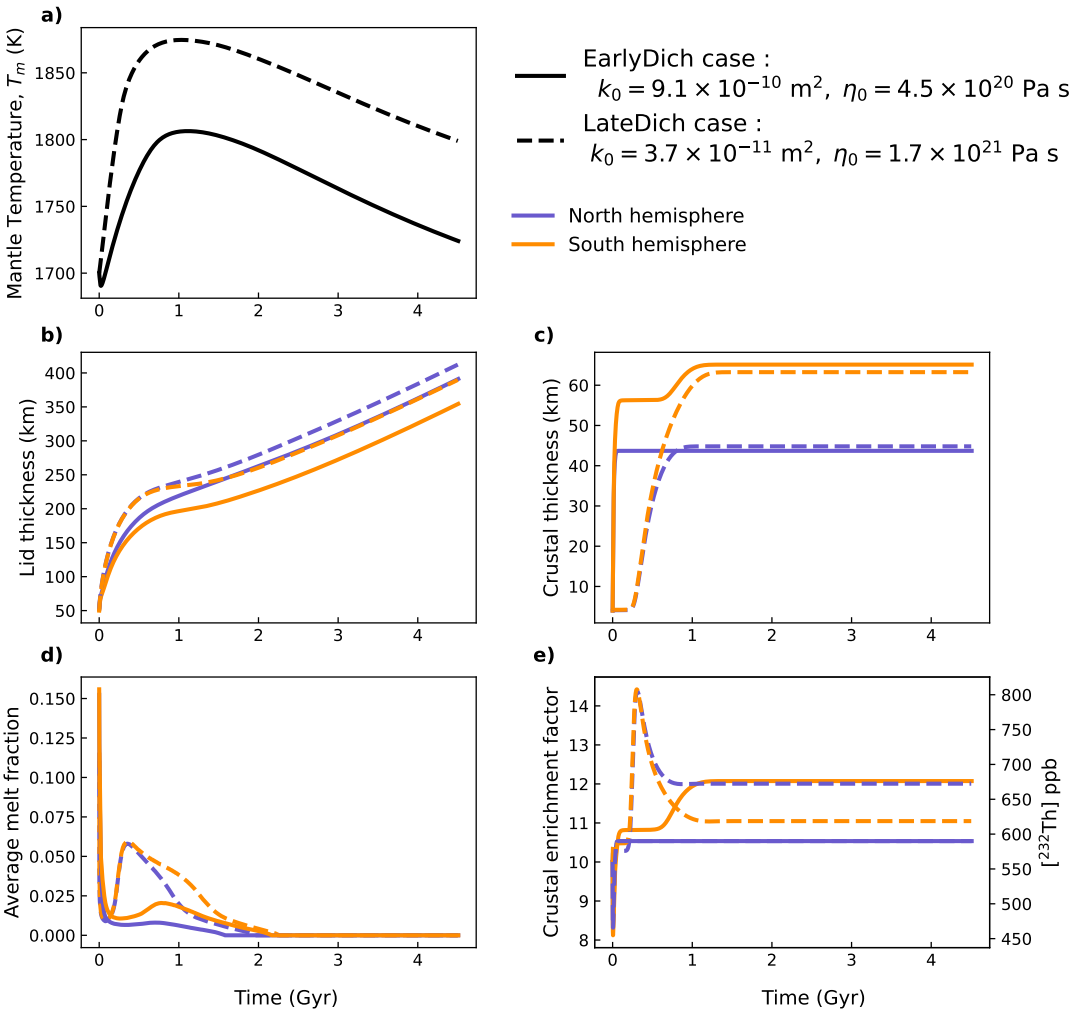

FIGURE 3.6 – Two types of thermal evolution for Mars matching InSight constraints on crust thickness : Evolution of (a) mantle temperature (b) lid thickness, (c) crustal thickness, (d) average melt fraction and (e) crustal enrichment factor in the North (blue lines) and in the South (orange lines) as a function of time. The evolution in solid lines is for a rather high permeability $k_0 = 9.1 \times 10^{-10}$ m^2 and low viscosity $\eta_0 = 4.5 \times 10^{20}$ Pa s and is associated with an early extraction of the crust (EarlyDich case). The evolution in dashed-lines is for a lower permeability $k_0 = 3.7 \times 10^{-11}$ m^2 and a higher viscosity $\eta_0 = 1.7 \times 10^{21}$ Pa s and is associated with a late extraction of the crust (LateDich case).

extraction in the North where the crust is thinner and the lid thicker. In the South, the melt fraction becomes significantly larger than in the North very early (because of the positive feedback mechanism and the early crustal extraction) ; this induces a larger and longer crustal extraction, generating a significant crustal dichotomy very early in Mars' evolution (in less than 100 Myr). The second phase of melting is large enough in the South for the second phase of crustal extraction to occur, which amplifies the crustal dichotomy. This second phase of extraction only occurs for permeability values that are low enough to retain sufficient heat-producing elements in the mantle, i.e. $k_0 \lesssim 10^{-8.5}$ m^2. In some rare cases, this second phase of extraction occurs in both hemispheres, but it is always more important in the South where the crust is thicker. The rather low viscosity leads to a relatively cold potential temperature at the present-day ($T_p \sim 1675$ K, Figure 3.5d).

The second region of parameters (k_0, η_0) that allows to match crustal thickness constraints is for a lower permeability of $\sim 10^{-10.6}$ m^2 and higher viscosity of $10^{21.2}$ Pa s (see case LateDich, dashed lines on Figure 3.6) ; it results in a higher present-day potential temperature ($T_p \sim 1750$ K Figure 3.5d). Because of the large viscosity value, the initial melt fraction is low, and the low permeability does not allow for a significant early crustal extraction during the initial phase of rapid lid growth (Figure 3.6b-c) ; heat-producing elements are thus preserved in the mantle and, together with the smaller convective heat flux caused by the higher viscosity, lead to a significant increase in melt fraction during the heating phase despite the thicker lid (Figure 3.6d). The melt fraction reaches values larger than ϕ_c in both hemispheres, allowing crustal extraction, although at a relatively low rate. This results in a late and prolonged extraction of the crust that occurs over ~ 700 Myr, from ~ 300 Myr to 1 Gyr (Figure 3.6c). Here again, the mantle melt fraction remains larger in the South because of the smaller lid growth rate, which results in a significantly larger crust in the Southern Hemisphere.

In both cases, the crust is extracted within the first billion years of Mars' evolution, but a significant melt fraction is preserved in the mantle over ~ 2 Gyr, i.e. up to 1 billion years after crust formation (Figure 3.6c). The final crustal enrichment is also similar in both cases : between 12 and 15, and corresponds to Thorium concentration in the crust of 672 to 840 ppb. North/South differences in crustal enrichment factors exist but remain small for both types of solutions (± 2, Figure 3.6e) and have different origins. In the case of an early extraction of the crust (EarlyDich), both crusts become progressively more enriched in HPEs as the melt fraction decreases during extraction (Figure 3.6c-d). The South is then more enriched by $\Lambda^S - \Lambda^N = 1.6$ which corresponds to a difference in Thorium concentration of 90 ppb because of its prolonged extraction. In the LateDich case, the South is characterised by higher melt fractions, less concentrated in HPEs (Figure 3.6d-e) which results in the northern crust being slightly more enriched in HPEs (by 60 ppb of Thorium).

3.5.2 Exploration of the effects of other model parameters

To well understand the effects of the different parameters on crust and dichotomy formation as well as on the location of the regions matching our crustal constraints in the parameter space (k_0, η_0), we perform a series of calculations centred on our reference case with (k_0, η_0) varying in the same range but changing the value of another single parameter at a time within a given range.

Effects of different model parameters on crustal formation

We first characterise the probability density distribution of the average crustal thickness $\bar{D}_{cr}$ and of the dichotomy amplitude ΔD_{cr} in our reference case (Figure 3.7a), for the same range of values (k_0, η_0) as for Figure 3.5. For this reference case (Figure 3.7a), the dichotomy amplitude is mostly distributed around low values with a peak at ∼12 km. Thinner average crustal thicknesses are more frequent, although two small peaks exist in the distribution around ∼64 and ∼90 km. These two peaks correspond respectively to the NoDich and LargeDich case, the latter giving a very thick southern crust, $D_{cr}^S > 100$ km.

The absence of a critical melt fraction for melt extraction (i.e. $\phi_c = 0$, Figure 3.7b) has a non-intuitive effect : although the melt volume available for extraction is higher, simulations tend to result in a thinner crust than in the reference case because the absence of critical melt fraction allows the extraction of melts highly enriched in heat-producing elements at low melt fraction. The convective mantle becomes more depleted in these elements, which reduces melting and leads to thinner crusts and smaller dichotomy amplitudes. The classical way to calculate the melt fraction with constant melt productivity, i.e. a linear evolution between the solidus and the liquidus (2.10), generates higher melt fractions than in our reference case ; inducing larger crustal growth rates, crustal thicknesses and dichotomy amplitudes (Figure 3.7c).

To ensure that the feedback mechanism we propose for the growth of the dichotomy is indeed linked to the enrichment of the crust in heat-producing elements, we perform a series of calculations where we remove different effects that strengthen this feedback. This is the case for the pressure-dependency of the viscosity which amplifies our positive feedback mechanism by two cumulative effects : i) a thicker lid grows faster because the convective heat flow at its base (q_{cm}, Equation 2.7) is reduced (2.42) and ii) a thicker boundary layer induces a lower melt fraction. Without this pressure effect ($V = 0$, Figure 3.7d) we obtain slightly smaller dichotomy amplitudes, as expected.

A lower thermal conductivity for the crust relative to the mantle also strengthens our feedback mechanism by inducing, in the same way as the crustal enrichment in HPEs, a higher temperature profile for a thicker crust. By imposing the same thermal conductivity for the crust and the mantle (i.e. $k_{cr} = k_m = 4$ W m^{-1} K^{-1}) the dichotomy amplitude is slightly reduced. The average crustal thickness is also reduced because we

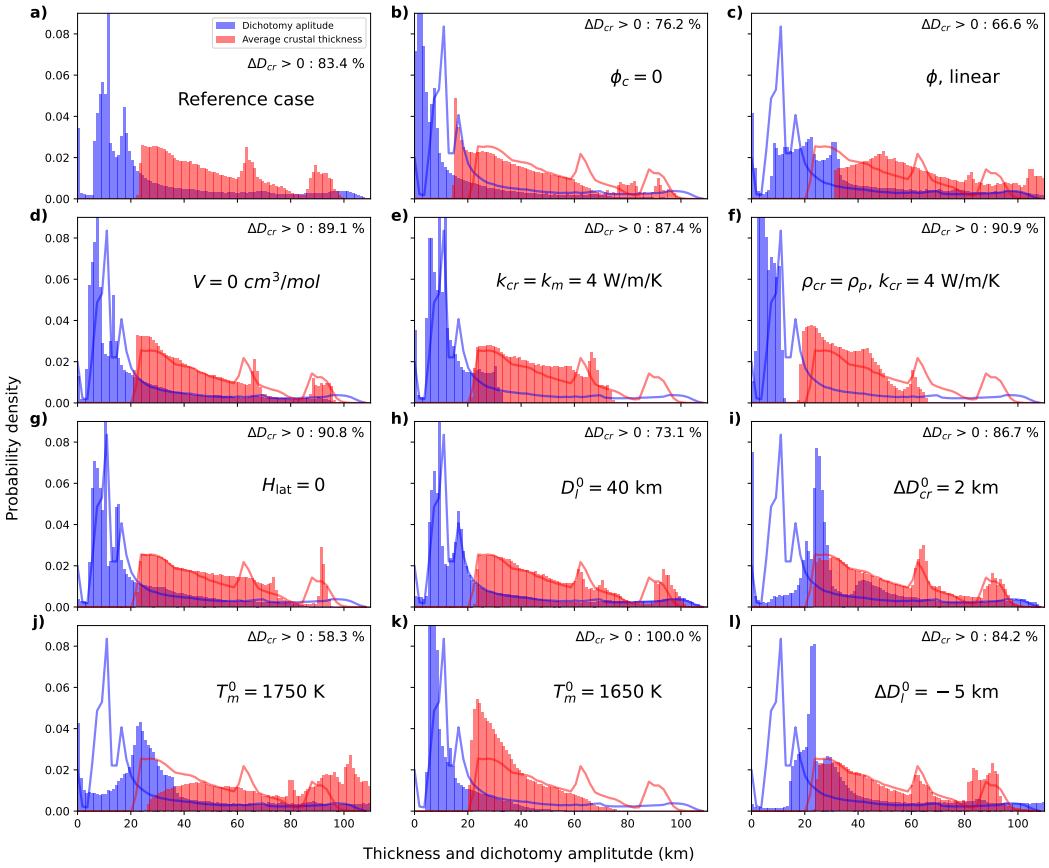

FIGURE 3.7 – a) Probability density distribution of the average crustal thickness (red histogram) and of the dichotomy amplitude (blue histogram) obtained for our reference case (Figure 3.5a-b-c). We only consider cases for which the final southern crust is thicker than in the North (i.e. positive dichotomy $\Delta D_{cr} > 0$). The percentage of runs with a present-day positive dichotomy amplitude is written at the top right of the plot ($\Delta D_{cr} > 0 = 83.5$ % for the reference case). The other subplots are the same as (a) but for a change in the value of only one parameter while the curves are the histogram envelopes of the reference case. (b) $\phi_c = 0$: no critical melt fraction for melt extraction. (c) $\phi = \phi_l$ linear : constant melt production between solidus and liquidus. (d) $V = 0$: no pressure dependency for the viscosity. (e) $k_{cr} = k_m = 4$ W m^{-1}K^{-1} : same thermal conductivity for the crust and the mantle. (f) $\rho_{cr} = \rho_p$, $k_{cr} = 4$ W m^{-1}K^{-1} : same density and same thermal conductivity for the crust and the mantle.(g) $H_{lat} = 0$ in (2.43) : no heat released by magmatism in the crust (h) $D_l^0 = 40$ km : thinner initial lid (i) $\Delta D_{cr}^0 = 2$ km and $\Delta D_l = 0$ initial perturbation in crust thickness instead of lid thickness. (j) $T_m^0 = 1750$ K : warmer initial mantle temperature. (k) $T_m^0 = 1650$ K : colder initial mantle temperature. (l) $\Delta D_l^0 = -5$ km, larger amplitude of the perturbation in lid thickness.

chose a larger value for the crust conductivity, favouring planet cooling and reducing melting ($D_{cr} \lesssim 75$ km, Figure 3.7e).

Another favourable effect is the thickening of the crust itself which reduces the pressure below the crust because of the lower density of the crust compared to the mantle. This also induces a higher melt fraction below a thicker crust. Keeping the same value of the thermal conductivity (as in Figure 3.7e) and of the density ($\rho_{cr} = \rho_m = \rho_p$) for the crust and mantle, we obtain a significantly lower average crust thickness ($D_{cr} \lesssim 65$ km). This is not only due to the higher pressure and larger surface heat flow (larger k_{cr}) but also to the higher extraction of energy and HPEs in the melt that both depend on crustal density (2.37-2.36). However, although smaller in amplitude, a significant dichotomy is still present ($2 \lesssim \Delta D_{cr} \lesssim 15$ km, Figure 3.7f).

The last effect that favours our feedback mechanism is the heating of the crust by magmatism which is more important where the crust thickens more rapidly. Cancelling the heating ($H_{\text{mag}} = 0$ in Equation 2.43, Figure 3.7g) leads to slightly smaller dichotomy amplitudes and limits the number of cases with very thick crusts.

We also explore the sensitivity of our results to the initial conditions. A warmer initial mantle temperature T_m^0 favours extreme cases of evolution similar to the NoDich and LargeDich cases because of the higher melt fractions (Figure 3.7j). Inversely, a colder mantle temperature gives less melting, thinner crusts, and smaller dichotomy amplitudes (Figure 3.7k). The variation of the initial core temperature plays in the same way as the initial mantle temperature, although its effect is less important. A lower initial lid thickness D_l^0 induces a larger initial amount of melt and hence thicker crusts (Figure 3.7h).

Finally, we investigate the amplitude and the nature of the initial imposed hemispherical perturbation. Imposing an initial difference in crustal thickness ($\Delta D_{cr}^i = 2$ km, Figure 3.7i) instead of a difference in lid thickness induces a larger average dichotomy amplitude. As expected, a larger initial perturbation in lid thickness ($\Delta D_l^i = 5$ km, instead of 2 km, Figure 3.7l) also generates larger dichotomy amplitudes than for the reference case ; however, it is still smaller than in the case of an initial crustal thickness perturbation. It is interesting to note that changing the amplitude of the initial perturbation in lid or crustal thickness has a negligible effect on the distribution of the average crust thickness (Figure 3.7l).

Effects of different model parameters on the range of k_0, η_0 matching our constraints

The range of (η_0, k_0) that matches InSight constraints on crustal thickness (purple contours on the right panels of Figure 3.5) depends on the value of all other model

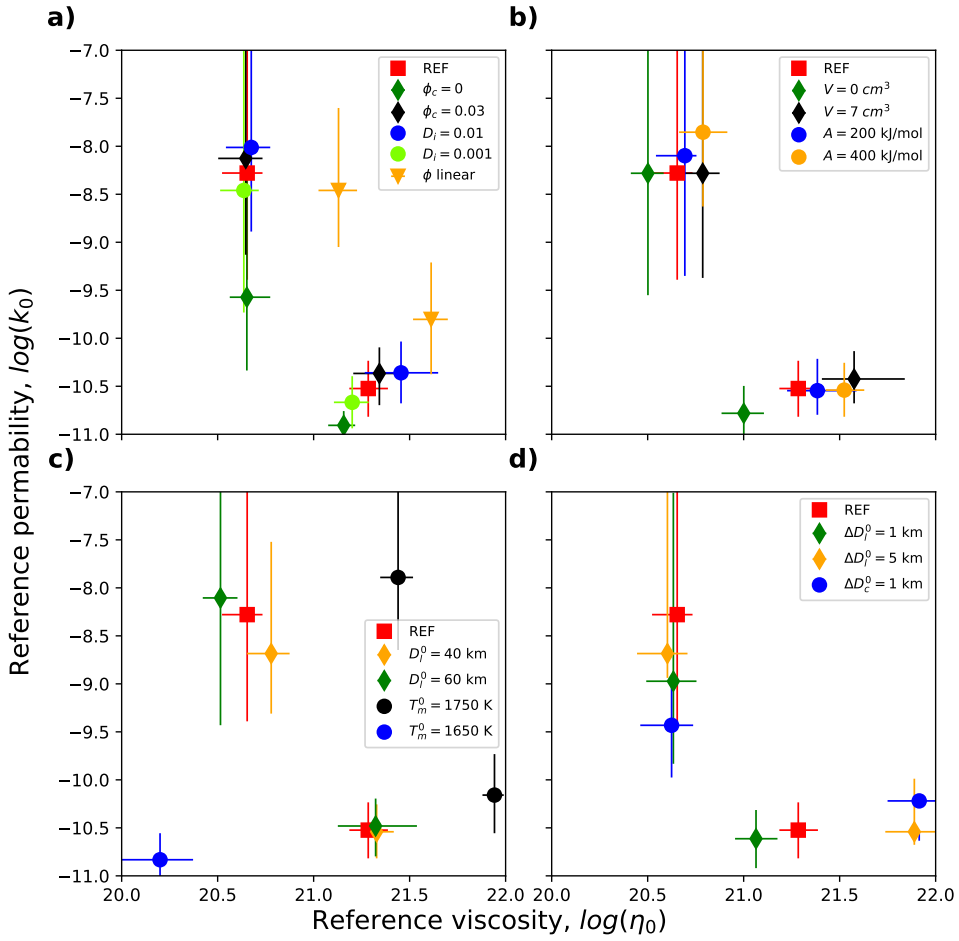

FIGURE 3.8 – Average position of the region of parameters matching InSight constraints on crustal thickness in the parameter space (k_0, η_0) for different values of the model parameters around our reference case noted 'REF' (red square). The value of the parameter that is being changed is indicated in the legend. The ranges are represented by a point, noting the average position, associated with horizontal and vertical bars indicating the minimum and maximum values of the reference viscosity η_0 and permeability k_0 allowing us to match our constraints. (a) Effect of the critical melt fraction $\phi_c = 0$ (green diamond) and 0.03 (black diamond) ; effect of the partition coefficient $D_i = 0.01$ (blue circle) and 0.001 (light green circle) ; effect of considering a constant melt productivity : ϕ linear (yellow triangle). (b) Effect of the activation volume $V =$ 0 cm^3 (green diamond) and 7 cm^3 (black diamond) ; Effect of the activation energy A = 200 kJ mol^{-1} (blue circle) and 400 kJ mol^{-1} (yellow circle) (c) Effect of the initial lid thickness $D_l^0 = 40$ km (yellow diamond) and 60 km (green diamond) ; effect of the initial mantle temperature $T_m^0 = 1650$ K (black circle) and 1750 K (blue circle). (d) Effect of the initial perturbation in lid thickness ΔD_l^0 = -1 km (green diamond) and -5 km (yellow diamond) ; effect of an initial perturbation in crust thickness $\Delta D_{cr}^0 = 1$ km (blue circle).

parameters. Here we investigate how these ranges shift in the space (k_0, η_0) following the modification of the value of a single parameter (Figure 3.8). In most cases, both regions (at either high permeability, low viscosity or at low permeability, high viscosity) are present and their associated thermal histories remain similar to the EarlyDich and LateDich cases (Figure 3.6).

The critical melt fraction ϕ_c and the partition coefficient D_i do not have a significant effect on the location of the region at low viscosity because the extraction occurs at high melt fraction and far from values of ϕ_c (0 to 0.03) (Figure 3.8a). However, the permeability must be significantly reduced if $\phi_c = 0$ for HPEs to be preserved in the mantle to obtain thick enough crusts (Figure 3.7b). The range at higher viscosity is shifted towards lower viscosity and permeability values as ϕ_c and D_i are reduced and inversely. For this range, melt extraction occurs at low average melt fractions and the melts are more enriched in heat-producing elements. Hence, as ϕ_c and D_i are reduced, the range of viscosity and permeability decreases to generate a larger melt fraction and slower extraction rate to preserve HPEs in the mantle and obtain thick enough crusts.

Using a constant melt productivity (i.e. a linear melt fraction ϕ_l) results in higher melt fractions and extraction rates. To mitigate this effect and match InSight constraints, the viscosity range is thus shifted to higher values to generate less melting (Figure 3.8a).

Crustal extraction occurs at pressures lower than the reference pressure ($P_0 = 3$ GPa). For pressure ranges characteristic of the top of the convective mantle, where crust extraction occurs, the viscosity is larger if V is larger (2.1). Hence, to alleviate this effect, the reference viscosity must be decreased as V increases and inversely (Figure 3.8b). The effect of the activation energy A is not straightforward as it plays not only on the absolute viscosity value but also on the thickness of the lid through its effect on the basal lid temperature (2.3). Larger activation energy results in larger viscosity and hence lower melt fractions, but it also leads to larger T_l values and hence thicker and hotter lids, promoting melting at depth. However, the effect of A, when varied within $\pm$ 100 kJ mol^{-1} is quite limited (Figure 3.8b).

A colder initial mantle temperature generates less melt and hence thinner crusts. Within the same range of values for (k_0, η_0), a single range of parameters match InSight constraints and is shifted to lower viscosity and permeability values (Figure 3.8c), towards the region where parameter values favour thicker crusts (see LargeDich case). Inversely, a warmer mantle induces more melt and requires larger viscosity values to form thinner crusts. A change in the initial lid thickness (D_l^0, Figure 3.8c) affects only the range at rather low viscosity where the crust and dichotomy form early (case EarlyDich) because it only modifies the initial melt fraction and therefore only plays in the initial phase of crustal extraction.

Varying the initial perturbation in lid thickness does not have much effect on the region at low viscosity (Figure 3.8d). For the high-viscosity region, if the perturbation is larger, the viscosity must be increased not to generate a too-large dichotomy (Figure 3.5c). The effect of an initial difference of 1 km in crustal thickness is similar to that of a -5 km difference in lid thickness (Figures 3.8d and 3.7l) because the perturbation in crustal thickness has a greater impact on dichotomy growth.

3.6 Discussion

3.6.1 Positive feedback mechanism

The positive feedback between crustal thickness and crustal growth allows forming a significant difference in crustal thickness between the Northern and Southern hemispheres of Mars for a large set of parameters (Figure 3.5c). This mechanism mainly results from the crustal enrichment in heat sources, which generates higher temperatures and hence more melting where the crust is thicker. The lower thermal conductivity of the crust relative to the mantle and the heat associated with magma intrusions also lead to higher temperatures in regions with thicker crust and facilitate this mechanism (Figure 3.7). Finally, the pressure dependence of the mantle viscosity creates a positive feedback between the stagnant lid thickness and lid growth through its effect on the convective mantle heat flow, strengthening the mechanism we propose (Figure 3.7d). Accounting for a dependence of the viscosity on the melt fraction would also play in the same way as the pressure dependence, enhancing this mechanism. Thus, this mechanism should apply not only on Mars but also possibly on other one-plate planets and should significantly promote crust growth wherever the crust is thicker early in the history of the planet. Through this mechanism, the dichotomy grows within $\sim$ 100 Myr to 1.1 Gyr depending on the scenario and initial thermal state of Mars (case EarlyDich versus LateDich).

3.6.2 Origin of the degree-one structure

Our linear stability analysis on a simplified setup shows that any thermal perturbation should grow with time and that the longest wavelengths (in particular the degree-one hemispheric perturbation) will be favoured (Section 3.2). With our numerical calculations, we have shown that the growth of an initially negligible perturbation can be significant even though planetary cooling ultimately stabilises our feedback mechanism and limits its growth. Lateral variations in temperature and chemical heterogeneities caused by accretion or mantle convection certainly exist early in the history of the planet and can provide initial perturbations of random wavelengths. The fact that the degree-one perturbation has the largest growth rate (Figure 3.3) suggests that it could grow the fastest and give rise to the observed dichotomy in crustal thickness through the positive feedback we describe. Therefore, this mechanism alone may ex-

plain the difference in crustal thickness between the northern lowlands and southern highlands of Mars.

Convection in a stagnant lid regime typically generates convection patterns and thermal perturbations of shorter wavelengths. Given that the dispersion curve of Figure 3.3 is rather flat at long wavelengths, it is not totally clear whether mantle convection could impose its pattern and the growth of shorter wavelengths than the degree one. Convection simulations in 2-3D considering two-phase melt extraction would be necessary to understand its effect on wavelength selection. Lateral melt transport in the lithosphere depends on its stress state (Michaut et al., 2020) and would then constitute another complicating factor.

On another hand, this mechanism might also significantly amplify any other mechanism that could independently generate large wavelength variations in lid or crustal thickness early in Mars history. Several studies have suggested that the dichotomy might originate from a degree-one mantle convection mode. (Zhong and Zuber, 2001; Roberts and Zhong, 2006) have for instance shown that a degree-one convection could develop because of viscosity stratification in the martian mantle. An upper low-viscosity layer could result from a partially molten layer of several hundreds of km thick with an average melt fraction of ~ 0.15 (Mei et al., 2002), which seems possible for early Mars in the frame of our thermal evolution model. The interaction and chemical exchange between a liquid magma ocean and the dense cumulates during magma ocean solidification could also trigger a degree-one convection mode in the cumulates (Morison et al., 2019). If such a degree-one indeed occurred during the late phase of magma ocean solidification, it could generate a degree-one perturbation in temperature and hence in lid thickness that could trigger the feedback mechanism we describe for the formation of the crustal dichotomy.

The most popular explanation for the Martian dichotomy is currently that of a large impact at ∼4.5 Gyr in the Northern Hemisphere (Marinova et al., 2008). Such a large impact would create a large difference in crustal thickness which would also trigger the mechanism we propose. Since this impact would have occurred at a time when significant melting occurs at depth, it is likely that the feedback mechanism would be strong and lead to very large differences in crustal thickness, potentially too large to match InSight constraints. Indeed, simulations show that initial differences in crustal thickness must be less than a few kilometres in order to fit observations (Figure 3.8).

3.6.3 Crust enrichment in HPE

Our model predicts a crust enrichment factor (Λ_{cr}) between 10 and 15 depending on the parameters and a possible North/South enrichment difference of ±2. This enrichment corresponds to a crustal Thorium concentration of $\simeq$ 560 to 840 ppb and a hemispheric difference of $\simeq$ 112 ppb. In the case of a rapid crust extraction (Early-

Dich), the bulk southern crust is more enriched than the North, and it is the opposite if crustal extraction is longer (case LateDich). The bulk Thorium concentration derived from GRS data is 620 ppb (Taylor et al., 2006) which is consistent with the crustal concentration predicted by our model (Figure 3.6e). Spatial variations of the Thorium concentration as deduced from GRS data tend to point to a Northern hemisphere slightly more enriched in HPEs than the South, which would be more consistent with our LateDich scenario. However, GRS data may not be representative of the bulk martian crust and observed spatial variations in Thorium concentration at the surface might as well be linked to surface weathering.

3.6.4 Melt extraction and formation of a crust of limited thickness

Although the Martian crust probably shows a significant difference in crustal thickness in between the North and South, InSight constraints (Wieczorek et al., 2022) suggest that its average bulk crustal thickness is not as large as suggested by some previous studies. Forming a limited amount of crust was rather challenging in previous thermal evolution studies (Morschhauser et al., 2011; Samuel et al., 2019; Knapmeyer-Endrun et al., 2021; Drilleau et al., 2021). In these studies, in order to limit melting, a significant amount in heat-producing elements had to be extracted from the mantle, pointing towards highly enriched crusts ($\Lambda_{cr} > 15$). However, previous studies considered a constant melt production (See Section 2.3.1) and a melt extraction rate parameterised from the convective velocity (Morschhauser et al., 2011; Samuel et al., 2019). Compared to our model, where the melt production is a non-constant function of temperature below $\sim 17\%$ melt and where melt extraction mainly occurs at the Darcy velocity (2.17), the model of (Morschhauser et al., 2011) leads to higher crustal extraction rates and hence thicker crusts for a given viscosity and initial thermal state. (Samuel et al., 2019) use the same model as (Morschhauser et al., 2011) but with a mantle viscosity decreasing with increasing melt fractions. At a given thermal state and reference viscosity, a higher Rayleigh number is thus obtained, leading to a thinner boundary layer and lid thickness and hence to higher melt fractions and crustal extraction rates. As a result, in order to produce an average crustal thickness of $\sim 40 - 70$ km, (Samuel et al., 2019) point towards higher viscosity values (of order $10^{22} - 10^{23}$ Pa s) and (Morschhauser et al., 2011) to colder initial thermal state ($T_m^0 \sim 1600$ K) than in our study.

3.6.5 Crust construction and volcanism on Mars

Our two different scenarios allowing to match InSight constraints (LateDich and EarlyDich) point towards different histories of crust construction (Figure 3.6c-d). The LateDich scenario predicts a late and single-long extraction of melt at a low melt fraction that would therefore be rather uniform chemically. On the contrary, the EarlyDich scenario predicts two different phases of extraction, the first one at a high melt frac-

tion and extraction rate in the early Noachian (<100 Myr) followed by a second one generating a peak in volcanism and crust thickening that would occur at a low melt fraction in the Hesperian ($\sim$ 3.7 Gyr, Figure 3.6).

Orbital spectroscopy in the different volcanic provinces suggests a difference in composition, in terms of low-Calcium and high-Calcium pyroxene (LCP versus HCP) content, in between the early Noachian terrains and Hesperian ones (Baratoux et al., 2013). In particular, Noachian terrains show high LCP over HCP ratios (Sautter and Payre, 2021; Baratoux et al., 2013) suggesting partial melt fractions close to pyroxene exhaustion (which occurs at $\sim$ 17%, Section 2.3.1). This early volcanism may have taken place during the final, mushy, stage of magma ocean solidification, after the rheological transition to solid-like convection, where the magma evolves chemically and its buoyancy increases ; it would correspond to the extraction of a primary crust from a primitive mantle. On the contrary, the LateDich case does not allow for high melt fractions and early extraction of the crust favourable to LCP-rich rocks.

A change in the sedimentary record from clay-dominated sedimentary rocks to sulfate-dominated rocks is observed in the Hesperian, requiring a large and rapid input of sulfur into the Martian atmosphere (Bibring et al., 2006) which could be explained by a peak in volcanism that is only predicted in the EarlyDich scenario. Hesperian terrains show lower LCP over HCP ratios (Poulet et al., 2009), pointing to lower melting degrees, as expected during the second melt extraction phase in the EarlyDich case. The increase in dichotomy amplitude expected at this peak may also explain the Hesperian tectonic structures present around the dichotomy boundary (McGill and Dimitriou, 1990).

Finally, we note that in all our simulations matching InSight crustal constraints, the most recent phase of melt extraction occurs in the Southern Hemisphere where the crust is thicker (Figure3.6c-d) while observations show that the Northern Hemisphere has been resurfaced more recently than the South. None of the other proposed mechanisms for the dichotomy neither explains the relatively young age of the Northern Hemisphere. Resurfacing of the northern lowlands is in fact not only volcanic in origin as it also comes from the erosion of the highlands and subsequent deposition. The geological map of (Tanaka et al., 2014) shows that the lowlands are divided into various units of three different origins : (i) a recent glacial or periglacial origin close to the North Polar Cap, (ii) a fluvial, lacustrine or marine origin that could be explained by a circumpolar ocean at the end of the Hesperian, a controversial hypothesis supported by (Schmidt et al., 2022), (iii) a volcanic origin concentrated around the Elysium and Tharsis formations. These volcanic eruptions are characterised by low LCP over HCP ratios, i.e. originate from rather low melting degrees (Farrand et al., 2011; Mangold et al., 2010), and were probably caused by decompression melting in large mantle plumes such as the one giving rise to Tharsis and Elysium. This volcanism cannot be predicted by our simple parameterised model.

3.6.6 Insight results on Mantle structure

Travel-time inversions for different seismic phases associated with teleseismic events recorded by SEIS on Mars suggest that the thickness of the lid, or the upper thermal boundary layer (i.e. lithosphere plus mobile thermal boundary layer) is between 400 and 600 km and also predict a rather cold present-day mantle potential temperature of $1600 - 1700$ K (Khan et al., 2021; Stähler et al., 2021). This range of thicknesses is in good agreement with our results : the value of $D_l + \delta_u$ reaches for instance 552 km in the EarlyDich case, where $\delta_u = 133$ km at the present-day, but they do not constrain our thermal evolution any more than the crustal constraints. The rather cold potential temperature is in line with the EarlyDich case (Figure 3.5d). (Drilleau et al., 2022) also used an inversion of the arrival time data with geodynamic constraints and found similar lid thicknesses but with a somewhat warmer potential mantle temperature of 1830 ± 60 K which is in better agreement with the LateDich scenario. However, the compositional model of (Drilleau et al., 2022) is less enriched in HPEs than the one we consider in this study which favours higher initial and hence final temperatures. The detection of the postolivine phase transition at depth provides additional constraints on the thermal state and chemistry of the martian mantle which also points to a rather cold mantle at the present-day with $T_p = 1605 \pm 100$ K (Huang et al., 2022). But uncertainties on these values do not allow to further constrain our thermal evolution scenario.

3.6.7 Interpretation of Bouguer anomalies in terms of crustal thickness

As the thermal profile in the lithosphere is warmer in the Southern Hemisphere, the mantle density should be slightly lower than in the colder Northern Hemisphere which should lead to a negative Bouguer gravity anomaly in the South that is not accounted for in Bouguer anomaly's inversions. This negative mass anomaly due to the hotter temperature profile in the southern lid leads to an increase in the apparent crustal thickness deduced from these inversions. We estimate the equivalent additional crustal thickness Δh_{cr} by equating the mass anomaly it generates to that due to the hotter temperature profile in the South :

$$\int_{\mathrm{R_l^N}}^{\mathrm{R_p}} \alpha_m \rho_m (T(r)^{\mathrm{S}} - T(r)^{\mathrm{N}}) 4\pi r^2 dr = (\rho_m - \rho_{cr}) \Delta h_{cr} 4\pi R_p^2, \tag{3.10}$$

where we use $T^S(R_l^N < r < R_l^S) = T_l$ in order to estimate only the effect of the North/South temperature difference in the lid and to avoid any effects due to the convective mantle. Using $\alpha = 2 \times 10^{-5}$ K^{-1}, we obtain $\Delta h_{cr} \sim 2.24$ km in the EarlyDich case. This value is small, although not necessarily negligible, and corresponds to $\sim$ 10-15% of the dichotomy amplitude.

3.7 Summary

The positive feedback mechanism between crustal growth and mantle melting that we propose, where a thicker crust grows faster, is able to produce the observed dichotomy in crustal thickness between the northern lowlands and southern highlands on Mars without a giant impact or persistent degree-one mantle convection mode. This mechanism is favoured by the higher enrichment of the crust in heat sources compared to the mantle, the lower thermal conductivity of the crust, magma intrusions in the crust, as well as by the pressure-dependence of the mantle viscosity. Our parameterised, bi-hemispherical thermal evolution model of Mars includes new features such as a Darcy velocity for mantle melt extraction, non-constant melt production at low melt fractions and evolving enrichments in heat-producing elements in the crust, lithospheric mantle and convective mantle. Our study points to two different types of thermal evolution that allow fitting InSight constraints on crustal thickness : an early and fast crustal extraction followed by a late phase of crustal extraction in the South or a late and progressive crustal extraction and dichotomy formation. The early scenario appears to fit several observations and constraints, including a widespread peak in volcanism together with a change in the crust composition at the Hesperian and a rather cold mantle potential temperature today.

Chapitre 4

Asymmetric vs Symmetric thermal evolution

4.1 Introduction

In this chapter, we focus on the geometry of our parametric thermal evolution model. Parametric models are classically used in a spherically symmetric geometry while we use here an asymmetric version with two hemispheres. An asymmetric model is useful to study the growth of a hemispheric dichotomy as on Mars, but one may ask if and how asymmetric and symmetric models diverge in their thermal evolution. In this chapter, we shall demonstrate the nonlinear nature of our thermal evolution model, meaning that the symmetrical case is not equivalent to the average of the asymmetrical one. Taking into account two hemispheres generates a difference in thermal evolution for the same set of model parameters as in the symmetric case. We examine the difference between both geometries in terms of present-day crustal thickness, mantle temperature or heat-producing elements content of the crust, and evaluate when these differences are significant or, on the contrary, when they are negligible.

When these differences are significant, they would imply that lateral variations in crustal thickness, as the hemispherical dichotomy, are important to account for the thermal evolution of stagnant lid planets and that asymmetric parametric models may be useful to properly calculate the thermal evolution of stagnant lid planets with strong hemispherical variations in crustal thickness, like Mars.

To study these differences we use two complementary methods. First, a systematic exploration of the two main parameters of our model, which define our two dimensionless numbers, the reference viscosity (η_0) and the reference permeability (k_0). This systematic exploration for both geometries allows to compare the results of the two models for the same parameters space. Second, we perform two inversions of our model using a Bayesian approach with a Monte Carlo Markov chain sampling algorithm, one for each geometry. A Bayesian inversion produces a distribution of models whose

outputs correspond to the observations. By comparing the distributions of models obtained for the two geometries, we can highlight the relevance of an asymmetric model to explaining the current Martian structure.

4.2 Observations

Observations from the InSight mission have better constrained the structure of the Martian crust and the thermal state of the mantle. In this section, we describe the current structure of Mars, the average thickness of its crust, the amplitude of its dichotomy and the thermal state of the mantle as deduced from InSight data. We then use these descriptions in the rest of this Chapter to see how our model, in its asymmetric or symmetric geometry, is able to reproduce them.

4.2.1 Crustal thickness and dichotomy amplitude

The present-day average thickness of the crust and amplitude of the dichotomy are two critical outputs of our model that can be compared to observations from InSight.

Data set

Constraints on crustal thicknesses are provided by Martian crustal thickness maps (Knapmeyer-Endrun et al., 2021; Wieczorek et al., 2022). These crustal thickness maps are obtained using gravity and topography fields. Crustal thickness variations are obtained by assuming that the Bouguer anomaly is entirely due to relief at the crust-mantle interface (Wieczorek, 2015). The crust thickness at a given location, defined by an independent method, then serves as an anchor point to obtain absolute crustal thickness values from lateral variations. Local crustal thickness estimates below InSight deduced from receiver function analysis served as an anchor point to these inversions (Knapmeyer-Endrun et al., 2021; Durán et al., 2022b; Joshi et al., 2023). These crustal thickness models depend mainly on 3 parameters : the density of the crust (ρ_{cr}), which is considered homogeneous in this study, the density of the upper mantle (ρ_m) which depends on the assumed mantle compositional and mineralogical model, and the local crustal thickness at the InSight landing site ($D^{\mathrm{gra}}_{\mathrm{InS}}$).

Here, we use the results of 1833 crustal thickness models built from different combinations of these three parameters, with crustal densities ρ_{cr} between 2550 and 3150 kg m^{-3}, mantle densities ρ_m between 3350 and 3500 kg m^{-3}, which correspond to different types of mineralogical models detailed in Wieczorek et al. (2022, Table 2) and crustal thicknesses below InSight between 37 and 47 km. From each calculation of the crustal thickness, we extract the global average thickness of the crust (D^{gra}_{cr}) and the difference in average thickness between the Lowlands and the Highlands ($\Delta D^{\mathrm{gra}}_{cr}$), where we use the dichotomy boundary proposed by Andrews-Hanna et al. (2008a).

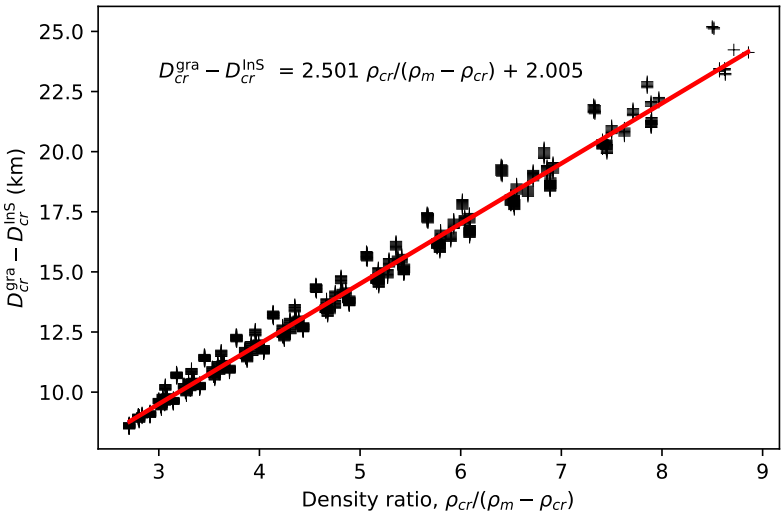

FIGURE 4.1 – Difference between the average crustal thickness calculated from Bouguer anomaly inversions and the assumed local crustal thickness below the InSight station as a function of the density ratio between the crustal density and the mantle-crust density contrast. The red line corresponds to the linear regression whose expression is given in the graph.

Crustal thickness

The average crustal thickness predicted from crustal thickness models (D_{cr}^{gra}) depends mainly on two parameters : the crustal thickness below InSight ($D_{\mathrm{InS}}^{\mathrm{gra}}$) and the ratio between the crustal density and the density contrast between the mantle and the crust $\frac{\rho_{cr}}{\rho_m - \rho_{cr}}$. In our thermal evolution model, the density of the crust is prescribed as a model parameter and the density of the mantle increases with the growth of the crust (Equation 2.38), but this increase is slight. Figure 4.1 shows the difference between the average crustal thickness calculated from crustal thickness models and the assumed local crustal thickness below InSight, as a function of the density ratio : a strong correlation exists between these two quantities (Figure 4.1).

A linear regression gives :

$$D_{cr}^{\mathrm{gra}} - D_{\mathrm{InS}}^{\mathrm{gra}} = a_{\mathrm{thick}} \left(\frac{\rho_{cr}}{\rho_m - \rho_{cr}} \right) + b_{\mathrm{thick}}, \tag{4.1}$$

with a slope $a_{\mathrm{thick}} = 2.501$ km and a y-intercept $b_{\mathrm{thick}} = 2.005$ km ; the correlation coefficient (r^2), equal to 0.998, confirms the very strong linear correlation (Figure 4.1). This relationship can be used to predict a theoretical thickness below InSight ($\mathbf{D_{InS}^{calc}}$) from the outputs and parameters (present-day average crustal thickness and density ratio) of a given thermal evolution model, to be compared with observations from InSight :

$$\mathbf{D}_{\mathbf{InS}}^{\mathrm{calc}} = D_{\mathrm{cr}}^{\mathrm{calc}} - a_{\mathrm{thick}} \left(\frac{\rho_{cr}}{\rho_m - \rho_{cr}} \right) - b_{\mathrm{thick}}. \tag{4.2}$$

The local crustal thickness below the InSight lander has indeed been estimated using receiver function analysis applied to P and S waves. The most recent works of Durán et al. (2022b) and Joshi et al. (2023) estimate it to be between 37 and 47 kilometres, which we write :

$$D_{\mathrm{InS}}^{\mathrm{SEIS}} \; = \; 42 \; \pm \; 5 \text{ km}. \tag{4.3}$$

For each thermal evolution model, we thus predict a thickness below InSight as a function of the density of the crust (input parameter), the density of the mantle and the thickness of the crust (model outputs). The mantle density calculated in our model is a volume average, but in the Bouguer anomaly inversions, it is the density at the crust-mantle interface that is used. The difference between the density at the top of the mantle and the average density depends on the mineralogical model. This difference is between 50 and 200 kg m^{-3} depending on the model. For simplicity, we subtract 100 kg m^{-3} from the mean value.

Dichotomy amplitude

The difference in north-south crustal thickness obtained from Bouguer anomaly inversions is plotted for each inversion as a function of the same density ratio (Figure 4.2). We recall that a homogeneous crustal density is assumed for the whole crust.
A linear regression performed between the dichotomy amplitude and the density ratio shows a very strong linear correlation with a correlation coefficient of $r^2 = 0.999$. We thus express the expected north-south crustal thickness difference as follows :

$$\Delta D_{cr}^{\mathrm{gra}} = D_{cr}^{S} - D_{cr}^{N} = a_{\mathrm{dich}} \left(\frac{\rho_{cr}}{\rho_m - \rho_{cr}} \right) + b_{\mathrm{dich}}, \tag{4.4}$$

with a slope $a_{\mathrm{dich}} = 3.447$ km and a y-intercept $b_{\mathrm{dich}} = 2.858$ km.

Assuming isostatic compensation, for an Airy model, the north-south difference in crustal thickness (ΔD_{Airy}) would be given by :

$$\Delta D_{\mathrm{Airy}} = h \left(\frac{\rho_{cr}}{\rho_m - \rho_{cr}} \right) + h, \tag{4.5}$$

with h the topography difference between the northern and southern hemispheres. Assuming that $h = a_{\mathrm{dich}} = 3.447$ km, which corresponds fairly well to the topographic data (Andrews-Hanna et al., 2008a), we obtain the red curve in Figure 4.2. A simple isostasy model can therefore correctly explain the difference in crustal thickness between north and south (Wieczorek and Zuber, 2004; Wieczorek, 2015).

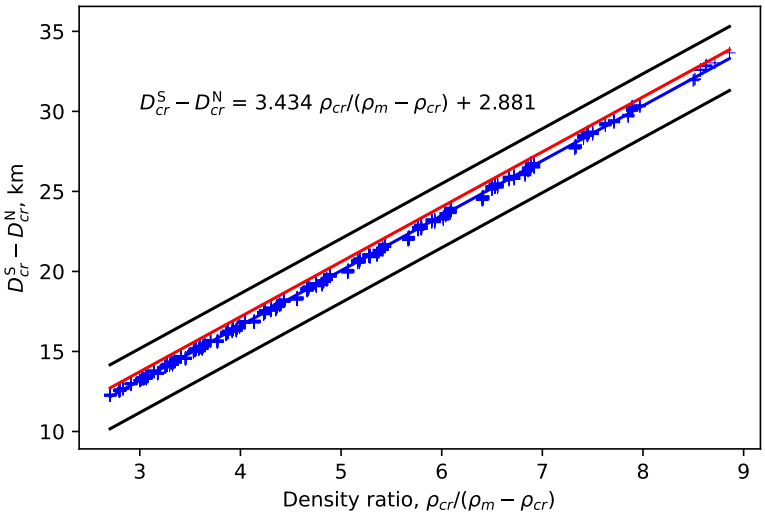

FIGURE 4.2 – North-South difference in crustal thickness calculated from Bouguer anomaly inversions as a function of the ratio between the crustal density and the density contrast between mantle and crust and where we consider the North-South boundary of Andrews-Hanna et al. (2008a). The blue line corresponds to a linear regression on the data points, its expression is given on the graph. The black lines correspond to a deviation of 2 km from this linear fit. The red curve shows the difference in crustal thickness assuming Airy isostasy and a Highland topography of $h = 3.447$ km.

4.2.2 Present-day thermal state of the Martian mantle

Mantle potential temperature

The mantle potential temperature corresponds to the temperature at the top of the convective mantle (T_m) projected to the planet's surface along the isentropic temperature gradient over the conductive layer thickness, sum of the lid thickness plus upper boundary layer thickness ($D_L = D_l + \delta_u$) :

$$\mathbf{T}_{\mathbf{p}}^{\text{calc}} = T_m - \frac{\alpha g T_m}{C_m}(D_l + \delta_u). \tag{4.6}$$

The range of pressure in the Martian mantle is sufficient for the phase change of olivine to wadsleyite (its higher pressure polymorph) to take place. This phase change generates a mid-mantle seismic discontinuity whereby the seismic velocity gradients significantly increases, generating seismic triplication. Huang et al. (2022) constrained the depth of this mantle transition zone to 1006 $\pm$40 km from the detection of triplicated P and S waves in five Martian teleseismic events. From this depth, we can deduce the pressure at which the phase change takes place and, for a given composition, estimate the temperature of the phase change. Taking into account the uncertainty in mantle chemistry, Huang et al. (2022) estimated a mantle temperature between 1670 and 1892 K at the depth of the phase transition. As this phase transition occurs in

the convective mantle assumed well-mixed, this temperature is projected along the isentropic gradient to provide a range for the mantle potential temperature of :

$$T_p = 1605 \ \pm 100 \text{ K}, \tag{4.7}$$

where the standard deviation includes the uncertainty in the depth and the uncertainty in the mineralogical model.

Average Thermal Lithosphere thickness

The total conductive layer thickness, which we define as the thermal lithosphere thickness, ($\mathbf{D_L^{calc}} = D_l + \delta_u$), is more difficult to constrain from seismology as it is not a lithological boundary but a thermal boundary. The conductive layer thickness is defined by the change in slope in the temperature profile between a conductive gradient and an isentropic gradient. The base of the thermal lithosphere also corresponds to the base of a low-velocity zone for seismic waves. Detecting this low-velocity zone by arrival-time analysis provides a direct measure of the thickness of the thermal lithosphere. Khan et al. (2021) found a thermal lithosphere thickness between 400 and 600 km. The more recent study of Durán et al. (2022b) proposes a value of 450 km with no standard deviation. We use a standard deviation of ±100 km, which is the difference between 400 and 600 km and 450 as a mean value :

$$D_L^{\text{avg}} = 450 \ \pm 100 \text{ km}. \tag{4.8}$$

4.3 Systematic exploration

4.3.1 Exploration method

For each geometry, we carry out two systematic parameter explorations, one with crust extraction and one where the crust thickness is fixed at the start of the thermal evolution and there is no further extraction.

With crustal extraction

For the symmetric and asymmetric systematic explorations considering crustal extraction, we use the complete model, which includes downward advection (Equation 2.23) caused by crust growth, magmatism (Equation 2.25) and crustal melting (Equation 2.31). We use the same parameter values as for the reference case of Chapter 3. The values of all the parameters used for this exploration are given in Table 2.1. We use an extended range of values for both the reference viscosity, varying from 10^{19} to 10^{22} Pa s, and the reference permeability, varying between 10^{-12} and 10^{-7} m^2.

Without crustal extraction

In the case without crust extraction, k_0 is set equal to 0 to ensure zero crust extraction (Equation 2.19 & 2.17). In these cases, there is no downward advection of the crust or magmatism, but there may be crustal melting. The range for the reference viscosity is the same as when considering crustal extraction, from 10^{19} to 10^{22} Pa s, and since k_0 is zero, different average crustal thicknesses are explored instead, ranging from 45 to 80 km. For the asymmetric case, the initial dichotomy amplitude is set to increase with the initial average thickness of the crust. This consideration is based on the two linear relations defined in Section 4.2. Equation 4.1 can be used to express the density ratio as a function of the average crustal thickness and the thickness below InSight, and this ratio can be substituted in Equation 4.4 to obtain the following equation :

$$\Delta D_{cr}^{0} = \frac{a_{\text{dich}}}{a_{\text{thick}}}(D_{cr}^{\text{gra}} - D_{\text{InS}}^{\text{gra}} - b_{\text{thick}}) + b_{\text{dich}}, \tag{4.9}$$

where we use $D_{\text{InS}}^{\text{gra}} = 42$ km, the average value obtained from seismology (Equation 4.3). The initial thickness of the lid is set to 100 km so that the lid is always thicker than the crust, even in the Southern Hemisphere.

Symmetric cases

The symmetric computations are obtained by imposing an initial North-South difference in lid thickness of zero ($\Delta D_l^0 = 0$ km) and a fraction of Northern lowlands (f) equal to 0. This is not optimal from a computational time point of view as each hemisphere is computed twice to obtain the same result, but the development time of a code that can do both the symmetric and the asymmetric case is much higher than the additional computation time. In the future, the *1PIECE* code should be able to do both geometries in an optimal way.

Range of thicknesses that fits the constraints.

To define the acceptable range of crustal dichotomy amplitude, we calculate the crustal thickness difference from Equation 4.4 that corresponds to the minimum and maximum density ratio of the data set. In the end, the amplitude of the crustal dichotomy ranges between 12.2 and 33.7 km, which is a slightly wider range than in Chapter 3 (between 18.1 and 28 km).

To define an acceptable range of average crustal thickness, we use the mean value of the crustal thickness below InSight 42 km (Equation 4.3) and calculate the crustal thickness value for the minimum and maximum density ratio of the data set from Equation 4.1. We obtain a range of average crustal thickness between 50.4 and 67.2 km, which is a slightly smaller range than in Chapter 3 where we considered the range 51-70 km.

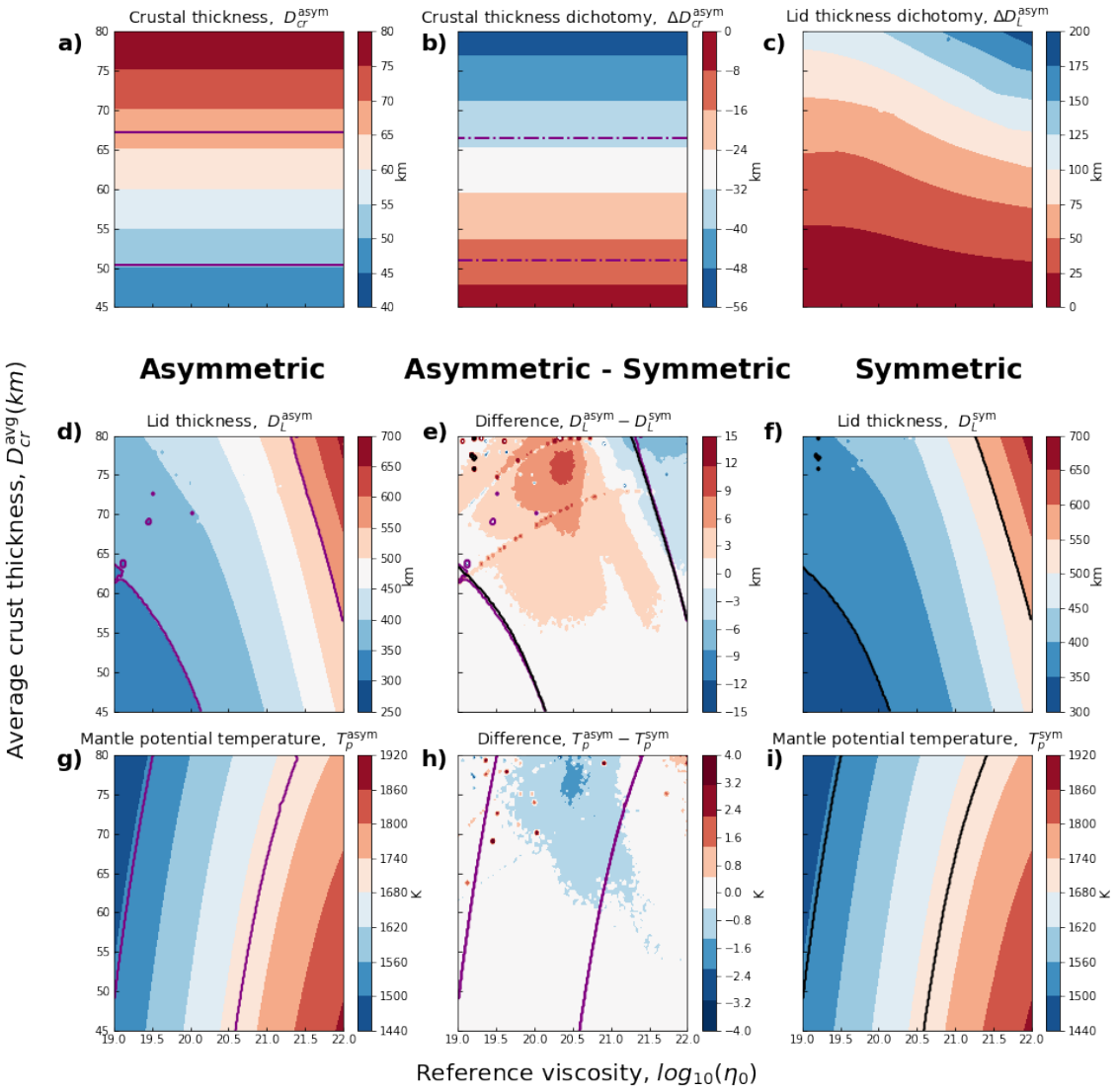

FIGURE 4.3 – Comparing asymmetric and symmetric geometries for a systematic exploration over D_{cr}^{avg}, η_0 in the case without crustal extraction. (Table 2.1). η_0 (x-axis) is between 10^{19} and 10^{22} Pa s and D_{cr}^{avg} (y-axis) is between 45 and 80 km. (a) Average crustal thickness for both geometry. (b) dichotomy in crustal thickness in the asymmetric geometry. (c) dichotomy in thermal lithosphere thickness in the asymmetric geometry ($\Delta D_L = D_L^N - D_L^S$) (d, f) Average thermal lithosphere thickness ($D_L = D_l + \delta_u$). (g, i) The potential temperature of the mantle at present-day (Equation 4.6). The left-hand side plots (d, g) are for the asymmetric geometry, the right-hand (f, i) side plots are for the symmetric geometry and the middle plots (e, h) are the difference between both geometries (asymmetric - symmetric). The purple outlines on (a,b,d,g) show the range of parameters that fit the constraints (Sections 4.2) in the asymmetric case. The black outlines on (f, i) show the range of parameters that fit the constraints in the symmetric case. The dashed-dotted outline on (b) shows the range of parameters that fit the dichotomy amplitude for the asymmetric case ($12.2 < |\Delta D_{cr}| < 28$ km).

4.3.2 Exploration results

Systematic exploration without crustal extraction

Results without crustal extraction are illustrated in Figure 4.3. The average crustal thickness is between 45 and 85 km, which, in the asymmetric case corresponds to a dichotomy amplitude between 0 and 56 km (Equation 4.9, Figure 4.3a-b). The dichotomy in lid thickness at present-day increases mainly with the amplitude of the crustal dichotomy but also slightly with the reference viscosity (Figure 4.3c). Growth rates are larger at higher viscosities, so the difference between the two hemispheres grows faster, resulting in wider differences in thickness.

Variations in thermal lithosphere thickness and mantle potential temperature are similar in both geometries (Figure 4.3d-i) : the lithosphere thickness increases with the crustal thickness and the viscosity while the mantle potential temperature increases with the viscosity and decreases with the crustal thickness. The thicker the crust, the larger the depletion of the mantle in radioactive elements, the colder the mantle temperature and the larger the lithosphere thickness is. A lower viscosity results in a higher convective heat flow, a colder mantle and a thinner conductive layer thickness (to balance the larger heat flow).

Differences between the two geometries are small, of the order of a few per cent, but increase with the amplitude of the crustal dichotomy (Figure 4.3e). They are the largest for dichotomy amplitudes larger than ∼30 km, corresponding to crust thicker than ∼ 67 km (Figure 4.3a-b). In general, the mantle cools a little more efficiently in an asymmetric geometry. Indeed, with an asymmetric geometry, the convective heat flow is stronger in the south, where the lid (D_l) is thinner, because of the pressure-dependence of the viscosity (Figure 4.4, left panel). In general, the increase in convective heat flux where the stagnant lid is thinned exceeds the decrease in convective heat flux where the lid is thickened. Furthermore, the larger heat flow applies on a larger surface area (larger radius at the base of the lid where the lid is thinned) and inversely, in the north, the convective heat flow is weaker but applies over a smaller surface area (Figure 4.4, right panel). This non-linear effect tends to induce a general cooling of the interior from the overall increase in heat loss (Equation 2.39), and hence a lower present-day mantle potential temperature and a thicker lid on average in the asymmetric case compared to the symmetric one.

This explanation works well at low viscosity ($\eta_0 \lesssim 10^{21}$ Pa s), but as the viscosity increases ($\eta_0 \gtrsim 10^{21}$ Pa s), another non-linear effect starts to take over. At larger viscosity, and larger pressure, the difference in heat flow between the two hemispheres decreases (Figure 4.4, left panel) and the effect described above decreases in amplitude (Figure 4.4, right panel). But, because the viscosity increases with pressure, the lid growth rate tends to be larger for a thicker lid (Equation 2.40). Thus, the lid grows more rapidly in the North, but on average, this effect is more pronounced in a symmetric geometry, and the lid is slightly thicker than in an asymmetric geometry

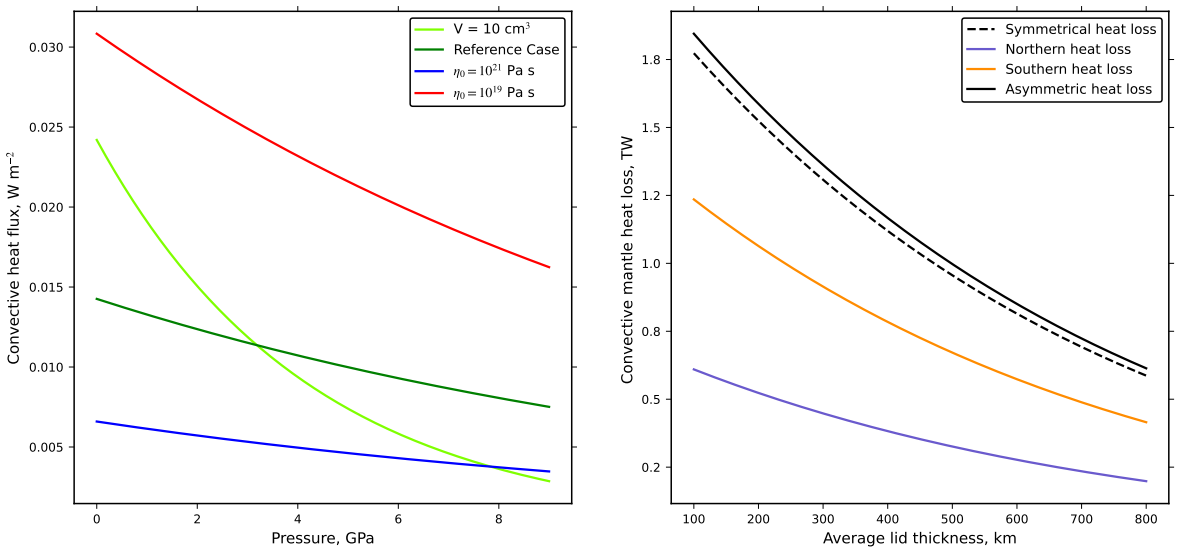

FIGURE 4.4 – **Left Panel** Convective heat flux as function of pressure (Equation 2.7) for different reference viscosity and activation volume (Equation 2.1). The parameters used for the reference case (green) are given in Table 1, with a mantle temperature of $T_m = 1700$ K, $\eta_0 = 10^{20}$ Pa s, V = 3 cm^3 and a mantle density of 3400 kg m^{-3}. For the other curves, only one parameter changes, for the red curve $\eta_0 = 10^{19}$ Pa s, for the blue curve $\eta_0 = 10^{21}$ Pa s and the chartreuse curve V = 10 cm^3. **Right Panel** Heat loss from the convective mantle as a function of the average thickness of the lid in a symmetrical (dashed line) or asymmetrical (solid line) geometry. The loss is the product of the convective flux (left panel) and the surface area at the base of the lid (Equation 2.44). For the asymmetric geometry, the two components, north and south, are plotted with the north in blue and the south in orange. The north-south difference in lid thickness is set at 100 km. We can see that the asymmetric geometry loses more heat than the symmetric geometry, but that this difference decreases as the lid thickens.

(Figure 4.3e). This effect is visible when the lid thickness is substantial. This has no significant consequences on the mantle temperature (Figure 4.3h).

Systematic exploration with crust extraction

The results of the systematic exploration in both geometries but considering crustal extraction are shown on Figures 4.5 & 4.6 & 4.7. Note that results of simulations with crustal extraction cannot be directly compared to the results without extraction because (i) runs without extraction do not depend on the mantle permeability k_0, (ii) the range of crustal thickness and dichotomy amplitude for runs without crustal extraction is set to correspond to InSight constraints ; it is not the case for runs with crustal extraction that result in broader ranges of values for both D_{cr} and ΔD_{cr} (Figures 4.5a-c & 4.6a). However, the range of lid thicknesses and mantle potential temperatures obtained are globally coherent.

At first-order, results in symmetric (right of Figures 4.5 & 4.7) and asymmetric geometries (left of Figures 4.5 & 4.7) are also very similar. Differences between the two geometries (middle plots, Figures 4.5 & 4.7), are relatively small. Also shown in Figure 4.6 are the amplitudes of the dichotomy in crustal thickness, lid thickness and HPE enrichment in the asymmetric case. Differences between the two geometries exist when the dichotomy amplitude is the largest (Figure 4.6a).

Crustal thickness The present-day values of the crustal thickness range between 40 and 110 km (Figure 4.5a-c), meaning that we cover a large diversity of crustal extraction scenarios. This range is larger than that for the case without extraction. The thickest crusts are obtained at low viscosity, whatever the value of the permeability. Lower viscosities ($< 10^{21}$ Pa s) induce thinner lids, in particular in the early times, when the crust is being extracted, and hence lower pressures at the top of the convective mantle. This causes more melting in the mantle and more crust extraction. At low permeability, thicker lids are however counterbalanced by slower extraction rates which delay crust formation, preserving heat producing elements in the mantle. The amount of internal heating in the mantle is then higher (Figure 4.7g-i), increasing the temperature of the mantle and generating more crust. At high viscosity ($> 10^{21}$ Pa s), the lids are thicker, but as mantle cooling becomes less efficient, the mantle temperatures rise, causing more melting and more crust. There is thus a minimum in crustal thickness that is reached around $\eta_0 \approx 10^{21}$ Pa s.

Expected values for crustal thicknesses are at the limit between a thick crust resulting from a low viscosity and/or a low permeability and a thin crust resulting from a high viscosity and high permeability (Figure 4.5a-c). We find very similar ranges of parameters that respect these constraints for the two geometries (Figure 4.5a-c, solid outline). The difference between the geometries (Figure 4.5b) is fairly small for a large

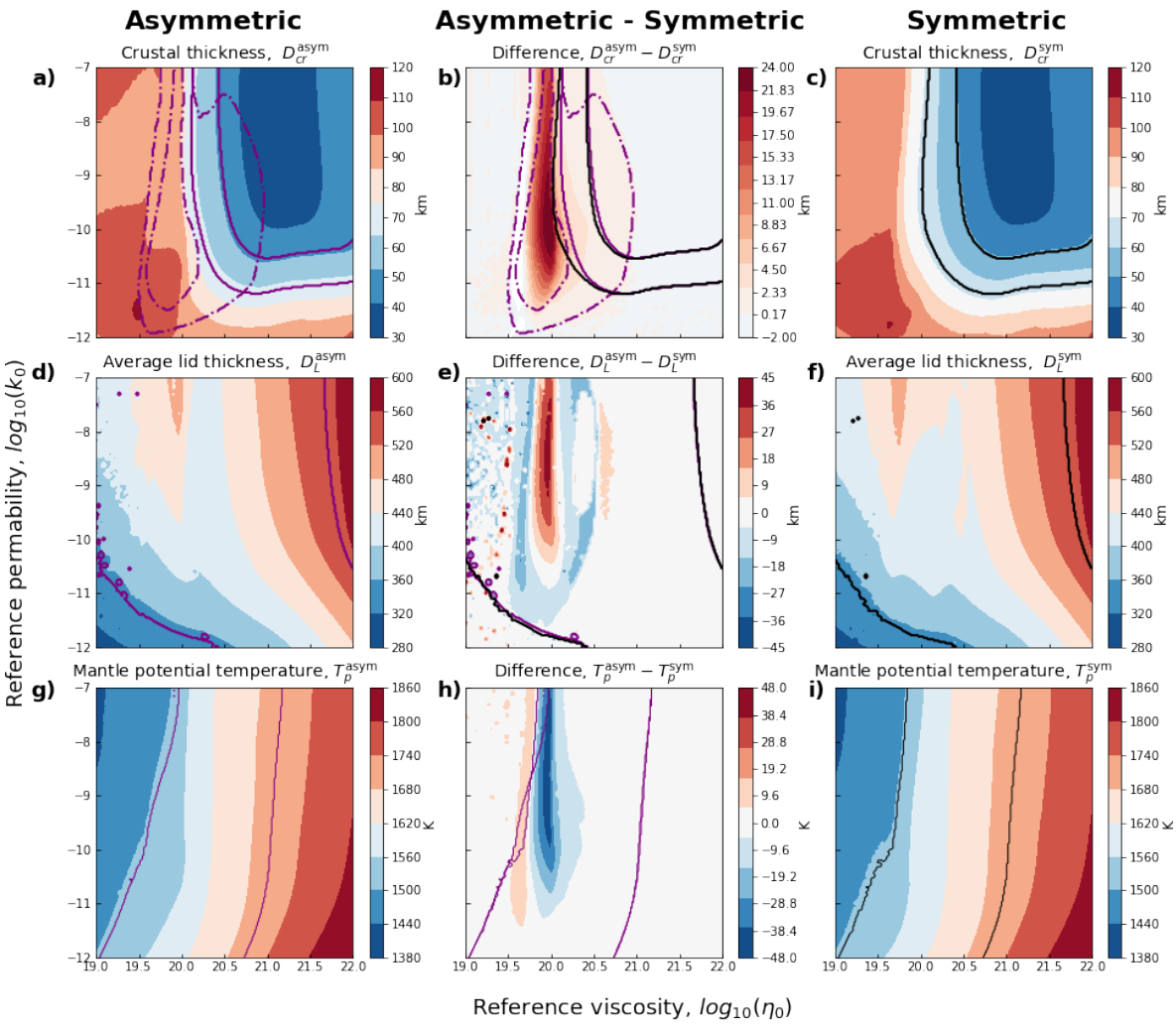

FIGURE 4.5 – Comparing the outputs of our thermal evolution model in an asymmetric and symmetric geometry with a systematic exploration over k_0, η_0 and for our reference case (Table 2.1). η_0 (x-axis) is between 10^{19} and 10^{22} Pa s and k_0 (y-axis) is between 10^{-12} and 10^{-7} m^2. (a, b, c) Average crustal thickness. (d, e, f) Average thermal lithosphere thickness ($D_l + \delta_u$). (g, h, i) Mantle potential temperature at present-day (Equation 4.6). The left-hand side plots (a, d, g) are for an asymmetric geometry, the right-hand side plots (c, f, i) are for a symmetric geometry and the middle plots (b, e, h) represent the difference between both geometries (asymmetric - symmetric). The purple outlines (a, d, g) show the range of parameters that fit the constraints (Sections 4.2) in the asymmetric case. The black outlines (c, f, i) show the range of parameters that fit the constraints in the symmetric case. The dashed-dotted outline (a, b) show the range of parameters that fit the dichotomy amplitude for the asymmetric case ($12.2 < |\Delta D_{cr}| < 28$ km).

number of parameters but becomes quite large for a range of viscosity centred around the value of $\sim 10^{20}$ Pa s and for permeability values larger than $\sim 10^{-11}$ m^2. This region of high difference coincides with a strong crustal dichotomy (Figure 4.6a). The range of parameters fitting the expected dichotomy amplitude in the asymmetric case closely surrounds this region (Figure 4.5a-b & 4.6a, dashed outline).

Average Lid thickness As for the case without crust extraction, the lid thickness at present-day mainly depends on mantle viscosity (Figure 4.5d-f) with higher viscosities leading to thicker lids. However, lower permeabilities $< 10^{-11}$ m^2 result in thinner lids, notably because they preserve heat-producing elements, hence internal heating, in the mantle. At high permeabilities ($k_0 > 10^{-9}$ m^2) and for a viscosity centred around $\sim 10^{20}$ Pa s, lid thickness values are particularly large. This is because, for this parameter range, the crust is very thick and forms early, resulting in a large extraction of heat-producing elements and a significant depletion of the mantle (Figure 4.7g-i). The mantle cools down quickly and the lid grows rapidly.

Constraints given by the InSight mission on the thickness of the Martian lid are too large, between 350 and 550 km, to be considered as a strong constraint. This expected range of thicknesses (Figure 4.5d-f, solid outline) is obtained for a wide range of parameters for the two geometries, except at low viscosities and permeabilities ($\mu_0 \lesssim 10^{20}$ Pa s, $k_0 \lesssim 10^{-11}$ m^2) or at high viscosities and permeabilities ($\mu_0 \gtrsim 5 \times 10^{21}$ Pa s $k_0 \gtrsim 10^{-9}$ m^2).

The difference in lid thickness (Figure 4.5e) between the two geometries is, as for the crustal thickness, linked to the parameter region generating strong North-South dichotomies (Figure 4.6b). Crustal dichotomies result indeed in significant differences in lid thickness (Figure 4.6b). Here the differences can be quite large ($\gtrsim 10\%$), much larger than in the case without crustal extraction. This is a feature linked to the dichotomy as well as to crustal extraction. The thicker crust in the South prolongs melting and crustal extraction in the Southern Hemisphere, which occurs at a low melt fraction, with melts highly enriched in heat-producing elements. This process significantly enriches the crust in heat-producing elements and depletes the mantle (Figure 4.7b-h), cooling the mantle and causing a more important lid thickening in comparison with the symmetric case (Figure 4.5e).

Mantle potential temperature Present-day mantle potential temperatures (Figure 4.5g-i) are strongly correlated to the value of the reference viscosity. Higher viscosities result in a slower cooling of the mantle and warmer mantle temperatures today. Mantle potential temperatures tend to be warmer at low permeability due to the late extraction of the crust and heat-producing elements. The two geometries give similar results with a viscosity range respecting InSight constraints between $\simeq 8 \times 10^{19}$and10^{21}

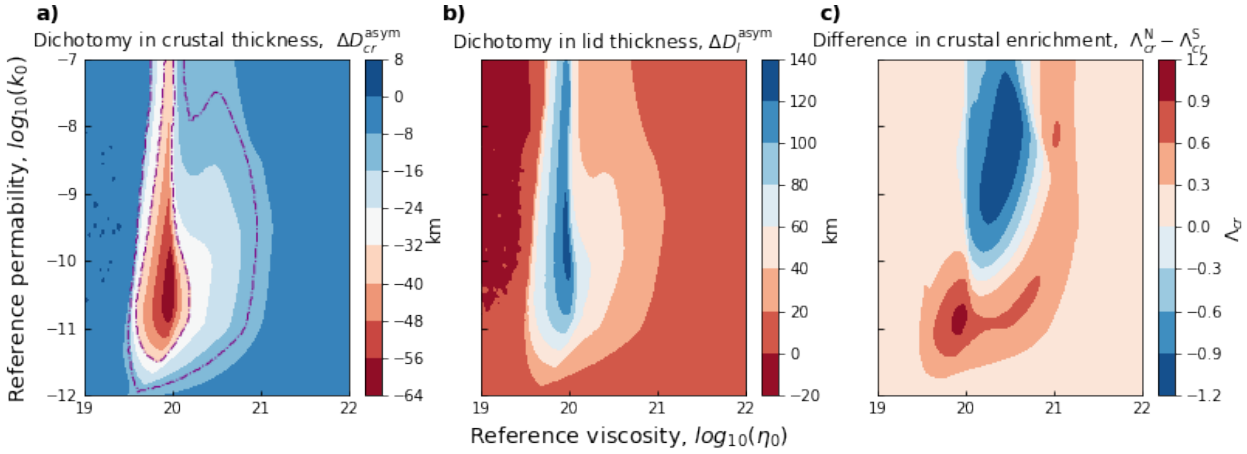

FIGURE 4.6 – Amplitude of the North-South dichotomy in (a) crustal thickness ($D_{cr}^N - D_{cr}^S$), (b) thermal lithosphere thickness ($D_L^N - D_L^S$), (c) heat-producing element enrichment relative to the primitive mantle ($\Lambda_{cr}^N - \Lambda_{cr}^S$) for an asymmetric geometry accounting for crustal extraction. Results of a systematic exploration over k_0, η_0 for our reference case (Table 2.1). η_0 is between 10^{19} and 10^{22} Pa s and k_0 is between 10^{-12} and 10^{-7} m^2. (a) The dashed outline shows the range of parameters that fit the dichotomy amplitude ($12.2 < |\Delta D_{cr}| < 28$ km).

Pa s. The potential temperature is, therefore, a good indication of the mantle viscosity whatever the geometry. The difference between the two geometries (Figure 4.5h) is again the largest in the same region of the parameter space where large differences in crustal thickness are reached. The difference in mantle potential temperatures between the two geometries is relatively small but not negligible. Larger dichotomies cause a more efficient cooling of the mantle. The difference in mantle cooling is about ten times larger than in the case where the crust is set initially and no extraction is considered (Figure 4.5h vs 4.3h). This difference means that the additional cooling caused by the difference in crust thickness is indeed different from the process described in the case without extraction, which involved a non-linear heat flow (see Section 4.3.2). As explained for the lid thickness, the more important cooling in the asymmetric case is well explained by an efficient extraction of heat-producing elements from the mantle caused by the late episode of crustal extraction at low melt fraction in the South (Figures 4.7a-g).

Distribution of heat-producing elements The percentage of radioactive heating in the crust (Figure 4.7a-c) depends on two parameters : the crustal thickness (Figure 4.5a-c) and the crustal enrichment in heat-producing elements (Figure 4.7d-f). In general, variations in heat-producing elements enrichment of the melt compensate for the variations in crustal thickness (compare Figures 4.7d-e & 4.5a-c which are anti-symmetric), resulting in an amount of radioactive heating in the crust of 50 to 55 %. Indeed, if melt extraction is limited by a low melt fraction (large viscosity $\gtrsim 10^{20}$ Pa s), the resulting crust is thin but the melt forming the crust is then much more enriched. Inversely, if melt extraction occurs at low permeability ($< 10^{-10}$ m^2) but large melt

fractions, the final crust thickness is large but formed by less enriched melts. However, at relatively low viscosities ($< 10^{20}$ Pa s) and high permeabilities ($> 10^{-9}$ m^2), we can form crusts that are both very enriched in heat-producing elements and thick because low viscosity favours melting in the mantle, hence thick crusts, and high permeabilities favour extraction at low melt fractions, i.e. large enrichment. The parameter space matching the thickest crustal thicknesses does not exactly correspond to that for the largest amount of heating in the crust ($> 70\%$) (Figures 4.5a-c & 4.7a-c) because, despite the crusts are thickest, they are not very enriched.

The difference between the two geometries is again larger when the crustal dichotomy is the most significant (Figure 4.6a). This difference is not affected by the difference in crustal enrichment between the two hemispheres (Figure 4.6c). In the asymmetrical case, the prolonged phase of melting and crustal extraction at low melt fraction below the thick crust in the Southern Hemisphere explains the observed differences : it results in a larger heat-producing element content in the crust and a more depleted, and hence colder, mantle.

Parameter ranges fitting all constraints We are now interested in the parameter ranges that respect all the constraints in the asymmetrical (Figure 4.7a-d-g, purple solid line) and symmetrical cases (Figure 4.7c-f-i, black solid line). Constraints that do not concern the asymmetry (average crust thickness, average lid thickness and mantle potential temperature) lead to more or less the same parameter ranges for the two geometries because the uncertainties are larger than the differences between the two geometries. Adding in the constraint concerning the dichotomy, i.e. the dichotomy amplitude (Figure 4.7a-d-g, purple solid line), we obtain only a slightly smaller range for the asymmetric case. However, the expected parameter ranges are those where the differences between the two geometries could be large. This is because the crustal dichotomy expected for Mars is rather large, and we expect the differences due to the geometry (symmetric/asymmetric) to be larger than for the rest of the parameter space.

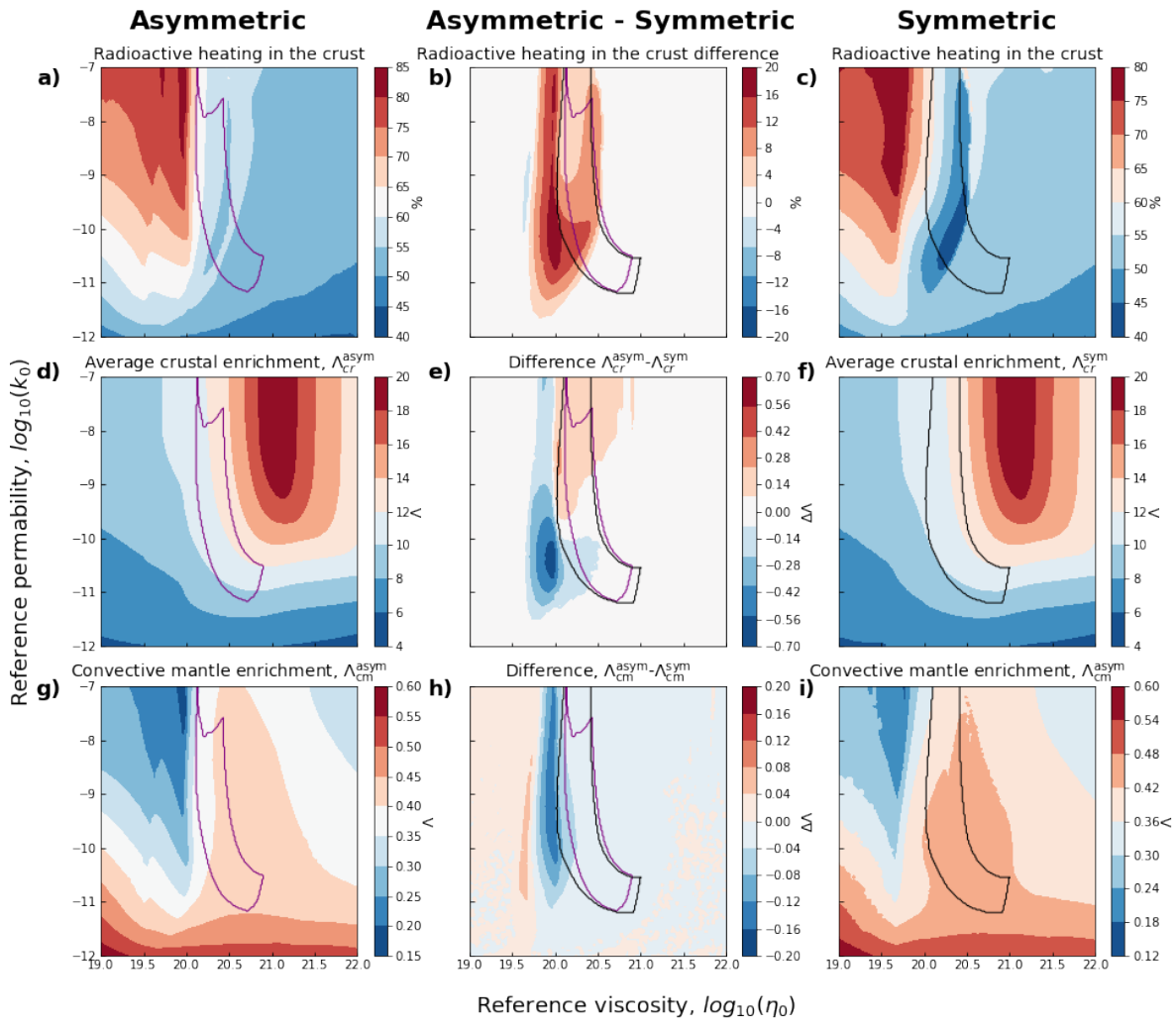

FIGURE 4.7 – Comparing asymmetric and symmetric geometry for a systematic exploration of k_0, η_0 on our reference case (Table 2.1). η_0 (x-axis) is between 10^{19} and 10^{22} Pa s and k_0 (y-axis) is between 10^{-12} and 10^{-7} m^2. (a,b,c) radioactive heating in the crust. (d, e, f) Enrichment of the crust. (g, h, i) Enrichment of the convective mantle. The left-hand side plots (a, d, g) are for the asymmetric geometry, the right-hand (c, f, i) side plots are for the symmetric geometry and the middle plots (b, e, h) are the difference between both geometries (asymmetric - symmetric). The contours show the parameter space in which the combination of all constraints is respected, taking into account the dichotomy constraint in the asymmetric case (Sections 4.2).

4.4 Inversion using a Monte Carlo Markov chain algorithm

Previously we were interested in the direct problem, we calculated the thermal evolution for different parameters and we looked at the outputs of our model to see which ones matched the observations. We would now like to get a better idea of which models match the observations of the structure of the Martian crust and mantle. To do this, we set up an inversion of our model in the two geometries, by formulating an inverse Bayesian problem that allows to estimate the probability of the different thermal evolutions. The likelihood of our models is established using the results of the NASA InSight mission on the crust and mantle structure. The inversion is then based on a Markov Chain Monte Carlo sampling algorithm. Such a random walk in the parameter space defines a collection of models that reconstruct our likelihood and provides the probability function of our models given the data. We can then discuss the shape of the probability function for each geometry and compare their differences.

4.4.1 Bayesian inverse problem

A Bayesian inference is used to formulate our inverse problem following the formalism proposed by Gallagher et al. (2009) and based on Bayes' equation (Bayes, 1763) :

$$p(\mathbf{m}|\mathbf{d})\ p(\mathbf{d}) = p(\mathbf{d}|\mathbf{m})\ p(\mathbf{m}), \tag{4.10}$$

where $\mathbf{m}$ represents the parameters of our thermal evolution model and $\mathbf{d}$ represents our data. The physics of our model is always the same and its results are deterministic. A thermal evolution is then mathematically described by the parameters that are used to calculate it. $p(\mathbf{m})$ is the prior probability of these parameters and therefore of the associated thermal evolution. The data here represent the observations we have for Mars and these observations have a certain probability $p(\mathbf{d})$. We always use the same data, so their probability, even if unknown, is constant. $p(a|b)$ is the probability of a knowing b or the probability of a conditional on b. $p(\mathbf{d}|\mathbf{m})$ is the data likelihood, i.e. the probability of $\mathbf{d}$ conditional on our model. In other words, it measures how well a model reproduces observations. For example, in a classical least squares inversion, we want to maximise the likelihood value to obtain the model that best reproduces the observations. $p(\mathbf{m}|\mathbf{d})$ is the probability of a model knowing the data, or knowing the observations. $p(\mathbf{m}|\mathbf{d})$ is also called the posterior probability of the model, i.e. the probability of a model improved by the likelihood. This is the probability we are trying to obtain using an inversion.

4.4.2 Prior distribution

The prior probability ($p(\mathbf{m})$) summarises what we know about our model before we carry out the inversion. For example, if one of the parameters we want to invert

follows a frequency or probability law, we can account for it. Here we have chosen to use a uniform probability law for the prior because we have no prior information on these parameters. Nevertheless, we want to cover a given area of the parameter space, either because the parameters have a limited range of values or to limit the calculation time. The prior probability is 1 for a model whose set of parameters lies within the space defined in Table 4.1. If a model is outside this space, its prior probability is set to 0.

We also choose to set to 0 the prior probability of models that encounter the situation where the crust becomes as thick as the lithosphere. Our model does not satisfactorily handle this type of thermal evolution, and, in all cases, they will differ significantly from the solutions we are looking for, as they result in too-thick crusts and/or excessively large dichotomies ; they also require long calculation times.

Parameters	Maximum	Minimum	σ_{perturb}	Unit
$\log_{10} \mathrm{k}_0$	-7	-11	0.16	$\log_{10}$ m^2
$\log_{10} \eta_0$	19.3	20.3	0.08	$\log_{10}$ Pa s
f_{mag}	1	0	0.03	
f_{base}	1	0	0.03	
A	400	200	6	kJ.kg^{-1}.mol^{-1}
V	10	0	0.3	cm^3
ρ_{cr}	3150	2550	30	kg.m^{-3}
k_{cr}	4.0	2.0	0.03	W.m^{-1}.K^{-1}
$X^p_{\mathrm{H_2O}}$	0.1	0.01	0.005	%wt H_2O
T^0_m	1775	1625	6	K
$\Delta\mathrm{T}^0_c$	300	50	40	K
$\Delta\mathrm{D}^0_l$	8	0.5	0.4	km

TABLE 4.1 – Parameters of our sampling algorithm with k_0, the reference permeability, η_0 the reference viscosity, f_{mag} the intrusive fraction, f_{base} the fraction of basal magmatism, A the activation energy, V the activation volume, ρ_{cr} the crust density, k_{cr} the crust thermal conductivity, $C_{\mathrm{H_2O}}$ the water concentration of the silicate bulk, T^0_m the initial mantle temperature, $\Delta\mathrm{T}^0_c$ the overheating of the core, $\Delta\mathrm{D}^0_l$ the initial perturbation in lid thickness.

4.4.3 Likelihood function

Our model generates outputs, i.e. values obtained during or at the end of a thermal evolution. Some of these outputs correspond to observations we have for Mars. These outputs are called forecasts because they are predictions that can then be compared with observations. We here use the observational constraints derived from InSight and described in Section 4.2 as our "data" or "observations". The data vector **d** is composed

of the crustal thickness below InSight ($\mathbf{D}_{\mathbf{InS}}^{\mathrm{calc}}$), the amplitude of the dichotomy in crustal thickness ($\mathbf{\Delta D}_{\mathbf{cr}}^{\mathrm{calc}}$), the mantle potential temperature ($\mathbf{T}_{\mathbf{p}}^{\mathrm{calc}}$) and the average thickness of the thermal lithosphere ($\mathbf{D}_{\mathbf{L}}^{\mathrm{calc}}$). To evaluate the likelihood of the data, we use a Gaussian probability distribution in its general form (Gallagher et al., 2009) :

$$p(\mathbf{d}|\mathbf{m}) = \frac{1}{(2\pi)^{\mathrm{N}/2}|\mathbf{V}|^{\mathrm{N}/2}} \exp\left\{-\frac{1}{2}((\mathbf{d} - g(\mathbf{m})^t|\mathbf{V}|^{-1}(\mathbf{d} - g(\mathbf{m}))\right\}, \tag{4.11}$$

where N is the number of observations used, 4 in our case, $g(\mathbf{m})$ is the vector containing the model forecasts and $\mathbf{V}$ is the covariance matrix. The covariance matrix is a square of size N^2 composed of the covariances of each pair of observations. In our case, the observations have no covariance, so the matrix is diagonal and made up of the variances of each observation. In the case of a diagonal covariance matrix, Equation 4.11 can be written as a product of four probabilities following a Gaussian distribution :

$$p(\mathbf{d}|\mathbf{m}) = p(\mathbf{\Delta D}_{\mathbf{cr}}^{\mathrm{calc}}) \times p(\mathbf{D}_{\mathbf{InS}}^{\mathrm{calc}}) \times p(\mathbf{T}_{\mathbf{p}}^{\mathrm{calc}}) \times p(\mathbf{D}_{\mathbf{L}}^{\mathrm{calc}}). \tag{4.12}$$

The probability of a forecast $p(\mathbf{X}^{\mathrm{calc}})$ is :

$$p(\mathbf{X}^{\mathrm{calc}}) = \frac{1}{\sigma_X\sqrt{2\pi}} \exp\left\{-\frac{1}{2}\left(\frac{\bar{X} - \mathbf{X}^{\mathrm{calc}}}{\sigma_X}\right)^2\right\}, \tag{4.13}$$

with σ_X the standard deviation of the data which corresponds to the root square of the variance and $\bar{X}$ the mean value of the data. A mean value and a standard deviation are then defined for each forecast.

Crust thickness at InSight landing site At the InSight landing site, the crust is on average $\mathbf{D}_{\mathbf{InS}}^{\mathrm{SEIS}} = 42$ km thick, with a standard deviation $\sigma_{D_{\mathrm{InS}}} = 5$ km (Equation 4.3). Note, however, that the ± 5 km in Durán et al. (2022b) is a range of values and we are assuming here that it corresponds to a standard deviation of 1 σ. The thickness below InSight predicted by our model ($\mathbf{D}_{\mathbf{InS}}^{\mathrm{calc}}$) is calculated using Equation 4.2.

Dichotomy amplitude The amplitude of the dichotomy depends on the density ratio of the model (Equation 4.4). The mean of the dichotomy is given by Equation 4.4 and is different for each model. The standard deviation around this mean value is more complex. We could use the standard deviation calculated from the linear regression, which is ± 0.1 km. This standard deviation is very small, which leaves little margin for our model. We therefore use a standard deviation of ± 2 km, which is close to our numerical step when solving for the temperature profile in the lid (see Appendices). Our model forecasts the amplitude of the crustal dichotomy ($\mathbf{\Delta D}_{\mathbf{cr}}^{\mathrm{calc}} = D_{cr}^{S} - D_{cr}^{N}$) formed by the extraction of the crust, but this dichotomy is reworked in the course of Mars' history, which justifies the use of a larger standard deviation. For instance, secondary processes, not modelled here, modify the north-south thickness difference formed initially, such as large impacts (Hellas, etc...), erosion and deposition or topographic relaxation.

Average Lid thickness The present-day average thickness of the thermal lithosphere is of $\bar{D}_L = 450$ km, with a standard deviation of $\sigma_{D_L} \pm 100$ km (Equation 4.7). In our model, the average thickness of the lid is calculated from a volume-weighted average of both hemispheres (Equation 2.45).

Mantle potential temperature The present-day average mantle potential temperature is $\bar{T}_p = 1605$ K with a standard deviation of $\sigma_{T_p} = \pm 100$ K (Equation 4.8). The forecast is calculated from Equation 4.6 using the average lid thickness.

4.4.4 Monte Carlo - Markov chain (MCMC) algorithm

The aim of the inversion is to reproduce the posterior distribution, i.e. the model distribution knowing the data or the model distribution reproducing the data. To reproduce this distribution, we implement a Monte Carlo Markov chain sampling algorithm that uses a random walk of a Markov chain and a Monte Carlo sampling algorithm (Sambridge et al., 2013). This method consists in starting with a model $\mathbf{m}_1$ with N_p parameters and applying a small random perturbation to it to obtain a model $\mathbf{m}_2$:

$$\mathbf{m}_2 = \mathbf{r}_a^{\text{gauss}}(\mathbf{m}_1, \boldsymbol{\sigma}_{\text{pertub}}), \tag{4.14}$$

where $\mathbf{r}_a^{\text{gauss}}$ is a vector of N_p random numbers following a Gaussian distribution centred around the $\mathbf{m}_1$-parameters with standard deviation $\boldsymbol{\sigma}_{\text{pertub}}$, where a given value for the standard deviation is defined for each parameter of our model (Table 4.1). We calculate the prior probability $p(\mathbf{m}_2)$ following the rules defined in Section 4.4.2. We then calculate the posterior probability of our two models which depends on the likelihood and the prior and we accept the new model $\mathbf{m}_2$ in our Markov chain if the following condition is verified :

$$\frac{p(\mathbf{m}_2|\mathbf{d})}{p(\mathbf{m}_1|\mathbf{d})} > \mathrm{r}_b \equiv \frac{p(\mathbf{d}|\mathbf{m}_2)p(\mathbf{m}_2)}{p(\mathbf{d}|\mathbf{m}_1)p(\mathbf{m}_1)} > \mathrm{r}_b, \tag{4.15}$$

where r_b is a random number chosen uniformly between 0 and 1. If the condition is met, model $\mathbf{m}_2$ is accepted, otherwise model $\mathbf{m}_1$ is accepted again. An accepted model is noted in a list (i.e. a file). Models with a prior of 0 are directly rejected without calculating the thermal evolution. The algorithm then restarts from the accepted model ($\mathbf{m}_1$ or $\mathbf{m}_2$), which is now called $\mathbf{m}_1$ and which is perturbed again. This operation is repeated a sufficient number of times to sample the entire parameter space. The list of accepted models forms a Markov chain which have the following properties : the distribution of the model in this chain is equivalent to the model posterior distribution $p(\mathbf{m}|\mathbf{d})$ and similar Markov chains are additive. We can then redraw the posterior probability function of our model in the parameter space by calculating the density function of this collection of models.

The acceptance of a Markov chain is the probability that a new model will be accepted. This acceptance rate increases if we reduce the amplitude of the perturbations

and decreases if we increase them. The optimal acceptance rate defined by statistics is around 44% (Roberts and Rosenthal, 2009).

4.4.5 Initial thermal state

For the initial thermal state of the mantle, a temperature at the top of the convective mantle (T_m^0) and a lithosphere thickness (D_l^0) are set. Both are taken such that the mantle is at the rheological transition to a solid-like convection, at a time of 4.5 billion years ago. The maximum melt fraction within the mantle must thus be equal to 0.3, which corresponds to an average melt fraction over the melt zone ($\phi_a^{\mathrm{N/S}}$) of ~ 0.14. For the crust, we start with an initial thickness of 4 km, for numerical reasons, and a classical crustal enrichment in heat-producing elements of 10. We impose a small initial perturbation to the symmetrical base state to trigger the instability : typically a north-south difference in lid thickness ΔD_l^0 (Table 4.1).

4.5 Inversions Results

Before carrying out the inversion of interest, a preliminary exploration phase is necessary. A series of inversions are first carried out with different perturbation values for each of the parameters (vector $\sigma_{\mathrm{perturb}}$, Table 4.1) to find the perturbation amplitudes that would give an acceptance close to the optimum value of 44%. Once the parameters of the random walk are defined, we need to determine the necessary number of accepted models, i.e. the length of the Markov chain, to ensure a good coverage of the parameter space. One way to determine the length of the chain is to perform an inversion without constraints on the data, i.e. an inversion where the probability of the data likelihood ($\mathrm{p}(\mathbf{d} \mid \mathbf{m})$) is equal to 1 and the posterior distribution should then be equal to the prior distribution. From a Markov chain with 2 million models, uniform distributions are reached, so this is the minimum number of models to gather for our inversions. The second purpose of this inversion with no observational constraints is to provide the prior distributions of the outputs of our model, including the forecasts. It is then possible to compare the posterior distributions of the outputs obtained with inversions constrained by the data with these prior distributions.

Following these preliminary phases, an inversion is performed for each geometry. They follow the same sampling algorithm over the same parameter space with the same constant parameters (Table 4.1). The asymmetric geometry is based on the 4 forecasts described in Section 4.4. The inversion in the symmetric geometry is calculated by setting ($f = 0$) and the likelihood calculation ignores the component on the crustal dichotomy ($p(\mathbf{\Delta D}_{\mathbf{cr}}^{\mathrm{calc}}) = 1$ in Equation 4.12). For each inversion, 486 independent Markov chains are calculated in parallel starting from an identical model. The first 500 models collected for each channel are not taken into account in the final distribution, a phase known as burn-in. The algorithm takes a certain number of iterations to find the high-probability parameter space that it has to sample. Since Markov chains are

additive, they are summed to obtain a single Markov chain. Our results then take the form of two chains with a length of $N_{\text{asym}} = 9.61 \times 10^6$ for the asymmetric geometry and $N_{\text{sym}} = 2.15 \times 10^6$ for the symmetric geometry, with acceptances of 31.27% and 47.24% respectively, i.e. close to the optimal value of 44%.

This Markov chain is a set of models that can be written as points in the parameter space with 12 dimensions (one for each inverted parameter, Table 4.1). We first describe the marginal probabilities, i.e. the projection of the distribution along one parameter, for each inverted parameter for the two geometries. Second, we look at the posterior distribution of the outputs of our model. Then, we show the difference in thermal evolution between the two geometries using the model that best fits the observations, i.e. the one that has the larger posterior probability. Finally, we look at the distribution of different parameters as a function of the initial perturbation ΔD_l^0 in the asymmetric case in order to understand how the initial asymmetry influences our results.

4.5.1 Marginal distribution

Reference viscosity The marginal distribution of the reference viscosity (Figure 4.8a blue histogram), in the asymmetric case, follows a Gaussian-like distribution centred around an average reference viscosity of 2.62×10^{20} Pa s. This is a rather low value which is needed to obtain the rather cold potential temperature at present-day. The distribution obtained for the symmetric case (Figure 4.8a green curve) is very similar though slightly shifted toward lower values. The average value is then 2.42×10^{20} Pa s. The symmetrical geometry produces slightly warmer mantle potential temperatures (see Section 4.3, Figure 4.5). To obtain the same mantle potential temperatures, slightly lower viscosities are required, which explains the shift.

Reference permeability The average value of the reference permeability (Figure 4.8b) is 10^{-9} m^2 in the asymmetric case with a less centred distribution. The maximum density is more around $\simeq 10^{-10}$ m^2 and above 10^{-9} the density is flat. The distribution in the symmetric case has a more pronounced maximum at $\simeq 10^{-10}$ m^2 which leads to a lower average value of 6.3×10^{-10} m^2. Our models tend to point to rather low viscosity values, which, with a low permeability, leads to large dichotomy amplitudes (Figure 4.6a). This may explain why the distribution is shifted towards slightly higher values in the asymmetric case, in order to form a smaller dichotomy because of the shorter crust extraction duration. The reference permeability distribution is rather uniform above 10^{-8} m^2 because, for these permeability values, melt extraction does not occur at the Darcy velocity, as it is limited by the rate at which the convective mantle can bring in new material (Equation 2.20). In these cases, the models do not depend anymore on the permeability, which explains the uniform distribution.

Initial thermal state The results point to rather cold initial mantle temperatures (Figure 4.8c) in both geometries with an average temperature of around 1678 K. In the asymmetric case, the density drops below 1650 K because the low initial temperatures do not allow sufficient extraction and instability growth duration to obtain large enough dichotomies. Warm initial mantle temperatures in both geometries form crusts that are too thick, in particular, if the viscosity is low, as obtained. Low viscosities and low initial mantle temperatures favour thin initial lid thicknesses to ensure an initial state at the rheological transition. A small initial overheating of the core (Figure 4.8f) seems to be more favourable than a warmer one in both geometries. The core acts as heat storage for the mantle. An initially warmer core has a similar effect to an initially warmer mantle. The transfer of this heat to the mantle depends on the heat flux at the CMB ; it is extracted more efficiently if the heat flux is larger. The lower the viscosity, the thinner the hot boundary layer and the colder the mantle temperature, and the larger the CMB heat flux is. As for the mantle, an initially rather cold core avoids the formation of an excessive amount of crust.

Viscosity parameters Larger values for the activation energy are slightly favoured by the inversion in both geometries ($> 250\,\mathrm{kJ\ mol^{-1}}$) ; this implies larger T_l and lower convective heat flux, (Figure 4.8d). The average value is $300\,\mathrm{kJ\ mol^{-1}}$ and the distribution does not significantly vary from the uniform prior distribution. The activation volume, on the other hand, is better constrained for the asymmetric case with a mean value of $4.65\,\mathrm{cm^3}$ (Figure 4.8g). The symmetric case has a close average value of $4.87\,\mathrm{cm^3}$ but shows a more uniform distribution. This difference is expected because the activation volume plays in the asymmetric case by causing a difference in the convective flux (Figure 4.4, left panel).

Crust properties We obtain a rather good constraint on the crustal densities (Figure 4.8e) with a Gaussian-like distribution in both geometries. The average value in the asymmetric case is $2833\,\mathrm{kg.m^{-3}}$ and it is slightly larger, equal to $2868\,\mathrm{kg.m^{-3}}$ in the symmetric case. The difference between the distributions is well explained by the likelihood of the observations : the larger the crustal density, the larger the crustal thickness and the larger the crustal dichotomy amplitude is. The lower densities in the asymmetric case indicate greater difficulty in producing strong dichotomies than thick crusts. The symmetrical case shows a flatter distribution with a larger average because the dichotomy does not have to be fitted. The density distribution for the crust thermal conductivity (Figure 4.8h) differs between the symmetric and asymmetric cases. In the asymmetric case, the density steadily increases from the minimum to the maximum conductivity. The average value is 3.4 $\mathrm{Wm^{-1}K^{-1}}$ but the maximum density is at 4 $\mathrm{Wm^{-1}K^{-1}}$. Whereas for the symmetric case, the average is 3.2 $\mathrm{W.m^{-1}.K^{-1}}$ and the probability is rather uniform above this value. The crustal thermal conductivity has a strong impact on the growth of the dichotomy. A lower conductivity increases the

gradient in the crust and favours our feedback mechanism. The higher conductivities in the asymmetric case indicate that the growth of the dichotomy has to be slowed down in order to satisfy the observations.

Crustal magmatism and melting The probability density for the fraction of magmatism f_{mag} (Figure 4.8j) decreases very slightly as f_{mag} goes from 0 to 1. This occurs in both geometries but seems more pronounced in the asymmetric case. A high magmatism fraction tends to amplify our mechanism, favouring the growth of the crustal thickness dichotomy, which may explain why low values are slightly more likely in the asymmetric case. For the fraction of basal magmatism (Figure 4.8k) and the water content of the primitive mantle (Figure 4.8i) no difference can really be seen between both geometries and the prior uniform distribution. This lack of difference means that these two parameters have no effect on the four forecasts of the model we are looking at. But this does not mean that they have no effects on the thermal evolution.

Initial perturbation Finally, the distribution of the amplitude of the initial perturbation in the asymmetric case (Figure 4.8l) shows that there exists an optimal perturbation around 3 km for this parameter. Above this value, the perturbation is too large and tend to form too strong dichotomies. Below 3 km, the dichotomy is more difficult to grow to expected values. But this distribution can be seen in another way. Whatever the value of ΔD_l^0, there are models that allow it to grow to expected values.

4.5.2 Posterior distribution of the Model outputs

We look at the posterior distribution of the outputs including the four forecasts from our model. We compare the distributions obtained in the two geometries with the expected distribution from the observation as well as with the distribution obtained without accounting for observations, which we call the "prior distribution".

Mantle potential temperature We obtain similar Gaussian distributions for the mantle potential temperature in both the asymmetric (Figure 4.9a blue histogram) and the symmetric geometry (Figure 4.9a green curve). The average potential temperature in both cases is 1620 K, with a standard deviation of ±54 K around this value. The outcome diverges from the distribution that we were aiming for, i.e. 1605 ± 100 K (Figure 4.9a red curve). Nevertheless, the distribution obtained is entirely within the expected range, which means that the inversion enables us to better constrain the value of the potential temperature thanks to the other observations used as constraints. The prior distribution of the mantle potential temperature covers a broad range of temperatures. The posterior distribution covers the upper range of our prior (Figure 4.9a

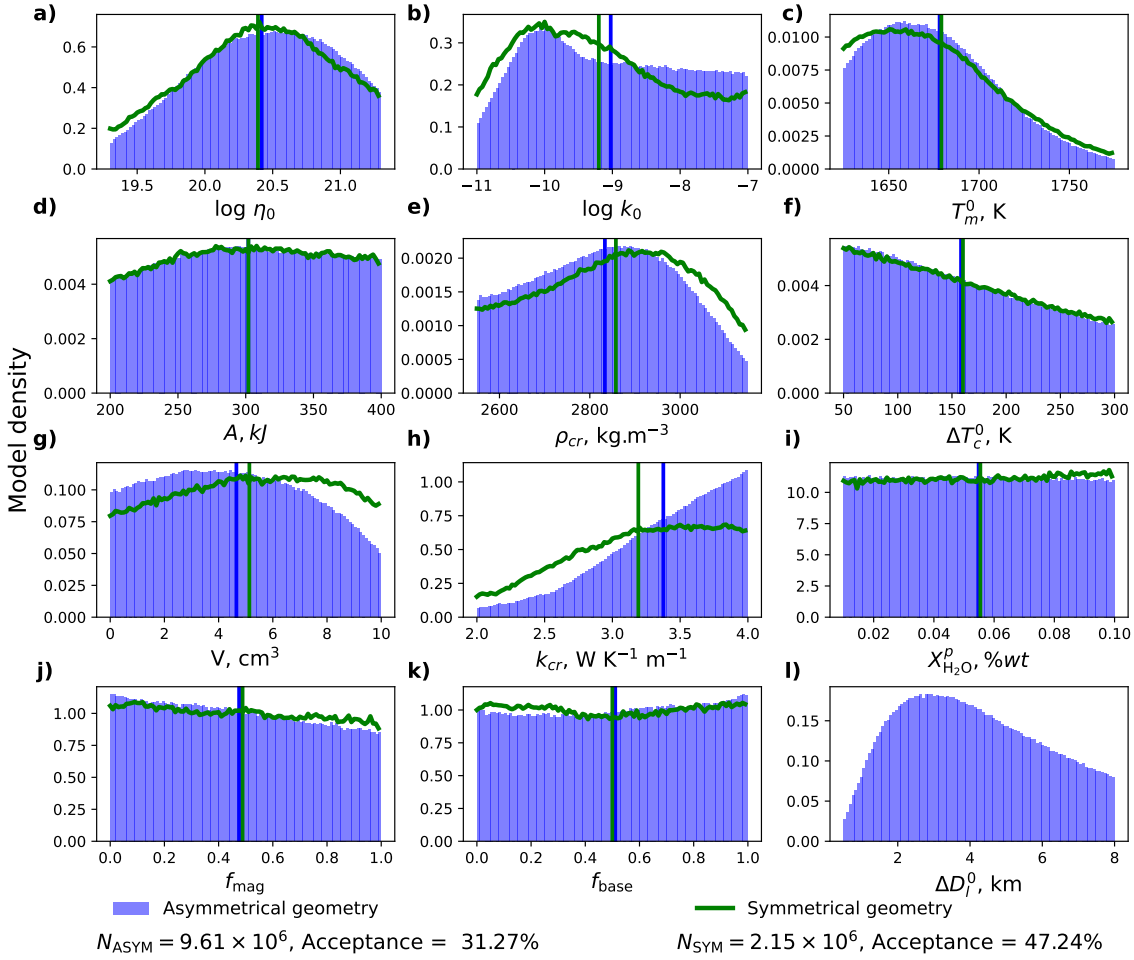

FIGURE 4.8 – Projection along the 12 inverted parameters of the probability distribution of our model, or marginal distribution. Inversion of the asymmetric model on N_{ASYM} models gives blue histograms. Inversion of the symmetric model on N_{SYM} models gives green curves, representing the histogram envelope. The vertical bars give the mean value of the histogram for the corresponding colour. **a)** Reference viscosity of the mantle (log scale) **b)** Reference permeability of the mantle (log scale) **c)** Initial temperature of the convective mantle. **d)** Activation energy, Equation 2.1 (kJ.mol^{-1}) **e)** Crustal density (kg.m^{-3}) **f)** Initial overheating of the core (K) **g)** Activation volume, Equation 2.1 (cm^3) **h)** Thermal conductivity of the crust (Wm^{-1}K^{-1}) **i)** Primitive mantle water content (%wt H_2O) **j)** Fraction of magmatism **k)** Fraction of basal magmatism **l)** Initial perturbation in lithosphere thickness (km)

black curve).

Lid thickness The distribution for the average lid thickness is also Gaussian for both geometries (Figure 4.9b). The obtained average lid thickness is 455 km with a standard deviation of ±50 km. Once again, our inversion allows to better constrain the observations. The average lid thickness is the expected one (450 km) but it has a different dispersion (±100 km). The distribution of our observation, or likelihood, is similar to the prior distribution, which means that our initial constraint on lid thickness is weak. However, our inversion allows us to obtain a much more precise constraint. The asymmetric case forms slightly thicker lids than the symmetric case because the symmetric case favours slightly smaller viscosity (see Section 4.3), hence thinner lids.

Crust thickness and dichotomy Inversions in both geometries perfectly match the expected distribution of the crustal thickness below InSight, i.e. a Gaussian with a mean of 42 km, with a standard deviation of ±5 km (Figure 4.9c). The prior distribution spreads over a wide range of values from -100 km to +180 km, negative thicknesses may theoretically be obtained when the crust is very thin and the density of the crust is very high (Equation 4.2). The gain in information thanks to our inversion compared with the prior is particularly visible here. However, the differences in the crustal density distributions (Figure 4.8e) imply that the average thicknesses obtained are slightly different. In the asymmetric case, the average thickness is 57 ± 6 km whereas in the asymmetric case, the average thickness is 59 ± 7 km. In the asymmetric case, the crustal dichotomy has a mean value of 21 km with a standard deviation of 7.5 km (Figure 4.9d). In the prior distribution, the larger the amplitude, the less likely it is, with an exponential-like decrease in probability (Figure 4.9d). As for the crust thickness, InSight constraint provides a significant gain in information.

Heat-producing elements distribution The percentage of radioactive heating in the crust is on average $58 \pm 5\%$ (Figure 4.9e). Unlike for the systematic exploration, values obtained here are the same in both geometries. Given that the enrichment varies slightly between the models and that the two geometries share the same distribution for the crustal thickness (Figure 4.9c), it is expected that the percentages of heat-producing elements are comparable. These percentages are in the low range of our prior, which tends to favour a significant extraction and a large crustal enrichment in heat-producing elements (>70%), either because the crust is very thick and/or very enriched.

Present-day thermal state Symmetric and asymmetric inversions both give the same core temperature distribution (Figure 4.9f) : an average temperature of 1860 ± 60

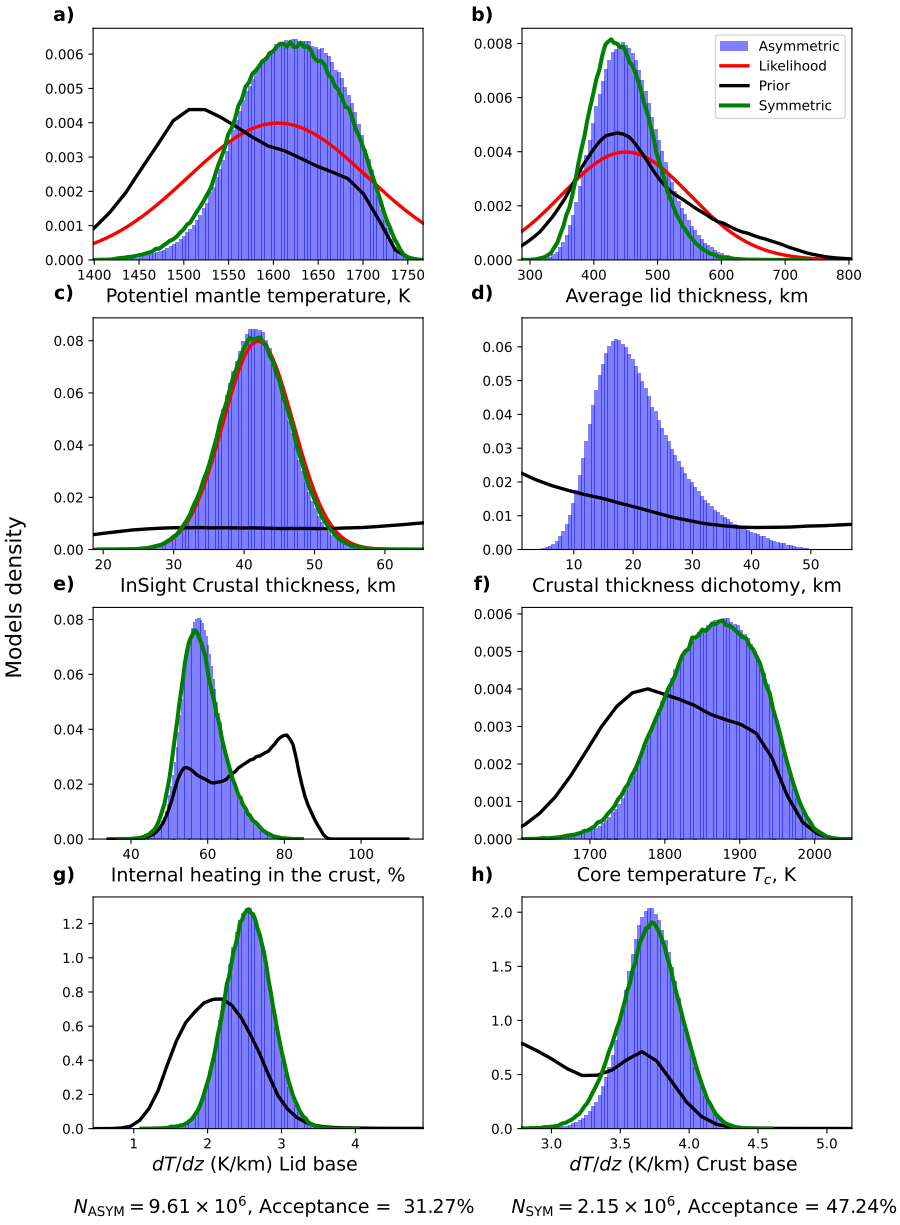

FIGURE 4.9 – Posterior marginal distribution of the likelihood and various outputs for both geometries compared with prior distributions for the asymmetric geometry. Inversion of the asymmetric model on N_{ASYM} models gives blue histograms. Inversion of the symmetric model on N_{SYM} models gives green curves, representing the histogram envelope. The black curve represents the envelope of the prior distribution. The red curve is the Gaussian distribution for likelihood defined in Section 4.4.3. The graphs are bounded on the x-axis by the minimum and maximum values obtained in the two geometries. **a)** Present-day mantle potential temperature (K) **b)** Present-day average lid thickness (km) **c)** Present-day forecast for the crustal thickness below InSight, Equation 4.2 (km) **d)** Present-day amplitude of the dichotomy (km) **e)** Amount of internal heating in the crust as per cent of the total internal heating (% **f)** Present-day core temperature (K) **g)** Present-day average temperature gradient at the base of the lid (K km^{-1}) **h)** Present-day average temperature gradient at the base of the crust (K km^{-1}).

K which is in the warmer range of the prior distribution. For the temperature gradient at the base of the crust and at the base of the lid, we also obtain the same distributions in the two geometries (Figure 4.9g-h). In the asymmetric case, the temperature gradients in each hemisphere are converted into heat flux and projected towards an intermediate radius, ensuring that the flux is conserved. A temperature gradient is then recalculated from these projected heat fluxes by taking the weighted average by f. The gradient at the base of the lid averages 2.5 ± 0.3 K km^{-1}, whereas, at the base of the crust, it averages 3.7 ± 0.2 K km^{-1} which indicates a significant change in temperature gradient within the lithospheric mantle.

4.5.3 Best fitting model

We here describe two thermal evolutions, one for each geometry, sharing the same physical parameters and initial conditions, because it is essential to look at thermal evolutions to understand where the differences between geometries appear. We study the asymmetric model that best fits all observations together (including the dichotomy), i.e. the one that has the highest posterior probability, and compare with the corresponding symmetric model (defined by the same parameters). A model that takes the mean of each parameter, or the average model, could have been another option. The best model has a low reference permeability of 3.2×10^{-11} m^2 and an average reference viscosity of 2.1×10^{20} Pa s (Figure 4.10). Initial conditions are such that the mantle is quite warm (1722 K) and the core slightly overheated (55 K), the lithosphere is 87 km thick. The initial perturbation in lithosphere thickness is 3.2 km and the crustal density is 3107 kg m^{-3}, hence, a rather thick crust and a large dichotomy amplitude are expected.

The thermal evolution is identical in both geometries up to $\sim$ 600 Myr. The difference between the two geometries starts to increase strongly when crust extraction stops in the symmetrical case, while it is prolonged in the asymmetrical geometry up to 1 Gyr ($\sim$ 400 Myr more) in the Southern Hemisphere (Figure 4.10c). The crust formed in the asymmetric case is therefore significantly thicker (60 vs 53 km). This difference in crustal thickness is consistent with the results of our systematic exploration (Figure 4.5h). The effective melt fractions are larger in the Southern Hemisphere (Figure 4.10d) and persist above zero for a longer duration. This prolonged melting explains the prolonged crust formation in the south and hence the thicker crusts in the asymmetric geometry.

The final enrichment of the crust is also impacted by these variations in melt fractions. In both cases, the average enrichment is around 12 (Figure 4.10e), equivalent to just over 650 ppb of Thorium. In the asymmetric case, this enrichment increases during the formation of the crust before falling in the Southern Hemisphere. Consequently, even if the difference is small, the two geometries produce distinct enrichments. However, as the crust in the asymmetric case is thicker (Figure 4.10c), the percentage of radioactive heating in the crust is greater than in the symmetric case (64% vs 58%),

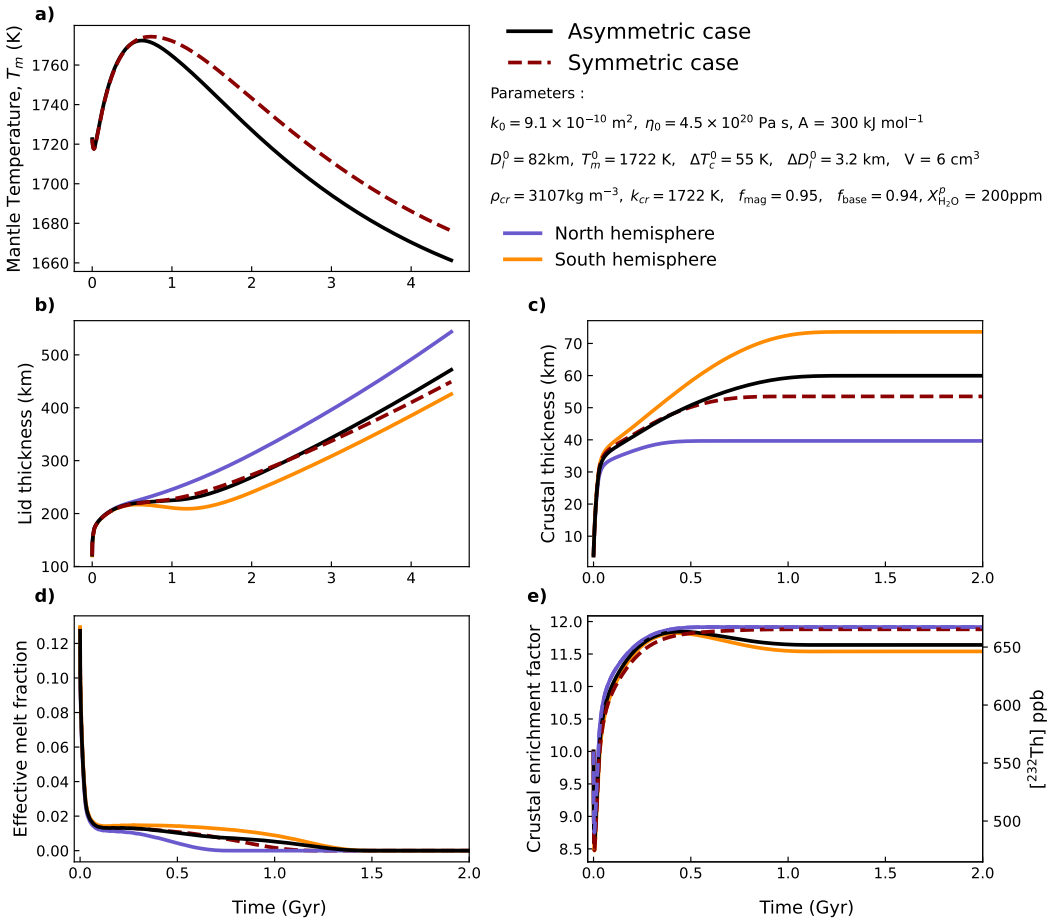

FIGURE 4.10 – Thermal evolution for the best-fit asymmetric model and comparison with the corresponding symmetric model, calculated for the same parameters : evolution of the **a)** convective mantle temperature, T_m **b)** lid thickness, D_{L} **c)** crustal thickness, D_{cr} **d)** Effective melt fraction, ϕ (Equation 2.15) and **e)** crustal enrichment factor, Λ_{cr}, in the North (blue lines) in the South (orange lines), and on average (black lines) as a function of time. Solid lines are for the asymmetric model and dashed red lines are for the corresponding symmetric model. (c-d-e) The x-axis is zoomed in between 0 and 2 Gyr because there is no change thereafter.

despite the lower enrichment. This different distribution of heat-producing elements - the asymmetric case has more heat-producing elements in its crust - explains the colder thermal state of the mantle in the asymmetric geometry. The potential temperature is 1603 K for the asymmetric case versus 1622 K for the asymmetric case (Figure 4.10a). This difference is significant and consistent with the results of the systemic exploration (Figure 4.5h). As the mantle is colder, the average thickness of the thermal lithosphere grows faster in the asymmetric geometry, resulting in a difference of 22 km in thickness between the two geometries after 4.5 Gyr (Figure 4.10b).

4.5.4 Joint distributions with the initial perturbation.

Differences in inversion results between the two geometries are due to the additional constraint on the amplitude of the dichotomy. In the asymmetric model, the growth of the dichotomy starts off from a small initial perturbation in lid thickness between the two hemispheres, a parameter that does not play in the symmetric model. Here, we look at the joint distributions between different parameters and this initial perturbation (Figure 4.11).

As we saw in Chapter 3 (Figure 3.7l), the larger the initial perturbation, the larger the dichotomy formed, but the average crustal thickness remains constant. For a model to be accepted, the parameters that influence the growth of the dichotomy must be adjusted according to the value of the initial perturbation. The larger the initial perturbation, the more these parameters tend towards values that favour the growth of a dichotomy. Thermal conductivity, for example, increases with the initial perturbation because low values of conductivity induce stronger temperature gradients in the crust, which favour our positive feedback mechanism (Figure 4.11a). The upper bound of the thermal conductivity is the conductivity of the mantle (4 W m^{-1} K^{-1}) because crustal ones are expected to be lower than those of the mantle (Clauser et al., 1995). Similarly, the activation volume decreases as the initial perturbation increases (Figure 4.11d). The dependence of viscosity on pressure leads to a positive feedback between lid thickness and lid thickening, which amplifies our positive feedback mechanism on crust thickness. This dependence must decrease when the perturbation increases to limit the growth of the crustal dichotomy.

The crustal density sets the expected value for the crustal dichotomy. Increasing the initial perturbation in lithosphere thickness leads to a larger dichotomy. So, as expected, the density of the crust is higher for larger initial perturbation (Figure 4.11b). But the increase in the density of the crust also increases the expected value for the average crust thickness. The crustal density reaches a limit at 2800 kg m^{-3} and increases much less after that. This interdependence between the two main constraints via the density of the crust helps to explain why it exists a maximum in density for the initial perturbation and crustal density. A large initial perturbation requires, at constant parameters, large crustal dichotomies and hence larger crustal thicknesses.

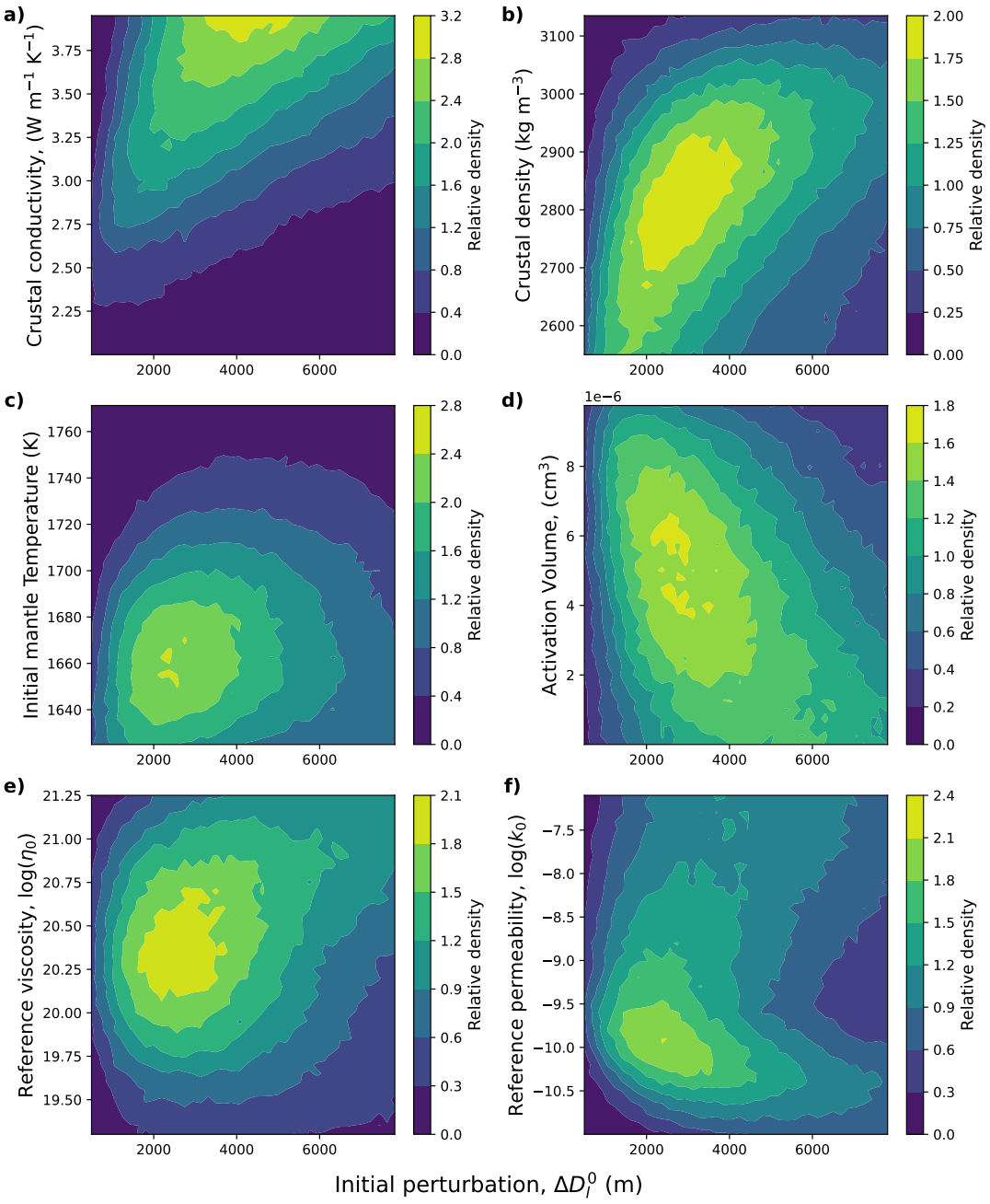

FIGURE 4.11 – Joint density distribution between the **a)** crustal conductivity ($Wm^{-1}K^{-1}$), **b)** crustal density (kgm^{-3}), **c)** initial mantle temperature (K), **d)** activation volume (cm^3), **e)** reference viscosity (log scale, Pa s), **f)** reference permeability (log scale, m^2), (y-axis), and the amplitude of the initial perturbation in lid thickness, ΔD_l^0 (m), (x-axis). The density is divided by the average density to obtain a relative value.

The constraint on crustal thickness limit large perturbations while the constraint on dichotomy penalises smaller perturbations. This explains the reduced crustal densities in the asymmetric case. We, therefore, obtain this optimum difference of 3 km in thickness between both hemispheres. Constraints resulting in thinner crusts would give a lower crust density and therefore a lower initial perturbation.

The reference permeability of the mantle controls the rate of extraction from the crust and therefore the duration of extraction. At low initial perturbation, reference permeabilities around 10^{-10} m^2 are favoured because they induce long extraction times which are favourable to the development of a dichotomy (Figure 4.11f). Then, when we increase the perturbation, we observe two trends, one where the reference permeability increases with the initial perturbation and the other where the reference permeability decreases. For a trend where the permeability increases ($> 10^{-9}$ m^2), this results in shorter extraction times which reduce the growth time of the dichotomy. The trend where the reference permeabilities decrease ($< 10^{-11}$ m^2) is explained by very slow extraction speeds which make the extraction of the crust and hence the growth of a dichotomy less efficient.

To a lesser extent, the initial temperature of the mantle and the reference viscosity also changes with the amplitude of the initial perturbation. Increasing the initial perturbation leads to warmer initial mantle temperatures and higher viscosities (Figure 4.11c-e). The increase in temperature induces higher melting rates, resulting in the formation of crusts and significant dichotomy. The higher reference viscosity results in a faster lid thickening which limits the time taken to extract the crust and develop the dichotomy (Figure 4.11e). These two effects result in larger dichotomies as the perturbation increases, but still within the expected values.

4.6 Discussion

4.6.1 Asymmetric vs symmetric geometry

For equal parameters, differences between the asymmetric and symmetric geometry only depend on the dichotomy amplitude (Figure 4.5b). Differences are almost negligible for small dichotomies but can become significant for large dichotomies (Figure 4.10b $\Delta D_{cr} > 30$ km, purple outline). The larger the crustal dichotomy, the larger the difference in lid thicknesses, the greater the asymmetry, and the larger the differences with the symmetric geometry are (Figure 4.3). However, the asymmetry is limited by the growth of the dichotomy itself, which can only occur over a period of time defined by the crust extraction time.

In the asymmetric model, the average of a quantity between the two hemispheres is not always equal to the symmetrical case. This non-linearity increases with the

asymmetry, i.e. with the crustal thickness dichotomy amplitude. It occurs because the governing equations of our model are non-linear. Such non-linear effects exist in the absence of crust extraction (See Section 4.3.2) and partly arise because of the non-linear convective heat flow dependence of the viscosity (Figure 4.4). This pressure dependence generates a difference in convective heat flow between the two hemispheres and induces a positive feedback mechanism between the lid thickness and its thickening (Section 3.6, Equation 2.40), strengthening the asymmetry (Watson et al., 2022). The average growth of the lid in the asymmetric case thus becomes different from that in the symmetric case. This difference in heat flux between the two hemispheres is also a source of non-linearity for the temperature of the convective mantle. The thinner the lid, the larger the convective heat flow is, and the more important the surface area over which this heat flow applies is (and inversely). As the increase in convective heat flux where the stagnant lid is thinned tends to exceed its decrease where the lid is thickened, the mantle tends to cool more efficiently in an asymmetric model (Figure 4.3h). However, this effect is very limited (a few degrees, Figure 4.3h) and quite negligible.

But the element that plays the most in the asymmetry and in the non-linearity of the asymmetric model is the mantle melt fraction, not only because of the non-linear production rate (Equation 2.13) but also because of the threshold effect (Equation 2.15). In our thermal evolution examples accounting for crustal extraction (Figure 4.10d) it can be seen that the average of the north and south does not exactly give the value of the symmetrical case. It is from this non-linearity that the difference in average crust thickness between both geometries arises (Figure 4.10b & 4.5c). Additionally, the enrichment of the extracted melt, and therefore of the crust, depends on the inverse of the melt fraction (Equation 2.34). As a result, differences in the heat producing elements content of the crust between the two geometries are due to (i) a difference in average crust thicknesses (Figure 4.5b) plus (ii) a difference in heat producing elements enrichment of the crust, both being caused by slight hemispherical differences in melt fractions.

In the dichotomy range expected for Mars, between 10 and 30 km (Figure 4.9d), the differences between the geometries are moderate. The uncertainties we have on our data on the crustal thickness and the mantle thermal structure are greater than the differences between geometries. The two geometries, therefore, explain the observations equally well, with the further advantage that the asymmetric case also provides the dichotomy.

The model distribution constructed by our Monte Carlo with Markov Chain inversion allows the recovery of the distribution of observation. In between inversions for the two geometries, there exists a slight shift in the distribution of the parameter space to recover the same observations. This shift occurs mainly along the parameters that have an effect on the growth of the dichotomy (in particular $k_c r$, ρ_{cr}, V, k_0). The large uncertainties in the thermal state (Section 4.2) combined with the small differences

between geometries at equal parameters (Figure 4.5 & 4.3) together explain why the shift in the parameter space is small. This is how we should understand the lack of differences in the present-day thermal state distributions between geometries : the final thermal states are equal but the thermal evolutions leading to this thermal state are only similar.

4.6.2 Comparison of asymmetric and symmetric parametric models with 3D ones

The comparison of symmetric models without crust extraction with 3D convection models (Thiriet et al., 2019) has shown that calculated thermal evolutions are very similar. These models work particularly well for planets with a high Rayleigh number, such as Mars, because the convective mantle is then relatively well-mixed, which is the basic assumption of parametric models. Asymmetric parametric models without crust extraction were also validated against asymmetric 3D convection models, where in the 3D case, the crustal thickness is different between each hemisphere (with an abrupt transition), as in the parametric one (Thiriet, 2018). The results of this comparison are quite edifying : the average temperature profiles in the two hemispheres are very similar. The parametric model overestimates the temperature of the convective mantle (T_m) by 10 K, but predicts the thickness of the lids and their temperature profiles very well. The transition zone between the two hemispheres is about 2 times the characteristic diffusion distance ($2\sqrt{\kappa_m t_{\text{char}}} \simeq 600$ km, with $t_{\text{char}} = 2.5$ Gyr the characteristic time for radioelement decay), which corresponds to the thickness of the thermal lithosphere. This rather small transition distance between the two hemispheres supports our hypothesis that lateral temperature transfer has a negligible effect on the temperature profile inside the lid. To some extent, these asymmetric models have also been compared to 3D models for mantle melting (Knapmeyer-Endrun et al., 2021). This comparison shows that asymmetric parametric models are in good agreement with 3D models regarding the prediction of the occurrence of partial melt in the mantle below the different geological provinces at the present-day.

However, parametric thermal evolution models with crust extraction have not been compared to 3D models. In fact, in 3D models, crust extraction is a physical and numerical challenge which is difficult to solve. Indeed, in the presence of magma at depth, mantle convection is supposed to be a two-phase flow problem (Ogawa and Yanagisawa, 2012a; Boukaré and Ricard, 2017). Such a dynamics is difficult to solve with realistic parameters, and even less so over 4.5 Gyr. And, even in the case where such dynamics can be solved, studying the 3D flow of magma towards the surface involves dealing with different rheology involving brittleness. This is why parametric models are often used to model crust formation, as they allow crustal growth to be obtained more simply. We, therefore, have uncertainties about the accuracy of crust extraction in these models, but we are well confident about their thermal evolution.

4.6.3 Learning from the Bayesian inversion

Thermal evolution constrained by crust extraction.

Three of our constraints can be reproduced in both geometries : the average crust thickness, the lid thickness and the potential mantle temperature. Among those three constraints, only the crust thickness distribution is properly reproduced by the inversion (Figure 4.9c). The other two forecast distributions (Figure 4.9a-b) are narrower than that of the observation (or likelihood). This shows that, in the frame of our thermal evolution model, these three constraints are related to each other. The constraint on the crust thickness then provides a better estimate of the mantle temperature and lid thickness, providing our model is valid.

Improvement of our knowledge of the crustal thickness of Mars will be the most effective in constraining Martian thermal evolution models. The constraints used in this Chapter are linked to the thickness at the InSight landing site, giving the average crustal thickness and given the average density of the crust (Knapmeyer-Endrun et al., 2021). New constraints on the Martian crust thickness have been given by Kim et al. (2023a). These new constraints are based on the detection of several Rayleigh wave arrivals after the S1222a marsquake. Since Rayleigh waves are dispersive, they determined a group velocity that depends on the thickness of the crust and the velocity profile on the great circle along which they propagated. For a given velocity profile, they estimated a thickness along the great circle of between 44 and 58 km. At the same time, they calculated the average thicknesses along the great circle in the crust thickness models (the same models as for Section 4.2). The thicknesses along the great circle, obtained by seismology, correspond to crust thickness models with an average thickness of between 42 and 58 km and a density contrast between the northern and southern hemispheres of less than 200 kg m^{-3}. These results are rather consistent with studies of seismic attenuation over the same seismic event (Menina et al., 2023). The diffusion thickness along the great circle is 60 km, which could correspond to a minimum crustal thickness.

A cold Martian mantle 4.5 Gyr ago.

The distribution of the initial mantle temperatures points to rather cold temperatures at the rheological transition (Figure 4.8c). Distribution of the initial core temperature also points to a small core overheating. This initial cold thermal state favours thinner crusts. We have considered here a rheological transition at a melt fraction of 30%, but this value is between 30 and 40%. With a higher melt fraction for the transition, the initial temperatures would be warmer. This would have an impact on the distributions obtained for the other parameters in order to remain within the constraints (or likelihood). Defining a prior distribution of thermal states that could result from a magma ocean phase for Mars would certainly improve the inversions.

A cold Martian mantle today

The current thermal state of the mantle as understood from seismological studies is a cold mantle (Huang et al., 2022) with a thick lid (Durán et al., 2022b; Khan et al., 2021). Our inversions perfectly match this description of the thermal state of Mars with the same gain in information. In fact, the potential temperature of the mantle estimated by our inversion is 1622 ± 40 K, i.e. a warmer temperature on average but with a smaller dispersion than the initial observation. The thickness of the lid is estimated at 450 ± 50 km, i.e. the same average but with a smaller dispersion than the initial observation. The inversion has therefore helped to better constrain the thermal state of the mantle thanks to the crustal constraint and our model. This thermal state implies a low reference viscosity and a depletion of heat-producing elements in the mantle to explain the current cold temperatures. Indeed, the large majority of heat-producing elements are contained in the crust ($58\% \pm 5\%$, Figure 4.9e). Interestingly, this depletion of the mantle is compatible with current melting only beneath the Tharsis dome (Knapmeyer-Endrun et al., 2021).

The temperature gradient at the base of the lid is estimated to between 2 and 3 K/km, in agreement with the values found in Khan et al. (2021) and Durán et al. (2022b) from their geophysical inversion. These strong gradients are at the origin of a low-velocity zone for S waves and also, theoretically, one for P waves, which are not currently observed. As the drop in speed is quite slight in the zone, this does not result in a shadow zone as expected, but in a reduction in the amplitude of the S waves. These gradients are used in inversions throughout the lithosphere, but the gradient increases from the lithosphere base to the Moho, where it is between 3.5 and 4 K/km. The temperature gradient in the lid has a significant influence on the ray path and wave travel time, and hence on the results of the arrival time inversions. This is why it is important to take into account the evolution of the temperature gradient over the lid thickness. This is the inversion approach in Drilleau et al. (2022), they use as thermal profiles those provided by a parametric thermal evolution model. However, their model is a symmetric model and differs from ours, in particular the velocities of crustal extraction correspond to our maximum speed, which means systematically larger than ours. They obtained warmer initial mantle temperatures (1780 ± 50 K) than we did from their inversion, which may be explained by the choice of a geochemical model less enriched in heat-producing elements.

The core temperature is fairly well constrained, with an average temperature of 1863 ± 62. This temperature is well above the Fe-FeS eutectic temperature between $1400 - 1800$ K at a pressure between $\simeq 20$ GPa (core-mantle boundary pressure) and $\simeq 50$ GPa (Pressure at the centre of Mars) (Mori et al., 2017). These temperatures involve a completely molten core without a solid inner core, as expected from the results of the InSight mission (Stähler et al., 2021; Irving et al., 2023; Le Maistre et al., 2023).

A water-rich mantle ?

Our inversion does not allow to determine the primordial water content of the mantle (Figure 4.8i). In our model, the water content only modifies the solidus of the crust, and its effect on mantle dynamics is not accounted for. In the literature, estimates of the water content of the Martian primordial mantle vary over 4 orders of magnitude, from 1 ppm (Mysen et al., 1998) to 1000 ppm (Johnson et al., 1991). They are mainly derived from geochemical studies of SNC meteorites and are based on geochemical models. Geodynamic estimates rely on the effect of water on mantle rheology (reference viscosity, activation volume and energy), searching for the rheology, among dry or wet olivine, that best explains the planet dynamics. For early Mars, a wet rheology was proposed to explain the thermal evolution (Hauck and Phillips, 2002) and relaxation of the dichotomy (Guest and Smrekar, 2005), which according to Taylor (2013) would correspond to a water content of 600 ppm. Our results are still in line with these predictions, a with low reference viscosity ($\simeq 10^{20}$ Pa s, Figure 4.8a) corresponding to a rheology intermediate between wet and dry olivine (Karato and Wu, 1993). For the other parameters, the distribution is much wider, covering almost all cases (Figure 4.8d-g). For the activation volume, the mean value is ~ 4.8 cm^3 (Figure 4.8g), which corresponds more to values for a wet rheology, while the average activation energy is 300 kJ mol^{-1} (Figure 4.8d), which is closer to a dry rheology (Karato and Wu, 1993). Overall, our results point to a non-negligible water content in the mantle, but without reaching wet rheology. Proposing a concentration in ppm in view of the rheological values is complicated, but the concentration is probably larger than 100 ppm (Karato and Jung, 2003).

Water content is not the only factor that could induce a more ductile rheology (Breuer and Spohn, 2006). The presence of a melt fraction reduces the bulk viscosity. Mei et al. (2002) proposes an exponential reduction in viscosity as a function of the melt fraction. This local effect is then difficult to take into account on a global scale. Samuel et al. (2019) use a viscosity depending on the melt rheology, which reduces the viscosity of the upper boundary layer, hence its thickness, increasing the convective heat flux. As a result, they find a much higher reference viscosity for the same parameters to obtain a similar thermal evolution. The increase in pressure and temperature has a dual effect. Viscosity increases with pressure due to the activation volume and the reduction in melt fraction, and viscosity decreases with temperature due to the activation energy and the increase in the melt fraction. In other words, adding the effect of melt fraction on the viscosity mimics a larger activation volume and lower activation energy, thus pointing towards the rheological parameters of dry olivine.

This raises the question of the origin of the low viscosities needed to explain the early Martian thermal evolution. Are they due to a water-rich mantle or a partially melted mantle ? Or both ? Models of mantle convection that include the effect of both a molten fraction and dehydration could answer this question. However, taking the melt fraction into account when calculating viscosity tends to go against the assumption of

a well-mixed mantle, which is the basis of parametric models. Indeed, the partial melt zone is concentrated on a thin layer ; this generates a stratification in mantle viscosity which can lead to convection on a smaller scale over the molten zone. Parametric models have to evolve to take this effect into account, as at present the parametrisation on which these models are based does not allow this.

4.6.4 Difference of the model with the previous version

New features have been added to the model in this Chapter that were not considered in Chapter 3, those are : the downward advection of the crust and lithosphere due to crust growth, a better treatment of the internal heating by magmatism, as well as crust melting. The systematic exploration we carry out here covers all the parameters included in our systematic exploration in the previous Chapter 3 with the former model version, as well as new ones. We therefore compare the results between the two versions of our model to understand the effect of these new features.

The main change is the addition of an advection term caused by crust growth and contemporary downward advection of the lid below it in both the heat conduction and lithosphere growth equations. This is a cooling term because the advection is in the opposite direction to the temperature gradient. This advection increases the lid growth rate calculated from a heat balance at the interface between the lithosphere and the convective mantle (Equation 2.40). In the equation for the conservation of heat in the lid (Equation 2.42), this cooling term increases the temperature gradient along the profile and consequently increases the heat flow, particularly at the base of the lid because the advection velocity increases with depth (Equation 2.23). The main effect of this faster growth of the lid, through these two cumulative effects, is to make it less likely that the crust becomes as thick as the lid. For this to happen, the growth rate obtained by heat balance must be greater than the growth rate of the crust ($\frac{\mathrm{d}D_l}{\mathrm{d}t} - w > w$, (Equation 2.40), which occurs in some rare cases in the Southern Hemisphere with a very thick crust. The advection term limits crust formation and, to compensate for this effect, the ranges of parameters that now fit the constraints are shifted towards a lower viscosity ($\simeq 10^{20.5}$ Pa s) and a lower permeability ($\simeq 10^{-10}$ m^2) compared to the results of Chapter 3. The two ranges fitting our constraints and identified in Chapter 3 are shifted toward a range at low viscosity and intermediate permeability. Our new range includes the parameters of the "EarlyDich" (solid line in Figure 3.6) case. On the other hand, the "LateDich" (dashed line in Figure 3.6) cases no longer seem possible, as the additional cooling term we considered no longer makes it possible to form the expected dichotomy.

We have also improved the treatment of magmatism in the crust by separating the extracted volume of melt into several deposition sites. The heat source term caused by magma cooling is then a function of the temperature of the crust at the site of deposition. In the former version, the heat source term was for simplicity considered

homogeneous in the crust and calculated using the temperature at the base of the crust. With $f_{\mathrm{mag}} = 1$, we would thus expect more heating than with the previous method. But the heating generated is partly if not totally, offset by the cooling due to downward advection. There is no visible effect of this implementation on our systematic exploration results. The inversion also shows that these parameters do not significantly affect the thermal evolution (Figure 4.8j-k).

Crust melting does not seem to have any significant effect on the thermal evolution of the planet, as expected. It, however, reduces strong dichotomies, since melting limits the rise in temperatures at the base of the crust. The smoother increase in temperature caused by the release of latent heat, in the case of strong dichotomies, implies a smaller temperature gradient and thicker lids. Crustal melting thus reduces our positive feedback mechanism if the crust starts to melt in one hemisphere and not in the other.

4.6.5 Dichotomy formation

The inversion of our model in its asymmetric geometry makes it possible to obtain a wide variety of thermal evolutions with the formation of a dichotomy through the mechanism we identified, and this over a very wide range of parameters (Figure 4.9d). The constraint on the dichotomy is absent in the symmetrical case, and this only slightly modifies the distribution. This suggests that the constraint on the dichotomy is therefore either redundant with the constraint on the crust or is less constraining. In the space of parameters required to explain the structure revealed by InSight, a crustal dichotomy grows from any initial low perturbation (0.5 and 8 km, Figure 4.8l). Hence, it appears that our mechanism can explain the growth of the Martian dichotomy despite the origin and magnitude of the initial perturbation. The differences in the distribution of the parameters can be accounted for by either amplifying or dampening the perturbation depending on its strength (Figure 4.11). Not all parameters are affected when accounting for the growth of the dichotomy. The ones that are the most affected are the activation volume, the density of the crust, the thermal conductivity of the crust, and the reference permeability of the mantle, as well as, to a lesser extent, the reference viscosity and the initial mantle temperature (Figure 4.8a-h). These parameters may tend towards less likely values for certain values of the initial perturbation, as for instance the crust density, which would tend towards larger values for smaller initial perturbation.

However, there is an optimal perturbation with a maximum probability density around $\sim$3 km. A hemispheric difference in lid thickness of 3 km corresponds to a variation between the two hemispheres in the heat flux at the base of the lid of $\sim$5 mW m^{-2} which corresponds to only 3% of the average heat flux, which is 78 mW m^{-2}) or a variation in temperature at the average depth of the base of the lid of 40 K (for a lid thickness of 50 km and a temperature jump in the lid of 1300 K). If we look at the parameter distributions at the optimum perturbation value (Figure 4.11), we find a

thermal conductivity of ~ 3 $Wm^{-1}K^{-1}$, a classic value used for a basaltic crust, a crustal density of ~ 2800 $kg.m^{-3}$, within the range estimated for Martian crusts (Goossens et al., 2017; Knapmeyer-Endrun et al., 2021). There are only small constraints on the activation volume, but for a perturbation of 3 km, the preferred value for it is ~ 5 cm^3, i.e. that of wet mantle rheology (Karato and Wu, 1993), while the reference permeability is 10^{-10} m^2, both close to values obtained for the symmetric case. Thus, for a relatively small perturbation, we obtain a distribution close to the symmetric case and therefore expected for Mars. Whether a long-wavelength perturbation is required to trigger the growth of our mechanism can thus be debated (Section 3.6). But this inversion, which tests the sensitivity of our thermal evolution model to the initial perturbation, shows that, after reaching a peak at ~ 3 km, the probability rapidly decreases. We, therefore, expect that strong perturbations are less likely to obtain the expected dichotomy, all the more if we consider an initial perturbation in crustal thickness, the effect of which is considerably larger than that of a difference in lid thickness (Figure 3.7i-l). The amplitude of this perturbation is not entirely negligible. Nevertheless, this small amplitude is irreconcilable with the theory of a giant impact. Recent work by Ballantyne et al. (2023) argues that a giant impact on the scale of the hemisphere inevitably leads to the formation of a local magma ocean that produces a large quantity of crust. If such an impact occurred on Mars, the resulting dichotomy would certainly be much larger than that observed. In fact, this is what studies pointing to an impact in the Southern Hemisphere tend to show : the differences in crustal thickness that they find are about a hundred kilometres larger than expected (Golabek et al., 2011; Leone et al., 2014). In contrast, an initial temperature anomaly with even a small degree 1 component formed by a plume (Roberts and Zhong, 2006; Šrámek and Zhong, 2012) or inherited from the magma ocean (Morison et al., 2019; Watson et al., 2022) is much more consistent with our results.

4.7 Conclusion

In this chapter, we have studied parametric models of thermal evolution with and without crust extraction in symmetric and asymmetric geometries. First, we conducted a systematic exploration of the two main parameters of our model (k_0, η_0) for each geometry. By comparing these explorations we have highlighted differences between geometries for the same parameters. These differences are slight, but they increase with the amplitude of the dichotomy. The asymmetric case tends to show thicker crusts and lids, colder potential mantle temperatures and higher percentages of internal heating in the crust. In the range of dichotomies expected for Mars, these differences cannot be ignored. We then performed two inversions, one for each geometry, using a Monte Carlo Markov chain algorithm. To implement this algorithm, we highlighted very strong correlations in the results of topography and gravity inversions. These relationships enabled us to develop a Bayesian description of the observations. The inversions in the two geometries both reproduce the observations but with slightly different parameters. In fact, the differences between the two geometries are smaller than the uncertainties

in the thermal state and crustal thickness of Mars. We are thus able to reproduce the current thermal state of Mars with both geometries, but the associated thermal evolutions are different.

The comparison between our two inversions has also provided information on the formation of the dichotomy. The parameter distributions obtained for both geometries are close. The constraint on the thickness of the dichotomy is therefore either less restrictive or redundant with the main constraint that is the thickness of the crust. This seems to go together with the observation that the more a parameter influences the growth of the dichotomy, the more its distribution differs from that of the symmetrical case. These differences are fairly well explained by the interaction of these parameters with the initial perturbation. Looking at the inversion results for the optimal value of the initial perturbation (i.e. 3 km), the parameter distributions between the two geometries are similar. Thus, for the parameters expected in the symmetric case with a fairly low initial perturbation (a hemispheric difference of 3 km in lithosphere thickness), we expect to see a crustal dichotomy amplitude that corresponds to the observations. This leads us to believe that the growth of the dichotomy with our mechanism seems very likely, whatever the origin of the initial perturbation.

Finally, the asymmetric case does not diverge significantly from the thermal evolution in symmetric geometry, and both can explain the current thermal state of Mars with only slight differences. Asymmetric models require more assumptions and calculations. But they allow to study the effects of the dichotomy on the thermal evolution of Mars ; they also provide a very good explanation of the differences in elastic thickness between the two hemispheres (Thiriet et al., 2018). Additionally, by adding crust extraction, we observe a positive feedback between the thickness of the crust and the extraction of melt, which could explain the formation of the Martian dichotomy (Bonnet Gibet et al., 2022). In the next chapter, we will study how the growth of the crustal dichotomy can explain the differentiation of the Highlands. Asymmetric models appear thus as a good compromise between 3D evolution models and symmetric models.

Chapitre 5

Martian Highlands differentiation

5.1 Introduction

The composition of the Martian crust seems to be mainly basaltic (Taylor, 2013). Discovered Martian meteorites have mafic to ultra-mafic compositions, as do a large proportion of the rocks observed in-situ by rovers. The density of the crust calculated from these samples and GRS data is quite high, between 3100 and 3300 kg m^3 (Baratoux et al., 2013), with potentially lower values in the Highlands. However, the geoid-to-topography ratios point to much lower crustal densities (Wieczorek and Zuber, 2004). Goossens et al. (2017) obtains an average crustal density of 2582 $\pm$ 209 kg m^{-3} with strong lateral variations, particularly between the Highlands, the northern plains and the recent volcanic massifs (Tharsis and Elysium). Variations in the calcium content of pyroxenes between rocks derived from Hesperian and Noachian volcanism cannot explain such a difference in density (Mangold et al., 2010; Baratoux et al., 2014). A high surface porosity (10%), forming a mega-regolith, is a proposed origin for a low-density component of the crust as well as the presence of sedimentary rocks, mainly clays and sulfate (Wieczorek et al., 2022). Nevertheless, these two contributions seem insufficient to explain the low bulk density (Baratoux et al., 2014), so a large felsic component buried beneath the Martian surface has also been proposed (Baratoux et al., 2014; Goossens et al., 2017), in agreement with other types of observations.

Orbital observations have identified plagioclase-rich outcrops in the Highlands (Carter and Poulet, 2013; Wray et al., 2013) that may be representative of felsic rocks, although the degree of differentiation of these rocks is still subject to debate (Phillips et al., 2022). In parallel, a great diversity of igneous rocks was detected in the Gale crater, from classic mafic rocks of the Martian surface to intermediate rocks and up to evolved rocks like trachytes dated from Noachian/late Hesperian (Sautter et al., 2015; Cousin et al., 2017). In addition, a pair of meteorites, NWA 7034 & 7533 which are breccia, show differentiated clasts ranging from intermediate to monazite in composition mixed with larger basaltic and gabbroic clasts (Agee et al., 2013). The formation of the breccia occurred only 225 Myr ago but the felsic clasts that compose it have

different ages with the oldest ones dated to between 4.42 and 4.47 Gyr (Cassata et al., 2018). This indicates the presence of a wide variety of differentiated rocks early in Mars' history. Lagain et al. (2022) propose a strong candidate for the source impact crater of this breach, located in the Terra Cimmeria-Sirenum province, southwest of Tharsis in the highlands. A visible-near infrared spectrometry study of this province has detected several feldspar-rich outcrops that appear to be evolved in composition (Payré et al., 2022).

It can be pointed out that observations of differentiated rocks are all located in the Martian Southern Hemisphere in the Highlands (Figure 5.1). This geological unit is characterised by a high topography and ancient terrains and contrast with the Northern Hemisphere characterised by a low topography and younger terrains. The difference in topography is usually related to a difference in crustal thickness, assuming a homogeneous crustal density between the two hemispheres. But if we assume that the Highlands have a large felsic component, similar to a continental crust, and therefore a lower density than the Northern Hemisphere, then a strong density difference can alone explain the topographic difference (Knapmeyer-Endrun et al., 2021; Wieczorek et al., 2022). It is therefore important to constrain the mechanism behind these differentiated rocks to constrain the nature of the dichotomy.

The mechanism allowing the formation of differentiated rocks is however subject to debate and different origins are proposed. The formation of an anorthositic primary crust extracted from a magma ocean similar to the Moon seems difficult in the Martian case (Collinet et al., 2015) and needs to be studied. Indeed, anorthositic crystals only form below 1 GPa, i.e. for Mars less than 90 km deep, the volume of crystals that can form seems too small to form a flotation crust. Nevertheless, it is also proposed that NWA 7034 evolved clasts formed from a similar mechanism than lunar KREEP-enriched rocks (Nyquist et al., 2016). They would be formed by extraction of residual melts from the crystallising magma ocean, which would be highly enriched in incompatible elements. However, crystallisation experiments have shown that the composition of the molten fraction of the mantle remains predominantly basaltic until the end of crystallisation (Collinet et al., 2015). Payré et al. (2022) also proposed that a partial magma ocean can preserve felsic components from planetesimals that formed Mars. In contrast to this primary origin for a felsic component, a secondary origin is also proposed. Udry et al. (2018) show that the chemistry and mineralogy of the differentiated rocks found at Gale are similar to that of differentiated terrestrial intraplate volcanic rocks. The felsic rocks would in this case come from fractional crystallisation, in the presence of water, of an ultramafic or mafic melt similar in composition to the Martian crust.

It is on a secondary origin that we will focus in this Chapter. Indeed, on one-plate planets like Mars, there exists a positive feedback mechanism between crustal thickness and melt extraction. This mechanism, described in Chapters 3 and 4, enables

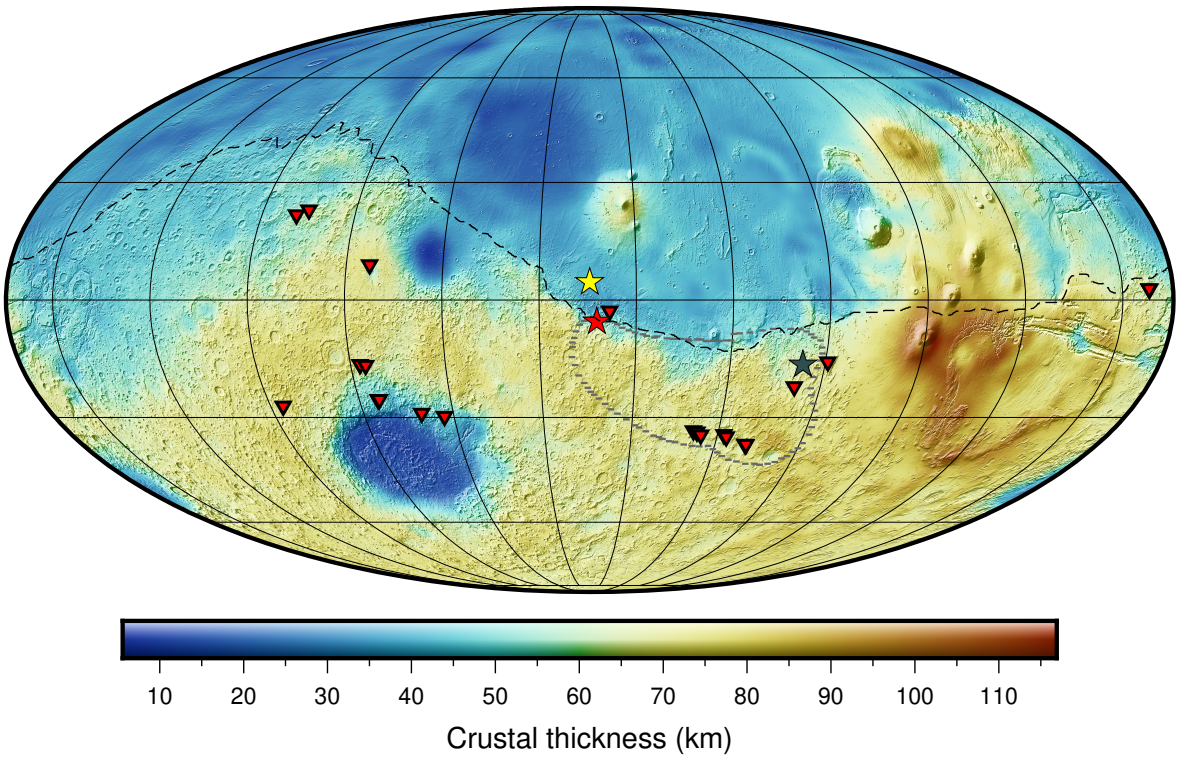

FIGURE 5.1 – Thickness of the crust of Mars and feldspar-rich rocks observations. The map is obtained using a crustal density of 2900 kg m^{-3}. For this model, the mantle density profile is that of Khan et al. (2021) and the crustal thickness at the Insight landing site (yellow star) is 39 km (Knapmeyer-Endrun et al., 2021). The black dashed line represents the dichotomy boundary from Andrews-Hanna et al. (2008a). The dotted grey line marks the boundary of the Terra Cimmeria-Sirenum province (Bouley et al., 2020). The red star marks the location of the Gale crater (Cousin et al., 2017). The grey star marks the location of Khujirt crate (Lagain et al., 2022). The red triangles represent the locations of feldspar-rich outcrops revealed by orbital spectroscopy (Carter and Poulet, 2013; Wray et al., 2013; Payré et al., 2022; Phillips et al., 2022). This map is presented on a Mollweide projection with a central meridian of 136°E longitude.

the formation of regions of thick crust on a hemispheric scale, such as the Highlands (Bonnet Gibet et al., 2022). This mechanism further implies that regions of thicker crusts, characterized by a larger amount of heat sources, a thinner lithosphere and increased magmatism, are also marked by higher temperatures at the crust base. Here we investigate whether crustal temperatures in thick crust regions may be maintained above the basalt solidus temperature during crust construction, which would allow for the formation of a partially molten layer at the base of the crust. If such a layer is stable over time during the extraction of the crust it would allow the formation of secondary evolved melts and hence differentiated rocks by extraction of the melt enriched in water and silica. In this scenario, felsic rock formation would be concomitant to crustal construction and dichotomy formation on Mars. This could explain the spatial correlation between the thick crust and differentiated rocks as observed on Mars.

In this Chapter, we do not produce any new calculations, but we use the results of our systematic exploration and our inversion in the asymmetric case with crustal extraction detailed in Chapter 4. The asymmetric case in Chapter 4 does take crustal melting into account during thermal evolution, so we intend to look at these same results but in the light of other quantities. We first study when crustal melting is observed in our a systematic exploration over the reference permeability and reference viscosity. Then, we study the set of inverted asymmetric models, which are able to sustain crustal melting in the Southern Hemisphere. We then look at the difference in distribution between these models and the global distribution in order to identify the model parameters that fit the observations and allow crustal melting to occur in the Southern Hemisphere. We identify two possible timings for crustal melting that emerge from the joint distributions and examine various thermal evolution scenarios that illustrate them.

5.2 Crustal solidus

The solidus of the crust is crucial to this Chapter and should be discussed before presenting our results. We have defined an anhydrous solidus for the crust (Figure 5.2, grey curve) with a temperature at 0 pressure close to that of a terrestrial basalt (1270 vs. 1320 K) and with a slope (100 K GPa^{-1}) typical of mafic rocks. This anhydrous solidus is modified by the presence of water in the melt fraction. Water enrichment of the magma is limited at low pressure by saturation. Saturation increases with pressure, allowing more and more water to be soluble in the magma. Based on our parameterisation, we define a saturation solidus (Figure 5.2, black curve) where the water content of the magma is always equal to saturation and thus where the effect of water is maximum. This solidus at 0 pressure is similar to the anhydrous case, because solubility is zero, and then decreases to colder temperatures as pressure and hence depth increase. Our saturated solidus decreases significantly with pressure, which is not an instinctive behaviour but is expected as shown by the saturated solidus proposed by Green and Ringwood (1967) for terrestrial basalts in subduction zones (Figure 5.2, blue dashed

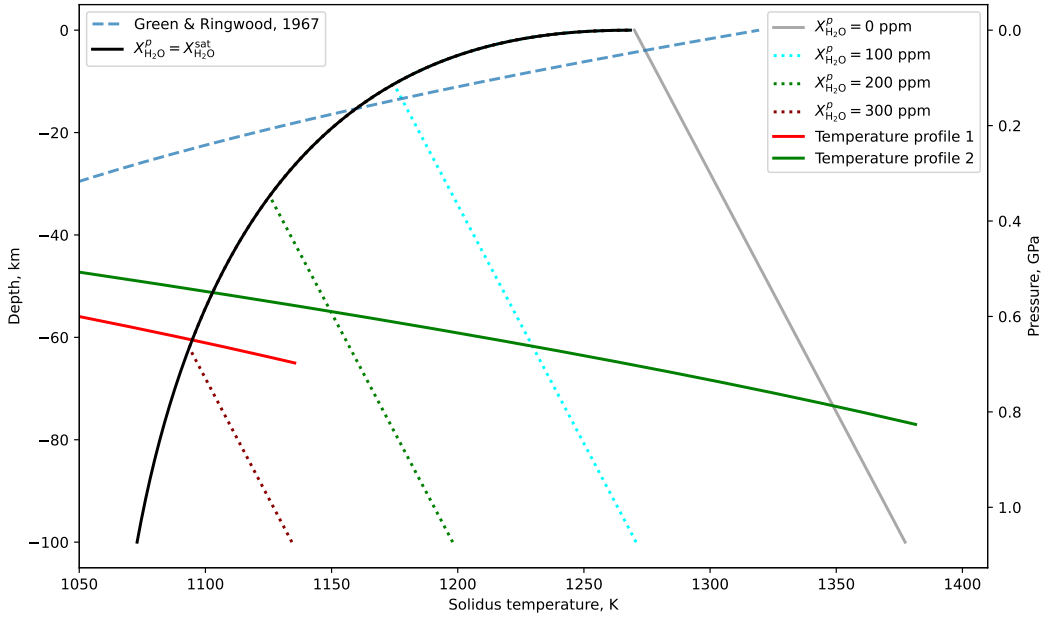

FIGURE 5.2 – Solidus of the crust according to the parameterisation described in Chapter 2, Section 1 2.4.3. The solid black curve represents the water-saturated solidus and the solid grey curve the anhydrous solidus. The dotted curves represent the crust solidus for increasing values of water content from 0 ppm to 300 ppm in 100 ppm increments. The dashed blue curve represents the saturated solidus proposed by Green and Ringwood (1967). The green and red solid curves represent two examples of temperature profiles in the crust (see text).

curve). The slope of their saturated solidus is much steeper and decreases to 900 K at 1 GPa, but these basalts are made up of hydrated minerals such as hornblende with a larger water content than expected for the Martian deep crust. In the case where the melt fraction is undersaturated with water, the solidus of the crust follows the slope of the saturated solidus until it reaches the depth at which the magma becomes undersaturated and the solidus then follows the same slope as the anhydrous solidus (Figure 5.2, dotted colored curve). We can then define the crustal melt fraction, which is calculated similarly to the average melt fraction in the mantle (Equation 2.13). The partially molten volume may be expressed as a thickness from the base of the crust to the depth at which the melt fraction becomes zero.

Partial melting of the crust is obtained if the temperature profile intersects the solidus curve of the crust before reaching the mantle. The thicker the crust and the larger the temperature gradient in the lithosphere, the more likely this is. The thicker the crust, the lower the saturated solidus temperature is, and the higher the temperatures at the base of the crust are. So if we assume that the crust is sufficiently enriched in

water, the two cumulative effects of a colder solidus and a hotter crust are going to facilitate melting at depth. To illustrate this, Figure 5.2 shows two hypothetical temperature profiles in the crust. These temperature profiles are obtained by considering a steady state in the crust with a temperature condition at the surface ($T_s = 220$ K) and a flow condition at the base of the crust ($q_{\text{moho}} = 26$ mW m^{-2}). The temperature as a function of depth in the crust (z) can then be expressed as follows :

$$T(z) = -\frac{HD_{cr}}{2k_{cr}}z^2 + \frac{q_{\text{moho}} + HD_{cr}}{k_{cr}}z + T_s, \tag{5.1}$$

where $k_{cr} = 3$ W m^{-1} K^{-1} is the thermal conductivity of the crust, $H = 5 \times 10^{-7}$ W m^{-3} the internal heating in the crust and D_{cr} the thickness of the crust. The only difference between the two temperature profiles is the crust thickness. Temperature profile 1 (Figure 5.2, red curve) considers a crust of 65 km, which corresponds to the average thickness of the crust in the Southern Hemisphere obtained from the inversion in an asymmetric geometry in Chapter 4. Temperature profile 2 has a higher thickness of 77 km (Figure 5.2, green curve) to show the effect of a thicker crust. The thickness effect is important on the temperature profile because it affects not only the temperature at the base but the whole temperature profile. Here we have two cases where the temperature exceeds the solidus at the base of the crust because the parameters chosen correspond to a crust formed very early with a fairly thin lid, which explains the choice of a large heat flow at the base of the crust. We can see that for profile 2, the temperature can even exceed the anhydrous solidus. If we consider the saturated solidus, we obtain a molten thickness of 5 km for profile 1, with an average molten fraction of 4%. Profile 2 has a crust 12 km thicker, so the melted thickness rises to 26 km with an average melt fraction of 27%. A slight increase in the thickness of the crust can therefore largely increase the extent of partial melting of the crust.

The melt fraction in the crust is monitored and quantified with 4 different quantities :

— the maximum average melt fraction of the partially molten volume in the crust,

— the maximum molten thickness, which represents the maximum molten volume of the crust,

— the total time over which the crust is partially molten,

— the age at which crustal melting ends.

The last two quantities are used to describe the timing of crustal melting. We assume that the melt fraction onset time is the difference between the melt fraction end age and the melt fraction duration, which is true when there is a single melt fraction episode. If there are two separate episodes the starting would be older. This second case is quite rare, and we still manage to describe it despite this simplification.

5.3 Systematic exploration

5.3.1 Exploration description

We use the results of the systematic exploration described in Chapter 4, for which the full version of the thermal evolution model described in Chapter 2 is used. The exploration of parameters presented in this Chapter is the same as that presented in Chapter 4. The parameters are given in Tables 2.1. The reference viscosity ranges from 10^{19} to 10^{22} Pa s and the reference permeability from 10^{-12} to 10^{-7} m^2. Note that the water content of the primordial mantle is taken to be 1000 ppm, a value which implies a saturated solidus for the crust in any case (Figure 5.2).

5.3.2 Exploration results

The crust thicknesses obtained are the same as those described in Chapter 4 (Figure 5.3a). The thickest crusts are obtained at low permeability ($\approx 10^{-11}$ m^2) and low viscosity ($\lesssim 10^{20}$ Pa s). The crustal dichotomy is maximum at a viscosity of $\approx 10^{20}$ Pa s and permeabilities of $\approx 10^{-9}$ to 10^{-11} m^2 (Figure 5.3b).

In the southern crust, for $\eta_0 \gtrsim 10^{20.5}$ Pa s there is no melt in the crust and below this value, the melt fraction increases rapidly when the reference viscosity decreases, reaching more than 50% at 10^{20} Pa s (Figure 5.3c). This is explained by both thicker crusts and thinner lids at the time of crust extraction. At low permeability, the maximum melt fraction decreases with permeability. The crust is extracted less quickly and becomes thick enough to melt only later in the thermal evolution, when the lithosphere is colder.

In the Northern Hemisphere, crustal melting is obtained at lower viscosity because the crustal thicknesses are lower (Figure 5.3d). Viscosities required to reach melting in the Northern Hemisphere are even lower for parameters inducing larger crustal thickness dichotomy. The growth of the crustal dichotomy preferentially thickens the crust of the Southern Hemisphere at the expense of the Northern Hemisphere, which has then a thinner crust that is less likely to melt. The crustal dichotomy causes a major difference in melt fraction at the base of the crust, with a Southern Hemisphere where crustal melting can be significant and a Northern Hemisphere where it is low or even absent. It emerges that a relatively small part of the range of parameters that fit the data enables the southern crust to melt during the thermal evolution of Mars and that a negligible part enables it for the Northern Hemisphere (Figure 5.3c-d, black curve). In this parameter range, the maximum crustal melt fraction is also relatively low (< 0.25).

The molten thickness in the crust for each hemisphere evolves in the same way as the maximum average melt fraction (Figure 5.3e). The lower the viscosity and the thicker the crust, the greater the molten thickness. The amount of melt generated thus increases very quickly as the viscosity decreases and crust thickness increases. It does

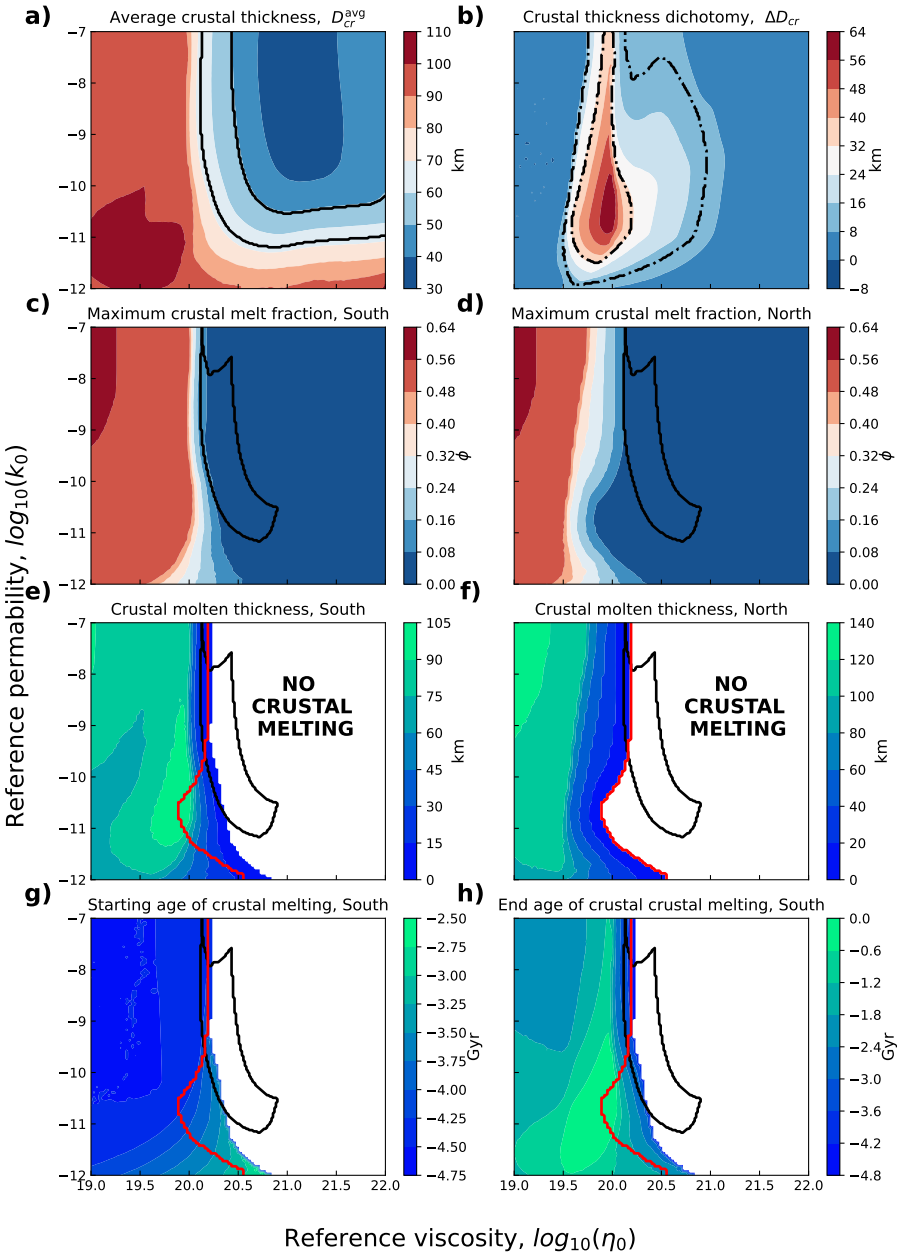

FIGURE 5.3 – Systematic exploration of (k_0, η_0) for our reference case, see Table 2.1, for η_0 (x-axis) between 10^{19} and 10^{22} Pa s and k_0 (y-axis) between 10^{-12} and 10^{-7} m^2. In colour scale : (a) Average crustal thickness (km), (b) Crustal thickness dichotomy (km), $D_{cr}^S - D_{cr}^N$, (c) Maximum crustal melt fraction in the south, (d) Maximum crustal melt fraction in the north, (e) Thickness of the partially molten layer (km) in the southern crust, (f) Thickness of the partially molten layer (km) in the northern crust, (g) Onset age of crustal melting (Gyr) in the South, (h) Duration of crustal melting (Gyr) in the South. On (a) The black outline represents the range of parameters that fit the constraints on crustal thickness ($50 < D_{cr} < 72$ km). On (b) The dash-dotted black outline shows the range of parameters that fit the crustal dichotomy constraint ($12 < |\Delta D_{cr}| < 33$ km). (c,d,e,f,g,h) The black outline represents the range where both constraints are met. (e,f,g,h) The red outline represents the limit between the parameters with and without melting in the northern crust.

not seem possible to generate high average melt fractions in thin molten layers. Within the range of parameters that fit the observations, molten thicknesses do not exceed 45 km in the Southern Hemisphere, so at most just over half the thickness of the Southern Hemisphere crust can melt partially ($D_{cr}^{S} = 82.4$ km at most Section 3.4.2).

For permeabilities above 10^{-9} m^2, the age at which crustal melting began corresponds to the start of the thermal evolution 4.5 billion years ago (Figure 5.3g). Below 10^{-9} m^2, the lower the permeability and the higher the viscosity, the later the onset of melting. Late onset of crustal melting corresponds to low maximum melt fraction and maximum molten thickness. These late-onset cases correspond in part to crustal melting in the south and not in the north on the Right of the red line on Figure 5.3. The larger the dichotomy and the thicker the crust in the Southern Hemisphere, the longer the crustal melting be sustained. In extreme cases, melting can last until the present-day (Figure 5.3h). For permeabilities larger than 10^{-9} m^2 and viscosities larger than 10^{20} Pa s, the end age is very early in the thermal history of Mars ($\lesssim -4.3$ Gyr). In these cases, crustal melting lasts a short time and the difference in melt fraction between both hemispheres is rather small. On the other hand, at lower permeability, the onset of melting is delayed, and the end age and the start age of crustal meeting are further apart, resulting in a longer duration of crustal melting. This seems to be the scenario that allows for melting only in the south.

5.4 Results of the inversion on crustal melting

5.4.1 Inversion with crustal melting

We used the set of models obtained by inverting our thermal evolution model in an asymmetric geometry from Chapter 4. This set contains $N_{\text{asym}} = 9.61 \times 10^6$ models whose distribution reproduces our observations on the crust and mantle (see Section 4.2). These models calculate the melt fraction at the base of the crust, although crustal melting does not influence the inversion. Here, we look at the proportion of models that are able to maintain partial melting at the base of the crust, which corresponds to thermal evolutions where the average maximum melt fraction is non-zero in the crust. The proportion of models with a non-zero maximum crustal melt fraction in the Southern Hemisphere is 12.37% and 1.33% in the Northern Hemisphere. The first important conclusion is then that crustal melting in the Southern Hemisphere is significant and an order of magnitude more likely than that in the Northern Hemisphere. The proportion of models with crustal melting in the Southern Hemisphere but not in the Northern Hemisphere is 11.04%, which is exactly the difference between the two previous percentages. This means that melting in the north is only possible in models with melting in the Southern Hemisphere. We define a subset of models having sustained crustal melting in the Southern Hemisphere and not in the Northern Hemisphere, i.e. a set that is part of the initial set. This subset represents $N_{\text{MELT}} = 1.06 \times 10^6$ models, or 11.04% of the total number of models.

5.4.2 Marginal distributions

The distribution in parameter space formed by the subset of models with a crustal melting episode only in the Southern Hemisphere (red histograms, Figure 5.4) diverges significantly from the distribution obtained for all models fitting our 4 constraints (blue curves, Figure 5.4). The marginal distribution for the reference viscosity for models with crustal melting in the Southern Hemisphere (Figure 5.4a) is shifted towards the reference viscosities with a mean of 1.35×10^{19} Pa s in contrast to a mean of 2.63×10^{20} Pa s for all models. The lower the viscosity, the thinner the lid and the thicker the crust, which favours crustal melting.

Low permeabilities, around 10^{-10} m^2, are less frequent in this subset than for all models (Figure 5.4b). High permeabilities ($> 10^{-9}$ m^2) result in large crustal extraction rates and lead to thick crusts very early. The crust forms when the lithosphere is thin, which is favourable to crustal melting. Lower permeabilities ($< 10^{-9}$ m^2) imply longer crustal extraction hence crust growth in a thicker and thus colder lid, less favourable to crustal melting. The average permeability is nevertheless fairly similar, $\approx 1.33 \times 10^{-9}$ m^2 for the subset of models with crustal melting and $\approx 9.44 \times 10^{-10}$ m^2 for the full set.

The initial temperatures are warmer on average for models with crustal melting than for all models (Figure 5.4c). This is because a warmer mantle leads to a warmer temperature at the base of the lid leading to larger temperature gradients in the lid (Figure 5.4d). Activation energies are also on average larger in the case of crustal melting than for all models. The higher the activation energy, the hotter the temperature at the base of the lid is (Equation 2.3). However, the jump in temperature across the upper boundary layer is then smaller, resulting in a lower convective heat flow. The lid thickens faster with a higher activation energy, but this effect is counterbalanced by low reference viscosities. An initially warmer core ($\Delta T_c^0 = 167K$) is also consistent with a warmer mantle initially (Figure 5.4f). In particular, lower viscosities help to extract heat more efficiently towards the mantle (Equation 2.8 & 2.4).

The mean crustal density is $\simeq 3000$ kg m^{-3}, in the case of melting compared with the mean of all models, $\simeq 2833$ kg m^{-3} (Figure 5.4e). The higher the crustal densities, the thicker the crusts and the larger the amplitude of the north-south difference in crustal thickness which maximises the southern crustal thickness. Saturated solidus temperatures decrease and the temperature at the base of the crust increases as the thickness of the crust increases which explains why crustal densities are shifted on average towards rather high values.

The lower the thermal conductivity, the larger the dichotomy and the warmer the temperature at the base of the crust is. The combination of these two effects strongly favours melting at the base of the southern crust. The distribution of thermal conductivities is therefore shifted towards lower values to obtain melting at the base of the

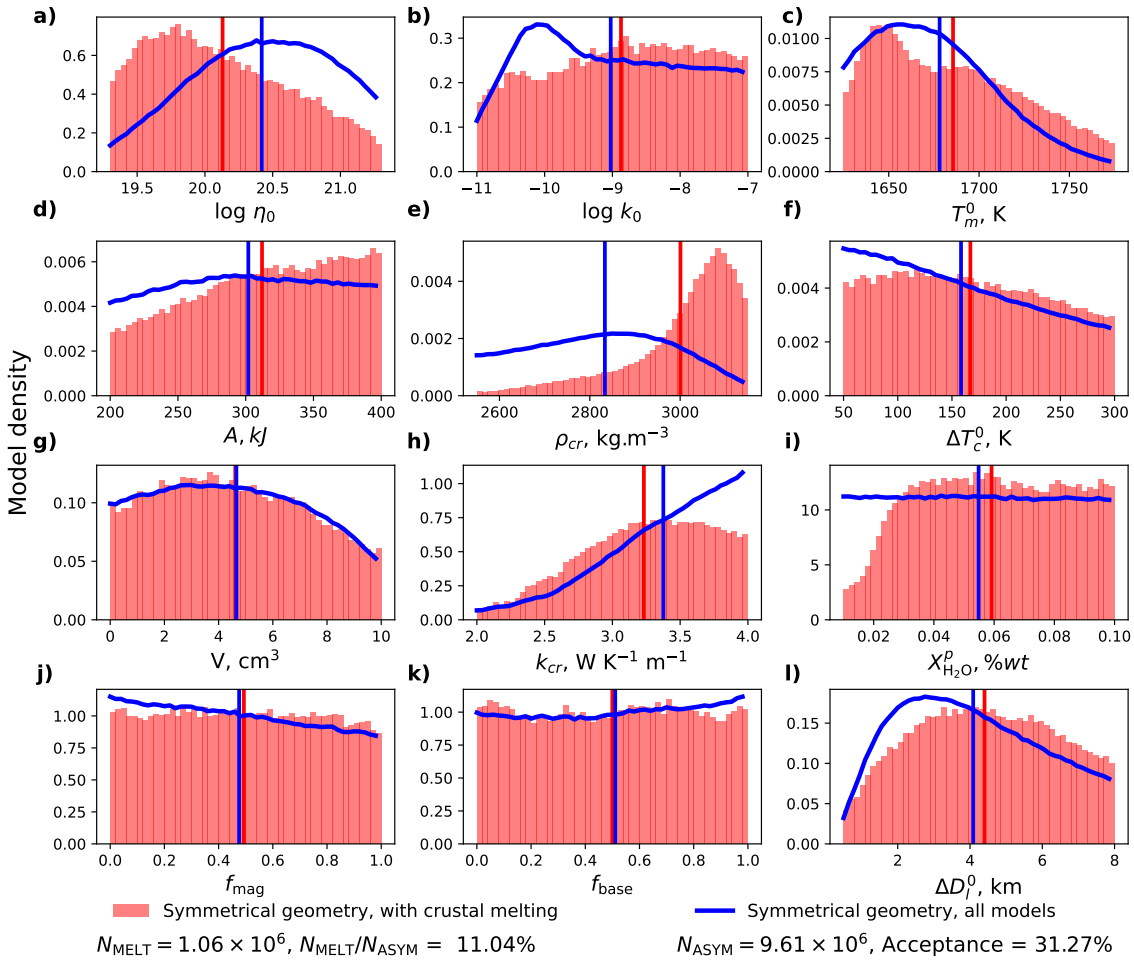

FIGURE 5.4 – Projection along different inverted parameters of the probability distribution of our model, also known as marginal distributions. The red histograms represent the distribution of N_{MELT} models with crustal melting in the south which represent 11.04% of the total models fitting our 4 constraints. The distribution of the N_{ASYM} models from the asymmetric case give the blue curves, representing the histogram envelopes. The vertical bars give the mean value of the histogram for the corresponding colour. **a)** Reference viscosity of the mantle (log scale), **b)** Reference permeability of the mantle (log scale), **c)** Initial temperature of the convective mantle, **d)** Activation energy, Equation 2.1 (kJ mol^{-1}), **e)** Homogeneous crustal density (kg m^{-3}), **f)** Initial overheating of the core (K), **g)** Activation volume (cm^3), **h)** Thermal conductivity of the crust (W m^{-1} K^{-1}), **i)** Primitive mantle water content (wt% H_2O), **j)** Fraction of magmatism **k)** Fraction of basal magmatism, **l)** Initial perturbation in lithosphere thickness (km).

southern crust (Figure 5.4l), giving an average value of 3.23 W m^{-1} K^{-1} compared to 3.38 W m^{-1} K^{-1} for all models. As crustal densities are greater, the expected dichotomy is larger. Initial perturbations are thus expected to be slightly larger for models with crustal melting than for the global set (Figure 5.4h). The average initial perturbation increases to 4 km, which is still a relatively small difference. However, there is no difference between the two model distributions for the activation volume, which also favours the growth of large dichotomies. We obtain the same mean in both cases with an activation volume of $\simeq 5$ cm^3.

The water content of the primordial mantle modifies the maximum reduction in solidus temperature. The larger the water content, the easier it is to reach the saturated solidus at depth in the crust and thus to melt. The distribution of this water content is constant above 300 ppm but drops sharply below (Figure 5.4i). 300 ppm of water in the primordial mantle would be sufficient to allow crustal melting. As with all models, the fractions of the different modes of magmatism are rather uniformly distributed (Figure 5.4j-k). The heat provided by magma is therefore not essential to the melting of the crust. Large temperatures at the base of the crust and a large enough pressure to reduce the hydrated solidus temperature are sufficient to reach melting.

5.4.3 Posterior distribution of different ouput

The distribution of models allowing melting in the crust diverges from that of all models with regard to the forecasts provided for the structure of Mars at the present day. The low reference viscosities required to observe crustal melting result in a potential mantle temperature distribution that is colder than in the global one (Figure 5.5a). The average temperature obtained for the subset is 1575 ± 52K, significantly lower than the 1621 ± 55 K for the global distribution, but still within the distribution of the observation. In contrast, the distribution obtained for the thickness of the lid at the present day is the same in both cases, 450 ± 50 km (Figure 5.5b). Lid thickness is therefore not a highly useful observation to constrain the thermal evolution of Mars. The low reference viscosities and the cold mantle lead also to colder core temperatures in the case of melting (Figure 5.5f).

Thick crusts favour melting at the base of the crust, because of hydrated solidus temperatures and warmer temperatures at the base of the crust. The distribution for the thickness under InSight is therefore slightly shifted towards larger thicknesses (Figure 5.5c). But above all, it is the crustal density that constrains crustal thicknesses to large values, with a mean of 65 km in the subset with melting and 57 km in the full set. The thicker crusts are associated with large dichotomies in the case of crustal melting, $\approx$ 30 km on average (Figure 5.5d), implying very thick crustal thicknesses in the Southern Hemisphere, favourable to melting. The consequence of a very thick crust is that most of the radioactive elements are in the crust, accentuating the low temperatures of the mantle today (Figure 5.5e).

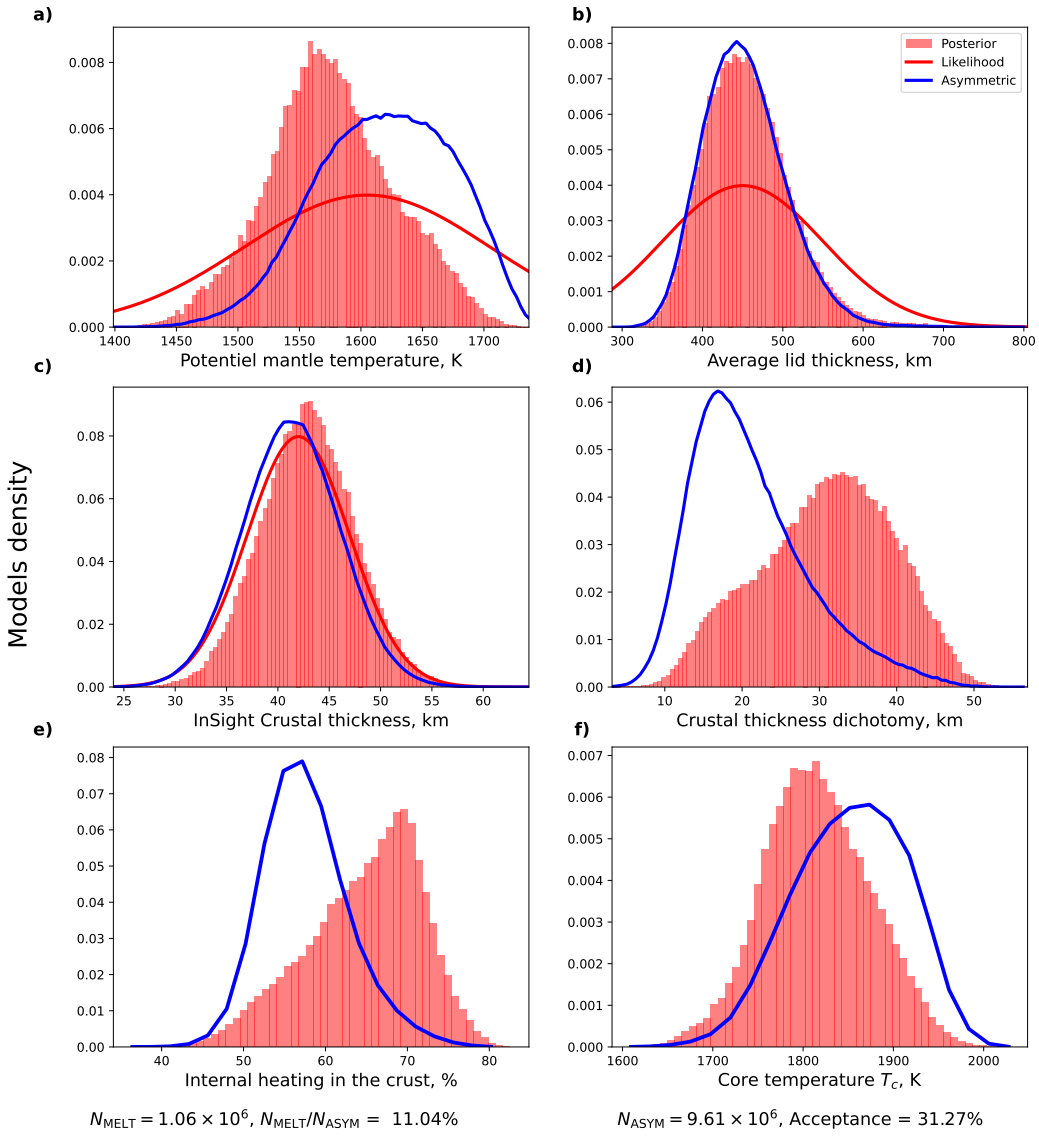

FIGURE 5.5 – Posterior marginal distribution for the observations and various outputs (red histograms and blue curves) with the prior distribution of the observations (red lines). The red histograms represent the distribution of N_{MELT} models showing crustal melting which represent 11.04% of the total of inversed models. All the N_{ASYM} models from the asymmetric case give blue curves, representing the histogram envelopes. Red curve are the Gaussian distributions for the likelihood defined in Section 4.4.3. **a)** Potential mantle temperature at the present day (K), **b)** Average lid thickness at present-day (km), **c)** forecast crustal thickness below InSight at present-day, Equation 4.2 (km), **d)** Dichotomy in crustal thickness at present-day (km), **e)** Radioactive heating in the crust (% of total), **f)** Maximum molten thickness in the southern crust (km).

5.4.4 Examples of thermal evolution with crustal melting

The model with the highest posterior likelihood probability and the model built from the mean of the parameters for the subset of models showing crustal melting in the south are two interesting examples of thermal evolution as they each represent two end-members cases.

Best fit model The model with the best fit (Figure 5.6) is characterised by a high reference permeability and a relatively low reference viscosity. The initial state is composed of an early cold mantle, a thin lid, an intermediate core overheating and a strong initial perturbation. These parameters lead to a rapid extraction of the crust and a rapid formation of the dichotomy, in less than 100 Myr (Figure 5.6a). This very rapid extraction of the crust with a thin lid thickening very quickly results in very hot temperatures at the base of the crust, up to 1200 K in the south and 1100 K in the north (Figure 5.6b). The larger temperature and larger pressure at the base of the crust in the Southern Hemisphere allow the crust to melt, unlike in the Northern Hemisphere (Figure 5.6d). The temperature at the base of the crust then drops quickly as the lid continues to grow, despite the increase in the potential temperature of the mantle and the second phase of crustal extraction in the Southern Hemisphere (Figure 5.6c). The melting episode is thus brief, starting after 15 Myr and ending 20 Myr later (Figure 5.6d). The maximum melt fraction reaches 5% over a thickness of 3 km (Figure 5.6e). The volume of magma that is produced would be small and over a very short period.

Mean model The second example is a model that uses the mean of the inverted parameters (Figure 5.7). The crust initially thickens rapidly (Figure 5.7a), but unlike the in the first example, the temperatures at the base of the crust in the southern and northern hemispheres do not allow to maintain melting (Figure 5.7b). In fact, the thicknesses formed during this first phase of rapid extraction are thinner than in the previous case. However, in this case, extraction in the south continues significantly for a further 1 Gyr, creating a very thick crust in the Southern Hemisphere ($\simeq$ 80 km) and therefore a significant dichotomy ($\simeq$ 40 km). This slower but significant growth of the southern crust leads to a gradual increase in temperature at its base. At the same time, the growth of a very thick crust results in the lid becoming thinner in the south while the mantle potential temperature is still close to its maximum (Figure 5.7c). These three combined effects (a warm mantle temperature, a thin southern lid and a thick southern crust) lead to a major episode of crustal melting. Melting starts after 800 Myr and lasts for about 1 Gyr. The average melt fraction reaches 12% in the Southern Hemisphere (Figure 5.7d) over a thickness of 12 km (Figure 5.7e). This represents

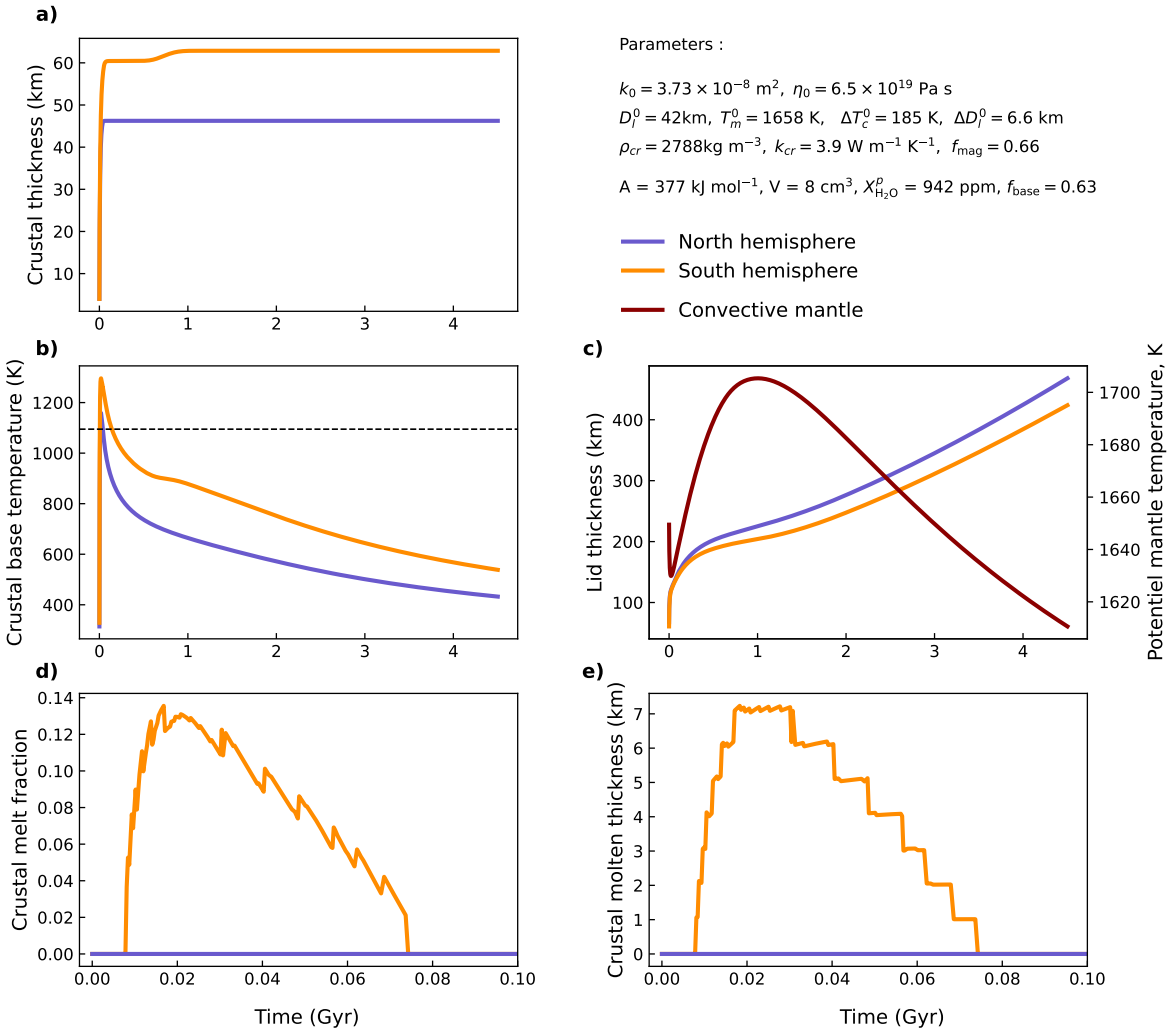

FIGURE 5.6 – Thermal evolution for the best fitting model with crustal melting. Evolution of the **a)** crustal thickness, D_{cr}, **b)** Temperature at the base of the crust, **c)** Lid thickness D_{L}, (left y-axis) and potential mantle temperature (red line), T_p (right y-axis), **d)** average crustal melt fraction, ϕ_{cr}^{avg} and **e)** Thickness of the molten layer in the crust in the North (blue lines) and in the South (orange lines). (b) The dotted black line corresponds to the solidus temperature calculated at the maximum depth reached by the southern crust. (d) & (e) The x-axis is between 0 and 100 Myr.

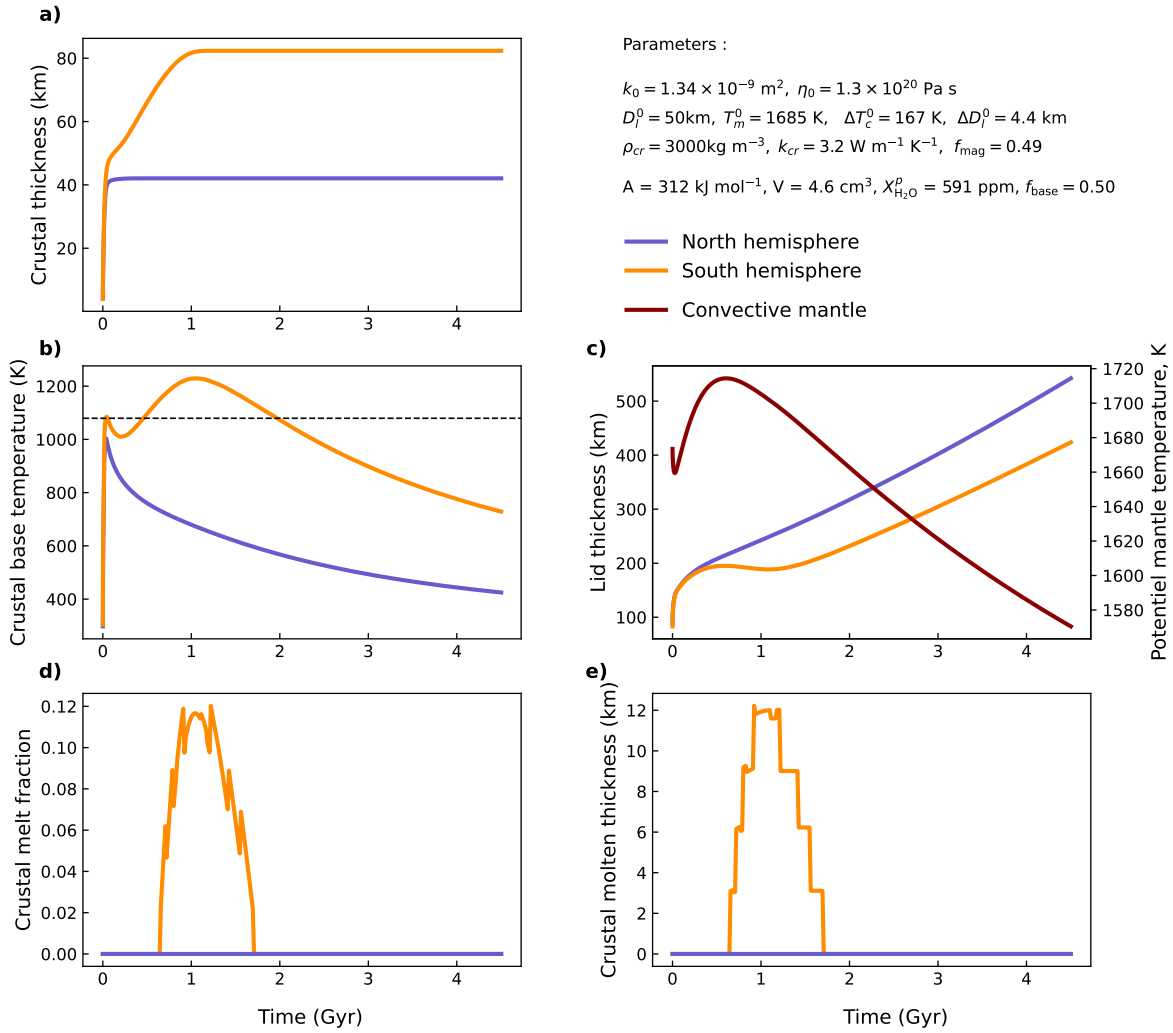

FIGURE 5.7 – Thermal evolution for the model built from the mean of the model parameters in the subset of models showing crustal melting. Evolution of the **a)** crustal thickness, D_{cr}, **b)** Temperature at the base of the crust, **c)** Lid thickness D_{L}, (left y-axis) and potential mantle temperature (red line), T_p (right y-axis), **d)** average crustal melt fraction, ϕ_{cr}^{avg} and **e)** Thickness of the molten layer in the crust in the North (blue lines) and in the South (orange lines). (b) The dotted black line corresponds to the solidus temperature calculated at the maximum depth reached by the southern crust.

a rather large volume of potentially generated magma. The melting maximum corresponds to the end of crustal growth and lasts for 500 Myr after the end of crustal growth.

Another example The last example is complementary to the two previous ones because it gives an interesting intermediate case (Figure 5.8). It is obtained using the parameters of the systematic exploration (Table 2.1) with a reference permeability of 10^{-10} m^2, a reference viscosity of 10^{20} Pa s and an initial mantle temperature of 1680 K. Crustal extraction is initially very rapid in both hemispheres, creating only a small dichotomy (Figure 5.8a). Temperatures at the base of the crust reach the solidus in both hemispheres, allowing crustal melting everywhere (Figure 5.8b-d). The base of the crust then cools and crustal melting stops fairly quickly. As in the average case (Figure 5.7), the extraction of the crust in the south continues for the first billion years and also leads to a thinning of the lid when the mantle reaches its maximum temperature (Figure 5.8c). This leads to an increase in temperature at the base of the crust in the south after 1 Gyr (Figure 5.8b), which exceeds the hydrated solidus temperature, reduced by the increase in pressure. A second melting event takes place, this time only in the Southern Hemisphere, over a shorter duration ($\approx$ 500 Myr) than in the average case (Figure 5.8d). In this second episode, melting also reaches its maximum at the end of the extraction of the crust and is maintained for longer. In the first episode, the melt fraction reaches 20% in the south over 6 km, whereas in the second episode, melting only reaches 6% over 4 km (Figure 5.8d-e). So we have an example that is midway between our two end members : the average case and the best-fit case (Figure 5.7 & 5.6).

5.4.5 Crustal meltings output

Molten fractions in the southern crust range from 2% (the minimum fraction, Equation 2.31) to $\simeq$ 35%, with an average of 11% and a maximum probability at $\simeq$ 8% (Figure 5.9a). Crustal melting is obtained for crustal thicknesses in the Southern Hemisphere that are higher than in the full set of models. The thickness in the south is on average 77.7 km with a minimum thickness of $\simeq$ 60 km (Figure 5.9b). The molten thickness in the crust is of a few tens of kilometres with an average of 13 km (Figure 5.9c). Thinner molten layers are more likely than thick ones. The case with a molten thickness of around ten kilometres and a melt fraction of 10% on average seems to be the most common.

The total duration of melting in the Southern Hemisphere ranges from very short (<10 Myr) to around 2 billion years (Figure 5.9d). The average melting time is 730 million years, but this average hides a double distribution. Very short durations form a density peak, while durations around the mean form another maximum with a wider distribution around it. This double distribution can also be seen in the distribution for the end age of melting in the Southern Hemisphere (Figure 5.9e). Here, we also see

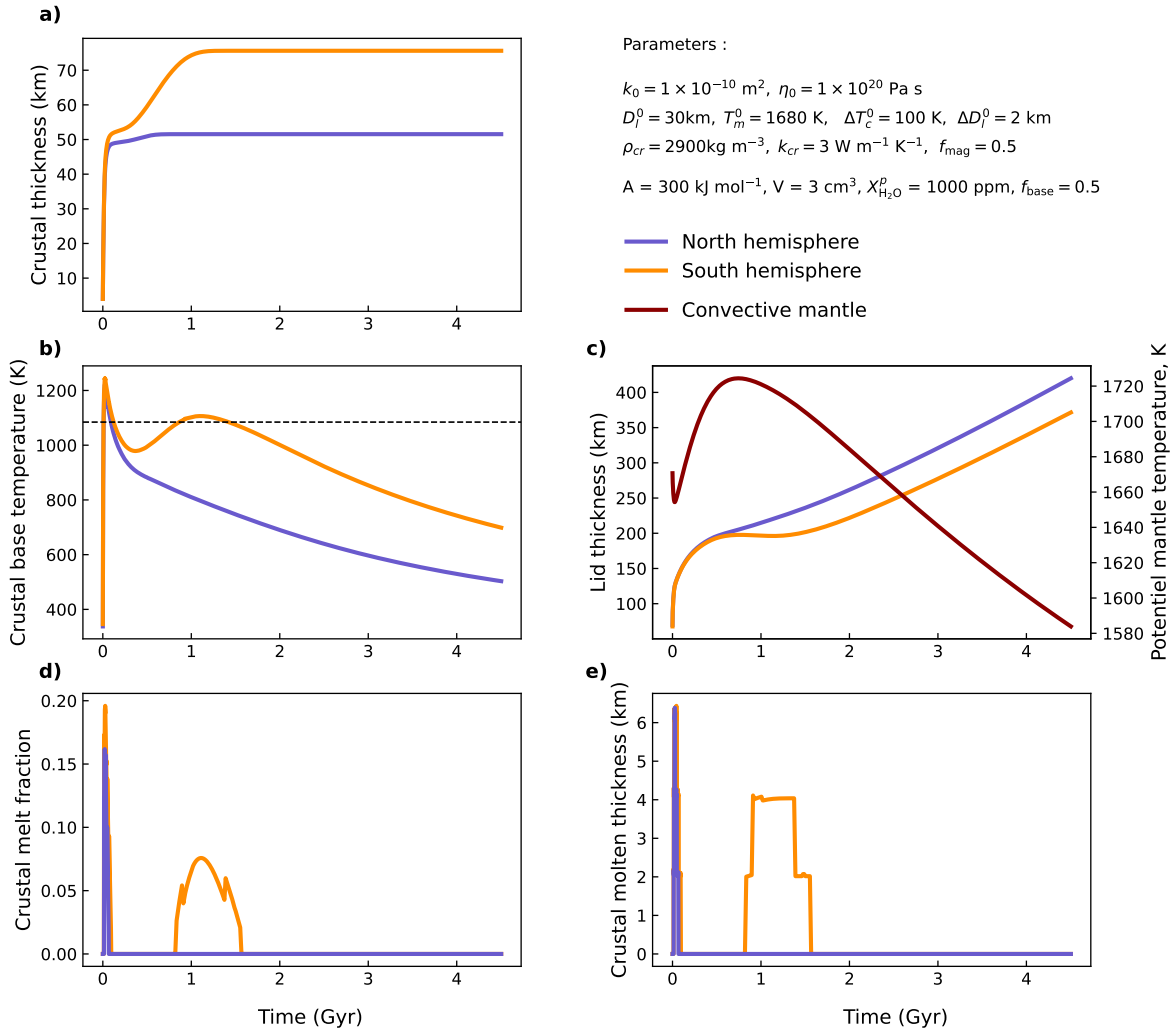

FIGURE 5.8 – Thermal evolution for a specific case with crustal melting. Evolution of the **a)** crustal thickness, D_{cr}, **b)** Temperature at the base of the crust, **c)** Lid thickness D_{L}, (left y-axis) and potential mantle temperature (red line), T_p (right y-axis), **d)** average crustal melt fraction, ϕ_{cr}^{avg} and **e)** Thickness of the molten layer in the crust in the North (blue lines) and in the South (orange lines). (b) The dotted black line corresponds to the solidus temperature calculated at the maximum depth reached by the southern crust.

a density peak shortly after the start of the thermal evolution, which is linked to the case with a short melting time (see the peak obtained at the start of melting 4.5 billion years ago, Figure 5.9f). There is also another broader peak with a start of melting a little after -4 Gyr and the end a little before - 3 Gyr, which corresponds well to the duration of melting around 750 Myr. We can therefore have two episodes of crustal melting, either a brief and very early melting episode and/or a late but longer melting episode.

To sum up, cases with melting in the southern crust are characterised by very thick crusts, particularly in the Southern Hemisphere, and by cold mantle and core temperatures due to low reference viscosities and to the significant extraction of large quantities of heat-producing elements. The crust in the Southern Hemisphere can be partially molten over a thickness of tens of kilometres. The melt fraction can also be significant and could produce rather large volumes of magma. Melting began either at the beginning of the thermal history (-4.5 Gyr ago) or much later (-3.8 Gyr ago) and the durations vary from $\approx 10s$ Myr to over a billion years. However, these values must be used carefully because we have neglected the potential eruption of the differentiated melt at the surface. The extraction and eruption of differentiated magma generate cooling because (i) the magma extracts its heat at the surface where it is dissipated more quickly (ii) this causes a downward advection of the crust due to surface deposition of this magma. These cooling terms would reduce these estimates, so they should be seen as upper bounds.

5.4.6 2D joint distribution

The joint distributions for the subset of models with crustal melting for different outputs linked to the melting of the crust can help to distinguish between the two episodes of crustal melting and better characterize them. Figure 5.10 shows some of these distributions. The maximum molten thickness in the Southern Hemisphere increases with the thickness of the final crust in that hemisphere (Figure 5.10a). Below 55 km of crust in the south, there is no melting and the thickness remains at ≈ 5 km up to 70 km of crust. Above this value the molten layer increases significantly. For some models, the molten thickness in the south reaches 30 km for a crustal thickness of 80 km in the south, i.e. more than a third of the thickness can be partially molten if the crust is very thick.

The melting duration in the Southern Hemisphere increases also with the average crust thickness. For thermal evolutions that form a crust of 55 ± 5 km thick, this duration remains below 200 Myr (Figure 5.10b). For these same models, the melting end time is older than ≈ -4.3 Gyr (Figure 5.10c), i.e. melting occurs at the very beginning of crust formation and lasts for a short duration. For models with crustal thicknesses larger than 60 km, melting durations increase with crustal thicknesses, reaching more than 1.5 Gyr for crusts with an average thickness of 70 km (Figure 5.10b). These thick

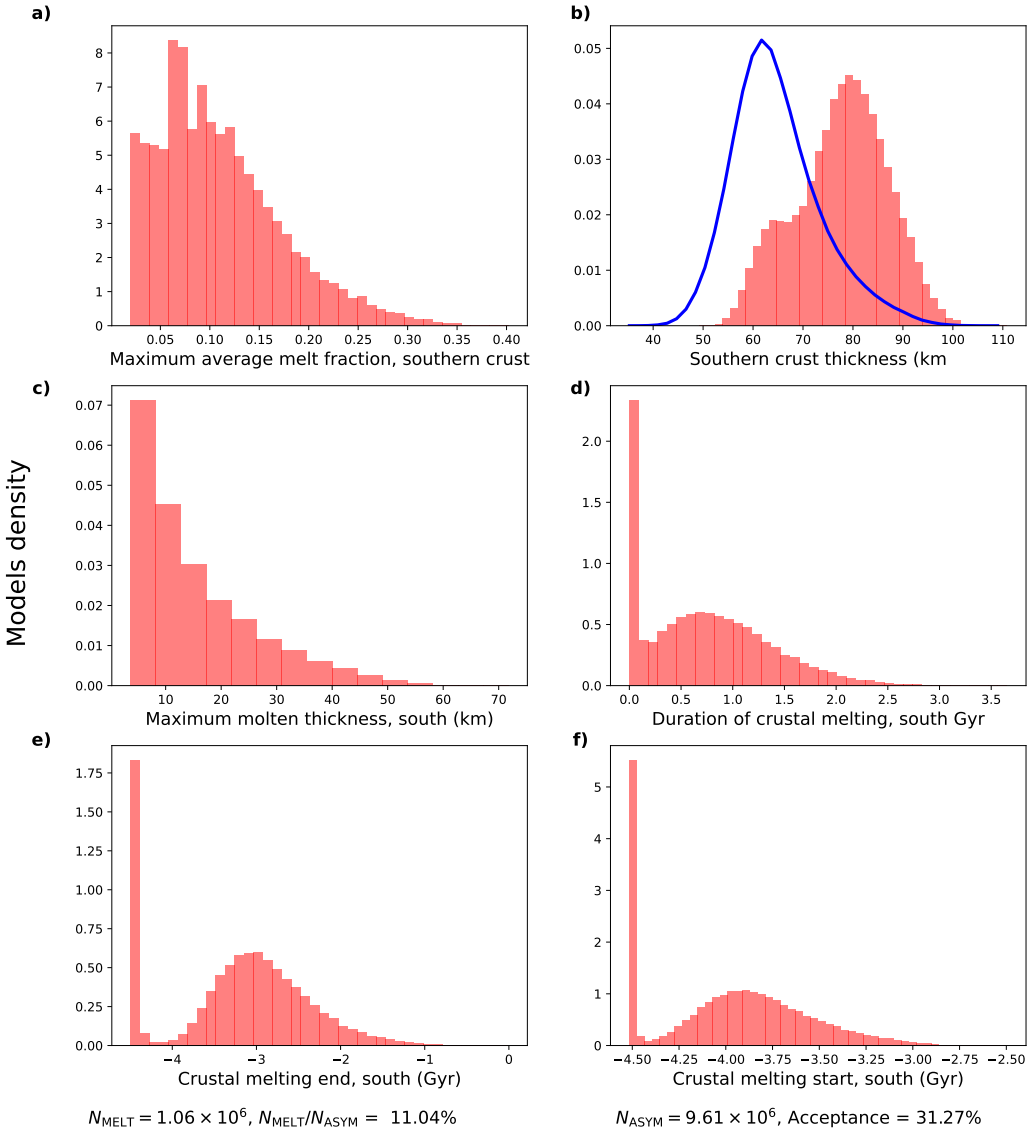

FIGURE 5.9 – Posterior marginal distribution of different model outputs. The red histograms represent the distribution of N_{MELT} models with crustal melting which represent 11.04% of the total of inverted models. All the N_{ASYM} models from the asymmetric case give blue curves, representing the histogram envelope. The red curve is the Gaussian distribution for the likelihood defined in Section 4.4.3. **a)** Maximum average crustal melt fraction (S) **b)** Southern crust thickness (km) **c)** Maximum thickness of the molten layer (S) **d)** Duration of crustal melting South Gyr, **e)** End age of crustal melting in the south, Gyr **f)** Start age of crustal melting in the south, Gyr

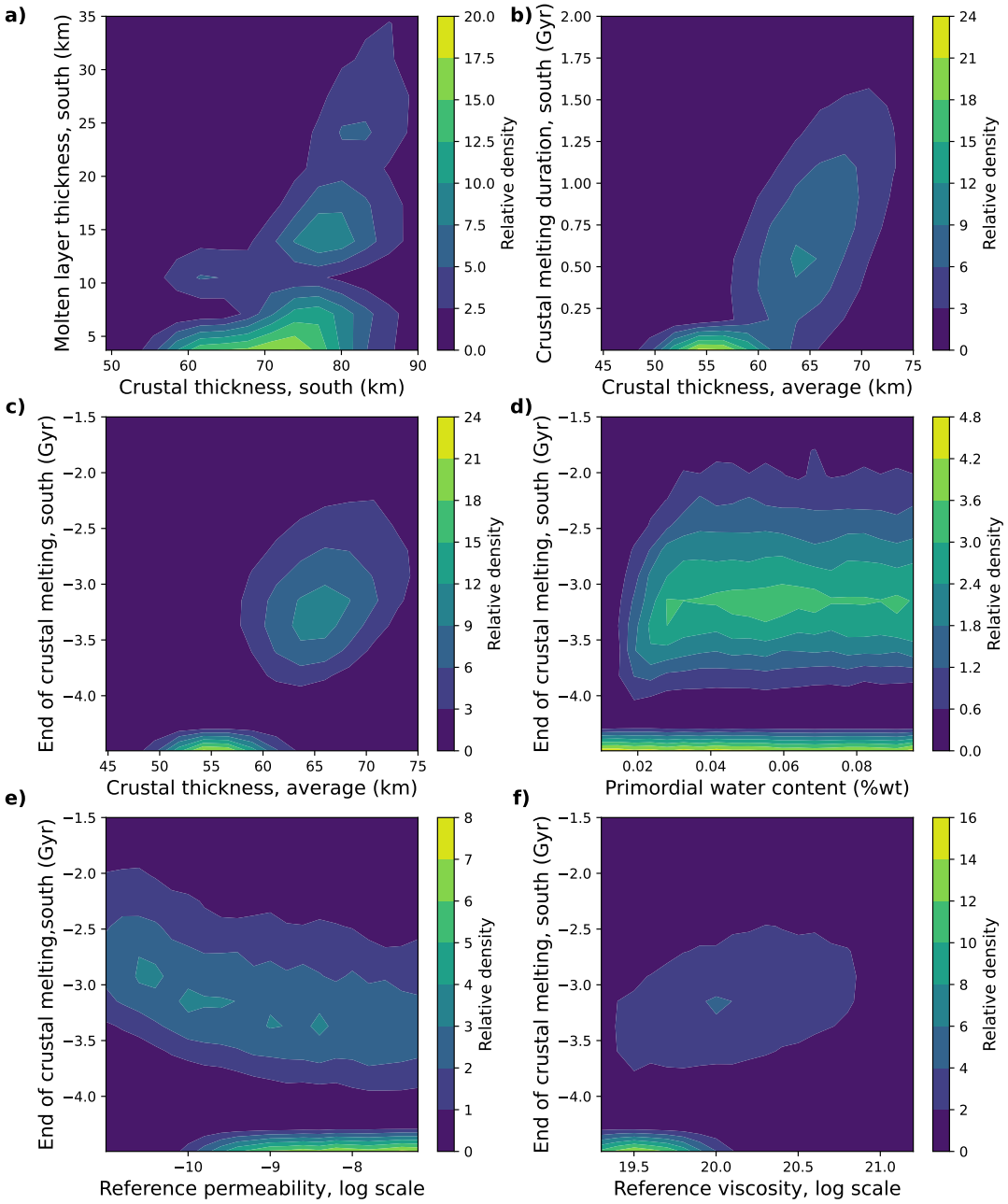

FIGURE 5.10 – The joint density distribution between **a)** Southern crustal thickness (x-axis, km) and maximum molten thickness, southern crust (y-axis, km) **b)** Average crustal thickness (x-axis, km) and Duration of crustal melting, southern crust (y-axis, Gyr) **c)** Average crustal thickness (x-axis, km) and end of crustal melting, southern crust (y-axis, Gyr) **d)** Water content of the primordial mantle (x-axis, $\%wt$ H_2O) and end of crustal melting, southern crust (y-axis, Gyr) **e)** Reference permeability (x-axis) and end of crustal melting, southern crust (y-axis, Gyr) **f)** Reference viscosity (x-axis) and end of crustal melting, southern crust (y-axis, Gyr). The density is divided by the average density to obtain a relative value.

crust models also correspond to rather young crustal melting ages with minimums between -4 Gyr and -2 Gyr (Figure 5.10c). We are thus left with two end-members : a short, early crustal melting and a long, late crustal melting. Since the distribution of melting duration is continuous, there is a hybrid case between our two end-members, in which melting starts early and finishes late with one or two episodes of melting.

In models characterised by an early and brief crustal melting episode, the water content of the primordial mantle has no influence (Figure 5.10d). In these cases, the reference permeability is high (10^{-9} m^2) and the reference viscosity is low ($< 10^{20}$ Pa s). Extraction of the crust is rapid but the lid growth is slower, resulting in very warm temperatures at the base of the crust. These temperatures exceed the solidus temperature even in the anhydrous case, explaining the lack of dependence on the water content of the primordial mantle. In models with a late episode of crustal melting, the crust is put in place later when the lid is colder. In these cases, the temperature at the base of the crust is not high enough to obtain melting if the crust is dry. The water content of the primordial mantle must be larger than 300 ppm (Figure 5.10d). These late melting models cover a wider range of reference permeability and reference viscosity and therefore different scenarios for thermal evolution. The lower the reference permeability and the higher the viscosity, the later the end of crustal melting is, as shown by our systematic exploration.

5.5 Discussion

5.5.1 Partial melting of the crust and differentiation of the Southern Highlands

Hemispheric scale

During the formation of the crust, melting at its base is possible at the hemispheric scale. The growth of a strong hemispheric dichotomy, caused by the positive feedback mechanism we identify, provides the conditions for melting in the Southern Hemisphere where the crust is thicker. A thick crust allows both higher temperatures and a lower melting temperature at its base. The strong temperature gradient in the crust, which induces higher temperatures at the base of the crust, also favours crustal melting. These strong temperature gradients are obtained in particular for low crustal thermal conductivity. Low reference viscosities also favour melting in the crust for two reasons : (1) the crust is thicker (2) the lid is thinner at the time the crust forms. A water content of 300 ppm in the primordial mantle is sufficient to achieve melting in the crust in all cases. This water content is consistent with estimations for Mars (Taylor, 2013). On the other hand, heating by magmatism does not seem to significantly modify the temperature gradient in the crust, as the heat deposited compensates for the cooling caused by downward advection. Contrary to what we might have expected, magmatic heating does not significantly plays.

Partial melting of the crust on a hemispheric scale, with a vertical extension of a few tens of kilometres and a temporal extension over millions or even billions of years, would produce quite large volumes of evolved magma. These magmas formed at the base of the crust are less dense than the surrounding crust and could be extracted and deposited at shallower depth. This could generate a three-layer crust (McCubbin et al., 2008) : (1) a surface layer composed of felsic rocks (2) a basal layer formed by the mafic residues and (3) an intermediate layer of non-molten basalts. However, the surface of the Highlands seems basaltic and not felsic, and we have no evidence of global resurfacing of the Highlands.

Alternatively, these differentiated magmas may have crystallised at depth before reaching the surface, particularly given the significant thickness of the crust. In this case, differentiated rocks could be buried at depth which would form an intermediate layer formed by a mixture of undifferentiated basalt and felsic rocks. The low density of a mega-regolith at the surface would also prevent these differentiated rocks from being brought up to the surface. Overall, our results suggest that, partial melting of the crust at the scale of a hemisphere is possible. However, it appears limited and did not affect more than a third of the crust thickness.

Local scale

The thickness of the crust is not uniform in the Highlands, and there are strong variations in between provinces such as Terra Cimmeria/Sirenum where the crust is very thick (Bouley et al., 2020). In these provinces, the temperature at the base of the crust is higher and the melting temperature is lower than on average. A small increase in crustal thickness, over a large enough province, can significantly increase melt fraction and the thickness of the partially molten layer (Figure 5.2). Models where melting on a hemispheric scale is limited could locally lead to large volumes of differentiated magma. Thermal evolutions where melting is not reached on a hemispheric scale could also sustain melting in the crust locally in these provinces. As on a hemispheric scale, a significant proportion of the magma produced may crystallise during its ascent and not reach the surface despite its low density. These differentiated rocks, whether buried or at the surface, also constitute a barrier to the ascent of denser melt and can prevent resurfacing of the province.

Timing for crustal melting

Episodes of sustained partial melting in the crust take place at specific periods. Our different examples of thermal evolution illustrate the two possible periods of crustal melting. The first period occurs very early between 4.5 and 4.3 billion years ago. The age of this crustal differentiation event corresponds to the ages of zircons found in NWA 7034 (Cassata et al., 2018) and to the ages proposed for the Terra Cimmeria/Sirenum

province (Bouley et al., 2020). This period is characterised by a short melting duration and low molten thicknesses of less than 10 km. It is a period suitable for low production of differentiated magma.

The second episode occurs towards the end of the formation of the crust, between 4 and 3 billion years ago. The base of the crust can sustain partial melting during around 1 Gyr and a maximum of melt is reached when the crust completes its formation at around 3.5 Gyr, i.e. during the Hesperian. This period would thus be suitable for the production of large quantities of differentiated magma over a long period. There is evidence of significant explosive volcanism in the Highlands at that time (Brož et al., 2021). Explosive volcanism is characteristic of magma enriched in volatiles, particularly water. For Mars, it is proposed that these explosive volcanoes are fed by basaltic magma enriched in volatiles because brought in underground water (Carr, 1979). However, a differentiated magma is by definition enriched in incompatible elements, in particular in volatiles which could lead to this type of volcanism. This also echoes the change in the sedimentary record that characterises the transition between the Noachian and Hesperian periods. The sedimentary deposits of the Noachian are dominated by clay, while those of the Hesperian is dominated by sulfates (Bibring et al., 2006). This change requires a significant input of sulphur into the atmosphere, which may have come from a differentiated sulphur-rich magma. Our two periods can be associated with observations of different, though not incompatible, nature.

sub-solidus crustal differentiation

Evolved magma can potentially form at sub-solidus temperatures where the crust is thick and has low hydrated solidus temperatures. Hence, it is possible to reach temperatures very close to the solidus implying that basaltic magma deposited at the base may take some time to cool down to the temperature of the crust. This means that the magma would have time to differentiate at the base of the crust before crystallizing. It is quite difficult to determine the cooling time of magma because it depends on the ratio between the surface area of the magma that cools and the volume of the magma (Michaut and Jaupart, 2006). This type of formation of differentiated magma out of thermal equilibrium could enormously increase the vertical, lateral and time extent of crustal melting. Hence, the formation of differentiated rocks may concern much more thermal evolution.

5.5.2 Terra Cimmeria-Sirenum : A continental crust under formation

Terra Sirenum/Cimmeria is a geological province characterised by a very thick crust (Figure 5.1 & Bouley et al. 2020) and feldspar-rich outcrops (Payré et al., 2022). It may be the region of origin of NWA 7034, and it is bounded by the Gusev and Gale craters,

where differentiated rocks have been observed. Zircon ages in the NWA7034 breccia, which are between 4.42 and 4.47 Gyr (Cassata et al., 2018), are compatible with a very early and rapid melting of the crust. The age of the Terra Sirenum/Cimmeria surface is exclusively Noachian, so the formation and eruption of differentiated Hesperian rocks in this region are not supported by observations. This geological province could have formed very early in the history of Mars, with the rapid growth of the crust giving rise to a thick crust. This thick crust would have been hot and would have maintained a melt fraction at the base of the crust for several tens of millions of years. This could have allowed fractional crystallisation of the incoming magma at the base of the crust. These evolved melts could have risen to the surface and crystallised within the volume of the crust and at the surface. These differentiated rocks would have prevented any resurfacing of the province, which explains the age of the province's surface. This mechanism for the formation of differentiated rocks seems to be consistent with the compositions of the rocks present in Gale Crater (Udry et al., 2018).

Sautter et al. (2015) suggest that the presence of differentiated rocks in the Martian highlands could indicate the presence of a Martian proto-continental crust. This raises the question of the extent to which the Terra Cimmeria/Sirenum province fits this description. The Earth's continental crust is characterised by rocks richer in silica than the basaltic oceanic crust. The majority (60%) of the rocks making up the continental crust belong to the TTG series (Tonalite-Trondhjemite-Granodiorite) (Rudnick and Holland, 2005). The samples of Martian felsic rocks described by Sautter et al. (2015) are petrologically quite similar to these TTGs. However, Udry et al. (2018) argue that the chemistry of Martian samples better correspond to icelandic rocks than to TTGs, hence it is not certain that the geochemistry of the Martian differentiated rocks corresponds to that of the Earth's continental crust, even though it is close. From a geodynamic point of view, the continental crust is characterised by a low density, allowing it to 'float' at the surface (Taylor and McLennan, 2009). The Earth's continental crust is buoyant because of its silica-rich composition. If we consider our scenario for the evolution of the Terra Cimmeria/Sirenum province, the region is composed of differentiated rocks, basalts and mafic residues at the base of the crust. The differentiated rocks formed are much less dense than the basalts, but the mafic roots are denser than the basalts. During differentiation, the volume of mafic roots produced is greater than the volume of differentiated rocks. The total density of the crust changes little by the process of differentiation and cannot by itself explain the lower density of the crust. On Earth, in the absence of orogeny, the maximum thickness of the continental crust is around 40 km (Laske et al., 2013). This observation is often explained by the loss of mafic roots, which become dynamically unstable, i.e. denser than the mantle (Jull and Kelemen, 2001), at this depth and sink back to the mantle because the lithosphere is not strong enough to hold them (Jaupart et al., 2018). By losing these mafic roots, the density of a continental crust is largely reduced.

At present-day on Mars, we do not have enough constraints to know the structure of

the crust in the TSC region. In the frame of our model, mafic roots would have formed very early in this region when the lithosphere was thin and hot. Such a lithosphere has a low strength and can easily deform. This may have allowed the roots to sink back into the convective mantle. If, on the contrary, the lithosphere is strong enough to support the denser mafic roots, they would be preserved. From a geodynamic point of view, the Terra Cimmeria/Sirenum province could well be a proto-continental crust at a more or less advanced stage. In conclusion, the study of the ancient Martian crust helps us to understand the formation of continental crust on Earth, since Terra Cimmeria/Sirenum could be a good analogue of a continental crust in formation.

5.5.3 Improving constraints on Highland differentiation.

Partial melting of the crust is a likely event during Mars' thermal evolution. A crustal melting occurs only in the Southern Hemisphere in a small but substantial part (11.04%) of the models that emerge from the inversion and that corresponds to probable evolutions for Mars. In addition, this proportion does not include models that could allow crustal melting only at a local scale. We can then ask ourselves how to better constrain this event. To do this, we can use two levers : (1) improve the physics of our model and better constrain the parameters (2) increase the precision of the observations and add other observations.

The first improvement to our model that comes to mind is to improve our solidus for the crust, whose parameters are in part derived from experiments using Earth's mantle compositions (Katz et al., 2003). Melting experiments on a basaltic rock with a Martian composition and a variable water content would enable us to refine the parameterisation used for the Martian crust. The impact on our results would, however, probably be limited and quite predictable. If our parameterisation underestimates solidus temperatures, we would obtain fewer models with melting, particularly in cases where a lot of water is necessary. But if, on the contrary, we overestimate the solidus, more models would be concerned with melting and perhaps other scenarios could appear, such as continuous melting during the formation of the crust. The solidus determined by Green and Ringwood (1967) for a terrestrial basalt is much lower than our parameterisation, so we can be confident that we are more likely to overestimate the solidus. One addition that could however modify our results is the addition of the effect of water and the melt fraction on the viscosity of the mantle. This would lead to lower viscosities at the time of extraction, which would facilitate melting at the base of the crust. In this case, as in the case of Samuel et al. (2019), the reference viscosities would be higher and the current potential temperatures would therefore be warmer. Constraining the thermodynamic values of the crust, such as thermal conductivity and density, would enable us to refine the possible thermal evolutions.

Our results clearly show that melting in the crust is strongly dependent on its thickness. Improving the constraints on crustal thickness in the Highlands would make it

possible to clarify the possible scenarios. Recent examples include the constraints on the thickness of the Martian crust from the detection of Rayleigh waves arrivals for Marsquake S1222a. Kim et al. (2023a) deduced a range of values for the average crustal thickness along the great circle path of these surface waves and, by comparison with crustal thickness maps, proposes constraints on the global crustal thickness of Mars. The average crustal thickness they propose is between 42 and 56 km, which would suggest small amounts of melting in the crust during the first period of melting early in the thermal history (Figure 5.10c). However, this is based on the analysis of only one marsquake and the inferred surface wave path. Furthermore, the crustal seismic velocity profile is prescribed and its effect is not discussed in this article.

The dating of Martian volcanic terrains, and in particular the Highlands, would provide a time constraint that is currently lacking. At present, only the NWA 7034 breccia provides information on the young crust of Mars, but its original location is still speculative. The Mars Sample Return (MSR) mission will enable samples to be returned to their geological context, even though, unlike the Gale and Gusev craters, the Jezero crater has not yet revealed any rocks with evolved compositions (Udry et al., 2022). Nevertheless, magmatic flows in place have been sampled and will significantly improve the age models of the Martian surface. Constraining the volume of differentiated rock on the surface and at depth (by crater rim studies) would add important data for the formation or not of a pre-continental type of crust.

5.6 Conclusion

In this Chapter, we have investigated the possibility that the differentiated rocks observed across the Martian Highlands were formed during the construction of the Highlands. We explored one possible formation mechanism for these rocks by fractional crystallisation of a basaltic crust. To enable fractional crystallisation, part of the crust must be maintained above its solidus temperature so that magma can evolve in composition before being extracted to potentially form differentiated rocks. We show that this mechanism is possible at the base of the Highlands for the whole hemisphere and given the constraints we have on crustal thickness. The thick crust of this geological province induces high temperatures at the base of the crust due to strong temperature gradients in the crust. The pressures associated with the great thicknesses of the crust enable a large quantity of water to be retained in the magmas and therefore significantly reduce the solidus temperature at the base of the crust. The combined effect of hot temperatures and low solidus temperatures helps to sustain a melt fraction over geological timescales. The low lid thicknesses induced by low mantle viscosities at the time of crust formation also favour crustal melting. Using the models collected from the inversion of the asymmetric thermal evolution case in Chapter 4, we find that a non-negligible set of these models can sustain partial melting in the southern crust. We have described how the distribution of this subset of models diverges from the full distribution, mainly by favouring lower reference viscosities and much thicker crusts in

the Southern Hemisphere. A double distribution of models with crustal melting corresponds to two end-members scenarios of melting in the crust : models with early melting over a very short duration and models with late and prolonged melting.

At the scale of the hemisphere, partial melting of the crust appears limited both in extent and fraction. Thus, a global differentiation of the Highlands appears unlikely. however, if partial melting at the scale of a hemisphere is possible, local melting and differentiation of the thickest and oldest geological provinces appear likely, for instance, in the Terra Sirenum-Cimmeria (TSC) province. We concluded that the TSC province is favourable for the formation of differentiated rock because of the thick crust of the region. Although this region accounts for a large proportion of our observations of differentiated rocks, we have no evidence that the mafic residues created during the formation of these rocks are still present at the base of the crust. This province could therefore be a continental crust that never completed its formation. Can this type of structure be called proto-continental crust ? It might be possible, at least from a geodynamic point of view, despite the difference in geochemistry with the Earth's continental crust. This chemical difference could indicate a difference in the formation mechanism between Earth and Mars.

Chapitre 6

Perspectives

6.1 La lithosphère martienne est-elle assez résistante pour soutenir la dichotomie ?

La dichotomie d'épaisseur crustale, telle que décrite dans ce manuscrit, explique la topographie martienne à grande longueur d'onde. Celle-ci est très proche d'un équilibre isostatique (Wieczorek, 2015), c'est-à-dire hydrodynamique. Néanmoins, la topographie impose une contrainte verticale supplémentaire sur la lithosphère de l'hémisphère sud. Dans le cas où cette contrainte est trop importante vis-à-vis de la résistance de la lithosphère, la croûte peut fluer latéralement (Jaupart et al., 2018). Ce fluage s'arrête lorsque la résistance devient suffisante, soit par une diminution de la topographie et de la contrainte, soit par une augmentation de la résistance due à un refroidissement, par exemple. La résistance de la lithosphère est également un facteur déterminant pour la stabilité des cumulats mafiques à la base de la croûte et la formation des croûtes continentales.

La résistance de la lithosphère (Str_L) est définie par :

$$\mathrm{Str}_L = \int_{R_l}^{R_p} \sigma_{\mathrm{ext}}(r) dr, \tag{6.1}$$

où R_l est le rayon de la base du couvercle stagnant, R_p est le rayon de Mars et $\sigma_{\mathrm{ext}}(r)$ est le profil de la contrainte minimum avant déformation, aussi appelé enveloppe de la résistance. On détermine cette contrainte minimum à une certaine profondeur en fonction du mécanisme de déformation dominant. Ce mécanisme peut soit être cassant et ne dépend dans ce cas que de la pression lithostatique, soit ductile et dépend alors fortement de la température. La contrainte minimum avant une rupture extensive (σ_{B}) est donnée par (Mueller and Phillips, 1995) :

$$\sigma_{\mathrm{B}}(r) = \begin{cases} 0.786\sigma_v(r) & \text{si } \sigma_v(r) < 529.9 \text{ MPa}, \\ 56.7 + 0.679\sigma_v(r) & \text{si } \sigma_v(r) > 529.9 \text{ MPa}, \end{cases}$$

Rheology	B ($\mathrm{Pa^{-n}\ s^{-1}}$)	A_n ($\mathrm{kJ\ mol^{-1}}$)	n [K]
Wet olivine	3.9×10^{-15}	430	3.0
Wet diabase	3.1×10^{-20}	276	3.05

TABLE 6.1 – Paramètres rhéologiques de Karato and Wu (1993) pour une olivine et une diabase mouillées. La rhéologie de l'olivine est représentative de celle du manteau et celle de la diabase de la croûte.

avec $\sigma_v(r)$ la contrainte verticale égale à la pression lithostatique. La déformation ductile dépend fortement de la température et fait intervenir une loi rhéologique qui relie la contrainte à la déformation. Une rhéologie non-linéaire est utilisé ici (Durham and Goetze, 1977; Durham et al., 1977) où la contrainte minimum pour la déformation ductile σ_D est défini comme :

$$\sigma_\mathrm{D}(r) = \left(\frac{\dot{\epsilon}}{B}\right)^{\frac{1}{\mathrm{n}}} \exp\left(\frac{A_\mathrm{n}}{nRT(r)}\right), \tag{6.2}$$

avec $T(r)$ le profil de température, $\dot{\epsilon}$ la vitesse de déformation ici 10^{-14} $\mathrm{s^{-1}}$, B, A_n et n des paramètres de la loi rhéologique qui dépendent de la lithologie (Table 6.1, Karato and Wu 1993). En référence à nos résultats, qui indiquent de faibles viscosités dans le manteau, nous avons sélectionné des paramètres de la loi rhéologique caractéristiques des roches riches en eau, tant pour la croûte que pour le manteau. L'enveloppe est alors obtenue en choisissant à chaque profondeur la valeur la plus faible entre la contrainte ductile et la contrainte fragile. Le résultat est une enveloppe avec une forme caractéristique d'arbre (Figure 6.1, graphique de droite).

La différence d'épaisseur de croûte (ΔD_{cr}) induit une différence en énergie potentielle de pesanteur (Jaupart et al., 2018) :

$$\Delta U = g(\rho_m - \rho_{cr})\Delta D_{cr}(D_{cr} + \frac{1}{2}\Delta D_{cr}), \tag{6.3}$$

avec ρ_m la densité du manteau, ρ_{cr} la densité de la croûte et D_{cr} l'épaisseur moyenne de la croûte. Nous avons calculé la résistance de la lithosphère et la différence d'énergie potentielle au cours du temps pour deux cas présentés dans ce manuscrit. Nous avons choisi le meilleur cas et le cas moyen du sous-ensemble des modèles présentant de la fusion dans la croûte (Chapitre 5, Section 5.4.4 et Figures 5.6 et 5.7). La résistance est calculée dans l'hémisphère sud, car c'est dans cet hémisphère que s'exerce la contrainte relative à la dichotomie.

Dans le cas le plus fidèle aux observations ("best case"), le résultat est simple : la résistance de la lithosphère est toujours plus importante que la différence d'énergie potentielle de pesanteur (Figure 6.1, courbes bleues, graphique de gauche). Dans ce

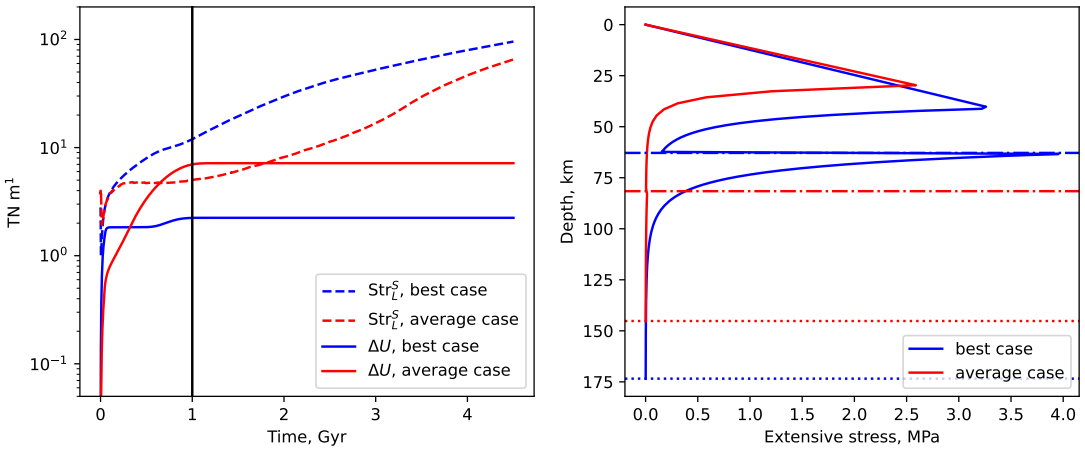

FIGURE 6.1 – **Volet de gauche** - évolution temporelle de la résistance de la lithosphère (courbes pleines) et différence d'énergie potentielle de pesanteur (courbes pointillées) pour le cas moyen (courbes rouges) et le meilleur cas (courbes bleues) **Volet de droite** Enveloppe de la résistance en fonction de la profondeur pour les deux cas à $t = 1$ Ga (courbe noir, volet de gauche) avec en pointillé l'épaisseur du couvercle rigide et en trait-point l'épaisseur de la croûte.

cas, on s'attend à ce que la dichotomie crustale et la topographie résultante soient préservées dans le temps. En effet, le modèle avec les paramètres moyens ("average case") est lui assez différent, la résistance de la lithosphère devient plus faible que la différence d'énergie potentielle pendant plus d'un milliard d'années (Figure 6.1, courbes rouges, graphique de gauche). La faible résistance de la lithosphère pourrait entrainer une déformation extensive de la base de la croûte et de la lithosphère et amener à une diminution de la dichotomie et de la topographie. Dans le premier cas, la dichotomie formée est relativement modérée ($\approx$ 16 km), entrainant une faible différence d'énergie potentielle et une lithosphère plus épaisse et moins chaude et donc plus résistante (Figure 6.1 courbe bleue, graphique de droite). La dichotomie obtenue dans le cas moyen est bien plus importante ($\sim$ 40 km). La lithosphère de l'hémisphère sud est alors moins épaisse et plus chaude, indiquant que le mécanisme ductile est dominant sur une très large épaisseur (Figure 6.1 courbe rouge, graphique de droite).

La période pendant laquelle la résistance de la lithosphère est insuffisante correspond également à celle où la base de la croûte est fondue. Cette période est propice à la formation de roches felsiques, extraites vers la surface et des cumulats mafiques accumulés en base de croûte. Comme vue dans le chapitre 5, la perte de ces cumulats est essentiel pour la formation d'une croûte continentale (Jaupart et al., 2018). Sur Terre, un changement minéralogique prendrait place vers 0.8 GPa et rendre les cumulats plus denses que le manteau (Jull and Kelemen, 2001; Jaupart et al., 2018). Dans cette situation, les racines crustales mafiques, plus denses, pourraient être recyclées dans le manteau si la lithosphère n'est pas assez résistante. Or, la pression de 0.8 GPa

est atteint à une profondeur de 77 km (pour une densité de croûte de 2900 Kg m^{-3}). Cette profondeur correspond tout juste à l'épaisseur de la croûte dans le cas moyen (Figure 6.1 courbe rouge, graphique de droite). Le modèle moyen réunit alors les conditions pour la perte de racines mafiques, notamment dans les régions de croûtes épaisses comme Terra Cimmeria-Sirenum. Néanmoins, la pression de 0.8 GPa est déterminée pour une chimie terrestre, la différence de composition entre la croûte et le manteau martien vont certainement modifier cette pression. Pour conclure sur une perte ou non des racines mafiques dans le cas martien, il est nécessaire de déterminer la densité des cumulats, avec une composition martienne, en fonction de la pression.

6.2 Un manteau lithosphérique fertile et primitif ?

L'enrichissement calculé pour le manteau lithosphérique (Équation 2.36, Figure 6.2a-c) est souvent intermédiaire entre celui du manteau convectif appauvri (Λ_{cm}) et un enrichissement primordial ($\Lambda = 1$). En effet, le manteau lithosphérique n'est pas remélangé avec le manteau convectif et il conserve sous la croûte des roches qui n'ont pas été modifiées par l'extraction de la croûte. Cette composition évolue suivant un gradient en profondeur, les roches étant de plus en plus affectées par l'extraction jusqu'à obtenir des roches autant appauvries que le manteau convectif.

Si le gradient de composition est négligé, le manteau lithosphérique peut être modélisé par deux volumes :

$$V_{lm} = V_{fl} + V_{al}, \tag{6.4}$$

avec V_{fl} le volume de manteau primitif et V_{al} le volume de manteau avec le même enrichissement que le manteau convectif. La conservation des HPEs donne alors :

$$\Lambda_{lm} V_{lm} = V_{fl} + \Lambda_{cm} V_{al}, \tag{6.5}$$

en utilisant ensuite les équations 6.4 et 6.5, il est possible de calculer le volume du manteau fertile :

$$V_{fl} = V_{lm} \frac{\Lambda_{lm} - \Lambda_{cm}}{1 - \Lambda_{cm}}. \tag{6.6}$$

Ce volume peut ensuite être exprimé comme une épaisseur (D_{fl}) en considérant qu'il s'étend d'un rayon R_{fl} à la base de la croûte (R_{cr}) :

$$D_{fl} = R_{cr} - \sqrt[3]{R_{cr}^3 - \frac{3V_{fl}}{4\pi}}. \tag{6.7}$$

Cette épaisseur équivalente de manteau fertile permet d'avoir une idée du caractère fertile ou non de la lithosphère.

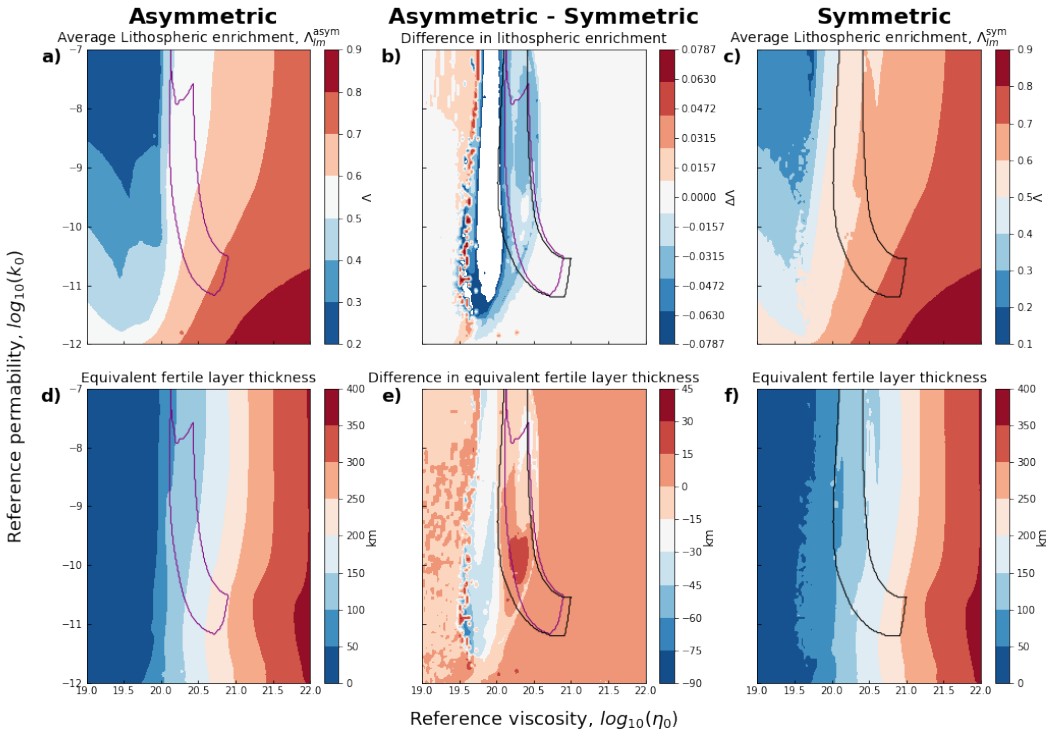

FIGURE 6.2 – Comparaison des géométries asymétrique et symétrique pour une exploration systématique de k_0, η_0 sur notre cas de référence (Table 2.1). η_0 (abscisse) est comprise entre 10^{19} et 10^{22} Pa s et k_0 (ordonnée) est comprise entre 10^{-12} et 10^{-7} m^2. (a, b, c) Enrichissement du manteau lithosphérique. (d, e, f) Épaisseur fertile équivalente (Équation 6.7). Les graphiques de gauche (a, d, g) correspondent à la géométrie asymétrique, les graphiques de droite (c, f, i) à la géométrie symétrique et les graphiques du milieu (b, e, h) à la différence entre les deux géométries (asymétrique - symétrique). Les contours montrent l'espace des paramètres dans lequel la combinaison de toutes les contraintes est respectée, en tenant compte de la contrainte de dichotomie dans le cas asymétrique (Sections 4.2).

Cette épaisseur a été calculée dans le cas de l'exploration systématique dans les deux géométries du Chapitre 4. L'enrichissement convectif du manteau et l'épaisseur fertile équivalente augmentent fortement avec la viscosité (Figure 6.2). Plus la viscosité est élevée, plus le couvercle rigide croît rapidement, ce qui permet de préserver davantage de matière fertile avant l'extraction de la croûte. De même, des perméabilités plus faibles retardent l'extraction de la croûte, ce qui permet de préserver plus de matériel fertile dans la lithosphère. Lorsque la viscosité est faible, l'épaisseur fertile équivalente est nulle. Dans ce cas, le manteau lithosphérique est complètement érodé pendant la formation de la croûte et croît à nouveau une fois l'extraction de la croûte terminée. L'enrichissement du manteau lithosphérique est alors strictement égal à celui du manteau convectif. La différence entre les deux géométries est assez faible, d'autant plus que la proportion de manteau fertile retenue dans la lithosphère est déterminée principalement avant la formation de la dichotomie, c'est-à-dire avant que la différence entre les deux géométries n'apparaisse. Néanmoins, pour les paramètres qui correspondent aux observations d'InSight (Figure 6.2, contours), l'enrichissement est plus important dans la géométrie symétrique, mais l'épaisseur équivalente est, elle, plus importante dans le cas asymétrique. Cette observation, à première vue contradictoire, peut s'expliquer par des différences d'enrichissement du manteau convectif, celui-ci étant plus appauvri dans le cas asymétrique (Figure 4.7).

Cette couche possède des propriétés distinctes du reste du manteau, enrichie en éléments producteurs de chaleur, en eau et en pyroxène. Elle est potentiellement observable dans les données sismologiques. Cependant, il ne s'agit pas d'une limite lithologique et la transition vers la couche appauvrie est graduelle, il semble donc difficile de l'observer dans les données sismiques. Néanmoins, les différences de vitesse sismique entre la lherzolite et l'harzburgite terrestre sont de l'ordre de quelques pourcents (Schutt and Lesher, 2006; Maguire et al., 2017) et la couche semble être épaisse, entre 50 et 200 km d'épaisseur (Figure 6.2d-f, contours). La lherzolite, plus riche en pyroxène que l'harzburgite (Wasylenki et al., 2003; Le Roux et al., 2007) présente des vitesses sismiques plus faibles et pourrait être un bon analogue de cette couche fertile. Cette couche formerait donc une zone de faible vitesse à faible profondeur et ajouterait une composante de composition au gradient de vitesse sismique, en plus des composantes de température et de pression. Cette composante fonctionne à l'inverse de la température, avec une vitesse faible près de la surface et élevée en profondeur, et pourrait expliquer la difficulté à observer la zone de faible vitesse attendue à la base de la lithosphère thermique sur Mars (Khan et al., 2021; Durán et al., 2022b).

6.3 Un Volcanisme actuel sous Tharsis est-il possible ?

Les traces d'un volcanisme récent (Hauber et al., 2011) donnent une contrainte supplémentaire sur l'état thermique du manteau. La fusion partielle sous Tharsis doit

être possible dans le manteau malgré les faibles températures de celui-ci (Huang et al., 2022). Pour déterminer si la fusion sous Tharsis est possible dans nos modèles paramétriques asymétriques, nous avons besoin de l'épaisseur de la lithosphère sous Tharsis, connaissant l'épaisseur de croûte moyenne sous Tharsis d'après les modèles d'épaisseurs crustales, et la température d'un panache ascendant à cette profondeur. Tout d'abord, la température en base de croûte sous le dôme de Tharsis (T^{cr}_{Tha}) est déterminé en considérant un état stationnaire dans la croûte ($\frac{\mathrm{d}T}{\mathrm{d}t} = 0$) :

$$T^{cr}_{\text{Tha}} = \frac{H_{cr}(R_p^2 - R_{\text{Tha}}^2)}{6\ K_{cr}} + R_{\text{Tha}}^2\left(\frac{H_{cr}R_p}{3} - q_{\text{moho}}\right)\left(\frac{R_p^{-1} - R_{\text{Tha}}^{-1}}{k_{cr}}\right) + T_s, \tag{6.8}$$

avec $H_{cr} = 1.8 \times 10^{-7}$ W m^{-3} le chauffage radioactif actuel dans la croûte, $k_{cr} = 3$ W m^{-1} K^{-1} la conductivité thermique de la croûte, $T_s = 220$ K la température de surface, R_p le rayon de Mars, R_{Tha} le rayon moyen de la base de Tharsis et q_{moho} le flux de chaleur à l'interface croûte-manteau. La température en base de croûte est ensuite prolongée suivant un gradient $\frac{q_{\text{moho}}}{k_{cr}}$, en négligeant la sphéricité et la production de chaleur radioactive (qui tendent à se compenser), jusqu'à atteindre la température de transition rhéologique T_l (Équation 2.3, avec $A = 3 \times 10^5$ J mol^{-1}), le rayon de la base de la lithosphère s'écrit alors :

$$R_{\text{plume}} = R_{\text{Tha}} - \frac{k_{cr}(T_l - T^{cr}_{\text{Tha}})}{q_{\text{moho}}}. \tag{6.9}$$

La température d'un panache en provenance de l'interface noyau-manteau en fonction de la profondeur peut s'écrire avec un gradient isentropique :

$$T_{\text{plume}}(r) = T_c - \frac{\alpha g T_c}{C_m}(R_p - r), \tag{6.10}$$

avec α l'expansivité thermique, g la gravité de surface, C_m la capacité calorifique du manteau et T_c la température de l'interface noyau-manteau. Comme Thiriet (2018) et Knapmeyer-Endrun et al. (2021) nous utilisons la température du panache au rayon de la lithosphère sous Tharsis, mais contrairement à Thiriet (2018) nous ne prenons pas en compte la pénétration du panache dans la lithosphère. La différence entre cette température et la température du solidus à cette même profondeur est :

$$\Delta T^{sol}_{\text{Tha}} = T_{\text{plume}}(R_{\text{Tha}}) - T_{sol}(P_{\text{Tha}}), \tag{6.11}$$

avec $T_{sol}(P_{\text{Tha}})$ la température du solidus au rayon R_{Tha} dont la pression s'écrit $P_{\text{Tha}} = g\left(\rho_{cr}(R_p - R_{\text{Tha}}) + \rho_m(R_{\text{Tha}} - R_{\text{plume}})\right)$. Le même solidus que celui décrit Chapitre 2 est utilisé (Section 2.3.1) :

$$T_{sol}(P) = 1340 + 130.4P - 6.38P^2 + 0.119P^3 + \frac{D^{\text{avg}}_{cr}}{D_{\text{ref}}}\Delta T_{sol} - \Delta T_{H_2O} \tag{6.12}$$

avec un ajout de $-\Delta T_{H_2O}$ qui est une dépendance du solidus vis-à-vis de l'enrichissement en eau. Cette différence de solidus est celle définie par Katz et al. (2003) et est

calculée exactement de la même manière que pour la croûte (voir Section 2.4.3).

Pour l'application numérique, nous avons choisi les valeurs moyennes obtenues avec l'inversion en géométrie asymétrique. La température potentielle est fixée à 1622 K avec une épaisseur de lithosphère thermique de 440 km, ce qui donne une température T_m de 1670 K et T_l de 1473 K. Deux types de manteau sont considérés : un manteau convectif appauvri et un manteau fertile de composition primordiale. L'épaisseur moyenne de la croûte est de 57 km, ce qui entraîne une augmentation du solidus de 45 K dans le cas appauvri et de 0 K dans le cas fertile. La teneur en eau du manteau primordial est de 300 ppm et l'enrichissement du manteau est de $\Lambda = 0,4$ dans le cas appauvri ou $\Lambda = 1$ dans le cas fertile. La diminution du solidus par rapport à la teneur en eau est alors de 45,9 K dans le cas appauvri et de 91,3 K dans le cas fertile. La température de l'interface noyau-manteau est de 1860 K et le gradient adiabatique correspondant est de 0,15 K km^{-1}. Pour les deux derniers paramètres, q_{moho} et R_{Tha}, une exploration systématique est effectuée. Pour q_{moho}, le gradient de température s'exprime $\frac{\mathrm{d}T}{\mathrm{d}r} = \frac{q_{\text{moho}}}{k_{cr}}$ avec des valeurs comprises entre 3,5 et 4,5 K km^{-1} (Figure 4.9), ce qui correspond à la gamme de valeurs obtenue lors de l'inversion. L'épaisseur sous Tharsis ($R_p - R_{\text{Tha}}$) est déterminée à partir des modèles d'épaisseur de la croûte (voir la Section 4.2) et dépend de l'épaisseur sous InSight et du rapport de densité avec une valeur minimale de 55 km et un maximum de 95 km.

Les épaisseurs de lithosphère sous Tharsis calculées par notre méthode varient entre 250 et 320 km. Plus l'épaisseur sous Tharsis est grande et plus le gradient de température à l'interface croûte-manteau est important, plus l'épaisseur de la lithosphère est faible (Figure 6.3). Cette épaisseur est à comparer à l'épaisseur moyenne de ≈ 328 km au sud, la différence d'épaisseur de lithosphère est inférieur à 100 km. Comme le gradient isentropique est faible, la température du panache varie légèrement, entre 1658 et 1674 K. Quatre différents solidus sont considérés, avec ou sans l'effet de l'eau, pour un manteau appauvri ou fertile. Pour le cas classique d'un solidus appauvri sans effet de l'eau (Figure 6.3c) la température du panache est systématiquement plus faible que celle du solidus (valeurs négatives). Cela contraste avec les résultats de Knapmeyer-Endrun et al. (2021) qui, avec ce type de solidus, obtiennent une fusion sous Tharsis pour des épaisseurs de croûte et des enrichissements similaires. La différence provient des viscosités plus faibles de nos modèles ($\approx 10^{20.5}$) par rapport à celles utilisées dans leur étude ($\approx 10^{21.5}$), ce qui se traduit par des températures plus chaudes dans le noyau actuel, et donc des températures de panache beaucoup plus chaudes. La diminution du solidus sous l'effet de la teneur en eau (Figure 6.3d) aboutit à la fusion (valeurs positives), mais uniquement pour des épaisseurs supérieures à 80 km et des gradients thermiques supérieurs à 4.2 K km^{-1}. La fusion est atteinte pour la même gamme de paramètres dans un cas fertile sans effet de l'eau (Figure 6.3e), car le changement de solidus causé par l'extraction de la croûte est presque le même que celui causé par l'effet de l'eau dans un cas appauvri (45 contre 45.9 K). Dans le dernier cas, un manteau fertile avec effet de l'eau (Figure 6.3f), la fusion est atteinte pour la majorité des

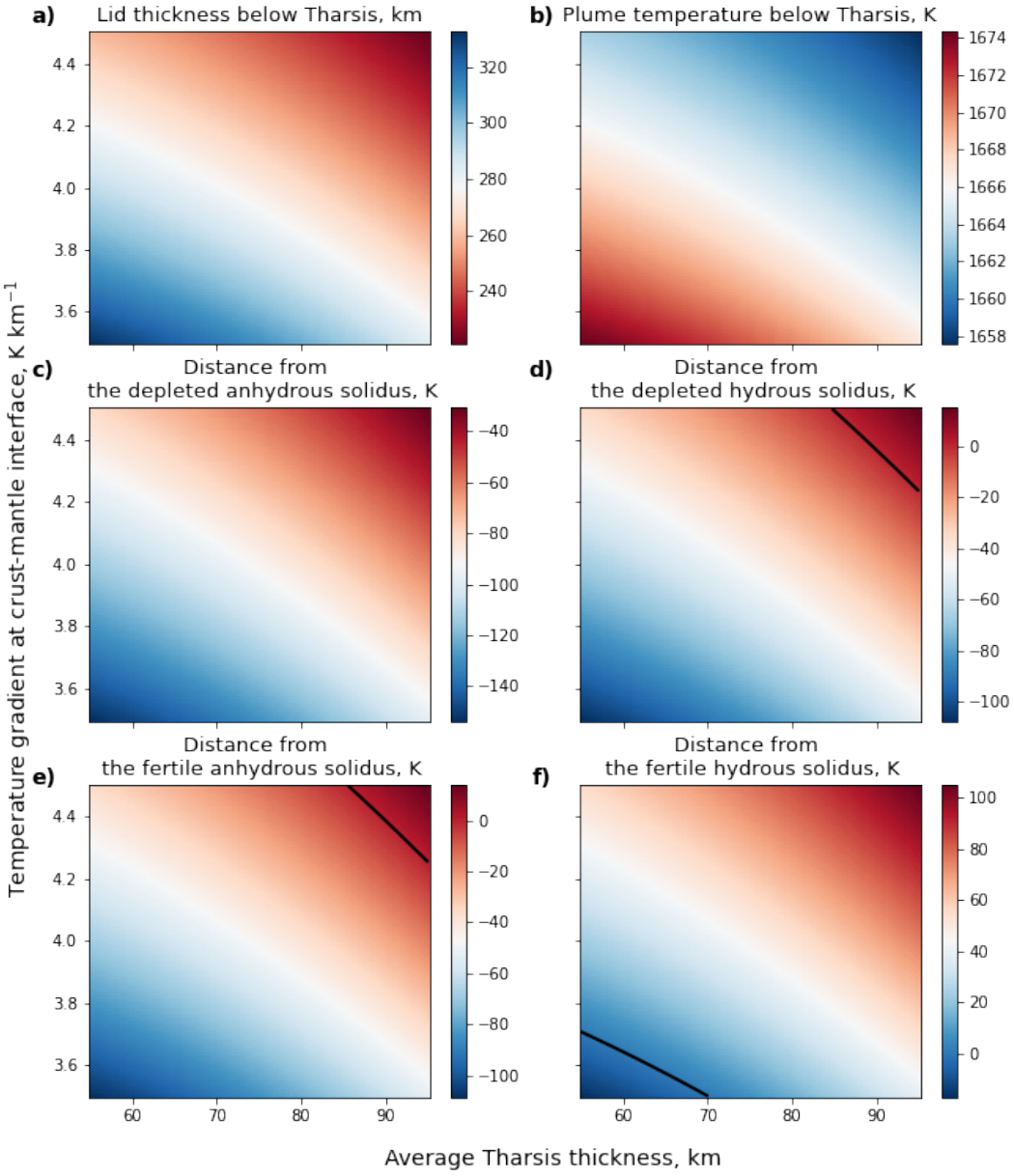

FIGURE 6.3 – Exploration systématique des paramètres $R_p - R_{\text{Tha}}$ et $\frac{q_{\text{moho}}}{k_{cr}}$ pour notre modèle de fusion sous Tharsis. $R_p - R_{\text{Tha}}$ est entre 55 et 95 km et $\frac{q_{\text{moho}}}{k_{cr}}$ entre 3.5 et 4.5 K km^{-1}. Les échelles de couleurs représentent (a) l'épaisseur de lithosphère sous Tharsis en km ($R_p - R_{\text{Tha}}$) (b), la température du panache en K ($T_{\text{plume}}(R_{\text{Tha}})$) et l'écart au solidus (c) appauvri anhydre, (d) appauvri avec de l'eau, (e) fertile anhydre et (d) fertile avec eau. La courbe noire est la limite entre les valeurs négative, la température du panache est inférieure au solidus, avec les valeurs positives, la température du panache est supérieure au solidus.

paramètres.

Ces résultats illustrent la difficulté de concilier les observations d'un manteau froid avec celles d'un volcanisme récent. Il existe néanmoins des moyens de résoudre cette difficulté :

— La pénétration du panache plus profondément dans la lithosphère, qui permettrait d'atteindre des pressions et des températures de solidus plus basses.

— La présence d'un océan de magma à la base du manteau qui pourrait être à l'origine de panaches plus chauds que ceux envisagés.

— Un manteau fertile moins réfractaire et appauvri en eau qui aurait des températures de solidus plus froides et pourrait expliquer les différentes sources des Shergottites.

Conclusion

La formation de la croûte martienne et de sa dichotomie est un des évènements majeurs de l'histoire de Mars. L'étude de leurs formations à l'aide d'un modèle d'évolution thermique paramétrique et asymétrique a permis d'apporter de nouvelles contraintes sur son évolution. Nous pouvons alors voir comment nos travaux permettent de répondre aux questions posées en fin d'introduction.

Quel mécanisme pour la formation de la dichotomie martienne ? J'ai proposé un nouveau mécanisme pour la formation de la dichotomie, une rétroaction positive entre l'épaisseur de la croûte et son épaississement (Bonnet Gibet et al., 2022). L'analyse de stabilité linéaire de notre mécanisme démontre que les perturbations initiales de grandes longueurs d'ondes sont plus amplifiées par notre mécanisme. Notre mécanisme forme alors préférentiellement des structures de degré 1 à l'image de la dichotomie martienne. Le modèle paramétrique d'évolution thermique asymétrique et son inversion ont ensuite démontré que notre mécanisme était capable de faire croître des dichotomies d'une taille de celle de Mars. Survient alors la question : quelle taille la perturbation doit-elle avoir ? Une perturbation infinitésimale semble suffire si le refroidissement séculaire est négligeable. Or, on ne peut négliger le refroidissement de Mars, le temps de croissance de la perturbation est limité au premier milliard d'années où la croûte se forme. Notre inversion (Chapitre 4) suggère qu'une différence initiale de 3 km dans l'épaisseur du couvercle est la à même de reproduire les observations. Il semble donc nécessaire que la perturbation initiale soit finie au moment de la transition rhéologique. L'origine de cette perturbation reste encore à définir mais des pistes sérieuses existent comme un héritage de l'océan magmatique (Morison et al., 2019; Watson et al., 2022). Les panaches mantelliques ont été négligés pendant cette thèse et leur prise en compte passe par des modèles de convection à 2 ou 3 dimensions. Pour confirmer notre modèle, cette étape est essentiel et fait l'objet d'un projet que je porte (Appendice B).

Ce mécanisme est endogène mais il est différent de ceux déjà proposés car il ne s'agit ni d'un impact ni d'un panache hémisphérique. Le mécanisme de Citron et al. (2018b) d'une origine hybride de la dichotomie est classé par Ballantyne et al. (2023) comme "HPE-induced Dichotomy", une dichotomie induite par les éléments producteurs de chaleurs, désignation qui est adapté à ce nouveau mécanisme. Une autre particula-

rité de notre mécanisme, c'est qu'il s'applique aussi dans un scénario où la dichotomie aurait une autre origine. Notre mécanisme amplifierait la dichotomie formée par un impact dans l'hémisphère sud par exemple. Cette amplification tardive de la dichotomie doit-être pris en compte par les autres mécanismes dans leur prédiction d'une épaisseur de croûte. Les dichotomies prévues par les modèles d'impact au sud sont déjà très importantes, c'est leur défaut principal. Soit ce mécanisme est déjà présent dans leurs modèles et n'a pas été décrit soit obtenir des dichotomies "modérées" pour Mars semble être compliqué avec cette approche.

Notre modèle de formation de la dichotomie prédit des épaisseurs crustales, une dichotomie crustale et un état thermique en accord avec les observations. Il prévoit la formation d'une dichotomie significative en moins de cents millions d'années, en accord avec certaines observations, et prévoit aussi une amplification de la dichotomie tout le long de la formation de la croûte pendant le premier milliard d'années. Cet âge ancien mais avec des modifications plus récentes permet de réconcilier les différents âges de la dichotomie martienne dans la littérature. Les âges anciens sont déterminés à partir de structures nécessitant la présence d'une dichotomie alors que l'âge récent date des structures tectoniques mises en mouvement lors de la croissance de la dichotomie (Gurgurewicz et al., 2022; McGill and Dimitriou, 1990).

Comment concilier l'épaisseur de la croûte et la structure thermique du manteau dans un modèle d'évolution thermique ? J'ai pu revisiter les modèles d'évolutions thermiques avec extraction de la croûte. Notre nouveau modèle considère une vitesse de Darcy pour l'extraction de la croûte, une production de magma non-linéaire, l'advection vers le bas de la lithosphère, la distribution dynamique des éléments producteurs de chaleurs et la fusion de la croûte. Ce nouveau modèle reproduit correctement les contraintes fournis par InSight. Les paramètres nécessaires pour cela sont tout à fait réalistes et cohérents avec les précédentes études. La viscosité du manteau doit être faible, notamment pour expliquer les basses températures actuel du manteau. L'origine de cette faible viscosité n'est pas encore très clair : un manteau partiellement fondu, l'effet de l'eau sur la rhéologie ou les deux ?

Quel est l'effet de la dichotomie et de sa formation sur l'évolution thermique ? La dichotomie d'épaisseur crustale peut impacter de manière non négligeable l'évolution thermique de Mars. L'évolution thermique martienne est non linéaire, la moyenne des deux hémisphères dans le cas asymétrique ne correspond pas au cas symétrique. L'origine principale de la non-linéarité est l'extraction de la croûte prolongée dans un cas asymétrique comparé au cas symétrique. Cette extraction prolongée conduit à une croûte plus épaisse et une distribution des éléments producteurs de chaleurs différentes. Néanmoins, les différences d'état thermiques entre les deux géométries sont inférieures aux incertitudes des observations.

Comment la dichotomie de l'épaisseur de la croûte peut-elle être reliée aux autres caractéristiques de la dichotomie (densité, minéralogie) ? La fusion de la croûte à sa base dans les Hauts Plateaux est très probable durant sa formation. Les fortes épaisseurs de croûtes, l'enrichissement en eau et les lithosphères minces sont les principaux paramètres qui favorisent l'émergence de la fusion. La fusion est donc plus probable dans les régions de croûtes épaisses comme les Hauts Plateaux et Terra Sirenum Cimmeria. Cette fusion peut avoir lieu avant 4.4 Ga sur une courte période au moment de l'extraction initiale de la croûte et/ou au cours de l'Hespérien sur une plus longue période. L'extension verticale de la fusion est de l'ordre de quelques dizaines de kilomètres sur une extension temporelle de plusieurs dizaines de millions d'années. La formation de magma avec une composition évoluée est alors très probable et expliquerait les observations de composants felsiques dans les Hauts Plateaux, au cratère Gale et dans la brèche NWA 7034. La différence de composition entre les hémisphères martiens serait alors une conséquence directe de la formation de la dichotomie martienne par notre mécanisme. Par contre, la formation de ces roches felsiques n'expliquent pas directement les faibles densités de l'hémisphère sud. Les cumulats formés en base de croûte, plus dense que la croûte basaltique représentent un volume plus important que les roches felsiques formées. Une série de questions émergent à la suite de nos résultats. Est-ce que ces cumulats sont plus denses que le manteau ? Est-ce qu'ils sont encore présent en base de croûte ? Quel est leur impact sur les anomalies de gravité ? Avons-nous des observations de cumulats ? Autant de futures questions auquel il est nécessaire de répondre avant de pouvoir conclure sur l'existence ou non d'une croûte continentale martienne.

Appendix - A - Numerical resolution

This appendix focuses on the description of the main methods used to solve our model. Indeed, the differential equations described in our model do not have analytical solutions. It is an initial-value problem, so a numerical resolution is necessary to resolve the thermal evolution. These equations are about 8 in number but in fact, by counting the equations doubled for each hemisphere we have 14 equations. These equations can be split into 6 differential equations of order 1 (2.4,.. name) linked together for the temporal evolution of the mantle and the crust growth. This system of 6 equations is solved by an implicit method following a Runge-Kutta scheme of order 4. Then, 6 other differential equations of order 1 are to be solved to obtain the enrichment in producing elements in the different reservoirs. As these values evolve relatively smoothly, we chose an explicit Taylor scheme for their resolution. Finally, the solution of two second-order differential equations corresponds to the unsteady heat equation in each of the lids. The conduction is solved with an implicit Taylor scheme with a finite volume spatial description.

First-order differential equation

Runge-Kutta methods are iterative methods allowing to rebuild of a function from its derivative. The method consists of calculating several estimates of the derivative and then making a weighted average of the different estimates. The Runge-Kutta method of order 4 is based on the calculation of 4 estimates of the derivative to an accuracy of the order of Δt^4. We will use vector notation to solve our system of differential equations. We consider the vector k which has as coordinates the values of the temporal derivatives of the 6 equations we are going to solve :

$$\vec{k_x} = \{k_{x_1} = \frac{\mathrm{d}D_l}{\mathrm{d}t},\ k_{x_2} = \frac{\mathrm{d}D_{cr}}{\mathrm{d}t},\ k_{x_3} = \frac{\mathrm{d}T_m}{\mathrm{d}t},\ k_{x_4} = \frac{\mathrm{d}T_c}{\mathrm{d}t}\}. \tag{6.13}$$

To present the method in a more reader-friendly way, the vector k has only 4 dimensions (T_c, T_m, D_l and D_{cr}). This vector is given by the function f :

$$\vec{k_1} = f(t,\ D_l,\ D_{cr},\ T_m,\ T_c,\ \dots), \tag{6.14a}$$

$$\vec{k_2} = f(t + \frac{\Delta t}{2},\ D_l + k_{11}\frac{\Delta t}{2},\ D_{cr} + k_{12}\frac{\Delta t}{2},\ T_m + k_{13}\frac{\Delta t}{2},\ T_c + k_{14}\frac{\Delta t}{2},\ \dots), \tag{6.14b}$$

$$\vec{k_3} = f(t + \frac{\Delta t}{2},\ D_l + k_{21}\frac{\Delta t}{2},\ D_{cr} + k_{23}\frac{\Delta t}{2},\ T_m + k_{23}\frac{\Delta t}{2},\ T_c + k_{24}\frac{\Delta t}{2},\ \dots), \tag{6.14c}$$

$$\vec{k_4} = f(t + \Delta t,\ D_l + k_{31}\Delta t,\ D_{cr} + k_{32}\Delta t,\ T_m + k_{33}\Delta t,\ T_c + k_{34}\Delta t,\ \dots)\ , \tag{6.14d}$$

where dt is the time step and $\vec{k_1}$, $\vec{k_2}$, $\vec{k_3}$ and $\vec{k_4}$ are the successive estimates. Each of them is estimated with the previous one at different intermediate time steps. A weighted average of the different estimates is then taken. The estimates at the intermediate time step ($\Delta t/2$) are weighted more heavily. The values at time step $t + \Delta t$ can then be calculated :

$$D_l^{n+1} = D_l^n + \frac{\Delta t}{6}\left(k_{11} + 2k_{21} + 2k_{31} + k_{41}\right), \tag{6.15a}$$

$$D_{cr}^{n+1} = D_{cr}^n + \frac{\Delta t}{6}\left(k_{12} + 2k_{22} + 2k_{32} + k_{42}\right), \tag{6.15b}$$

$$T_m^{n+1} = T_m^n + \frac{\Delta t}{6}\left(k_{13} + 2k_{23} + 2k_{33} + k_{43}\right), \tag{6.15c}$$

$$T_c^{n+1} = T_c^n + \frac{\Delta t}{6}\left(k_{14} + 2k_{24} + 2k_{34} + k_{44}\right). \tag{6.15d}$$

Runge-Kutta provides good accuracy in exchange for a longer calculation time. For the enrichment of the different reservoirs, we do not need such accuracy because the values change relatively little in time. Therefore, an explicit Taylor scheme is used for these equations, which is less accurate but has a lower computation time. The enrichment of a reservoir j at time step n+1 can then be easily obtained :

$$\Lambda_j^{n+1} = \frac{\Lambda_j^n V_j^n + \mathrm{RHS}_j}{V_j^{n+1}}, \tag{6.15e}$$

where V_j is the reservoir volume and RHS_j is the right-hand side term in the equations 2.38.

Second-order differential Equation, conduction in a spherical shell.

The second-order heat equation is solved by considering a non-stationary state. In this case it is a differential equation of order 1 in time and order 2 in space. Considering spherical symmetry, the temperature varies according to the radial dimension (r) and the temporal dimension (t). We use the finite volume method to spatially discretise our problem, following the formalist proposed by Patankar (2018) (Figure 6.4). We start from the conservation of heat in a finite volume :

$$\partial U = -\boldsymbol{\nabla} \cdot \vec{Q} + SV, \tag{6.16}$$

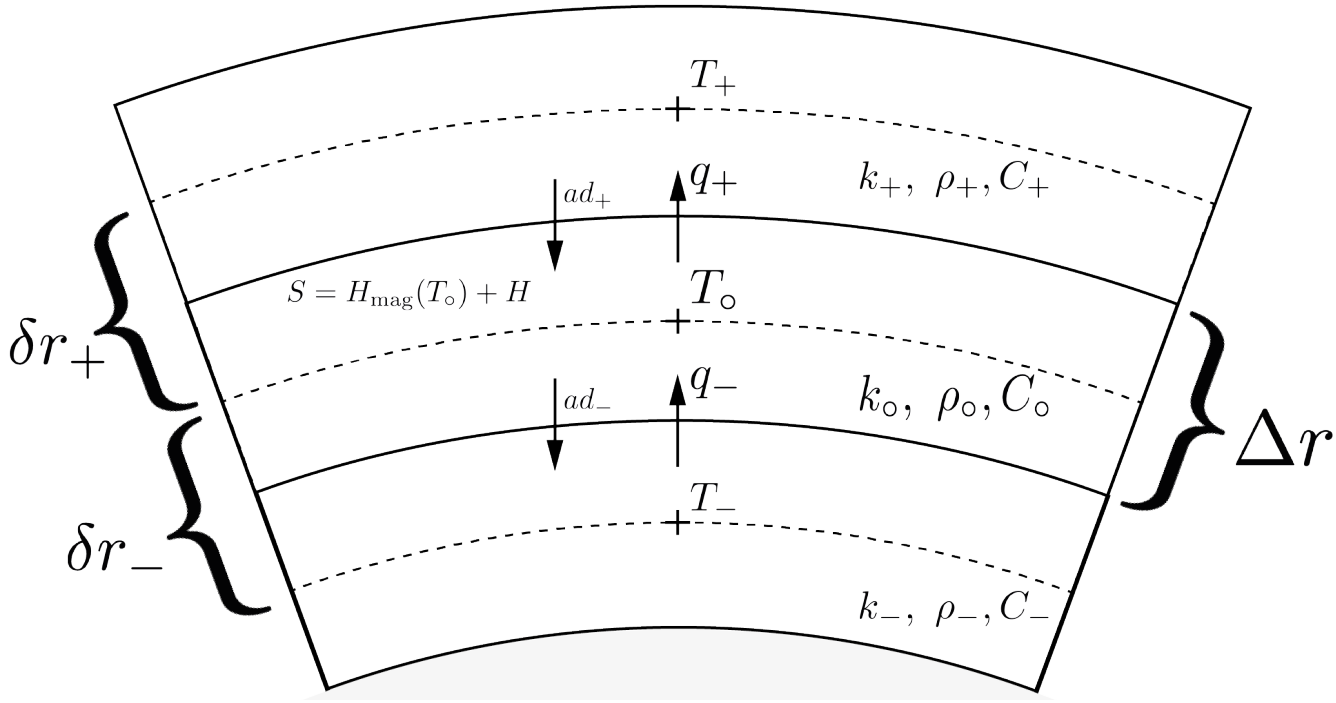

FIGURE 6.4 – Numerical diagram by finite volume see text for different variables.

where S is the heat source, V is the finite volume, ∂U is the variation in internal energy and Q is the heat transfer. The equation developed is expressed as :

$$V\left(\rho C + \frac{L\alpha}{\Delta T_{l-s}}\right)\frac{\partial T}{\partial t} = 4\pi r^2(q_- + ad_-) - 4\pi(r+dr)^2(q_+ + ad_+) + SV, \tag{6.17}$$

where ρ is the density, C the heat capacity, $\frac{L\alpha}{\Delta T_{l-s}}$ the energy need to form new melt (see Section 2.4.3), $q_{+/-}$ the heat flux from conduction, $ad_{+/-}$ the heat flux from advection, S the internal heating term. The + symbol refers to the volume or interface above, the − symbol to the volume or interface below and the ∘ symbol to the volume in which the energy balance is made. These different terms are calculated using the Patankar (2018) formalisation and linearisation :

$$ad_{+/-} = -\,u_{+/-}\rho_{+/-}C_{+/-}\frac{(T_{+/\circ} - T_{+/\circ})}{2} = v_{+/-}\frac{(T_{\circ/+} - T_{-/\circ})}{2}, \tag{6.18}$$

$$q_{+/-} = \kappa_{+/-}\frac{\left(T_{\circ/+} - T_{-/\circ}\right)}{(\partial r)_{+/-}} = a_{+/-}\left(T_{+/\circ} - T_{\circ/-}\right), \tag{6.19}$$

$$\kappa_{+/-} = \left(\frac{1-f_{+/-}}{k_{+/\circ}} + \frac{f_{+/-}}{k_{\circ/-}}\right)^{-1}, \tag{6.20}$$

$$f_{+/-} = \frac{\Delta r}{2\delta r_{+/-}}, \tag{6.21}$$

$$S = H + H_{\text{mag}}(T_\circ) = H_\circ + \gamma_\circ T_\circ + \beta_\circ, \tag{6.22}$$

$$\Gamma = \rho_\circ C_\circ + \frac{L\alpha}{\Delta T_{l-s}}, \tag{6.23}$$

where $\delta r_{+/-}$ is the distance between the centre point of two volumes, $\kappa_{+/-}$ the thermal conductivity at the interface, H the internal heating from HPEs, $H_{\text{mag}}(T_\circ)$ Equation 2.37), internal heating from the cooling of magma (Equation 2.25) which is a linear function of the temperature of the volume with a temperature-dependent component ($\gamma_\circ$) and a temperature-independent ($\beta_\circ$) component, $u_{+/-}$ is the downward advection at the radius of the interface r or $r + \Delta r$ (Equation 2.23) with r the radius at the base of the volume and Δr the radial step. The heat conservation give then :

$$\Gamma \frac{\partial T}{\partial t} = \frac{1}{\Delta r}\left(a_-(T_\circ - T_-) + v_- \frac{(T_\circ - T_-)}{2}\right) - \frac{(r+\Delta r)^2}{r^2 \Delta r}\left(a_+(T_+ - T_\circ) + v_+ \frac{(T_+ - T_\circ)}{2}\right) + S, \quad (6.24)$$

also written as :

$$\Gamma \frac{\partial T}{\partial t} = \frac{1}{\Delta r}\left(a_- + \frac{v_-}{2}\right)(T_\circ - T_-) - \frac{(r+\Delta r)^2}{r^2 \Delta r}\left(a_+ + \frac{v_+}{2}\right)(T_+ - T_\circ) + S, \quad (6.25)$$

$$\Gamma \frac{\partial T}{\partial t} = T_- \frac{-\left(a_- + \frac{v_-}{2}\right)}{\Delta r} + T_\circ \left[\frac{\left(a_- + \frac{v_-}{2}\right)}{\Delta r} - \frac{(r+\Delta r)^2}{r^2 \Delta r}\left(a_+ + \frac{v_+}{2}\right) + \gamma_\circ\right] + T_+ \left[\frac{(r+\Delta r)^2}{r^2 \Delta r}\left(a_+ + \frac{v_+}{2}\right)\right] + H_\circ + \beta_\circ. \quad (6.26)$$

An implicit Taylor scheme is then used :

$$\frac{\partial T}{\partial t} = \frac{T_\circ^{j+1} - T_\circ^{j}}{\Delta t}, \quad (6.27)$$

with Δt the time step, j the current time t and $j+1$ the time $t + \Delta t$. We can then write :

$$T_\circ^{j} = B\ T_\circ^{j+1} + C\ T_-^{j+1} + A\ T_+^{j+1} + \frac{(H_\circ^{j+1} + \beta_\circ^{j+1})\,\Delta t}{\Gamma}, \quad (6.28)$$

with :

$$A = \frac{-\Delta t}{\Gamma} \times \frac{\left(a_- + \frac{v_-}{2}\right)}{\Delta r}, \quad (6.29a)$$

$$B = 1 + \left[\frac{\left(a_- + \frac{v_-}{2}\right)}{\Delta r} - \frac{(r+\Delta r)^2}{r^2 \Delta r}\left(a_+ + \frac{v_+}{2}\right) + \gamma\right] \times \frac{\Delta t}{\Gamma}, \quad (6.29b)$$

$$C = \frac{\Delta t}{\Gamma} \times \frac{(r+\Delta r)^2 \times \left(a_+ + \frac{v_+}{2}\right)}{r^2 \Delta r}, \quad (6.29c)$$

which give a matrix form :

$$\boldsymbol{T}^{j} = \boldsymbol{M}\boldsymbol{T}^{j+1} - \frac{\left(\boldsymbol{H}^{j+1} + \boldsymbol{\beta}^{j+1}\right)\Delta t}{\boldsymbol{\Gamma}}, \quad (6.30)$$

where $\boldsymbol{T}^j$ and $\boldsymbol{T}^{j+1}$ are respectively the current temperature vector and the next temperature vector, $\boldsymbol{H}^{j+1}$ the internal heating vector, $\boldsymbol{\beta}^{j+1}$ temperature-independent from magma heating, $\boldsymbol{\Gamma}$ vector with the Γ components and $\boldsymbol{M}$ the following matrix :

$$\boldsymbol{M} = \begin{pmatrix} CL_1 & CL_2 & \cdots & \cdots & \cdots & 0 \\ B & A & C & 0 & \cdots & 0 \\ 0 & B & A & C & \cdots & 0 \\ 0 & \vdots & \ddots & \ddots & \ddots & \vdots \\ \vdots & \cdots & \cdots & B & A & C \\ 0 & \cdots & 0 & 0 & CL_2 & CL_1 \end{pmatrix}^N . \tag{6.31}$$

The subsequent temperature vector is then obtained by subtracting the temperature-independent term and multiplying by the inverse matrix, giving :

$$\boldsymbol{T}^{j+1} = \boldsymbol{M}^{-1} \left(\boldsymbol{T}^j + \frac{\boldsymbol{H}^{j+1} - \boldsymbol{\beta}^{j+1}}{\boldsymbol{\Gamma}} \right). \tag{6.32}$$

Numerical issues

Interpolation in the lithosphere

One of the numerical difficulties with our model is the growth of the lithosphere over time. Between two time steps, the thickness of the conductive part is not the same. It is therefore not just possible to use the previous vector as the current vector ; we need to consider a transformation. A classic way of dealing with this problem is to scale the conduction by adding a term that depends on the growth of the lid. The problem with this approach is that it considers the increase in volume of the lithosphere to be global, as if it were inflating, whereas only the base of the lithosphere is affected. We therefore preferred to implement an interpolation algorithm combined with a variable number of finite volumes in the lithosphere (Figure 6.5).

Initially, a minimum radial step ($\Delta r_{\min}$) is set which, together with the initial thickness of the lithosphere, determines the number of N points initially required. When the lithosphere grows, two scenarios are possible. We test whether adding a point in the lithosphere causes the radial step size to fall below the set minimum :

$$\frac{D_l}{N+1} < \Delta r_{\min}. \tag{6.33}$$

If it's true, the number of points is retained for the new time step ($N_{\text{new}} = N$), otherwise a point is added ($N = N + 1$). The radial step is then recalculated using the number of points and the thickness of the lithosphere. The temperature on the new mesh is then obtained by interpolation from the old mesh, using boundary half-volumes whose temperature is fixed with

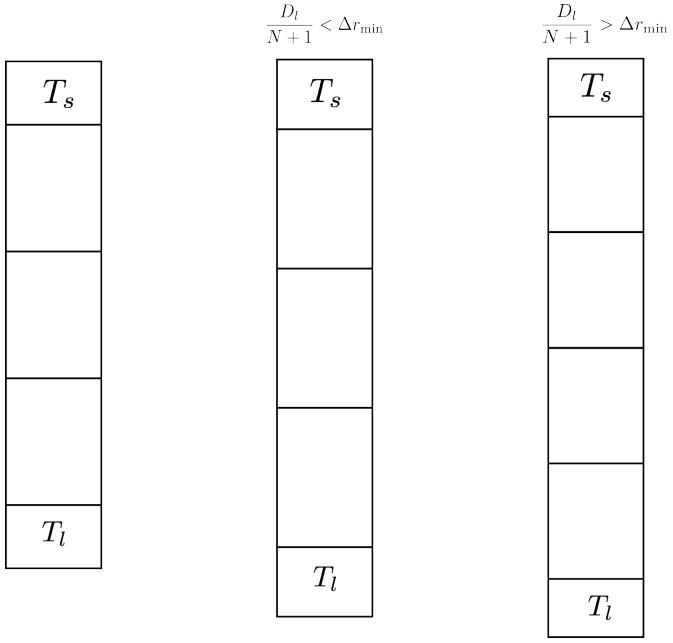

FIGURE 6.5 – Mesh size diagram as a function of lithosphere thickening rate. On the left the initial case and on the right the two possibilities, either the Δr increases or a new point is added.

a Dirichlet condition. This interpolation creates a constraint : the lithosphere must not grow by more than half a radial step during a time step. Otherwise, it would be impossible to interpolate the entire temperature profile.

time stepper

As our different methods have either implicit descriptions or small variations, the time step (Δt) can be chosen freely. Nevertheless, interpolation imposes a maximum rate of lithospheric growth ($\frac{\mathrm{d}D_l}{\mathrm{d}t}$) that depends on the size of the radial step (Δr). The time step must therefore satisfy the following condition :

$$\frac{\mathrm{d}D_l}{\mathrm{d}t}\Delta t < \frac{\Delta r}{2}. \tag{6.34}$$

We can generalise this condition to the growth of the crust and add a maximum temperature difference ($\Delta T_{\max}$) between two time steps for the temperature of the mantle T_m and the core T_c. The time step can then be written as :

$$\Delta t = \min(\frac{\Delta r_{\min}}{2k_{11}}, \frac{\Delta r_{\min}}{2k_{12}}, \frac{\Delta T_{\max}}{2k_{13}}, \frac{\Delta T_{\max}}{2k_{14}}). \tag{6.35}$$

This condition is very restrictive and can lead to very small-time steps in some cases, making the calculation very long. To limit this, a minimum and maximum time step are imposed. These limit the calculation time without having too large an impact on accuracy.

1PIECE tool

Our thermal evolution model with crust extraction presented in Chapter 2 is solved using the numerical methods described above in a tool we have called 1PIECE (1D-Planetary Interior Evolution with Crust Extraction).

Programming language and libraries

The language used is C++ because it is compilable and easy to use. The functions used are mainly taken from the standard library and the code is written with a functional approach. However, for linear algebra, the code uses the external Eigen library (Guennebaud et al., 2010). This library allows matrix inversion using various methods, the strategy used being a QR decomposition of a matrix with column pivoting. This method is the appropriate balance between computation time and accuracy. Its precision is always very good, but its calculation time is only correct below the 1000x1000 matrices, since the size of the lithosphere rarely exceeds 1000 km and the radial pitch rarely falls below 1 km, we are in the right size range. Interpolation also uses a function from the Eigen library, but an unsupported function, the Spline function. This function allows you to easily define an interpolation function from 2 vectors and then use this function to determine a vector from another mesh.

Algorithm

The summary of the algorithm used by our tool is shown in Figure 6.6 and its caption. This is an algorithm for a single thermal evolution that can be interfaced with codes for systematic exploration or MCMC inversion.

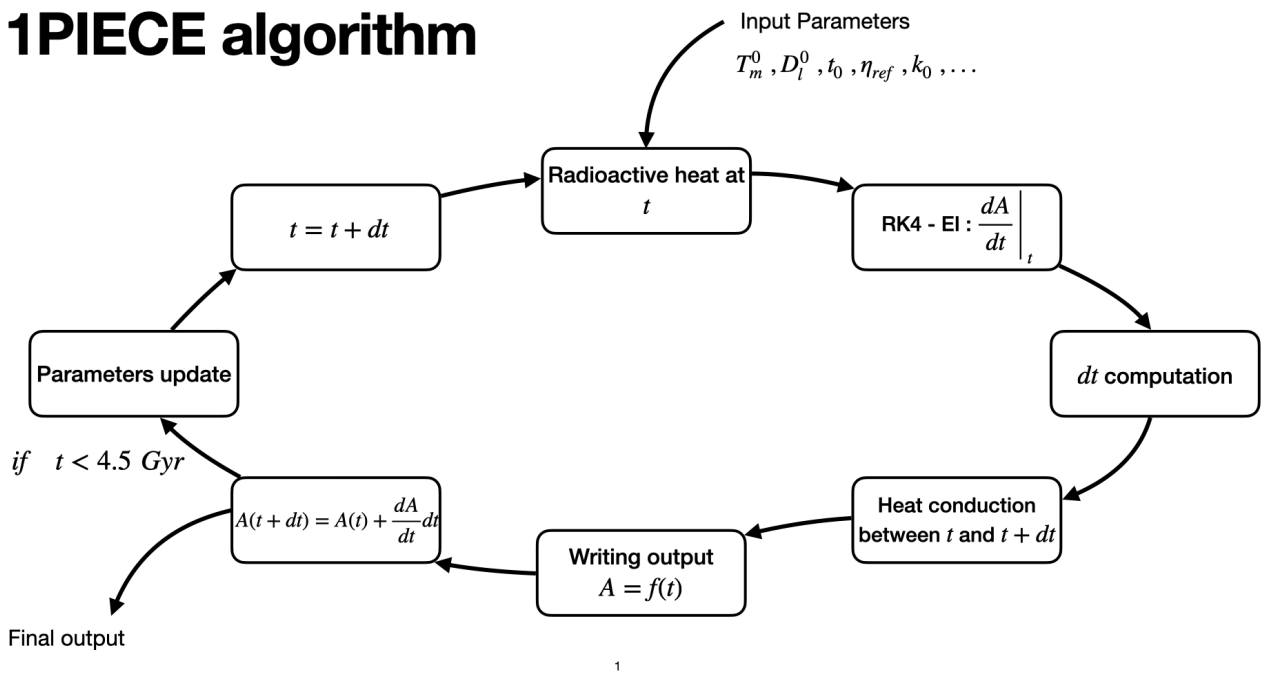

FIGURE 6.6 – 1PIECE algorithm for calculating thermal evolution over 4.5 Ga. 1/ Radioactive heating is calculated for each tank 2/ Derivatives are evaluated using RK4 or an implicit Euler method. 3/ With the derivatives, the time step is calculated and the estimates 2, 3 and 4 of RK3 are calculated. 4/ Heat conduction is solved in both hemispheres 5/ The different outputs are written for a time t. 6/ The quantities are updated with the derivatives 7/ If t+dt is less than 4.5 Ga, the model parameters are updated, such as enrichment, interpolation in the lithosphere etc. 8/ The time is modified 9/ The loop starts again.

Appendix - B - Origin of lateral variation in crustal thickness on Mars and Mercury.

Ce court document était prévu pour candidater à une bourse allemande de la fondation Humboldt. L'équipe du DLR m'a finalement proposé un poste sur un autre projet. L'objectif à présent est de déposer ce projet pour un appel à projet du DFG allemand après l'avoir amélioré pendant mon premier postdoc. C'est néanmoins un document que j'ai écrit pendant ma thèse et en lien avec mes travaux, je l'ai donc inclus dans cette annexe.

State of the research

Planetary crusts are widely studied as they are both the seat of surface processes at the interface with the atmosphere and they are a main source of information about planetary interiors. For terrestrial planets, the crusts are mainly composed of igneous rocks and two types of igneous crust are usually distinguished. A primary crust forms during the cooling and crystallisation of a magma ocean. Secondary crust results from partial melting of the mantle and since the melt is less dense, it is extracted and builds a crust with a basaltic composition at the surface. Mars and Mercury's crusts are mainly secondary crusts, and their extraction has a key role in their thermal and chemical evolution. Indeed, the melts formed by mantle partial melting are enriched in incompatible elements such as volatiles (water, CO2, sulphur) and heat-producing elements (HPE : U, Th, and K). The extracted magma brings with it these incompatible elements to the crust where the volatile are partially outgas to the atmosphere. It is, therefore, crucial to be able to model the formation of magma in the mantle and its extraction over time on a planetary scale to constrain the thermochemical evolution of the planet.

After the Earth-Moon system, the Martian crust is the one with the most constraints. The Bouguer gravity anomaly can be inverted to provide the relief along the crust-mantle interface, and hence the crust thickness variations. These inversions depend upon the crustal density, upper mantle density profile and the local value of the seismic

crustal thickness at the InSight landing site as an anchor point (Knapmeyer-Endrun et al., 2021). These inversions reveal a dichotomy of crustal thicknesses between 10 and 30 km between the two hemispheres, with an average value between 30 and 60 km. There are two types of proposed origin for the Martian dichotomy. An external origin, with a giant impact that, according to the most recent models, most probably took place in the southern hemisphere (Ballantyne et al., 2023). The impact would have formed a local magma ocean in the southern hemisphere, which, when it cooled, would have formed a very thick crust. An internal origin has also been proposed for the dichotomy. Šrámek and Zhong (2012) were able to show that it is possible to form a thick crustal hemisphere through the migration of the Tharsis plume. This migration would have been caused by the higher viscosity of the residue formed by extraction from the crust. In my first paper, Bonnet Gibet et al. (2022), I propose a positive feedback mechanism between the melt extraction rate and the crustal thickness, which makes it possible to form variations in crust thickness at large wavelengths and in particular at hemispherical ones.

Recently, a reinterpretation of Messenger data has revealed a geological province characterized by an Mg-rich composition (Beuthe et al., 2020). This magnesium-rich crust is interpreted as a basalt formed in the mantle with very large molten fractions at the time of crustal extraction. The Mg-rich basalts are denser than the rest of the crust. From the gravity and topography data available for Mercury, and using a similar inversion method to that used for Mars, we obtained a thicker crustal region for the Mg-rich province. On average, the mercury crust would be around 35 km thick, but there are very strong lateral variations, with a 30 km difference between the northern plains and the Mg-rich region. The Messenger data on mostly cover the northern hemisphere, so we can expect the same kind of variations in the southern hemisphere with a better coverage of the surface. Thermal evolution models for Mercury manage to reproduce the volume of crust produced but not the lateral variations (Tosi et al., 2013a). The Rayleigh number for Mercury is low ($10^3 - 10^4$), which implies that the upwellings pattern remain stretched horizontally throughout the secular cooling. Because of this and how extraction models are currently constructed, variations in crustal thickness monitor the shape of the upwellings.

Mars and Mercury, therefore, have similar characteristics, with stagnant lid dynamics, thick crusts compared to the amount of silicate and strong variations in crust thickness at long wavelengths.

Scientific question and motivation

The purpose of this project is to propose explanations for the significant lateral variations in crustal thickness for Mars and Mercury. These strong lateral variations in crustal thickness are evidence of important processes at work in the dynamics of

the mantle at the time the secondary crust formed. This may lead us to consider whether these processes are common to Mars and Mercury because they share the same stagnant lids regime of mantle convection. The differences in thickness are also linked to differences in composition, outgassing of volatiles and crustal differentiation processes. Constraining this process thus gives us a better understanding of the thermo-chemical evolution of a stagnant lid planet and the main features of planetary surfaces. We need then to consider the crustal extraction over time and its impact on the dynamics. To carry out this project, we will be working on improving thermal evolution models with crust extraction in 2D and 3D for Mars and Mercury.

The Martian dichotomy

For Mars, there are several models to explain the formation of the dichotomy. The models described in the introduction for the formation of the Martian dichotomy, the giant impact or the migration of a plume, have in common that the subsequent thermal evolution following the process of formation has never been computed. This is not the case for the mechanism I described Bonnet Gibet et al. (2022). We revisited Mars, parametric thermal evolution models with crust extraction in an asymmetric geometry. We have demonstrated that there exists a positive feedback mechanism between melt extraction rate and crustal thickness on stagnant lid planets. As the crust is enriched in heat-producing elements, the conductive lid of a one-plate planet is hotter and thinner where the crust is thicker, inducing a larger amount of partial melting in the well-mixed convective mantle below the thinner lid and hence a larger rate of melt extraction and crustal thickening. We have proposed this mechanism as an explanation for the formation of the Martian dichotomy in crustal thickness. Our model allows us to form a dichotomy like the one expected for Mars, but also to obtain a current thermal state that corresponds to the InSight mission's observations on the structure of the crust and mantle. In these models, the convective mantle is considered to be well mixed and the 3D flow is not resolved. We, therefore, do not have access to the convection patterns and the effects of these shapes on this mechanism.

In this project, we will use 2D and 3D models to study the formation of the Martian crust. We will use a 2D and 3D convection model that will be improved from the existing one. Firstly, we will test the existence of our positive feedback mechanism in 2D and 3D geometry with the convection patterns. We will observe and quantify the interaction between this mechanism and the convection. Secondly, by using the same model, we will test the different origins of the dichotomy. We will define thermal evolution and crustal thickness distributions specific to each mechanism. We will then be able to distinguish, or not, which of the different mechanisms best corresponds to the observations on the thickness of the crust (Knapmeyer-Endrun et al., 2021) and the thermal state of the mantle.

Mercury's Mg-rich province

The study of crust formation for Mercury using 2D and 3D convection models, as for Mars, must address two problems. (i) Explain the formation of a geological province of the thick crust with a Mg-rich composition. For Mercury, this constraint is more recent and less precise than for Mars. For the time being, there is no mechanism for the formation of this province. The positive feedback mechanism proposed for Mars seems to be valid for all planets in a stagnant lid regime and could explain the formation of this province of the thick crust associated with larger densities. Mg-rich basalts appear to be formed at higher melt fractions in the mantle, which would be consistent with our mechanism. Nevertheless, the assumption of a well-mixed mantle preferable for this mechanism is conceivable for Mars but seems to be more difficult for Mercury. As with Mars, we could also investigate other origins, such as an impact or the formation of a feather. (ii) Mercury's low Rayleigh number results in stationary mantle dynamics. The forms of this stationary convection, 2D rollers, are not found in the crust thicknesses as we might expect. The expected crustal thickness distribution is characterised by slight lateral variations, except for one geological province where this is linked to a difference in chemistry. Unlike Mars, we have no precise estimate of crustal thickness or lateral variations with which to compare our results. However, the BepiColombo ESA mission, which is on its way to Mercury, will provide many new constraints, particularly on the crust, such as topogravimetric and compositional data. We will therefore be able to use our results to determine observables that can be detected by the mission and that will enable us to distinguish between the different scenarios that will emerge.

Choice of the institute

The Institute of Planetary Sciences of the DLR is an ideal environment for this project. Indeed, the Planetary Physics team has long-standing expertise in the modelling of the thermal evolution of telluric planets as well as the necessary equipment (computer facilities, numerical model, etc.). The extraction of planetary crusts in 2D and 3D models is a recurrent topic of the team to which I can bring the experience acquired during my PhD on the extraction of the crust in 1D. The institute will also allow me to evolve in a multidisciplinary laboratory such as experimental mineralogy or the observation of planetary surfaces which are essential in the understanding of planetary crust formation. Members of the institute are also involved in the scientific teams of future and past space missions to Mars and Mercury, and I myself am a member of the InSight Science Team. For me, joining the Institute of Planetary Sciences is a way of combining my multidisciplinary approach to planetary sciences with my commitment to space missions.

Method

The extraction of the crust is linked to the dynamics of magma from its formation in the mantle to its deposition and cooling to form the crust. The magma dynamics in a ductile zone are obtained by solving for a two-phase flow and taking into account compaction and damage (Bercovici et al., 2001). The physics involved in solving this type of flow is more challenging and time-consuming than solving solid-convection flow. It is therefore quite difficult to model the 4.5 billion years of thermal evolution of Mars or Mercury even with a crust that forms over the first 1.5 billion years after their formation.

To address this difficulty, convection models mainly rely on one strong assumption : the characteristic extraction time is much smaller than the characteristic convection time, and the magma extraction can be considered therefore instantaneous. It is the case for the thermal and chemical evolution of one-plate planets. Plesa and Breuer (2014) described a classic way of accounting for crustal extraction by advection of composition tracers. These tracers track the enrichment of radioactive elements, water and refractory elements of the mantle that are modified by the extraction of the crust. If the temperature exceeds the solidus in a cell, an amount equivalent to the volume of melt formed is extracted and the cell is fixed at the solidus temperature. The compositional tracer value is then updated according to the extracted melt fraction in the cell in which it is located. A second strong hypothesis is then required : magma has a purely radial upward movement and is placed on the surface as crustal material. The growth of the crust is then obtained locally by summing the liquid melts extracted at the depth below.

The majority of crust extraction models in 2D and 3D (Tosi et al., 2013a; Šrámek and Zhong, 2012) are based on the same two strong assumptions : 1. The newly formed magma is extracted instantaneously. 2. Its movement is purely radial to the surface. These two assumptions pose some problems ; I will question these assumptions and propose new methods and assumptions for numerical models to treat the extraction of the crust with a more physical approach.

Problems with the actual assumptions

Firstly, instantaneous extraction means giving an extraction velocity to the magma which depends on a numerical parameter, the time step of the model. This time step is variable over time, depending in particular on the strength of global convection, so the extraction rate is globally uniform. However, if we consider a Darcy speed, then the extraction rate depends on the buoyancy of the melt and the permeability, which increases with the melt fraction. The extraction rate is therefore overestimated, especially for magma formed at depth. Instantaneous extraction is also problematic for the chemical evolution of the mantle as the partitioning of elements (HPE, volatiles, etc.)

depends on the melt fraction at the time of extraction. The current method, where the temperature is limited by the solidus after extraction, only produces low melting fractions. However, these low melt fractions are associated with larger enrichment in incompatible elements and this tends to overestimate the depletion of these elements. Instantaneous extraction also implies that all the melts formed are extracted while some may recrystallize in the mantle, so the amount of crust produced could be overestimated. It is the case if the initial state of the thermal evolution is taken at the time of the solidification of the magma ocean, where a large amount of melt is still present at depth, which leads to extracting large amounts of crust very early and very quickly. Moreover, the radial projection of the melt formed at depth through the surface to obtain the growth of the crust has the consequence of projecting the pattern of convection onto the crustal thickness. Indeed, one expects a movement with a non-negligible lateral component, especially on the way through the lithosphere. Indeed, the brittle rheology of the lithosphere induces a different mode of transport than in the ductile part and as shown by Keller et al. (2013) the ascent is not purely radial. In view of all these elements, it is crucial to provide the community with numerical tools to deal with this topic in a more optimal way. All the more so as crust extraction has important implications for other fields such as the formation of atmospheres or the geochemistry of planetary crusts.

Modification

To improve existing 2D and 3D crust extraction models, we will focus on three axes which can be treated independently and which are based on existing models. The first one would focus on the calculation of crustal thickening as a function of the extraction rate. Secondly, the calculation of melt extraction rates as a function of the melt fraction field. And finally, the description of the melt fraction field and its effects on the dynamics of convection (density, viscosity, etc.) The methods are presented for a 3-dimensional geometry, one radial (r_k) and two angulars (θ, φ), but these methods are also valid for the 2-dimensional case by removing the φ dimension.

Crustal growth rate

The magma is laterally spreading during its rising. The radial component of the motion is the highest but the lateral or angular component cannot be ignored. I propose a method that can be seen as a smoothing function that takes the radial melt extraction rate field calculated by a classical method and transforms it into a smoothed crust growth field. To do this, one would need to determine a smoothing function with parameters that would reflect the geometry of the magma transport. For example, in 3D, we could use a Gaussian function and express the 2D crustal growth field ($\frac{\mathrm{d}D_{cr}}{\mathrm{d}t}(\theta, \varphi)$) as a sum of continuous Gaussian functions along the two angular directions θ and φ :

$$\frac{\mathrm{d}D_{cr}}{\mathrm{d}t}(\theta,\varphi) = \sum_{i}^{n_\theta}\sum_{j}^{n_\varphi} w_{\theta_i,\varphi_j} A \exp\left[-\left(\frac{(\theta-\theta_i)^2}{2\sigma_{\theta_i}^2} + \frac{(\varphi-\varphi_j)^2}{2\sigma_{\varphi_j}^2}\right)\right] \tag{6.36}$$

where n_θ and n_φ are that number of discrete points in our model along the two angular directions, w_{θ_i,φ_j} is the melt extraction rate calculated at discrete coordinate (θ_i, φ_j), A the normalization factor ($\mathrm{A} = \frac{1}{\sigma_{\varphi_j}\sigma_{\theta_i}2\pi}$), σ_{θ_i} that allows for mass conservation and σ_{φ_j} the characteristic spreading lengths according to the two coordinates. These lengths could be either constant or laterally variable. For example, these distances can evolve as a function of the depth (Z_{θ_i}) at which the magma is extracted. The deeper the magma, the more it spread out with an angle α ($\sigma_{\theta_i} = \frac{2\tan\alpha}{3} Z_{\theta_i}$). In this way, we can try out different functions that depend on different variables. These methods may be compared with studies of magma rising in the lithosphere (Keller et al., 2013).

Melt extraction rate

In order to calculate the melt extraction rate w_{θ_i,φ_j}, I propose to calculate from the melt fraction field $\phi(r_k, \theta_i, \varphi_j)$ the magma velocity field $v_{r_k,\theta_i,\varphi_j}$. As I have implemented in a parameteric model (Bonnet Gibet et al., 2022), We will use Darcy's law to calculate this velocity (Bercovici et al., 2001) :

$$v(r_k, \theta_i, \varphi_j) = \mathrm{k}_0 \phi^3 \frac{\Delta\rho g}{\eta_l}(1-\phi) \tag{6.37}$$

where k_0 is the reference permeability of the mantle, $\Delta\rho$ the difference in density between the mantle and the melt, g the gravity, η_l the melt viscosity and ϕ the melt fraction field. Then, we will test several ways of calculating from Darcy's velocity field ($v(r_k, \theta_i, \varphi_j)$) the melt extraction rate (w_{θ_i,φ_j}) from the partially molten volume. Indeed ϕ depends of r so we can use for example the radially average or the radially maximum of Darcy's velocity. We should also propose an assumption on the effect of the extraction on the chemistry (refractoriness, HPE, water) and energy balance on the mantle residue. We are going to test two end-members, (i) chemical equilibration takes place locally where the melt is extracted, i.e. in the volume with melting closest to the surface (ii) chemical equilibration takes place throughout the whole molten volume due to magma circulation. We will test these two very different hypotheses to determine whether or not they diverge.

Dynamics of a partially molten mantle

As melt extraction is not instantaneous, the temperature in the mantle is no longer limited by the solidus temperature. This means that a molten fraction remains in the mantle despite extraction. We can then consider the dynamics of these melts in the mantle and their interactions with solid convection. That is why I would like to add some features that could be applied to solid convection in order to take into account the melt fraction. I will add features that could approximate a two-phase flow as a melt

fraction field, $\phi(r, \theta, \varphi)$ that is advected and have some effects on the dynamics. For example, the viscosity of the mantle, which depends on temperature and pressure (η), decreases as the melt fraction increases, $\eta(T, P, \phi) = \eta(T, P) \exp(-E_\phi \phi)$. This effect of the melt fraction can create strong viscosity gradients, which can modify the dynamics of the whole mantle.

In parallel, I would like to explore convection models including the two-phase flow using, for example, the code of Dannberg et al. (2019). It would thus be possible to obtain typical evolutions for a mantle with a two-phase flow and to compare these evolutions with those obtained with our method. It would help to refine the methods in order to obtain the most similar dynamics. Indeed, it might be impossible to reproduce perfectly the dynamics of a two-phase flow with a solid convection model, which would imply that it is purely a two-phase flow problem. In any case, I will try to design a method for solid convection that is as faithful as possible to the two-phase flow while keeping the target of a low-cost parameterization in terms of computation time. We can also compare our results with Ogawa and Yanagisawa (2012b) calculations for Mars which use a simplified two-phase flow in Cartesian geometry.

Tools, planning and risk management

Numerical Tool I plan to use the convection GAIA code (Hüttig and Stemmer, 2008) to implement the numerical methods I will create. GAIA is the numerical tool for mantle convection developed by the Institute's Planetary Physics team. It should be noted that GAIA is coded in C++, a language I have a solid knowledge of. In the first step, I will use a 2D ring geometry which allows to have good spatial and temporal resolutions for a rather low computation time. When the new modifications will have be validated in 2D, I will switch to 3D geometry.

planning and risk management The project will be carried out in several successive stages. To familiarise myself with the Gaia code, I will start by run the model in its existing form, without new features, to get a starting point for Mars and Mercury. We can then run these reference cases again throughout the project and see the impact of our new features on our results step by step. I will start by adding the first two parts of the method, surface spreading and Darcy velocity, because they don't involve changing the dynamics of the mantle and are simpler to implement.These first two modifications will potentially be sufficient to write a first paper on the case of the Martian dichotomy. For Mercury, the implementation of the last one on the dynamics of the partial mantle seems to me to be necessary to achieve our objectives. This last point is the most challenging and could lead to more work than expected, which is why it will not be a priority.

Bibliographie

Acuña, M., Connerney, J., Ness, Lin, R., Mitchell, D., Carlson, C., McFadden, J., Anderson, K., Reme, H., Mazelle, C., et al. (1999). Global distribution of crustal magnetization discovered by the Mars Global surveyor MAG/ER experiment. *Science*, 284(5415) :790–793.

Agee, C. B., Wilson, N. V., McCubbin, F. M., Ziegler, K., Polyak, V. J., Sharp, Z. D., Asmerom, Y., Nunn, M. H., Shaheen, R., Thiemens, M. H., et al. (2013). Unique meteorite from early Amazonian Mars : Water-rich basaltic breccia Northwest Africa 7034. *Science*, 339(6121) :780–785.

Anders, E. (1996). Evaluating the evidence for past life on Mars. *Science*, 274(5295) :2119–2121.

Anderson, R. C., Dohm, J. M., Buczkowski, D., and Wyrick, D. Y. (2022). Early Noachian terrains : Vestiges of the early evolution of Mars. *Icarus*, 387 :115170.

Anderson, R. C., Dohm, J. M., Golombek, M. P., Haldemann, A. F., Franklin, B. J., Tanaka, K. L., Lias, J., and Peer, B. (2001). Primary centers and secondary concentrations of tectonic activity through time in the western hemisphere of Mars. *Journal of Geophysical Research : Planets*, 106(E9) :20563–20585.

Andrews-Hanna, J. C. (2012). The formation of Valles Marineris : 2. Stress focusing along the buried dichotomy boundary. *Journal of Geophysical Research : Planets*, 117(E4).

Andrews-Hanna, J. C., Zuber, M. T., and Banerdt, W. B. (2008a). The Borealis basin and the origin of the martian crustal dichotomy. *Nature*, 453(7199) :1212–1215.

Andrews-Hanna, J. C., Zuber, M. T., and Hauck, S. A. (2008b). Strike-slip faults on Mars : Observations and implications for global tectonics and geodynamics. *Journal of Geophysical Research : Planets*, 113(E8).

Arvidson, R. E., Ruff, S. W., Morris, R. V., Ming, D. W., Crumpler, L. S., Yen, A. S., Squyres, S. W., Sullivan, R. J., Bell III, J. F., Cabrol, N. A., et al. (2008). Spirit

Mars rover mission to the Columbia Hills, Gusev Crater : Mission overview and selected results from the Cumberland Ridge to Home Plate. *Journal of Geophysical Research : Planets*, 113(E12).

Aubaud, C., Hauri, E. H., and Hirschmann, M. M. (2004). Hydrogen partition coefficients between nominally anhydrous minerals and basaltic melts. *Geophysical Research Letters*, 31(20).

Baker, M. B. and Stolper, E. M. (1994). Determining the composition of high-pressure mantle melts using diamond aggregates. *Geochimica et Cosmochimica Acta*, 58(13) :2811–2827.

Ballantyne, H. A., Jutzi, M., Golabek, G. J., Mishra, L., Cheng, K. W., Rozel, A. B., and Tackley, P. J. (2023). Investigating the feasibility of an impact-induced Martian Dichotomy. *Icarus*, 392 :115395.

Bandfield, J. L., Edwards, C. S., Montgomery, D. R., and Brand, B. D. (2013). The dual nature of the martian crust : Young lavas and old clastic materials. *Icarus*, 222(1) :188–199.

Banerdt, W. B., Smrekar, S. E., Banfield, D., Giardini, D., Golombek, M., Johnson, C. L., Lognonné, P., Spiga, A., Spohn, T., Perrin, C., et al. (2020). Initial results from the Insight mission on Mars. *Nature Geoscience*, 13(3) :183–189.

Baratoux, D., Samuel, H., Michaut, C., Toplis, M. J., Monnereau, M., Wieczorek, M., Garcia, R., and Kurita, K. (2014). Petrological constraints on the density of the Martian crust. *Journal of Geophysical Research : Planets*, 119(7) :1707–1727.

Baratoux, D., Toplis, M., Monnereau, M., and Sautter, V. (2013). The petrological expression of early Mars volcanism. *Journal of Geophysical Research : Planets*, 118(1) :59–64.

Batra, K. and Foley, B. (2021). Scaling laws for stagnant-lid convection with a buoyant crust. *Geophysical Journal International*, 228(1) :631–663.

Bayes, T. (1763). LII. an essay towards solving a problem in the doctrine of chances. by the late rev. mr. bayes, frs communicated by mr. price, in a letter to john canton, amfr s. *Philosophical transactions of the Royal Society of London*, (53) :370–418.

Bellucci, J., Nemchin, A., Whitehouse, M. J., Snape, J., Kielman, R. B., Bland, P., and Benedix, G. (2016). A Pb isotopic resolution to the Martian meteorite age paradox. *Earth and Planetary Science Letters*, 433 :241–248.

Bercovici, D., Ricard, Y., and Schubert, G. (2001). A two-phase model for compaction and damage : 1. general theory. *Journal of Geophysical Research : Solid Earth*, 106(B5) :8887–8906.

Beuthe, M., Charlier, B., Namur, O., Rivoldini, A., and Van Hoolst, T. (2020). Mercury's crustal thickness correlates with lateral variations in mantle melt production. *Geophysical Research Letters*, 47(9) :e2020GL087261. e2020GL087261 10.1029/2020GL087261.

Bibring, J.-P., Langevin, Y., Mustard, J. F., Poulet, F., Arvidson, R., Gendrin, A., Gondet, B., Mangold, N., Pinet, P., Forget, F., et al. (2006). Global mineralogical and aqueous Mars history derived from OMEGA/Mars Express data. *science*, 312(5772) :400–404.

Birnstiel, T., Fang, M., and Johansen, A. (2016). Dust evolution and the formation of planetesimals. *Space Science Reviews*, 205 :41–75.

Blichert-Toft, J., Gleason, J. D., Télouk, P., and Albarède, F. (1999). The Lu–Hf isotope geochemistry of shergottites and the evolution of the Martian mantle–crust system. *Earth and Planetary Science Letters*, 173(1-2) :25–39.

Bogard, D. D. and Johnson, P. (1983). Martian gases in an Antarctic meteorite ? *Science*, 221(4611) :651–654.

Bonnet Gibet, V., Michaut, C., Wieczorek, M., and Lognonné, P. (2022). A positive feedback between crustal thickness and melt extraction for the origin of the martian dichotomy. *Journal of Geophysical Research : Planets*, 127(12) :e2022JE007472.

Boukaré, C.-E. and Ricard, Y. (2017). Modeling phase separation and phase change for magma ocean solidification dynamics. *Geochemistry, Geophysics, Geosystems*, 18(9) :3385–3404.

Bouley, S., Baratoux, D., Matsuyama, I., Forget, F., Séjourné, A., Turbet, M., and Costard, F. (2016). Late Tharsis formation and implications for early Mars. *Nature*, 531(7594) :344–347.

Bouley, S., Keane, J. T., Baratoux, D., Langlais, B., Matsuyama, I., Costard, F., Hewins, R., Payré, V., Sautter, V., Séjourné, A., et al. (2020). A thick crustal block revealed by reconstructions of early Mars Highlands. *Nature Geoscience*, 13(2) :105–109.

Bourdon, B., Touboul, M., Caro, G., and Kleine, T. (2008). Early differentiation of the Earth and the Moon. *Philosophical Transactions of the Royal Society A : Mathematical, Physical and Engineering Sciences*, 366(1883) :4105–4128.

Bouvier, A., Blichert-Toft, J., and Albarede, F. (2009). Martian meteorite chronology and the evolution of the interior of Mars. *Earth and Planetary Science Letters*, 280(1-4) :285–295.

Bouvier, A. and Wadhwa, M. (2010). The age of the solar system redefined by the oldest Pb - Pb age of a meteoritic inclusion. *Nature geoscience*, 3(9) :637–641.

Bouvier, L. C., Costa, M. M., Connelly, J. N., Jensen, N. K., Wielandt, D., Storey, M., Nemchin, A. A., Whitehouse, M. J., Snape, J. F., Bellucci, J. J., et al. (2018). Evidence for extremely rapid magma ocean crystallization and crust formation on Mars. *Nature*, 558(7711) :586–589.

Boynton, W., Taylor, G., Evans, L. G., Reedy, R., Starr, R., Janes, D., Kerry, K., Drake, D., Kim, K., Williams, R., et al. (2007). Concentration of H, Si, Cl, K, Fe, and Th in the low-and mid-latitude regions of Mars. *Journal of Geophysical Research : Planets*, 112(E12).

Breuer, D. and Spohn, T. (2003). Early plate tectonics versus single-plate tectonics on Mars : Evidence from magnetic field history and crust evolution. *Journal of Geophysical Research : Planets*, 108(E7).

Breuer, D. and Spohn, T. (2006). Viscosity of the Martian mantle and its initial temperature : Constraints from crust formation history and the evolution of the magnetic field. *Planetary and Space Science*, 54(2) :153–169.

Broquet, A. and Andrews-Hanna, J. C. (2023). Geophysical evidence for an active mantle plume underneath Elysium Planitia on Mars. *Nature Astronomy*, 7(2) :160–169.

Broquet, A., Wieczorek, M., and Fa, W. (2021). The composition of the south polar cap of Mars derived from orbital data. *Journal of Geophysical Research : Planets*, 126(8) :e2020JE006730.

Brož, P., Bernhardt, H., Conway, S. J., and Parekh, R. (2021). An overview of explosive volcanism on Mars. *Journal of Volcanology and Geothermal Research*, 409 :107125.

Caldwell, J. and Turcotte, D. (1979). Dependence of the thickness of the elastic oceanic lithosphere on age. *Journal of Geophysical Research : Solid Earth*, 84(B13) :7572–7576.

Canup, R. M. (2012). Forming a Moon with an Earth-like composition via a giant impact. *Science*, 338(6110) :1052–1055.

Carr, M. H. (1979). Formation of Martian flood features by release of water from confined aquifers. *Journal of Geophysical Research : Solid Earth*, 84(B6) :2995–3007.

Carr, M. H. (1987). Water on mars. *Nature*, 326(6108) :30–35.

Carter, J. and Poulet, F. (2013). Ancient plutonic processes on Mars inferred from the detection of possible anorthositic terrains. *Nature Geoscience*, 6(12) :1008–1012.

Carter, J., Poulet, F., Bibring, J.-P., Mangold, N., and Murchie, S. (2013). Hydrous minerals on Mars as seen by the CRISM and OMEGA imaging spectrometers : Updated global view. *Journal of Geophysical Research : Planets*, 118(4) :831–858.

Carter, J., Riu, L., Poulet, F., Bibring, J.-P., Langevin, Y., and Gondet, B. (2023). A mars orbital catalog of aqueous alteration signatures (MOCAAS). *Icarus*, 389 :115164.

Cassata, W. S., Cohen, B. E., Mark, D. F., Trappitsch, R., Crow, C. A., Wimpenny, J., Lee, M. R., and Smith, C. L. (2018). Chronology of martian breccia NWA 7034 and the formation of the martian crustal dichotomy. *Science Advances*, 4(5) :eaap8306.

Cheng, K. W., Rozel, A., Ballantyne, H., Jutzi, M., Golabek, G., and Tackley, P. (2022). Martian crustal dichotomy formation and its effect on volcanisms : mantle convection models. In *European Planetary Science Congress*, pages EPSC2022–1045.

Christensen, P., McSween Jr, H., Bandfield, J., Ruff, S., Rogers, A., Hamilton, V., Gorelick, N., Wyatt, M., Jakosky, B., Kieffer, H., et al. (2005). Evidence for magmatic evolution and diversity on Mars from infrared observations. *Nature*, 436(7050) :504–509.

Christeson, G., Goff, J., and Reece, R. (2019). Synthesis of oceanic crustal structure from two-dimensional seismic profiles. *Reviews of Geophysics*, 57(2) :504–529.

Citron, R. I., Manga, M., and Hemingway, D. J. (2018a). Timing of oceans on Mars from shoreline deformation. *Nature*, 555(7698) :643–646.

Citron, R. I., Manga, M., and Tan, E. (2018b). A hybrid origin of the Martian crustal dichotomy : degree-1 convection antipodal to a giant impact. *Earth and Planetary Science Letters*, 491 :58–66.

Clauser, C., Huenges, E., et al. (1995). Thermal conductivity of rocks and minerals. *Rock physics and phase relations : a handbook of physical constants*, 3 :105–126.

Cohen, B. E., Mark, D. F., Cassata, W. S., Lee, M. R., Tomkinson, T., and Smith, C. L. (2017). Taking the pulse of Mars via dating of a plume-fed volcano. *Nature Communications*, 8(1) :640.

Collinet, M., Médard, E., Charlier, B., Vander Auwera, J., and Grove, T. L. (2015). Melting of the primitive Martian mantle at 0.5–2.2 GPa and the origin of basalts and alkaline rocks on Mars. *Earth and Planetary Science Letters*, 427 :83–94.

Collinet, M., Plesa, A.-C., Grove, T. L., Schwinger, S., Ruedas, T., and Breuer, D. (2021). MAGMARS : A melting model for the Martian mantle and FeO-rich peridotite. *Journal of Geophysical Research : Planets*, 126(12) :e2021JE006985.

Connelly, J. N., Bizzarro, M., Krot, A. N., Nordlund, Å., Wielandt, D., and Ivanova, M. A. (2012). The absolute chronology and thermal processing of solids in the solar protoplanetary disk. *Science*, 338(6107) :651–655.

Connolly, J. (2009). The geodynamic equation of state : what and how. *Geochemistry, geophysics, geosystems*, 10(10).

Costard, F., Séjourné, A., Kelfoun, K., Clifford, S., Lavigne, F., Di Pietro, I., and Bouley, S. (2017). Modeling tsunami propagation and the emplacement of thumbprint terrain in an early Mars ocean. *Journal of Geophysical Research : Planets*, 122(3) :633–649.

Cousin, A., Sautter, V., Payré, V., Forni, O., Mangold, N., Gasnault, O., Le Deit, L., Johnson, J., Maurice, S., Salvatore, M., et al. (2017). Classification of igneous rocks analyzed by ChemCam at Gale crater, Mars. *Icarus*, 288 :265–283.

Dannberg, J., Gassmöller, R., Grove, R., and Heister, T. (2019). A new formulation for coupled magma/mantle dynamics. *Geophysical Journal International*, 219(1) :94–107.

Davaille, A. and Jaupart, C. (1993). Transient high-Rayleigh-number thermal convection with large viscosity variations. *Journal of Fluid Mechanics*, 253 :141–166.

Davaille, A. and Jaupart, C. (1994). Onset of thermal convection in fluids with temperature-dependent viscosity : Application to the oceanic mantle. *Journal of Geophysical Research : Solid Earth*, 99(B10) :19853–19866.

Debaille, V., Brandon, A., o'Neill, C., Yin, Q.-Z., and Jacobsen, B. (2009). Early martian mantle overturn inferred from isotopic composition of nakhlite meteorites. *Nature Geoscience*, 2(8) :548–552.

Debaille, V., Forni, O., Anderson, R., Beck, P., Beyssac, O., Clavé, E., Clegg, S., Cousin, A., Dehouck, E., Fouchet, T., et al. (2023). Investigation of the petrogenetic relationship between the two igneous formations in Jezero crater by using trace element concentrations acquired by the Perseverance SuperCam instrument. In *Goldschmidt 2023 Conference*. GOLDSCHMIDT.

Deit, L. L., Hauber, E., Fueten, F., Pondrelli, M., Rossi, A. P., and Jaumann, R. (2013). Sequence of infilling events in Gale crater, Mars : Results from morphology, stratigraphy, and mineralogy. *Journal of Geophysical Research : Planets*, 118(12) :2439–2473.

Deschamps, F. and Sotin, C. (2001). Thermal convection in the outer shell of large icy satellites. *Journal of Geophysical Research : Planets*, 106(E3) :5107–5121.

Di Achille, G. and Hynek, B. M. (2010). Ancient ocean on Mars supported by global distribution of deltas and valleys. *Nature Geoscience*, 3(7) :459–463.

Drilleau, M., Garcia, R., Samuel, H., Rivoldini, A., Wieczorek, M., Lognonné, P., Panning, M., and Perrin, C. (2022). Marsquakes' Location and 1-D Seismic Models for Mars from Insight Data. *Journal of Geophysical Research : Planets*.

Drilleau, M., Samuel, H., Rivoldini, A., Panning, M., and Lognonné, P. (2021). Bayesian inversion of the Martian structure using geodynamic constraints. *Geophysical Journal International*, 226(3) :1615–1644.

Dumoulin, C., Doin, M.-P., and Fleitout, L. (1999). Heat transport in stagnant lid convection with temperature-and pressure-dependent Newtonian or non-Newtonian rheology. *Journal of Geophysical Research : Solid Earth*, 104(B6) :12759–12777.

Durán, C., Khan, A., Ceylan, S., Charalambous, C., Kim, D., Drilleau, M., Samuel, H., and Giardini, D. (2022a). Observation of a core-diffracted P-wave from a far-side impact with implications for the lower-mantle structure of Mars. *Geophysical Research Letters*, 49(21) :e2022GL100887.

Durán, C., Khan, A., Ceylan, S., Zenhäusern, G., Stähler, S., Clinton, J., and Giardini, D. (2022b). Seismology on Mars : An analysis of direct, reflected, and converted seismic body waves with implications for interior structure. *Physics of the Earth and Planetary Interiors*, 325 :106851.

Durham, W. and Goetze, C. (1977). Plastic flow of oriented single crystals of olivine : 1. mechanical data. *Journal of geophysical Research*, 82(36) :5737–5753.

Durham, W., Goetze, C., and Blake, B. (1977). Plastic flow of oriented single crystals of olivine : 2. Observations and interpretations of the dislocation structures. *Journal of Geophysical Research*, 82(36) :5755–5770.

Elkins-Tanton, L. T. (2008). Linked magma ocean solidification and atmospheric growth for Earth and Mars. *Earth and Planetary Science Letters*, 271(1-4) :181–191.

Elkins-Tanton, L. T., Hess, P. C., and Parmentier, E. (2005). Possible formation of ancient crust on Mars through magma ocean processes. *Journal of Geophysical Research : Planets*, 110(E12).

Elkins-Tanton, L. T., Parmentier, E., and Hess, P. (2003). Magma ocean fractional crystallization and cumulate overturn in terrestrial planets : Implications for Mars. *Meteoritics & Planetary Science*, 38(12) :1753–1771.

Farrand, W. H., Lane, M. D., Edwards, B. R., and Yingst, R. A. (2011). Spectral evidence of volcanic cryptodomes on the northern plains of Mars. *Icarus*, 211(1) :139–156.

Fitoussi, C., Bourdon, B., and Wang, X. (2016). The building blocks of Earth and Mars : A close genetic link. *Earth and Planetary Science Letters*, 434 :151–160.

Flesch, L. M., Li, B., and Liebermann, R. C. (1998). Sound velocities of polycrystalline $MgSiO_3{}^-$ orthopyroxene to 10 GPa at room temperature. *American Mineralogist*, 83(5-6) :444–450.

Foley, B. J. and Smye, A. J. (2018). Carbon cycling and habitability of Earth-sized stagnant lid planets. *Astrobiology*, 18(7) :873–896.

Frey, H. and Schultz, R. A. (1988). Large impact basins and the mega-impact origin for the crustal dichotomy on Mars. *Geophysical Research Letters*, 15(3) :229–232.

Gallagher, K., Charvin, K., Nielsen, S., Sambridge, M., and Stephenson, J. (2009). Markov chain Monte Carlo (MCMC) sampling methods to determine optimal models, model resolution and model choice for Earth Science problems. *Marine and Petroleum Geology*, 26(4) :525–535.

Garvin, J. B., Frawley, J. J., and Abshire, J. B. (1999). Vertical roughness of Mars from the Mars Orbiter Laser Altimeter. *Geophysical research letters*, 26(3) :381–384.

Gaudin, A., Dehouck, E., and Mangold, N. (2011). Evidence for weathering on early Mars from a comparison with terrestrial weathering profiles. *Icarus*, 216(1) :257–268.

Gerya, T. V. and Yuen, D. A. (2007). Robust characteristics method for modelling multiphase visco-elasto-plastic thermo-mechanical problems. *Physics of the Earth and Planetary Interiors*, 163(1-4) :83–105.

Golabek, G. J., Emsenhuber, A., Jutzi, M., Asphaug, E. I., and Gerya, T. V. (2018). Coupling SPH and thermochemical models of planets : Methodology and example of a Mars-sized body. *Icarus*, 301 :235–246.

Golabek, G. J., Keller, T., Gerya, T. V., Zhu, G., Tackley, P. J., and Connolly, J. A. (2011). Origin of the Martian dichotomy and Tharsis from a giant impact causing massive magmatism. *Icarus*, 215(1) :346–357.

Gomes, R., Levison, H. F., Tsiganis, K., and Morbidelli, A. (2005). Origin of the cataclysmic Late Heavy Bombardment period of the terrestrial planets. *Nature*, 435(7041) :466–469.

Goossens, S., Sabaka, T. J., Genova, A., Mazarico, E., Nicholas, J. B., and Neumann, G. A. (2017). Evidence for a low bulk crustal density for Mars from gravity and topography. *Geophysical research letters*, 44(15) :7686–7694.

Grasset, O. and Parmentier, E. (1998). Thermal convection in a volumetrically heated, infinite Prandtl number fluid with strongly temperature-dependent viscosity : Implications for planetary thermal evolution. *Journal of Geophysical Research : Solid Earth*, 103(B8) :18171–18181.

Green, D. H. and Ringwood, A. (1967). An experimental investigation of the gabbro to eclogite transformation and its petrological applications. *Geochimica et Cosmochimica Acta*, 31(5) :767–833.

Grott, M., Baratoux, D., Hauber, E., Sautter, V., Mustard, J., Gasnault, O., Ruff, S. W., Karato, S.-I., Debaille, V., Knapmeyer, M., et al. (2013). Long-term evolution of the Martian crust-mantle system. *Space Science Reviews*, 174 :49–111.

Grott, M. and Breuer, D. (2008). The evolution of the Martian elastic lithosphere and implications for crustal and mantle rheology. *Icarus*, 193(2) :503–515.

Grott, M. and Wieczorek, M. (2012). Density and lithospheric structure at Tyrrhena Patera, Mars, from gravity and topography data. *Icarus*, 221(1) :43–52.

Guennebaud, G., Jacob, B., et al. (2010). Eigen v3. http ://eigen.tuxfamily.org.

Guest, A. and Smrekar, S. E. (2005). Relaxation of the martian dichotomy boundary : Faulting in the ismenius region and constraints on the early evolution of mars. *Journal of Geophysical Research : Planets*, 110(E12).

Gurgurewicz, J., Mège, D., Schmidt, F., Douté, S., and Langlais, B. (2022). Mega-shears and hydrothermalism at the Martian crustal dichotomy in valles Marineris. *Communications Earth & Environment*, 3(1) :282.

Gyalay, S., Nimmo, F., Plesa, A.-C., and Wieczorek, M. (2020). Constraints on thermal history of Mars from depth of pore closure below Insight. *Geophysical Research Letters*, 47(16) :e2020GL088653.

Hamilton, V. E., Wyatt, M. B., McSween Jr, H. Y., and Christensen, P. R. (2001). Analysis of terrestrial and Martian volcanic compositions using thermal emission spectroscopy : 2. Application to Martian surface spectra from the Mars Global Surveyor Thermal Emission Spectrometer. *Journal of Geophysical Research : Planets*, 106(E7) :14733–14746.

Hartmann, W. K. (1973). Martian cratering, 4, Mariner 9 initial analysis of cratering chronology. *Journal of Geophysical Research*, 78(20) :4096–4116.

Hartmann, W. K. and Neukum, G. (2001). Cratering chronology and the evolution of Mars. In *Chronology and evolution of Mars : Proceedings of an ISSI Workshop, 10–14 April 2000, Bern, Switzerland*, pages 165–194. Springer.

Hauber, E., Brož, P., Jagert, F., Jodłowski, P., and Platz, T. (2011). Very recent and wide-spread basaltic volcanism on Mars. *Geophysical Research Letters*, 38(10).

Hauck, S. A. and Phillips, R. J. (2002). Thermal and crustal evolution of Mars. *Journal of Geophysical Research : Planets*, 107(E7) :6–1.

Head, J. W., Kreslavsky, M. A., and Pratt, S. (2002). Northern lowlands of Mars : Evidence for widespread volcanic flooding and tectonic deformation in the Hesperian Period. *Journal of Geophysical Research : Planets*, 107(E1) :3–1.

Head III, J. W., Hiesinger, H., Ivanov, M. A., Kreslavsky, M. A., Pratt, S., and Thomson, B. J. (1999). Possible ancient oceans on Mars : evidence from Mars Orbiter Laser Altimeter data. *Science*, 286(5447) :2134–2137.

Heap, M. J. (2019). P-and S-wave velocity of dry, water-saturated, and frozen basalt : Implications for the interpretation of Martian seismic data. *Icarus*, 330 :11–15.

Hirschmann, M., Asimow, P. D., Ghiorso, M., and Stolper, E. (1999). Calculation of peridotite partial melting from thermodynamic models of minerals and melts. III. Controls on isobaric melt production and the effect of water on melt production. *Journal of Petrology*, 40(5) :831–851.

Hoogenboom, T. and Smrekar, S. E. (2006). Elastic thickness estimates for the northern lowlands of Mars. *Earth and Planetary Science Letters*, 248(3-4) :830–839.

Horvath, D. G., Moitra, P., Hamilton, C. W., Craddock, R. A., and Andrews-Hanna, J. C. (2021). Evidence for geologically recent explosive volcanism in Elysium Planitia, Mars. *Icarus*, 365 :114499.

Huang, Q., Schmerr, N. C., King, S. D., Kim, D., Rivoldini, A., Plesa, A.-C., Samuel, H., Maguire, R. R., Karakostas, F., Lekić, V., Charalambous, C., Collinet, M., Myhill, R., Antonangeli, D., Drilleau, M., Bystricky, M., Bollinger, C., Michaut, C., Gudkova, T., Irving, J. C. E., Horleston, A., Fernando, B., Leng, K., Nissen-Meyer, T., Bejina, F., Bozdağ, E., Beghein, C., Waszek, L., Siersch, N. C., Scholz, J.-R., Davis, P. M., Lognonné, P., Pinot, B., Widmer-Schnidrig, R., Panning, M. P., Smrekar, S. E., Spohn, T., Pike, W. T., Giardini, D., and Banerdt, W. B. (2022). Seismic detection of a deep mantle discontinuity within Mars by Insight. *Proceedings of the National Academy of Sciences*, 119(42) :e2204474119.

Humayun, M., Nemchin, A., Zanda, B., Hewins, R., Grange, M., Kennedy, A., Lorand, J.-P., Göpel, C., Fieni, C., Pont, S., et al. (2013). Origin and age of the earliest Martian crust from meteorite NWA 7533. *Nature*, 503(7477) :513–516.

Hüttig, C. and Stemmer, K. (2008). The spiral grid : A new approach to discretize the sphere and its application to mantle convection. *Geochemistry, Geophysics, Geosystems*, 9(2).

Hynek, B. M., Beach, M., and Hoke, M. R. (2010). Updated global map of Martian valley networks and implications for climate and hydrologic processes. *Journal of Geophysical Research : Planets*, 115(E9).

Irving, J. C., Lekić, V., Durán, C., Drilleau, M., Kim, D., Rivoldini, A., Khan, A., Samuel, H., Antonangeli, D., Banerdt, W. B., et al. (2023). First observations of core-transiting seismic phases on Mars. *Proceedings of the National Academy of Sciences*, 120(18) :e2217090120.

Jaupart, C., Labrosse, S., Lucazeau, F., and Mareschal, J. (2015). Treatise on geophysics. Temperatures, heat and energy in the mantle of the Earth.

Jaupart, C., Mareschal, J.-C., and Roman, A. (2018). The Formation of Continental Crust from a Physics Perspective. *Geochemistry International*, 56 :1289–1321.

Johnson, C. L. and Phillips, R. J. (2005). Evolution of the Tharsis region of Mars : Insights from magnetic field observations. *Earth and Planetary Science Letters*, 230(3-4) :241–254.

Johnson, M. C., Rutherford, M. J., and Hess, P. C. (1991). Chassigny petrogenesis : Melt compositions, intensive parameters and water contents of martian (?) magmas. *Geochimica et Cosmochimica Acta*, 55(1) :349–366.

Joshi, R., Knapmeyer-Endrun, B., Mosegaard, K., Wieczorek, M. A., Igel, H., Christensen, U. R., and Lognonné, P. (2023). Joint Inversion of receiver functions and apparent incidence angles to determine the crustal structure of Mars. *Geophysical Research Letters*, 50(3) :e2022GL100469.

Jull, M. and Kelemen, P. á. (2001). On the conditions for lower crustal convective instability. *Journal of Geophysical Research : Solid Earth*, 106(B4) :6423–6446.

Karato, S.-I. and Jung, H. (2003). Effects of pressure on high-temperature dislocation creep in olivine. *Philosophical Magazine*, 83(3) :401–414.

Karato, S.-i. and Wu, P. (1993). Rheology of the upper mantle : A synthesis. *Science*, 260(5109) :771–778.

Karunatillake, S., Wray, J., Gasnault, O., McLennan, S., Rogers, A., Squyres, S., Boynton, W., Skok, J., Ojha, L., and Olsen, N. (2014). Sulfates hydrating bulk soil in the Martian low and middle latitudes. *Geophysical Research Letters*, 41(22) :7987–7996.

Karunatillake, S., Wray, J. J., Squyres, S. W., Taylor, G. J., Gasnault, O., McLennan, S. M., Boynton, W., El Maarry, M. R., and Dohm, J. M. (2009). Chemically striking regions on Mars and Stealth revisited. *Journal of Geophysical Research : Planets*, 114(E12).

Katz, R. F., Rees Jones, D. W., Rudge, J. F., and Keller, T. (2022). Physics of melt extraction from the mantle : speed and style. *Annual Review of Earth and Planetary Sciences*.

Katz, R. F., Spiegelman, M., and Langmuir, C. H. (2003). A new parameterization of hydrous mantle melting. *Geochemistry, Geophysics, Geosystems*, 4(9).

Ke, Y. and Solomatov, V. (2009). Coupled core-mantle thermal evolution of early mars. *Journal of Geophysical Research : Planets*, 114(E7).

Keller, T., May, D. A., and Kaus, B. J. (2013). Numerical modelling of magma dynamics coupled to tectonic deformation of lithosphere and crust. *Geophysical Journal International*, 195(3) :1406–1442.

Keller, T. and Tackley, P. J. (2009). Towards self-consistent modeling of the martian dichotomy : The influence of one-ridge convection on crustal thickness distribution. *Icarus*, 202(2) :429–443.

Khan, A., Ceylan, S., van Driel, M., Giardini, D., Lognonné, P., Samuel, H., Schmerr, N. C., Stähler, S. C., Duran, A. C., Huang, Q., et al. (2021). Upper mantle structure of mars from Insight seismic data. *Science*, 373(6553) :434–438.

Khan, A., Liebske, C., Rozel, A., Rivoldini, A., Nimmo, F., Connolly, J., Plesa, A.-C., and Giardini, D. (2018). A geophysical perspective on the bulk composition of Mars. *Journal of Geophysical Research : Planets*, 123(2) :575–611.

Khan, A., Sossi, P., Liebske, C., Rivoldini, A., and Giardini, D. (2022). Geophysical and cosmochemical evidence for a volatile-rich Mars. *Earth and Planetary Science Letters*, 578 :117330.

Kim, D., Duran, C., Giardini, D., Plesa, A.-C., Stähler, S. C., Boehm, C., Lekić, V., McLennan, S. M., Ceylan, S., Clinton, J., et al. (2023a). Global crustal thickness revealed by surface waves orbiting Mars. *Geophysical Research Letters*, 50(12) :e2023GL103482.

Kim, D., Lekić, V., Irving, J. C., Schmerr, N., Knapmeyer-Endrun, B., Joshi, R., Panning, M., Tauzin, B., Karakostas, F., Maguire, R., et al. (2021). Improving constraints on planetary interiors with PPS receiver functions. *Journal of Geophysical Research : Planets*, 126(11) :e2021JE006983.

Kim, D., Stähler, S., Ceylan, S., Lekic, V., Maguire, R., Zenhäusern, G., Clinton, J., Giardini, D., Khan, A., Panning, M., et al. (2023b). Structure along the Martian dichotomy constrained by Rayleigh and Love waves and their overtones. *Geophysical Research Letters*, 50(8) :e2022GL101666.

Kleine, T., Münker, C., Mezger, K., and Palme, H. (2002). Rapid accretion and early core formation on asteroids and the terrestrial planets from Hf–W chronometry. *Nature*, 418(6901) :952–955.

Knapmeyer-Endrun, B., Panning, M. P., Bissig, F., Joshi, R., Khan, A., Kim, D., Lekić, V., Tauzin, B., Tharimena, S., Plasman, M., et al. (2021). Thickness and structure of the martian crust from Insight seismic data. *Science*, 373(6553) :438–443.

Konopliv, A. S., Asmar, S. W., Folkner, W. M., Karatekin, Ö., Nunes, D. C., Smrekar, S. E., Yoder, C. F., and Zuber, M. T. (2011). Mars high resolution gravity fields from MRO, Mars seasonal gravity, and other dynamical parameters. *Icarus*, 211(1) :401–428.

Konopliv, A. S., Park, R. S., Rivoldini, A., Baland, R.-M., Le Maistre, S., Van Hoolst, T., Yseboodt, M., and Dehant, V. (2020). Detection of the Chandler wobble of Mars from orbiting spacecraft. *Geophysical Research Letters*, 47(21) :e2020GL090568.

Kruijer, T. S., Kleine, T., Borg, L. E., Brennecka, G. A., Irving, A. J., Bischoff, A., and Agee, C. B. (2017). The early differentiation of Mars inferred from Hf–W chronometry. *Earth and Planetary Science Letters*, 474 :345–354.

Labrosse, S., Hernlund, J., and Coltice, N. (2007). A crystallizing dense magma ocean at the base of the Earth's mantle. *Nature*, 450(7171) :866–869.

Lagain, A., Bouley, S., Zanda, B., Miljković, K., Rajšić, A., Baratoux, D., Payré, V., Doucet, L., Timms, N., Hewins, R., et al. (2022). Early crustal processes revealed by the ejection site of the oldest martian meteorite. *Nature Communications*, 13(1) :3782.

Langlais, B., Thébault, E., Houliez, A., Purucker, M. E., and Lillis, R. J. (2019). A new model of the crustal magnetic field of Mars using MGS and MAVEN. *Journal of Geophysical Research : Planets*, 124(6) :1542–1569.

Lapen, T. J., Righter, M., Andreasen, R., Irving, A. J., Satkoski, A. M., Beard, B. L., Nishiizumi, K., Jull, A. T., and Caffee, M. W. (2017). Two billion years of magmatism recorded from a single Mars meteorite ejection site. *Science advances*, 3(2) :e1600922.

Lapen, T. J., Righter, M., Brandon, A., Debaille, V., Beard, B., Shafer, J., and Peslier, A. (2010). A younger age for ALH84001 and its geochemical link to shergottite sources in Mars. *Science*, 328(5976) :347–351.

Laske, G., Masters, G., Ma, Z., and Pasyanos, M. (2013). Update on CRUST1. 0—A 1-degree global model of Earth's crust. In *Geophysical research abstracts*, volume 15 Issue 15, page 2658. EGU General Assembly 2013, Vienna, Austria.

Le Maistre, S., Rivoldini, A., Caldiero, A., Yseboodt, M., Baland, R.-M., Beuthe, M., Van Hoolst, T., Dehant, V., Folkner, W. M., Buccino, D., et al. (2023). Spin state and deep interior structure of Mars from Insight radio tracking. *Nature*, pages 1–5.

Le Roux, V., Bodinier, J.-L., Tommasi, A., Alard, O., Dautria, J.-M., Vauchez, A., and Riches, A. (2007). The Lherz spinel lherzolite : refertilized rather than pristine mantle. *Earth and Planetary Science Letters*, 259(3-4) :599–612.

Leone, G., Tackley, P. J., Gerya, T. V., May, D. A., and Zhu, G. (2014). Three-dimensional simulations of the southern polar giant impact hypothesis for the origin of the Martian dichotomy. *Geophysical Research Letters*, 41(24) :8736–8743.

Lesur, G., Ercolano, B., Flock, M., Lin, M.-K., Yang, C.-C., Barranco, J., Benitez-Llambay, P., Goodman, J., Johansen, A., Klahr, H., et al. (2022). Hydro-,

magnetohydro-, and dust-gas dynamics of protoplanetary disks. *arXiv preprint arXiv :2203.09821*.

Li, J., Beghein, C., McLennan, S. M., Horleston, A. C., Charalambous, C., Huang, Q., Zenhäusern, G., Bozdağ, E., Pike, W. T., Golombek, M., et al. (2022). Constraints on the martian crust away from the Insight landing site. *Nature communications*, 13(1) :7950.

Lognonné, P., Banerdt, W., Clinton, J., Garcia, R., Giardini, D., Knapmeyer-Endrun, B., Panning, M., and Pike, W. (2023). Mars Seismology. *Annual Review of Earth and Planetary Sciences*, 51(1) :643–670.

Lognonné, P., Banerdt, W. B., Pike, W., Giardini, D., Christensen, U., Garcia, R. F., Kawamura, T., Kedar, S., Knapmeyer-Endrun, B., Margerin, L., et al. (2020). Constraints on the shallow elastic and anelastic structure of Mars from Insight seismic data. *Nature Geoscience*, 13(3) :213–220.

Lognonné, P., Gagnepain-Beyneix, J., and Chenet, H. (2003). A new seismic model of the Moon : implications for structure, thermal evolution and formation of the Moon. *Earth and Planetary Science Letters*, 211(1-2) :27–44.

Maguire, R., Ritsema, J., and Goes, S. (2017). Signals of 660 km topography and harzburgite enrichment in seismic images of whole-mantle upwellings. *Geophysical Research Letters*, 44(8) :3600–3607.

Mangold, N., Gupta, S., Gasnault, O., Dromart, G., Tarnas, J., Sholes, S., Horgan, B., Quantin-Nataf, C., Brown, A., Le Mouélic, S., et al. (2021). Perseverance rover reveals an ancient delta-lake system and flood deposits at Jezero crater, Mars. *Science*, 374(6568) :711–717.

Mangold, N., Loizeau, D., Poulet, F., Ansan, V., Baratoux, D., LeMouelic, S., Bardintzeff, J.-M., Platevoet, B., Toplis, M., Pinet, P., et al. (2010). Mineralogy of recent volcanic plains in the Tharsis region, Mars, and implications for platy-ridged flow composition. *Earth and Planetary Science Letters*, 294(3-4) :440–450.

Mangold, N., Thompson, L., Forni, O., Williams, A., Fabre, C., Le Deit, L., Wiens, R., Williams, R., Anderson, R., Blaney, D. L., et al. (2016). Composition of conglomerates analyzed by the Curiosity rover : Implications for Gale Crater crust and sediment sources. *Journal of Geophysical Research : Planets*, 121(3) :353–387.

Marinova, M. M., Aharonson, O., and Asphaug, E. (2008). Mega-impact formation of the Mars hemispheric dichotomy. *Nature*, 453(7199) :1216–1219.

Marinova, M. M., Aharonson, O., and Asphaug, E. (2011). Geophysical consequences of planetary-scale impacts into a Mars-like planet. *Icarus*, 211(2) :960–985.

Matsuyama, I. and Manga, M. (2010). Mars without the equilibrium rotational figure, tharsis, and the remnant rotational figure. *Journal of Geophysical Research : Planets*, 115(E12).

McCubbin, F. M., Nekvasil, H., Harrington, A. D., Elardo, S. M., and Lindsley, D. H. (2008). Compositional diversity and stratification of the Martian crust : Inferences from crystallization experiments on the picrobasalt Humphrey from Gusev crater, Mars. *Journal of Geophysical Research : Planets*, 113(E11).

McDonough, W. F. and Sun, S.-S. (1995). The composition of the Earth. *Chemical geology*, 120(3-4) :223–253.

McGill, G. E. and Dimitriou, A. M. (1990). Origin of the Martian global dichotomy by crustal thinning in the late Noachian or early Hesperian. *Journal of Geophysical Research : Solid Earth*, 95(B8) :12595–12605.

McGovern, P. J., Solomon, S. C., Smith, D. E., Zuber, M. T., Simons, M., Wieczorek, M. A., Phillips, R. J., Neumann, G. A., Aharonson, O., and Head, J. W. (2004). Correction to "Localized gravity/topography admittance and correlation spectra on mars : Implications for regional and global evolution". *Journal of Geophysical Research : Planets*, 109(E7).

McKay, D. S., Gibson Jr, E. K., Thomas-Keprta, K. L., Vali, H., Romanek, C. S., Clemett, S. J., Chillier, X. D., Maechling, C. R., and Zare, R. N. (1996). Search for past life on mars : possible relic biogenic activity in Martian meteorite ALH84001. *Science*, 273(5277) :924–930.

McKenzie, D. (1985). The extraction of magma from the crust and mantle. *Earth and Planetary Science Letters*, 74(1) :81–91.

McSween, H. Y. and Stolper, E. M. (1980). Basaltic meteorites. *Scientific American*, 242(6) :54–63.

Mei, S., Bai, W., Hiraga, T., and Kohlstedt, D. (2002). Influence of melt on the creep behavior of olivine–basalt aggregates under hydrous conditions. *Earth and Planetary Science Letters*, 201(3-4) :491–507.

Menina, S., Margerin, L., Kawamura, T., Heller, G., Drilleau, M., Xu, Z., Calvet, M., Garcia, R., Knapmeyer-Endrun, B., Carrasco, S., et al. (2023). Stratification of Heterogeneity in the Lithosphere of Mars from Envelope Modeling of Event S1222a and Near Impacts : Interpretation and implications for very-high-frequency events. *Geophysical Research Letters*, 50(7) :e2023GL103202.

Michaut, C. and Jaupart, C. (2006). Ultra-rapid formation of large volumes of evolved magma. *Earth and Planetary Science Letters*, 250(1-2) :38–52.

Michaut, C. and Neufeld, J. A. (2022). Formation of the Lunar primary crust from a long-lived slushy magma ocean. *Geophysical Research Letters*, 49(2) :e2021GL095408.

Michaut, C., Pinel, V., and Maccaferri, F. (2020). Magma ascent at floor-fractured craters diagnoses the lithospheric stress state on the Moon. *Earth and Planetary Science Letters*, 530 :115889.

Mignard, F. (1981). Evolution of the martian satellites. *Monthly Notices of the Royal Astronomical Society*, 194(2) :365–379.

Miller, K. J., Zhu, W.-l., Montési, L. G., and Gaetani, G. A. (2014). Experimental quantification of permeability of partially molten mantle rock. *Earth and Planetary Science Letters*, 388 :273–282.

Mittelholz, A., Johnson, C., Feinberg, J., Langlais, B., and Phillips, R. (2020). Timing of the martian dynamo : New constraints for a core field 4.5 and 3.7 Ga ago. *Science Advances*, 6(18) :eaba0513.

Mocquet, A., Rosenblatt, P., Dehant, V., and Verhoeven, O. (2011). The deep interior of Venus, Mars, and the Earth : A brief review and the need for planetary surface-based measurements. *Planetary and Space Science*, 59(10) :1048–1061.

Morbidelli, A., Nesvorny, D., Laurenz, V., Marchi, S., Rubie, D. C., Elkins-Tanton, L., Wieczorek, M., and Jacobson, S. (2018). The timeline of the lunar bombardment : Revisited. *Icarus*, 305 :262–276.

Mori, Y., Ozawa, H., Hirose, K., Sinmyo, R., Tateno, S., Morard, G., and Ohishi, Y. (2017). Melting experiments on Fe–Fe_3S system to 254 GPa. *Earth and Planetary Science Letters*, 464 :135–141.

Morison, A., Labrosse, S., Deguen, R., and Alboussière, T. (2019). Timescale of overturn in a magma ocean cumulate. *Earth and Planetary Science Letters*, 516 :25–36.

Morschhauser, A., Grott, M., and Breuer, D. (2011). Crustal recycling, mantle dehydration, and the thermal evolution of Mars. *Icarus*, 212(2) :541–558.

Moser, D., Chamberlain, K., Tait, K., Schmitt, A., Darling, J. R., Barker, I., and Hyde, B. (2013). Solving the Martian meteorite age conundrum using micro-baddeleyite and launch-generated zircon. *Nature*, 499(7459) :454–457.

Mueller, S. and Phillips, R. J. (1995). On the reliability of lithospheric constraints derived from models of outer-rise flexure. *Geophysical Journal International*, 123(3) :887–902.

Mustard, J., Poulet, F., Gendrin, A., Bibring, J.-P., Langevin, Y., Gondet, B., Mangold, N., Bellucci, G., and Altieri, F. (2005). Olivine and pyroxene diversity in the crust of Mars. *Science*, 307(5715) :1594–1597.

Mutch, T. A., Arvidson, R. E., Head III, J. W., Jones, K. L., and Saunders, R. S. (1976). The geology of Mars. *Princeton*.

Mysen, B. O., Virgo, D., Popp, R. K., and Bertka, C. M. (1998). The role of H_2O in Martian magmatic systems. *American Mineralogist*, 83(9-10) :942–946.

Nataf, H. and Richter, F. (1982). Convection experiments in fluids with highly temperature-dependent viscosity and the thermal evolution of the planets. *Physics of the Earth and planetary interiors*, 29(3-4) :320–329.

Neukum, G., Jaumann, R., Hoffmann, H., Hauber, E., Head, J., Basilevsky, A., Ivanov, B., Werner, S., Van Gasselt, S., Murray, J., et al. (2004). Recent and episodic volcanic and glacial activity on Mars revealed by the High Resolution Stereo Camera. *Nature*, 432(7020) :971–979.

Neumann, G., Lemoine, F., Smith, D., and Zuber, M. (2008). Marscrust3-A crustal thickness inversion from recent MRO gravity solutions. In *39th Annual Lunar and Planetary Science Conference*.

Neumann, G., Zuber, M., Wieczorek, M. A., McGovern, P., Lemoine, F. G., and Smith, D. (2004). Crustal structure of Mars from gravity and topography. *Journal of Geophysical Research : Planets*, 109(E8).

Newsom, H., Crumpler, L., Reedy, R., Nelson, M., Petersen, M., Evans, L., Taylor, G., Keller, J., Janes, D., Boynton, W., et al. (2007a). Geochemistry of martian surficial materials with gamma ray data from Mars Odyssey : initial observations for calcium. In *38th Annual Lunar and Planetary Science Conference*.

Newsom, H. E., Crumpler, L. S., Reedy, R. C., Petersen, M. T., Newsom, G. C., Evans, L. G., Taylor, G. J., Keller, J. M., Janes, D. M., Boynton, W. V., et al. (2007b). Geochemistry of Martian soil and bedrock in mantled and less mantled terrains with gamma ray data from Mars Odyssey. *Journal of Geophysical Research : Planets*, 112(E3).

Nimmo, F., Hart, S., Korycansky, D., and Agnor, C. (2008). Implications of an impact origin for the martian hemispheric dichotomy. *Nature*, 453(7199) :1220–1223.

Nimmo, F. and Tanaka, K. (2005). Early crustal evolution of Mars. *Annu. Rev. Earth Planet. Sci.*, 33 :133–161.

Nyquist, L., Bogard, D., Shih, C.-Y., Greshake, A., Stöffler, D., and Eugster, O. (2001). Ages and geologic histories of Martian meteorites. In *Chronology and Evolution of Mars : Proceedings of an ISSI Workshop, 10–14 April 2000, Bern, Switzerland*, pages 105–164. Springer.

Nyquist, L. E., Shih, C.-Y., McCubbin, F. M., Santos, A. R., Shearer, C. K., Peng, Z. X., Burger, P. V., and Agee, C. B. (2016). Rb-sr and sm-nd isotopic and ree studies of igneous components in the bulk matrix domain of martian breccia northwest africa 7034. *Meteoritics & Planetary Science*, 51(3) :483–498.

Ogawa, M. and Yanagisawa, T. (2012a). Two-dimensional numerical studies on the effects of water on Martian mantle evolution induced by magmatism and solid-state mantle convection. *Journal of Geophysical Research : Planets*, 117(E6).

Ogawa, M. and Yanagisawa, T. (2012b). Two-dimensional numerical studies on the effects of water on Martian mantle evolution induced by magmatism and solid-state mantle convection. *Journal of Geophysical Research : Planets*, 117(E6).

Ohtake, M., Uemoto, K., Yokota, Y., Morota, T., Yamamoto, S., Nakamura, R., Haruyama, J., Iwata, T., Matsunaga, T., and Ishihara, Y. (2014). Geologic structure generated by large-impact basin formation observed at the South Pole-Aitken basin on the Moon. *Geophysical Research Letters*, 41(8) :2738–2745.

Palme, H. and O'Neill, H. S. C. (2003). Cosmochemical estimates of mantle composition. *Treatise on geochemistry*, 2 :568.

Pan, L., Quantin-Nataf, C., Tauzin, B., Michaut, C., Golombek, M., Lognonné, P., Grindrod, P., Langlais, B., Gudkova, T., Stepanova, I., et al. (2020). Crust stratigraphy and heterogeneities of the first kilometers at the dichotomy boundary in western Elysium planitia and implications for Insight lander. *Icarus*, 338 :113511.

Pasckert, J. H., Hiesinger, H., and Reiss, D. (2012). Rheologies and ages of lava flows on Elysium Mons, Mars. *Icarus*, 219(1) :443–457.

Patankar, S. (2018). *Numerical heat transfer and fluid flow*. Taylor & Francis.

Pauer, M. and Breuer, D. (2008). Constraints on the maximum crustal density from gravity–topography modeling : Applications to the southern highlands of Mars. *Earth and Planetary Science Letters*, 276(3-4) :253–261.

Payré, V., Salvatore, M., and Edwards, C. (2022). An evolved early crust exposed on Mars revealed through spectroscopy. *Geophysical research letters*, 49(21) :e2022GL099639.

Peacock, S. M., Rushmer, T., and Thompson, A. B. (1994). Partial melting of subducting oceanic crust. *Earth and planetary science letters*, 121(1-2) :227–244.

Perron, J. T., Mitrovica, J. X., Manga, M., Matsuyama, I., and Richards, M. A. (2007). Evidence for an ancient martian ocean in the topography of deformed shorelines. *Nature*, 447(7146) :840–843.

Phillips, M. S., Viviano, C. E., Moersch, J. E., Rogers, A. D., McSween, H. Y., and Seelos, F. P. (2022). Extensive and ancient feldspathic crust detected across north Hellas rim, Mars : Possible implications for primary crust formation. *Geology*, 50(10) :1182–1186.

Phillips, R. J., Zuber, M. T., Smrekar, S. E., Mellon, M. T., Head, J. W., Tanaka, K. L., Putzig, N. E., Milkovich, S. M., Campbell, B. A., Plaut, J. J., et al. (2008). Mars north polar deposits : Stratigraphy, age, and geodynamical response. *Science*, 320(5880) :1182–1185.

Phillips, R. J., Zuber, M. T., Solomon, S. C., Golombek, M. P., Jakosky, B. M., Banerdt, W. B., Smith, D. E., Williams, R. M., Hynek, B. M., Aharonson, O., et al. (2001). Ancient geodynamics and global-scale hydrology on Mars. *Science*, 291(5513) :2587–2591.

Pieterek, B., Laban, M., Ciążela, J., and Muszyński, A. (2022). Explosive volcanism in Noctis Fossae on mars. *Icarus*, 375 :114851.

Platz, T., Michael, G., Tanaka, K. L., Skinner Jr, J. A., and Fortezzo, C. M. (2013). Crater-based dating of geological units on Mars : Methods and application for the new global geological map. *Icarus*, 225(1) :806–827.

Plesa, A.-C. and Breuer, D. (2014). Partial melting in one-plate planets : Implications for thermo-chemical and atmospheric evolution. *Planetary and Space Science*, 98 :50–65.

Plesa, A.-C., Tosi, N., and Breuer, D. (2014). Can a fractionally crystallized magma ocean explain the thermo-chemical evolution of Mars ? *Earth and Planetary Science Letters*, 403 :225–235.

Plesa, A.-C., Tosi, N., Grott, M., and Breuer, D. (2015). Thermal evolution and Urey ratio of Mars. *Journal of Geophysical Research : Planets*, 120(5) :995–1010.

Pou, L., Nimmo, F., Rivoldini, A., Khan, A., Bagheri, A., Gray, T., Samuel, H., Lognonné, P., Plesa, A.-C., Gudkova, T., et al. (2022). Tidal constraints on the Martian interior. *Journal of Geophysical Research : Planets*, 127(11) :e2022JE007291.

Poulet, F., Bibring, J.-P., Mustard, J., Gendrin, A., Mangold, N., Langevin, Y., Arvidson, R., Gondet, B., and Gomez, C. (2005). Phyllosilicates on Mars and implications for early Martian climate. *Nature*, 438(7068) :623–627.

Poulet, F., Mangold, N., Platevoet, B., Bardintzeff, J.-M., Sautter, V., Mustard, J., Bibring, J.-P., Pinet, P., Langevin, Y., Gondet, B., et al. (2009). Quantitative compositional analysis of Martian mafic regions using the MEx/OMEGA reflectance data : 2. Petrological implications. *Icarus*, 201(1) :84–101.

Purucker, M., Ravat, D., Frey, H., Voorhies, C., Sabaka, T., and Acuna, M. (2000). An altitude-normalized magnetic map of Mars and its interpretation. *Geophysical Research Letters*, 27(16) :2449–2452.

Quantin-Nataf, C., Carter, J., Mandon, L., Thollot, P., Balme, M., Volat, M., Pan, L., Loizeau, D., Millot, C., Breton, S., et al. (2021). Oxia Planum : The landing site for the ExoMars "Rosalind Franklin" rover mission : Geological context and prelanding interpretation. *Astrobiology*, 21(3) :345–366.

Reese, C., Orth, C., and Solomatov, V. (2010). Impact origin for the Martian crustal dichotomy : Half emptied or half filled ? *Journal of Geophysical Research : Planets*, 115(E5).

Reese, C. and Solomatov, V. (2006). Fluid dynamics of local martian magma oceans. *Icarus*, 184(1) :102–120.

Richter, F. M. and McKenzie, D. (1984). Dynamical models for melt segregation from a deformable matrix. *The Journal of Geology*, 92(6) :729–740.

Riu, L., Carter, J., and Poulet, F. (2022). The M3 project : 3–Global abundance distribution of hydrated silicates at Mars. *Icarus*, 374 :114809.

Robbins, S. J., Di Achille, G., and Hynek, B. M. (2011). The volcanic history of Mars : High-resolution crater-based studies of the calderas of 20 volcanoes. *Icarus*, 211(2) :1179–1203.

Roberts, G. O. and Rosenthal, J. S. (2009). Examples of adaptive MCMC. *Journal of computational and graphical statistics*, 18(2) :349–367.

Roberts, J. H. and Arkani-Hamed, J. (2014). Impact heating and coupled core cooling and mantle dynamics on Mars. *Journal of Geophysical Research : Planets*, 119(4) :729–744.

Roberts, J. H. and Zhong, S. (2006). Degree-1 convection in the Martian mantle and the origin of the hemispheric dichotomy. *Journal of Geophysical Research : Planets*, 111(E6).

Robinson, J., Wood, B., and Blundy, J. (1998). The beginning of melting of fertile and depleted peridotite at 1.5 GPa. *Earth and Planetary Science Letters*, 155(1-2) :97–111.

Rodriguez, J. A. P., Fairén, A. G., Tanaka, K. L., Zarroca, M., Linares, R., Platz, T., Komatsu, G., Miyamoto, H., Kargel, J. S., Yan, J., et al. (2016). Tsunami waves extensively resurfaced the shorelines of an early Martian ocean. *Scientific reports*, 6(1) :25106.

Rogers, A. D. and Farrand, W. H. (2022). Spectral evidence for alkaline rocks and compositional diversity among feldspathic light-toned terrains on Mars. *Icarus*, 376 :114883.

Rogers, A. D. and Nekvasil, H. (2015). Feldspathic rocks on Mars : Compositional constraints from infrared spectroscopy and possible formation mechanisms. *Geophysical Research Letters*, 42(8) :2619–2626.

Rosenblatt, P., Charnoz, S., Dunseath, K. M., Terao-Dunseath, M., Trinh, A., Hyodo, R., Genda, H., and Toupin, S. (2016). Accretion of Phobos and Deimos in an extended debris disc stirred by transient moons. *Nature Geoscience*, 9(8) :581–583.

Rudnick, R. L. and Holland, H. D. (2005). *Treatise on geochemistry. 3. The crust.* Elsevier Pergamon.

Ruedas, T. (2017). Radioactive heat production of six geologically important nuclides. *Geochemistry, Geophysics, Geosystems*, 18(9) :3530–3541.

Ruedas, T. and Breuer, D. (2017). On the relative importance of thermal and chemical buoyancy in regular and impact-induced melting in a Mars-like planet. *Journal of Geophysical Research : Planets*, 122(7) :1554–1579.

Salvador, A., Massol, H., Davaille, A., Marcq, E., Sarda, P., and Chassefière, E. (2017). The relative influence of H_2O and CO_2 on the primitive surface conditions and evolution of rocky planets. *Journal of Geophysical Research : Planets*, 122(7) :1458–1486.

Sambridge, M., Bodin, T., Gallagher, K., and Tkalčić, H. (2013). Transdimensional inference in the geosciences. *Philosophical Transactions of the Royal Society A : Mathematical, Physical and Engineering Sciences*, 371(1984) :20110547.

Samuel, H., Ballmer, M. D., Padovan, S., Tosi, N., Rivoldini, A., and Plesa, A.-C. (2021). The thermo-chemical evolution of Mars with a strongly stratified mantle. *Journal of Geophysical Research : Planets*, 126(4) :e2020JE006613.

Samuel, H., Lognonné, P., Panning, M., and Lainey, V. (2019). The rheology and thermal history of Mars revealed by the orbital evolution of Phobos. *Nature*, 569(7757) :523–527.

Sanloup, C., Jambon, A., and Gillet, P. (1999). A simple chondritic model of Mars. *Physics of the Earth and Planetary Interiors*, 112(1-2) :43–54.

Sautter, V., Fabre, C., Forni, O., Toplis, M., Cousin, A., Ollila, A., Meslin, P., Maurice, S., Wiens, R., Baratoux, D., et al. (2014). Igneous mineralogy at Bradbury Rise : The first ChemCam campaign at Gale crater. *Journal of Geophysical Research : Planets*, 119(1) :30–46.

Sautter, V. and Payre, V. (2021). Alkali magmatism on Mars : an unexpected diversity. *Comptes Rendus. Géoscience*, 353(S2) :1–30.

Sautter, V., Toplis, M., Wiens, R., Cousin, A., Fabre, C., Gasnault, O., Maurice, S., Forni, O., Lasue, J., Ollila, A., et al. (2015). In situ evidence for continental crust on early Mars. *Nature Geoscience*, 8(8) :605–609.

Sautter, V., Toplis, M. J., Beck, P., Mangold, N., Wiens, R., Pinet, P., Cousin, A., Maurice, S., LeDeit, L., Hewins, R., et al. (2016). Magmatic complexity on early Mars as seen through a combination of orbital, in-situ and meteorite data. *Lithos*, 254 :36–52.

Schmidt, F., Way, M. J., Costard, F., Bouley, S., Séjourné, A., and Aleinov, I. (2022). Circumpolar ocean stability on Mars 3 Gyr ago. *Proceedings of the National Academy of Sciences*, 119(4) :e2112930118.

Schutt, D. and Lesher, C. (2006). Effects of melt depletion on the density and seismic velocity of garnet and spinel lherzolite. *Journal of Geophysical Research : Solid Earth*, 111(B5).

Semprich, J., Schwenzer, S., Treiman, A., and Filiberto, J. (2019). Phase equilibria modeling of low-grade metamorphic Martian rocks. *Journal of Geophysical Research : Planets*, 124(3) :681–702.

Smith, D. E., Zuber, M. T., Frey, H. V., Garvin, J. B., Head, J. W., Muhleman, D. O., Pettengill, G. H., Phillips, R. J., Solomon, S. C., Zwally, H. J., et al. (2001). Mars Orbiter Laser Altimeter : Experiment summary after the first year of global mapping of Mars. *Journal of Geophysical Research : Planets*, 106(E10) :23689–23722.

Solomatov, V. (1995). Scaling of temperature-and stress-dependent viscosity convection. *Physics of Fluids*, 7(2) :266–274.

Solomatov, V. and Moresi, L.-N. (1997). Three regimes of mantle convection with non-newtonian viscosity and stagnant lid convection on the terrestrial planets. *Geophysical Research Letters*, 24(15) :1907–1910.

Solomon, S. C., Aharonson, O., Aurnou, J. M., Banerdt, W. B., Carr, M. H., Dombard, A. J., Frey, H. V., Golombek, M. P., Hauck, S. A., Head III, J. W., et al. (2005). New perspectives on ancient Mars. *science*.

Sotin, C. and Labrosse, S. (1999). Three-dimensional thermal convection in an isoviscous, infinite Prandtl number fluid heated from within and from below : applications to the transfer of heat through planetary mantles. *Physics of the Earth and Planetary Interiors*, 112(3-4) :171–190.

Squyres, S. W., Arvidson, R. E., Blaney, D. L., Clark, B. C., Crumpler, L., Farrand, W. H., Gorevan, S., Herkenhoff, K. E., Hurowitz, J., Kusack, A., et al. (2006). Rocks of the Columbia Hills. *Journal of Geophysical Research : Planets*, 111(E2).

Šrámek, O. and Zhong, S. (2010). Long-wavelength stagnant lid convection with hemispheric variation in lithospheric thickness : Link between Martian crustal dichotomy and Tharsis ? *Journal of Geophysical Research : Planets*, 115(E9).

Šrámek, O. and Zhong, S. (2012). Martian crustal dichotomy and Tharsis formation by partial melting coupled to early plume migration. *Journal of Geophysical Research : Planets*, 117(E1).

Stähler, S. C., Khan, A., Banerdt, W. B., Lognonné, P., Giardini, D., Ceylan, S., Drilleau, M., Duran, A. C., Garcia, R. F., Huang, Q., et al. (2021). Seismic detection of the martian core. *Science*, 373(6553) :443–448.

Stähler, S. C., Mittelholz, A., Perrin, C., Kawamura, T., Kim, D., Knapmeyer, M., Zenhäusern, G., Clinton, J., Giardini, D., Lognonné, P., et al. (2022). Tectonics of Cerberus Fossae unveiled by marsquakes. *Nature Astronomy*, 6(12) :1376–1386.

Stevenson, D. J., Spohn, T., and Schubert, G. (1983). Magnetism and thermal evolution of the terrestrial planets. *Icarus*, 54(3) :466–489.

Sun, V. Z., Hand, K. P., Stack, K. M., Farley, K. A., Simon, J. I., Newman, C., Sharma, S., Liu, Y., Wiens, R. C., Williams, A. J., et al. (2023). Overview and results from the Mars 2020 Perseverance rover's first science campaign on the Jezero crater floor. *Journal of Geophysical Research. Planets*, 128.

Suzuki, A. and Ohtani, E. (2003). Density of peridotite melts at high pressure. *Physics and Chemistry of Minerals*, 30(8) :449–456.

Tackley, P. J. (2008). Modelling compressible mantle convection with large viscosity contrasts in a three-dimensional spherical shell using the yin-yang grid. *Physics of the Earth and Planetary Interiors*, 171(1-4) :7–18.

Tackley, P. J., Stevenson, D. J., Glatzmaier, G. A., and Schubert, G. (1993). Effects of an endothermic phase transition at 670 km depth in a spherical model of convection in the Earth's mantle. *Nature*, 361(6414) :699–704.

Takahashi, E. (1990). Speculations on the Archean Mantle : Missing link between komatiite and depleted garnet peridotite. *Journal of Geophysical Research : Solid Earth*, 95(B10) :15941–15954.

Tanaka, K. L. (1986). The stratigraphy of Mars. *Journal of Geophysical Research : Solid Earth*, 91(B13) :E139–E158.

Tanaka, K. L., Robbins, S., Fortezzo, C., Skinner Jr, J., and Hare, T. M. (2014). The digital global geologic map of Mars : Chronostratigraphic ages, topographic and crater morphologic characteristics, and updated resurfacing history. *Planetary and Space Science*, 95 :11–24.

Tanaka, K. L., Skinner Jr, J., Hare, T. M., Joyal, T., and Wenker, A. (2003). Resurfacing history of the northern plains of Mars based on geologic mapping of Mars Global Surveyor data. *Journal of Geophysical Research : Planets*, 108(E4).

Taylor, G. J. (2013). The bulk composition of Mars. *Geochemistry*, 73(4) :401–420.

Taylor, G. J., Stopar, J., Boynton, W. V., Karunatillake, S., Keller, J. M., Brückner, J., Wänke, H., Dreibus, G., Kerry, K. E., Reedy, R. C., et al. (2006). Variations in K/Th on Mars. *Journal of Geophysical Research : Planets*, 111(E3).

Taylor, S. R. and McLennan, S. (2009). *Planetary crusts : their composition, origin and evolution*, volume 10. Cambridge University Press.

Thiriet, M. (2018). *Effect of the north/south dichotomy on the thermal structure and evolution of Mars*. PhD thesis, Sorbonne Paris Cité.

Thiriet, M., Breuer, D., Michaut, C., and Plesa, A.-C. (2019). Scaling laws of convection for cooling planets in a stagnant lid regime. *Physics of the Earth and Planetary Interiors*, 286 :138–153.

Thiriet, M., Michaut, C., Breuer, D., and Plesa, A.-C. (2018). Hemispheric dichotomy in lithosphere thickness on Mars caused by differences in crustal structure and composition. *Journal of Geophysical Research : Planets*, 123(4) :823–848.

Tillotson, J. H. (1962). *Metallic equations of state for hypervelocity impact*. General Dynamics Falls Church, VA.

Tonks, W. B. and Melosh, H. J. (1993). Magma ocean formation due to giant impacts. *Journal of Geophysical Research : Planets*, 98(E3) :5319–5333.

Tosi, N., Grott, M., Plesa, A.-C., and Breuer, D. (2013a). Thermochemical evolution of Mercury's interior. *Journal of Geophysical Research : Planets*, 118(12) :2474–2487.

Tosi, N., Plesa, A.-C., and Breuer, D. (2013b). Overturn and evolution of a crystallized magma ocean : A numerical parameter study for Mars. *Journal of Geophysical Research : Planets*, 118(7) :1512–1528.

Treiman, A. H. (2019). Meteorite Allan Hills (ALH) 84001 : Implications for Mars' inhabitation and habitability. *The First Billion Years : Habitability*, 2134 :1032.

Turbet, M. and Forget, F. (2019). The paradoxes of the Late Hesperian Mars ocean. *Scientific Reports*, 9(1) :5717.

Turcotte, D. L. and Schubert, G. (2002). *Geodynamics*. Cambridge university press.

Udry, A., Gazel, E., and McSween Jr, H. Y. (2018). Formation of evolved rocks at Gale crater by crystal fractionation and implications for Mars crustal composition. *Journal of Geophysical Research : Planets*, 123(6) :1525–1540.

Udry, A., Howarth, G. H., Herd, C., Day, J. M., Lapen, T. J., and Filiberto, J. (2020). What martian meteorites reveal about the interior and surface of Mars. *Journal of Geophysical Research : Planets*.

Udry, A., Ostwald, A., Sautter, V., Cousin, A., Beyssac, O., Forni, O., Dromart, G., Benzerara, K., Nachon, M., Horgan, B., et al. (2022). A Mars 2020 Perseverance SuperCam Perspective on the igneous nature of the Máaz formation at jezero crater and link with Séítah, Mars. *Journal of Geophysical Research : Planets*, page e2022JE007440.

Vigneron, Q. (2020). 1+ 3 formulation of Newton's equations. *Physical Review D*, 102(12) :124005.

Vinnik, L., Chenet, H., Gagnepain-Beyneix, J., and Lognonne, P. (2001). First seismic receiver functions on the Moon. *Geophysical Research Letters*, 28(15) :3031–3034.

Walsh, K. J., Morbidelli, A., Raymond, S. N., O'Brien, D. P., and Mandell, A. M. (2011). A low mass for Mars from Jupiter's early gas-driven migration. *Nature*, 475(7355) :206–209.

Wang, S. and Tkalčić, H. (2022). Scanning for planetary cores with single-receiver intersource correlations. *Nature Astronomy*, 6(11) :1272–1279.

Wänke, H. and Dreibus, G. (1994). Chemistry and accretion history of Mars. *Philosophical Transactions of the Royal Society of London. Series A : Physical and Engineering Sciences*, 349(1690) :285–293.

Wasson, J. T. and Kallemeyn, G. W. (1988). Compositions of chondrites. *Philosophical Transactions of the Royal Society of London. Series A, Mathematical and Physical Sciences*, 325(1587) :535–544.

Wasylenki, L. E., Baker, M. B., Kent, A. J., and Stolper, E. M. (2003). Near-solidus melting of the shallow upper mantle : partial melting experiments on depleted peridotite. *Journal of Petrology*, 44(7) :1163–1191.

Watson, C., Neufeld, J. A., and Michaut, C. (2022). Early asymmetric growth of planetary stagnant lids. *Journal of Fluid Mechanics*, 952 :A3.

Watters, T. R., Leuschen, C. J., Plaut, J. J., Picardi, G., Safaeinili, A., Clifford, S. M., Farrell, W. M., Ivanov, A. B., Phillips, R. J., and Stofan, E. R. (2006). MARSIS radar sounder evidence of buried basins in the northern lowlands of Mars. *Nature*, 444(7121) :905–908.

Watters, T. R., McGovern, P. J., and Irwin Iii, R. P. (2007). Hemispheres apart : The crustal dichotomy on Mars. *Annu. Rev. Earth Planet. Sci.*, 35 :621–652.

Wetherill, G. W. (1990). Formation of the Earth. *Annual Review of Earth and Planetary Sciences*, 18(1) :205–256.

Wieczorek, M. A. (2008). Constraints on the composition of the Martian south polar cap from gravity and topography. *Icarus*, 196(2) :506–517.

Wieczorek, M. A. (2015). Gravity and topography of the terrestrial planets. *Treatise on geophysics*, 10 :165–206.

Wieczorek, M. A., Broquet, A., McLennan, S. M., Rivoldini, A., Golombek, M., Antonangeli, D., Beghein, C., Giardini, D., Gudkova, T., Gyalay, S., et al. (2022). Insight constraints on the global character of the Martian crust. *Journal of Geophysical Research : Planets*, page e2022JE007298.

Wieczorek, M. A., Neumann, G. A., Nimmo, F., Kiefer, W. S., Taylor, G. J., Melosh, H. J., Phillips, R. J., Solomon, S. C., Andrews-Hanna, J. C., Asmar, S. W., et al. (2013). The crust of the Moon as seen by GRAIL. *Science*, 339(6120) :671–675.

Wieczorek, M. A. and Phillips, R. J. (1997). The structure and compensation of the lunar highland crust. *Journal of Geophysical Research : Planets*, 102(E5) :10933–10943.

Wieczorek, M. A. and Zuber, M. T. (2004). Thickness of the Martian crust : Improved constraints from geoid-to-topography ratios. *Journal of Geophysical Research : Planets*, 109(E1).

Wilhelms, D. E. and Squyres, S. W. (1984). The Martian hemispheric dichotomy may be due to a giant impact. *Nature*, 309(5964) :138–140.

Williams, D. A., Greeley, R., Werner, S. C., Michael, G., Crown, D. A., Neukum, G., and Raitala, J. (2008). Tyrrhena Patera : geologic history derived from Mars express high resolution stereo camera. *Journal of Geophysical Research : Planets*, 113(E11).

Williams, D. A., Greeley, R., Zuschneid, W., Werner, S. C., Neukum, G., Crown, D. A., Gregg, T. K., Gwinner, K., and Raitala, J. (2007). Hadriaca Patera : insights into its volcanic history from Mars express high resolution stereo camera. *Journal of Geophysical Research : Planets*, 112(E10).

Williams, J.-P. and Nimmo, F. (2004). Thermal evolution of the Martian core : Implications for an early dynamo. *Geology*, 32(2) :97–100.

Wood, J. A., Dickey Jr, J. S., Marvin, U. B., and Powell, B. (1970). Lunar anorthosites and a geophysical model of the moon. In *Geochimica et Cosmochimica Acta Supplement, Volume 1. Proceedings of the Apollo 11 Lunar Science Conference held*

5-8 January, 1970 in Houston, TX. Volume 1 : Mineraolgy and Petrology. Edited by AA Levinson. New York : Pergammon Press, 1970., p. 965, volume 1, page 965.

Wray, J. J., Hansen, S. T., Dufek, J., Swayze, G. A., Murchie, S. L., Seelos, F. P., Skok, J. R., Irwin, R. P., and Ghiorso, M. S. (2013). Prolonged magmatic activity on Mars inferred from the detection of felsic rocks. *Nature Geoscience*, 6(12) :1013–1017.

Wright, V., Dasent, J., Kilburn, R., and Manga, M. (2022). A minimally cemented shallow crust beneath Insight. *Geophysical Research Letters*, 49(15) :e2022GL099250.

Xiao, L., Huang, J., Christensen, P. R., Greeley, R., Williams, D. A., Zhao, J., and He, Q. (2012). Ancient volcanism and its implication for thermal evolution of Mars. *Earth and Planetary Science Letters*, 323 :9–18.

Yan, C., Barik, A., Stanley, S., Leung, J. S.-Y., Mittelholz, A., Johnson, C. L., Plesa, A.-C., and Rivoldini, A. (2023). An ancient Martian dynamo driven by hemispheric heating : Effect of thermal boundary conditions. *The Planetary Science Journal*, 4(1) :11.

Yoshida, M. and Kageyama, A. (2006). Low-degree mantle convection with strongly temperature-and depth-dependent viscosity in a three-dimensional spherical shell. *Journal of Geophysical Research : Solid Earth*, 111(B3).

Yoshizaki, T. and McDonough, W. F. (2020). The composition of Mars. *Geochimica et Cosmochimica Acta*, 273 :137–162.

Zheng, Y., Nimmo, F., and Lay, T. (2015). Seismological implications of a lithospheric low seismic velocity zone in Mars. *Physics of the Earth and Planetary Interiors*, 240 :132–141.

Zhong, S. (2009). Migration of Tharsis volcanism on Mars caused by differential rotation of the lithosphere. *Nature Geoscience*, 2(1) :19–23.

Zhong, S. and Zuber, M. T. (2001). Degree-1 mantle convection and the crustal dichotomy on Mars. *Earth and Planetary Science Letters*, 189(1-2) :75–84.

Abstract :
Seismology has recently provided important information about the structure of the interior of Mars, and in particular its crust. The average thickness of the crust is constrained to between 50 and 67 km, with a difference of 12 to 34 km between the northern and southern hemispheres. This dichotomy is an essential feature of the Martian surface. In this thesis, I propose a new mechanism to explain its formation, based on a positive feedback process between the thickness of the crust and its extraction. As the crust is enriched in heat-producing elements, when it is thicker, the base of the lithosphere, which is a rheological and therefore thermal limit, is reached at a shallower depth. Under a thinned lithosphere, the fraction of liquid in the mantle is higher, because it is at the same temperature but at lower pressure. Magma extraction rates are therefore higher and the crust grows faster where it is thicker. Since heat diffusion in the lithosphere favours long wavelengths, we propose that this mechanism could have generated the Martian dichotomy. To test this, I have developed an asymmetric parametric thermal evolution model that includes the extraction of the crust. With this model, we demonstrate that a crustal dichotomy develops and grows from an initial negligible hemispherical perturbation. For a certain range of parameters, our model is able to reproduce observations of crustal thickness and mantle thermal structure. We also show that a stagnant layer planet with a strong crust thickness dichotomy cools slightly faster than a planet with a constant crust thickness. Finally, we show that our dichotomy growth model also provides an explanation for the formation of differentiated rocks in the Southern Highlands.

Résumé :
La sismologie a récemment apporté d'importantes informations sur la structure de l'intérieur de Mars et en particulier de sa croûte. L'épaisseur moyenne de la croûte est contrainte entre 50 et 67 km avec une différence de 12 à 34 km entre les hémisphères Nord et Sud. Cette dichotomie est une caractéristique essentielle de la surface Martienne. Dans cette thèse, je propose un nouveau mécanisme pour expliquer sa formation, basé sur un processus de rétroaction positive entre l'épaisseur de la croûte et son extraction. La croûte étant enrichie en éléments producteurs de chaleur, lorsqu'elle est plus épaisse, la base de la lithosphère, qui est une limite rhéologique et donc thermique, est atteinte à une profondeur moindre. Sous une lithosphère amincie, la fraction de liquide dans le manteau est plus élevée, car à une même température mais à plus faible pression. Les vitesses d'extraction de magma sont alors plus élevées et la croûte croit plus rapidement là où elle est plus épaisse. La diffusion de la chaleur dans la lithosphère favorisant les grandes longueurs d'onde, nous proposons que ce mécanisme ait pu générer la dichotomie martienne. Pour le tester, j'ai développé un modèle d'évolution thermique paramétré asymétrique incluant l'extraction de la croûte. Avec ce modèle, nous démontrons qu'une dichotomie crustale se développe et croit à partir d'une perturbation hémisphérique initiale négligeable. Pour une certaine gamme de paramètres, notre modèle est capable de reproduire les observations sur l'épaisseur de la croûte et la structure thermique du manteau. Nous montrons aussi qu'une planète en couche stagnante avec une forte dichotomie d'épaisseur de croûte se refroidit légèrement plus vite qu'une planète dont la croûte est d'épaisseur constante. Enfin, nous démontrons que notre modèle de croissance de la dichotomie fournit également une explication pour la formation de roches différenciées dans les Hautes Plateaux du Sud.